FLORIDA INTERNATIONAL UNIVERSITY

Miami, Florida

SEARCH FOR EXCITED CASCADE HYPERONS (Ξ^{*-}) USING THE CLAS12 SPECTROMETER AT JEFFERSON LABORATORY

A dissertation submitted in partial fulfillment of

the requirements for the degree of

DOCTOR OF PHILOSOPHY

in

PHYSICS

by

Achyut Khanal

2022

To: Dean Michael Heithaus
College of Arts, Sciences and Education

This dissertation, written by Achyut Khanal, and entitled Search for Excited Cascade Hyperons (Ξ^{*-}) using the CLAS12 Spectrometer at Jefferson Laboratory, having been approved in respect to style and intellectual content, is referred to you for judgment.

We have read this dissertation and recommend that it be approved.

Daniel S. Carman

David Chatfield

Misak M. Sargsian

Lei Guo, Co-Major Professor

Brian A. Raue, Co-Major Professor

Date of Defense: October 11, 2022

The dissertation of Achyut Khanal is approved.

Dean Michael Heithaus
College of Arts, Sciences and Education

Andrés G. Gil
Vice President for Research and Economic Development
and Dean of the University Graduate School

Florida International University, 2022

DEDICATION

To my parents Lekhanath Khanal and Manorama Khanal, whose support has been invaluable for me to accomplish my academic and professional goals.

ACKNOWLEDGMENTS

I would like to express my sincere gratitude to my advisors, Prof. Brian A. Raue and Prof. Lei Guo, for their invaluable support and guidance throughout this work. They introduced me as a Ph.D. researcher to the fascinating world of experimental nuclear physics and allowed me to be involved in various exciting physics programs at the Thomas Jefferson National Accelerator Facility. Their years of research experience in baryon spectroscopy and cascade physics helped me accomplish my academic and professional goals in time. I will forever be grateful and indebted to them for providing me with such opportunities, support, and guidance throughout my Ph.D. research. I respect the enormous amount of time and effort they dedicated to my education and have taken their advice to heart.

I am grateful to Eugene Pasyuk, Daniel Carman, and Raffaella De Vita for their mentoring at JLab and to other staff scientists from JLab's experimental Hall B for their willingness to discuss any physics-related topics. I want to express my gratitude to the entire CLAS12 Very Strange Group for guiding my analysis, providing feedback, and following my research progress throughout my Ph.D. studies. My dissertation committee equally deserves my gratitude for participating in this project and guiding me along the way. They have taken time out of their busy schedules to ensure that my thesis meets publication requirements.

I want to thank the Hall-B research group of the Experimental Nuclear Physics Division, the entire CLAS Collaboration, and the CEBAF facility at Thomas Jefferson National Laboratory for their outstanding efforts in making RG-A experiments possible.

The path to a Ph.D. is complex, and family and friends' support is essential. I will be eternally grateful to my wife, Sabita Acharya, for being such an essential part of my life and always supporting me emotionally. I am also thankful for the unwavering

support of my parents (Lekhanath Khanal and Manorama Khanal), brother (Bedan Khanal), and sister (Upama Khanal) throughout this incredible journey.

I would also like to remember Abishek, Resma, Hem, Jose, Shankar, Taya, Lamya, Trevor, and Rupesh. Thank you all for your friendship. The journey would have been difficult without you all.

ABSTRACT OF THE DISSERTATION

SEARCH FOR EXCITED CASCADE HYPERONS (Ξ^{*-}) USING THE CLAS12 SPECTROMETER AT JEFFERSON LABORATORY

by

Achyut Khanal

Florida International University, 2022

Miami, Florida

Professor Lei Guo, Co-Major Professor

Professor Brian Raue, Co-Major Professor

The number of experimentally observed doubly strange Cascade states to date is far fewer than has been predicted theoretically. The CLAS12 Very Strange physics program ($E12-11-005A$) at the Thomas Jefferson National Accelerator Facility aims to study the electroproduction of these states using the newly upgraded CEBAF Large Acceptance Spectrometer for 12 GeV (CLAS12) in experimental Hall B. In this project, the reaction $ep \rightarrow e'K^+K^+\Xi^{*-} \rightarrow e'K^+K^+K^-(\Lambda/\Sigma^0)$ is studied using CLAS12 Run Group A (RG-A) data sets taken by impinging electron beams of 10.2 and 10.6 GeV energies on an LH_2 target. Scattered electrons are detected with either the Forward Detector (FD), covering a polar angle range of 5° to 35° to study electroproduction, or with the Forward Tagger (FT), covering a polar angle range of 2.5° to 4.5°, to study quasi-real photoproduction. The CLAS12 detector with nearly a 4π solid angle coverage is used to detect scattered electrons and charged kaons in the final state. Λ/Σ^0 hyperons are reconstructed using the missing mass technique to explore intermediate doubly-strange hyperons (Ξ^{*-}) that decay to K^- and Λ/Σ^0. No statistically significant Ξ^{*-} states other than the $\Xi^{*-}(1530)$ were found in the missing mass spectra based on the currently available statistics in the CLAS12-FD acceptance only. A maximum log-likelihood method is implemented to determine the statistical significance and the upper limits on the $\Xi^{*-}(1820)$ electroproduction

cross section by constructing 95% confidence level boundaries on the $\Xi^{*-}(1820)$ yields. Additional research was conducted to investigate the upper limit electroproduction cross section of the reaction $ep \rightarrow e'K^+K^+\Xi^{*-} \rightarrow e'K^+K^+K^-(\Lambda/\Sigma^0)$ as a function of the electroproduced Ξ^{*-} mass and the differential cross section $(\frac{d\sigma}{dMM(e'K^+K^+)})$ as a function of missing mass $MM(e'K^+K^+)$ for electroproduction and quasi-real photoproduction processes.

TABLE OF CONTENTS

LIST OF TABLES

TABLE PAGE

LIST OF FIGURES

CHAPTER 1

Introduction

A scattering experiment by Robert Hofstadter and collaborators in the 1950's at Stanford University using electrons to peer inside the proton of the hydrogen atom revealed that protons and neutrons are not fundamental (i.e. point-like) [1, 2] in nature. The revolutionary discovery of that time in the field of particle physics was awarded the 1961 Nobel Prize. Following that discovery, several electron scattering experiments from all around the world discovered that protons and neutrons themselves have a rich internal structure. Protons and neutrons are made up of electrically charged constituent particles called quarks [3, 4]. Moreover, a growing number of other particles showing different properties than protons and neutrons also made up of quarks was discovered.

To organize these subatomic particles, Murray Gell−Mann first came up with an abstract concept of grouping them based on their properties like charge, spin, flavor content, and isospin. Gell−Mann published a book describing his abstract concept in 1964 called the "The Eightfold Way" [5]. Gell−Mann introduced three fundamental quark flavors, up, down, and strange, for the first time. Each of these quarks has a corresponding anti-quark. Quarks and anti-quarks have been assigned fractional electric charges of $-1/3e$ or $2/3e$, where e is the magnitude of the electron charge. They have positive parity by convention. Other than the fractional electric charge, quarks also carry a color charge and anti-quarks an anti-color charge. Gell−Mann realized that these three fundamental quarks and anti-quarks could form all of the hadrons known at that time.

The family of subatomic particles made with three quark combinations is called baryons. The eightfold way organizes the lowest-lying spin$-1/2$ baryons into an octet

and spin$-3/2$ baryons into a decuplet. One of the predicted particles with three strange quarks in the baryon decuplet, known as Ω^-, was discovered in early 1964 [6]. This discovery, based on the Gell-Mann's prediction was a key to the advancement of the quark model.

Similarly, the family of subatomic particles composed of quark and anti-quark combinations is called mesons. The eightfold way organized mesons into octets and singlets. The lowest-lying spin-0 mesons are organized into an octet. The chargeless, strangeless eta prime meson (η') was originally classified by itself as a singlet in the eightfold way. Later in time, after the discovery of the quark model, all mesons were viewed as part of a meson nonet.

Both the baryon and meson families of subatomic particles are included in the hadron family of subatomic particles. Such an organizational scheme of hadrons proposed by Gell$-$Mann in his book led to the development of the quark model. Gell-Mann's contributions and discoveries for the classification of subatomic particles and their interactions were recognized with the 1969 Nobel Prize in physics.

With the advancement of time and scientific discovery, three heavier mass quarks were also added to the list of quarks, resulting in a total of six quarks. The three fundamental light up, down, and strange quarks initially proposed by Gell$-$Mann, along with three heavier quarks top, bottom, and charm, as shown in Fig. 1.1, constitute three generations of quarks. The six different types of quarks with different masses are known as the six flavors of quarks.

Besides quarks, there is a lepton family of elementary particles. The best known of all leptons is the electron. Just like quarks, there are three generations of leptons that include the electron, muon, and tau lepton, and their respective neutrinos. The three generations of leptons are shown in Fig. 1.1.

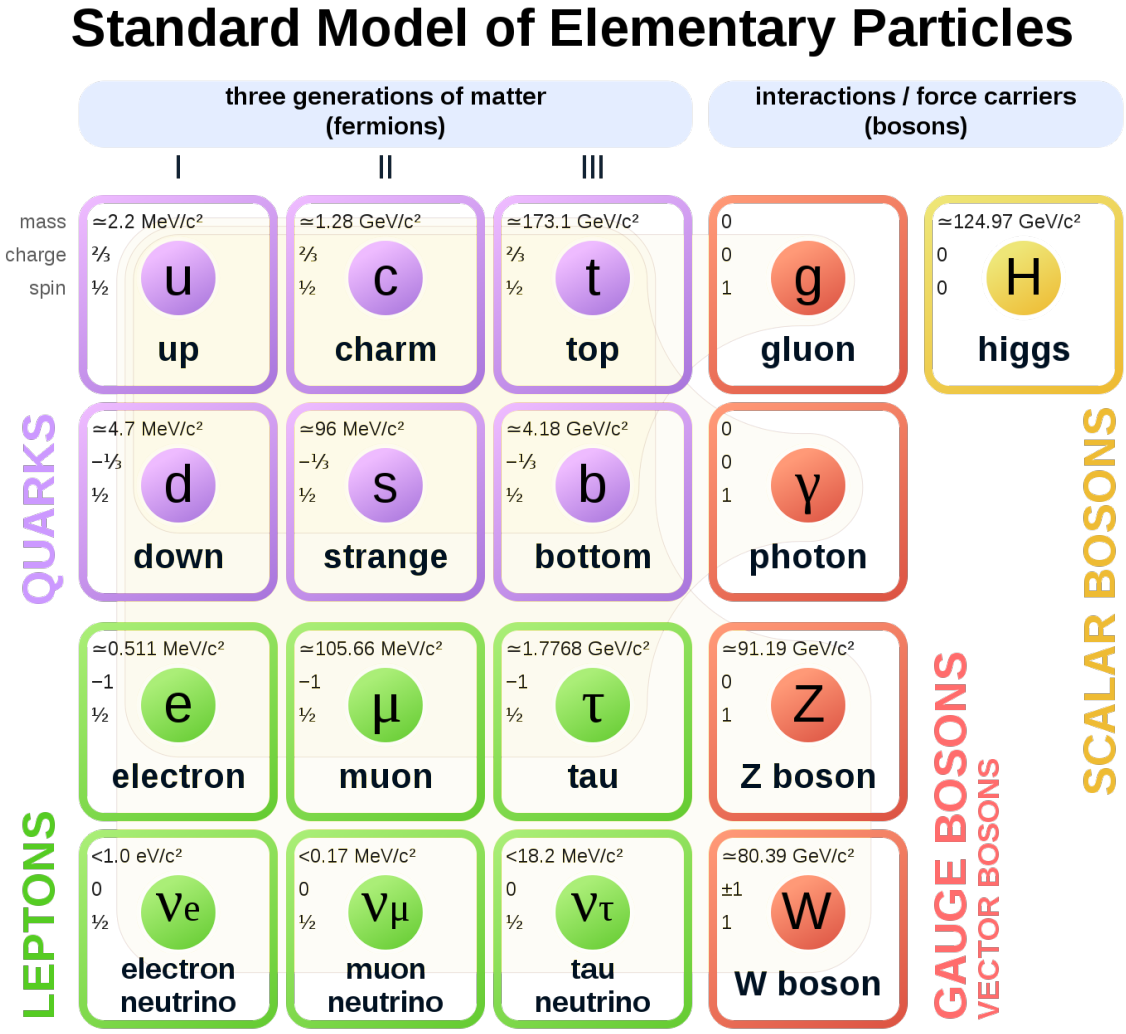

Figure 1.1: The Standard Model of elementary particles shows three generations of quarks, leptons, and force carrier bosons. Image available to download in Ref. [7].

Quarks and leptons are fermions with half−integer spin and they obey Fermi-Dirac statistics. The interaction between quarks and leptons is mediated by quanta called gauge bosons. Bosons have an integer spin and they obey Bose-Einstein statistics.

To explain all of the observed interactions involved in the different families of subatomic particles, physicists developed a simple and comprehensive theory, which is known as the Standard Model of elementary particles [7]. It explains hundreds of ele-

mentary particles and most of the complex phenomena observed in their interactions. The Standard Model in today's picture can be summarized as a theory that explains the visible universe in terms of six quarks, six leptons, and four gauge bosons that mediate the strong (gluon), weak (W and Z), and electromagnetic (photon) forces. Predictions of the Standard Model at high energy have been shown to be valid with incredible precision. Hence, it is an extraordinarily brilliant and successful theory as it fits beautifully even in today's quantum world. However, it does not explain everything in the universe. For example, the gravitational force is not explained by the Standard Model, and the corresponding force-mediating gauge boson, named the graviton, has not yet been observed experimentally. It also does not say anything about the dark matter and dark energy that pervades the universe.

The strong force is responsible to keep protons and neutrons inside the nucleus of an atom. Quarks inside nucleons interact with each other by exchanging gluons [8, 9]. Properties of such strong interactions acting between quarks and gluons inside nucleons are described by the field theory of Quantum Chromodynamics (QCD) [10–12].

1.1 Quantum Chromodynamics

Quantum Chromodynamics (QCD) is a non-abelian gauge field theory that describes the strong interaction between quarks and gluons. In analogy to the electric charge in the electromagnetic interaction described within Quantum Electrodynamics (QED), there are three color charges and corresponding anti-color charges associated with the strong interaction. These three color charges are known as the green, red, and blue charges of the strong interaction, and have three corresponding anti-color charges known as anti-green, anti-red, and anti-blue. Since quarks possess color charge, they are said to be in the fundamental representation of the $SU(3)_c$ color Lie group.

Gluons are massless, spin-1 gauge bosons with no electric charge. Gluons carry color charge and anti-color charge, and hence they mediate color interactions among quarks. There are 8 allowed color, anti-color charge combinations for gluons. Since gluons carry color charges, they can self interact even in the absence of quarks, unlike photons in QED. Gluons transform under the adjoint representation of the $SU(3)_c$ color Lie group [13].

The Lagrangian density governing the strong interaction between quarks and gluons in QCD is given by

$$\mathcal{L}_{QCD} = \bar{\psi}_{f,i}(\imath\gamma^{\mu}(D_{\mu})_{i,j} - m_f\delta_{i,j})\psi_{f,j} - \frac{1}{4}G^{\mu,\nu}_{a}G^{a}_{\mu,\nu}. \tag{1.1}$$

A summation is assumed over the repeated indices. $\bar{\psi}_{f,i}$ and $\psi_{f,j}$ are quark-field Dirac spinors for a quark of flavor f and mass m_f with anti-color and color indicies of i and j, respectively. Hence, the indicies i and j run from 1 to 3 to represent the three colors of quarks. γ^{μ} are the contravariant 4×4 gamma matrices of the Dirac representation. $(D_{\mu})_{i,j}$ is the covariant derivative associated with the fundamental representation of the color group $SU(3)_c$, which contains the quark-gluon interaction term, and $G^{\mu,\nu}_{a}$ is the gluon field strength tensor for a color-charge a. These are given by

$$(D_{\mu})_{i,j} = \partial_{\mu}\delta_{i,j} - g_s A^{a}_{\mu}\gamma^{\mu}T^{a}_{i,j}, \tag{1.2}$$

$$G^{\mu,\nu}_{a} = \partial^{\mu}A^{\nu}_{a} - \partial^{\nu}A^{\mu}_{a} + g_s f_{abc}A^{\mu}_{b}A^{\nu}_{c}, \tag{1.3}$$

where g_s is the strong interaction coupling constant of QCD analogous to the electric charge, e, in the QED Lagrangian. f_{abc} are the $SU(3)_c$ structure constants. $T^{a}_{i,j}$ corresponds to the eight linearly-independent 3×3 Gell-Mann matrices and are the

generators of the fundamental representation of $SU(3)_c$. A^a are the eight vector fields for a gluon with color charge and anti-charge combination a running from 1 to 8.

The strong interaction compared to the electromagnetic interaction possesses two unique features: asymptotic freedom [11,12] and color confinement [14]. According to asymptotic freedom, quarks feel a decrease in their interaction strength when they get very close to each other. The distance between two quarks is inversely proportional to the momentum transfer Q between them. This implies that at high Q, quarks can move more freely with less constraint. This freedom of motion of quarks at short distances, for example, when they are inside a hadron, is known as asymptotic freedom.

Another unique feature of the strong interaction, color confinement, describes the effect in which the quarks always exist in a group, i.e. with baryons or mesons. Quarks in a hadron are confined in such a way that it results in a state with zero total color charge. Such color neutrality in hadrons can be achieved in two different ways: by combining color and anti-color quarks, as in mesons, or by combining quarks with all of the colors or anti-colors, as in baryons. In this way, only color-neutral combination of quarks can exist as a valid physical state in nature.

Since quarks themselves are not color neutral, we cannot observe and isolate individual quarks in nature. So one can think about what happens if we try to separate bound quarks. If we try to separate bound quarks, the strength of the strong interaction increases with increasing distance between them. Eventually, a point will be reached where the energy required to separate bound quarks is greater than the energy required to form a quark-anti-quark pair from the vacuum. Such pairs spontaneously produced from the vacuum can combine with the originally bound quarks, resulting in new bound states of hadrons.

1.2 Hadron Spectroscopy

Hadron spectroscopy is the study of the spectrum of the hadrons. It characterizes hadrons in different groups based on their properties such as quantum numbers, mass, and quark content. Since hadrons are the bound states of quarks and gluons, properties of hadrons come from their constituents. Although the quantum numbers of the hadrons are naively given by their constituent quarks, known as valance quarks and anti-quarks, many properties are not. For example, the major contribution ($\sim$ 98.5%) to the total rest mass of the proton is believed to arise from the interaction between the sea of virtual quark-anti-quark pairs, known as sea quarks, and virtual gluons confined within the proton. Also, the total spin of the proton has contributions from sea quarks and gluons in addition to that from the valance quarks. Table 1.1 shows the additive quantum numbers assigned to the six quark flavors from the Standard Model.

The major quantum numbers used to describe a hadron are its total angular momentum, J, parity, P, and isospin, I. The total angular momentum quantum number J is the sum of the orbital angular momentum L of the constituent valance quarks and their total intrinsic spin S. Baryon parity is given by $(-1)^L$. On the other hand, meson parity is given by $(-1)^{L+1}$ to account for the fact that mesons are bound states with opposite parity quark-anti-quark combinations. All ground state ($L = 0$) baryons have even parity ($P = -1^0$), while all ground state mesons have odd parity $P = -1$. The isospin quantum number reveals how many different charged states of a hadron can exist with the same spin and parity configuration. There are $2I + 1$ different charged states possible for a particle with isospin quantum number I. The proton and neutron are the well-known charged states of the nucleon with isospin 1/2.

Characteristic Quantum Numbers of Six Quarks

Flavor	d	u	s	c	b	t
$Q-$ electric charge	$-\frac{1}{3}$	$+\frac{2}{3}$	$-\frac{1}{3}$	$+\frac{2}{3}$	$-\frac{1}{3}$	$+\frac{2}{3}$
$I-$ isospin	$\frac{1}{2}$	$\frac{1}{2}$	0	0	0	0
I_z- isospin z-component	$-\frac{1}{2}$	$+\frac{1}{2}$	0	0	0	0
J^P	$\frac{1}{2}^+$	$\frac{1}{2}^+$	$\frac{1}{2}^+$	$\frac{1}{2}^+$	$\frac{1}{2}^+$	$\frac{1}{2}^+$
$S-$ strangeness	0	0	-1	0	0	0
$C-$ charm	0	0	0	$+1$	0	0
$B-$ beauty	0	0	0	0	-1	0
$T-$ truth	0	0	0	0	0	$+1$
Current-quark mass	$4.67^{+0.48}_{-0.17}$ MeV	$2.16^{+0.49}_{-0.26}$ MeV	$93.4^{+8.6}_{-3.4}$ MeV	$1.27^{+0.03}_{-0.04}$ GeV	$4.18^{+0.04}_{-0.03}$ GeV	$172.69\pm$ 0.30 GeV

Table 1.1: Three generations of quarks from the Standard Model with their additive quantum numbers [15].

In addition to J, P, and I quantum numbers describing a hadron, there are a few more quantum numbers used while mapping the spectrum of hadrons. These include electric charge (Q), baryon number (B), strangeness (S), charge conjugation (C), and G-parity (G). The total electric charge of a hadron, Q, is an additive combination of the electric charges of the constituent quarks. The baryon number, B, for mesons and baryons is, respectively, 0 and 1.

The strangeness quantum number, S, is the flavor quantum number assigned to strange quarks. The flavor of the quark determines its flavor quantum number. There are six flavor quantum numbers uniquely defined to differentiate the six flavors of quark. By convention, the flavor quantum number of a quark has the same sign as its electric charge. For example, the strangeness of the strange quark is $S = -1$, while the truth of the top quark is $T = +1$. Table 1.1 summarizes the different quantum numbers of all six quark flavors.

Charge conjugation describes a transformation that switches particles with their corresponding antiparticles by changing the sign of all associated quantum charges. The quantum number of particles that describes its behavior under the symmetry operation of charge conjugation is called charge conjugation parity, C-parity. C-parity applies only to the electrically neutral system. C-parity of an electrically neutral $q\bar{q}$ system made up of quark, q, and its own antiquark, $\bar{q}$, is given by $C(q\bar{q}) = (-1)^{L+S}$. In the case of electrically charged particles such as $u\bar{d}$ and $d\bar{u}$ states, C-parity cannot be applied to describe charge conjugation symmetry. However, there is another quantum number in particle physics that results from the generalization of C-parity and can be applied to multiplets of all charged particles. Such a generalized version of C-parity is known as G-parity. G-parity of all charged states of a given multiplet of particles is given by $(-1)^{L+S+I}$. In the pion triplet with π^+, π^0, and π^-, C-parity can only be applied to the π^0. On the other hand, generalized G-parity can be applied to all

members of the multiplet regardless of their electrical charge by considering $I = 0$ and $I = 1/2$, respectively, for π^0 and $\pi^{\pm}$.

In order to uniquely identify and map a baryon state in the baryon spectrum, mass, constituent quarks, and quantum numbers I and J^P are sufficient. However, to uniquely identify a meson, an extra quantum number C-parity has to be defined as well; that is, mesons are classified in J^{PC} multiplets.

In modern particle physics, almost all hadrons are arranged in different groups using classification schemes developed based on a successful theoretical model called the quark model [16]. The quark model classifies hadrons in different groups based on their valance quark content. Any observed hadron that does not fall into any of the quark model classification schemes and is different from the ordinary quark structure of $q\bar{q}$ for mesons and qqq for baryons is considered exotic. Exotic hadrons are not allowed by the quark model. There are certain combinations of J^{PC} meson states that are not allowed in the quark model. For example, mesons with $J^{PC} = 0^{--}, 0^{+-}, 1^{-+}, 2^{+-}, 3^{-+}$, etc. are forbidden in the $q\bar{q}$ model.

Directly related to this work, baryon spectroscopy deals with the mapping of the spectrum of baryons. Baryon spectroscopy helps to understand the structure and dynamics of the nucleons and their excited states. Baryons are strongly interacting fermions. In the most general case, baryons contain three constituent valance quarks, although there is evidence of several charmed "pentaquark" baryon states that fall in the exotic category. In the Particle Data Group (PDG) [15], baryons are named as N or Δ, respectively, for baryons with isospin 1/2 or 3/2. N and Δ baryons are comprised of light quark u, d combinations only. Particles comprised of two quarks u, d and one s quark combination are named Λ or Σ baryons and generically known as hyperons. The two light quarks in the Λ and Σ baryons couple to isospin 0 and 1, respectively. Particles with one u or d quark and two s quarks are called

Cascade, Ξ, baryons. Ξ baryons have isospin 1/2. An Omega, Ω, baryon has no u or d quarks but all three s quarks in it with 0 isospin. These baryons are organized into an octet and decuplet of baryon states in the flavor symmetry $SU(3)_F$ of Quantum Chromodynamics. The nucleons, hyperons, and Cascades with spin $J = 1/2$ complete the octet of ground state baryons. Whereas Δs, excited Σs, excited Ξs, and the Ω with spin $J = 3/2$ complete the decuplet of the first excited state baryons. Figure 1.2 shows the octet and decuplet states of baryons from $SU(3)$ flavor symmetry.

All baryons acquire a certain mass. Quarks are nearly massless and gluons have zero mass. The total mass of any baryon is very high compared to its constituent quark masses. Almost 99% of the baryon mass does not come from the quark masses. So, how does a baryon acquire its mass? It is believed that almost all of the mass of a baryon comes from the strong interaction energy of the quark and gluon fields. The strong interaction between any quark pair in baryons is governed by the Lagrangian density of QCD given by Eq. (1.1). We can separate the QCD Lagrangian into two parts. The first part depends only on the quark and gluon fields, which do not contain quark masses. The second part has the quark mass (second term in Eq. (1.1)) and is actually the one that is dependent on quark flavor. In the limit that quark masses are very small in comparison to the total baryon mass, one can treat the quark-mass term in the QCD Lagrangian as a perturbation. This implies that the flavor independent part of the QCD Lagrangian, which depends only on the quark and gluon fields, sets the mass scale for a given baryon $SU(3)_F$ multiplet. As a consequence of such symmetry, known as flavor symmetry of $SU(3)$, the excitation spectra of baryons are independent of the flavor of the constituent quarks. Thus, for every state of an octet of light baryons N^* and decuplet of light baryons Δ^*, there will be a corresponding octet or decuplet of Ξ^* states possessing similar properties [16–19].

Baryon octet and decuplet from $SU(3)$ flavor symmetry

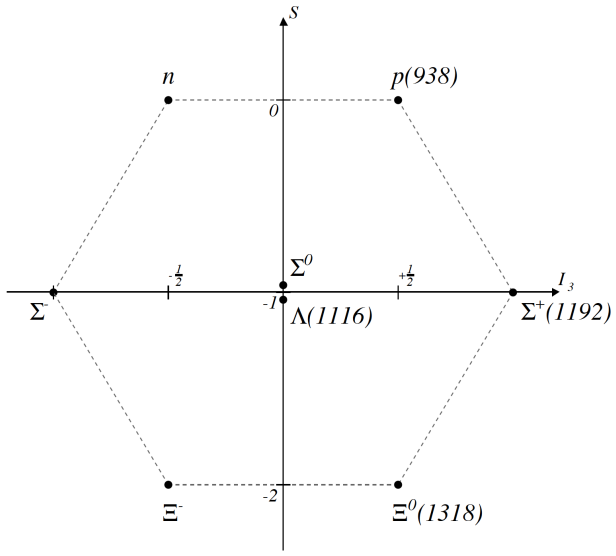

(a) Spin $\frac{1}{2}$ ground state baryon octet.

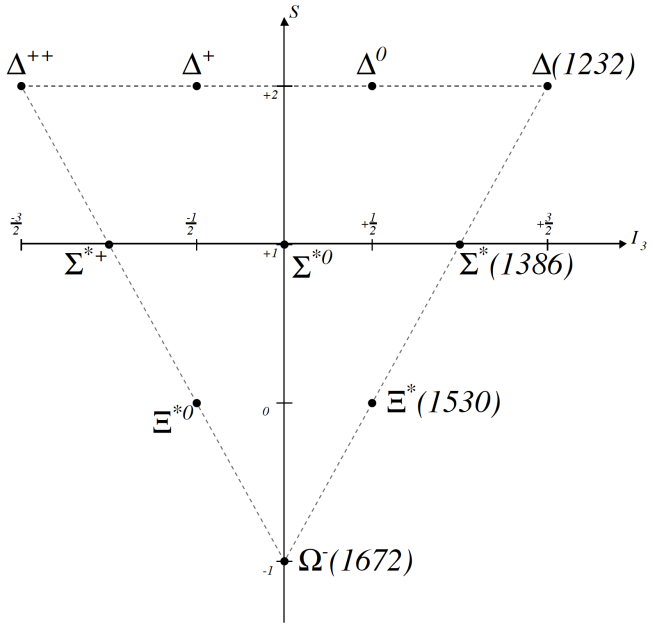

(b) Spin $\frac{3}{2}$ ground state baryon decuplet.

Figure 1.2: Octet and decuplet states of ground state baryons from $SU(3)$ flavor symmetry [16].

Among all of these ground state and excited state baryons in the baryon spectrum, we are particularly interested in the spectra of double-strange-quark Cascade

hyperons. The double strangeness feature of Cascade hyperons has some advantages while searching for Cascade states in comparison to N^* states and Δ^* states, which are summarized in the next section.

1.3 Importance of Cascade Physics in Baryon Spectroscopy

After the discovery of the Δ in the early 1950's, particle physicists began to experimentally explore the structure and dynamics of the nucleon and its excited states. While much has been accomplished to this date, there is still much work left in order to address several unanswered questions in the field of baryon spectroscopy. The setup of the experiment, collection, processing, and analysis of a big data set utilizing restricted computational resources made the nature of the work involved technically challenging and expensive. Even if you were able to collect and analyze experimental data, the broad and overlapping spectrum of the excited states N^*, Δ^* makes it very difficult to identify and extract the details of the individual excited states [20]. Hence, sophisticated analysis techniques like partial wave analyses are required to study the resonances from the experimental data in such a broad and overlapping spectrum. Therefore, to give a new way to study the baryon spectrum, one can look for particles with a narrow width compared to N^* and Δ^* states, but still possessing properties similar to those states. Experimentally searching for Cascade baryon resonances can be a suitable option in order to alleviate the overall situation and to move forward with a new method of baryon spectroscopy. Indeed, the very existence of the CLAS spectrometer in the past and the new CLAS12 spectrometer, along with the upgraded CEBAF accelerator at Jefferson Lab and improvements in computing, made doing the spectroscopy experiments possible.

As previously mentioned, evidence of flavor symmetry $SU(3)_F$ by baryons implies that we should expect an octet of Ξ^* with properties similar to every excited N^*

and a decuplet of Ξ^* with properties similar to every Δ^* state. There are far fewer experimentally observed Cascade states than have been predicted from the quark model. Theoretical calculations to date based on $SU(3)$ flavor symmetry using several models such as relativistic and non-relativistic quark models [16], along with algebraic [19] and chiral-symmetric [18] models, and more recent lattice QCD calculations [21], predict a lot of possible Cascade states. However, there are only eleven Ξ states listed in the Review of Particle Physics by the Particle Data Group (PDG) updated in 2022 as shown in Table 1.2. The number of experimentally discovered Cascade states in the PDG has not been changed since the early 1980's. To date, we have only two Cascade states, the ground state $\Xi(1320)$ and first excited state $\Xi^*(1530)$, with four-star $(****)$ ratings, meaning that their quantum numbers, masses, and decay widths are well established. There are a few more Cascade states in the exploration stage demanding further experimental evidence of their existence and many more theoretically predicted Cascade states yet to be discovered experimentally.

Searching for missing Ξ states experimentally has a great advantage in the field of baryon spectroscopy. It addresses the well-known missing baryon problem by adding new baryon states in the PDG baryon table. Moreover, it would serve as an experimental means to directly test different theoretical models of baryon structure. The small number of experimentally observed Ξ states in the PDG clearly demands searching for the missing Ξ states with novel experimental techniques to validate the $SU(3)$ flavor symmetry of QCD, which predicts many more Ξ states.

The experimental production cross section of Ξ states is very low in comparison to their N and Δ cousins because of their higher mass and double-strange nature. However, the same double-strange feature makes it more appealing to search for Ξ^* states over N^* and Δ^* states due to the narrower widths expected for Cascades [22]. Narrow widths (typically a factor of 10 smaller) for Ξ^* in comparison to their N^*

Experimental status of Ξ states with observed decay modes

Particle	J^P	PDG rating	$\Xi\pi$	ΛK	$\Sigma^0 K$	$\Xi(1530)\pi$
$\Xi(1320)$	$1/2^+$	$****$				
$\Xi(1530)$	$3/2^+$	$****$	$***$			
$\Xi(1620)$		$*$	$*$			
$\Xi(1690)$		$***$		$***$	$**$	
$\Xi(1820)$	$3/2^-$	$***$	$**$	$***$	$**$	$**$
$\Xi(2030)$	$5/2^?$	$***$		$**$	$***$	
$\Xi(2120)$		$*$		$*$		
$\Xi(2250)$		$**$				
$\Xi(2370)$		$**$				
$\Xi(2500)$		$*$		$*$	$*$	

Table 1.2: The status of experimentally observed Ξ resonances with overall PDG ratings assigned to them. $****$ rating indicates the existence is certain and properties are fairly well explored. $***$ rating is assigned to those particles whose existence needs further confirmation. $**$ or $*$ rating, respectively, indicates that the experimental evidence of the existence of such particles is only fair or very poor [15, 22].

counterparts, make it practically feasible to single out specific Cascade resonances relative to the experimental backgrounds.

With all of these advantages of Cascade baryons in baryon spectroscopy, this dissertation aims to study the electroproduction of excited Cascade states. The goal is to experimentally explore missing excited Cascade states that are theoretically predicted by QCD based on $SU(3)$ flavor symmetry. Eventually, this study will shed light on the deeper understanding of the QCD Lagrangian Eq. (1.1).

1.4 Previous Experiments on Cascade Physics

Cascade baryons were first discovered at the Lawrence Radiation Laboratory [23]. A K^- beam with a momentum ranging from 1.7 to 2.7 GeV was incident on a hydrogen bubble chamber to obtain different Cascade data samples, leading to a determination of the lifetimes of the Ξ^- and Ξ^0. In addition, production and decay properties of Ξ^-, Ξ^0, and a few low-lying Ξ^* were also studied [24–26] by further analyzing the collected Cascade data sample. Similarly, a K^- beam of higher momentum at 5.5 GeV was used with a hydrogen bubble chamber to investigate Ξ^- production in K^-p interactions at Argonne National Laboratory [27]. Similar bubble chamber experiments at Brookhaven National Laboratory using a K^- beam to investigate K^-p interactions presented suggestive experimental evidence for the existence of the higher-mass Cascade states $\Xi(1820)$, $\Xi(2030)$, $\Xi(2430)$, and $\Xi(1930)$ [28, 29]. For the first time, evidence of the $\Xi(1620)$ [30] state was presented, although the suggested resonance was highly dominated by statistical fluctuations. They also presented evidence for the decay of $\Xi(1820)$ and $\Xi(1930)$ states via $\Xi(1530)\pi$ [31] channels.

Further experiments [32, 33] at CERN using a K^- beam and a bubble chamber to study the K^-p interaction showed suggestive evidence of higher mass Cascade states and determined the spin of the $\Xi(1820)$ resonance. Later on, CERN conducted

several experiments with the CERN SPS charged hyperon beam [34] to study the production of hyperons and hyperon resonances in $\Xi^- N$ interactions. These experiments produced much higher statistics in comparison to previous bubble chamber experiments of several previously observed Ξ resonances [35, 36]. However, using a charged hyperon beam on hydrogen could not produce any Ξ signal in the mass range around 1620 MeV, in contrast to what was observed from the kaon beam on hydrogen. From the study of the $\Xi^- Be$ interaction using a Ξ^- beam, it was concluded that the spin of the $\Xi(1820)$ is 3/2 and it has negative parity [37].

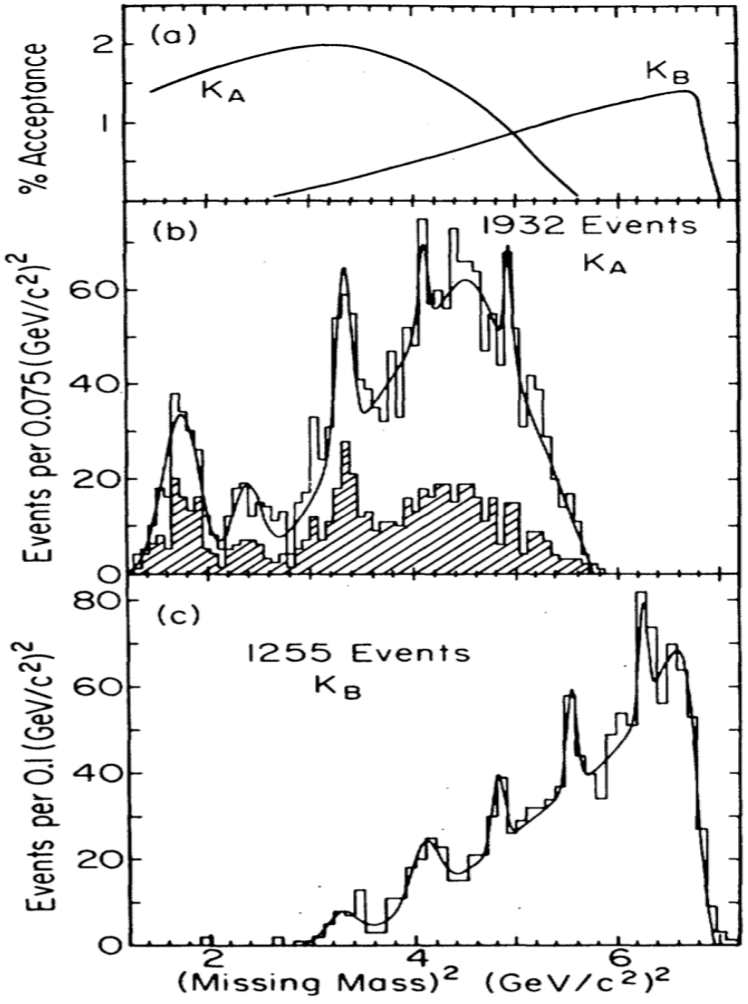

Figure 1.3: Observed Ξ states from the kaon production experiment performed at Brookhaven National Laboratory using the MultiParticle Spectrometer (MPS) in the missing mass squared (X) for $K^- p \to K^+_{slow}(X^-)$ [38].

All of these experimental pieces of evidence for higher-mass Ξ states from early experiments were very encouraging. However, the data from the low-sensitivity bubble chambers were not enough to provide strong confirmation of the properties and existence of Cascade states. Scientists from around the world started to design and develop more sensitive and sophisticated detectors for further study.

During the 1980's collaborators from Brookhaven National Laboratory performed a kaon production experiment using the MultiParticle Spectrometer (MPS). The MPS ramped up the experimental particle physics technique by using tracking detectors like proportional multiwire chambers and spark chambers to track the charged particles produced in the reactions. They used the missing mass technique to study the reaction $K^- p \to K^+_{slow}(X^-)$, where only a slow K^+ was detected in the final state [38]. All of the Ξ^* states produced in the reaction were then observed in the missing mass off of K^+_{slow}. Many Cascade baryon resonances, as shown in the missing-mass spectra in Fig. 1.3, appear to be present. The claimed Ξ states from this experiment were $\Xi(1320)$, $\Xi(1530)$, $\Xi(1820)$, $\Xi(2030)$, $\Xi(2250)$, $\Xi(2370)$, and $\Xi(2500)$. The experiment was not conclusive enough to differentiate the $\Xi(1620)$ and $\Xi(1690)$.

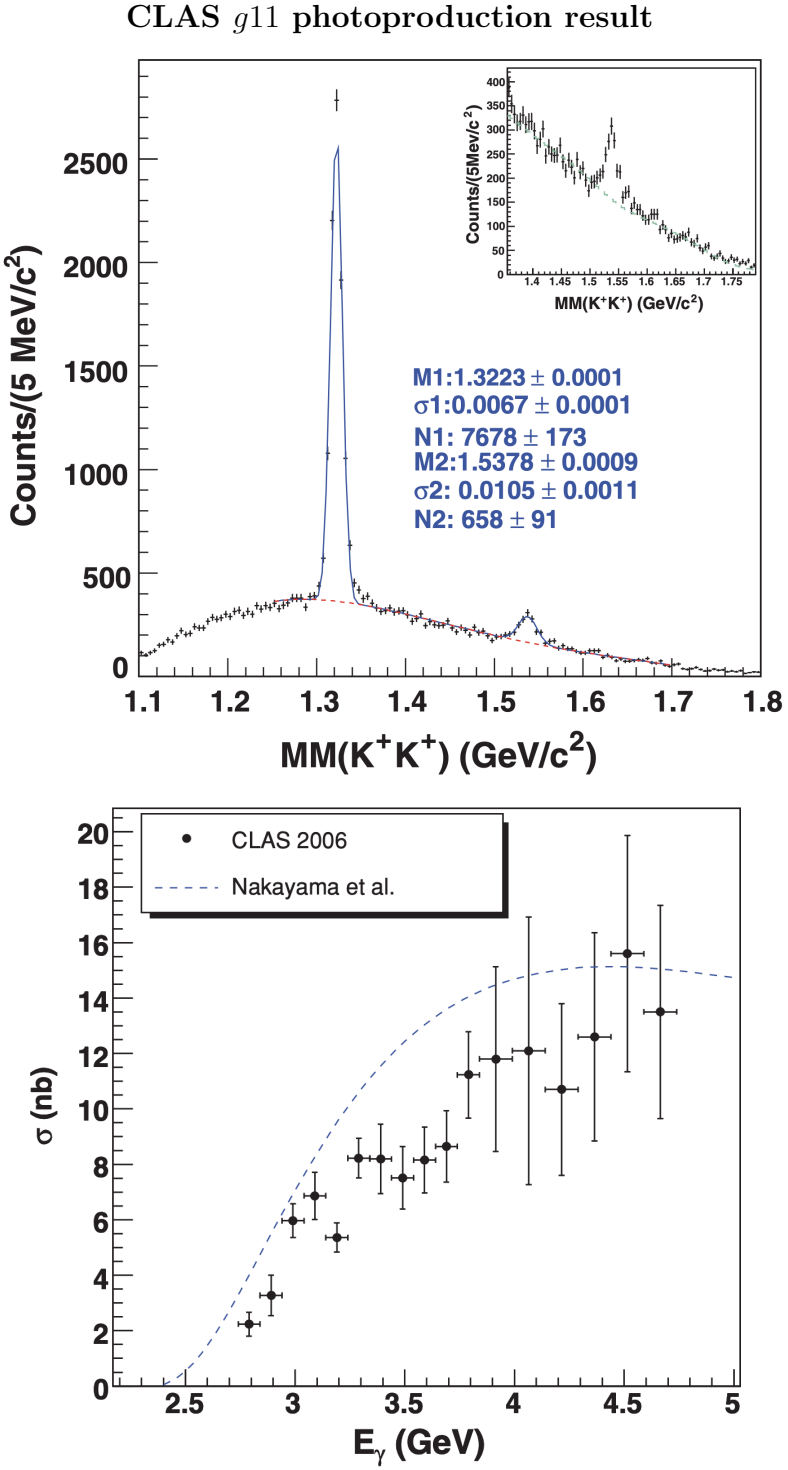

Figure 1.4: Missing mass spectra of K^+K^+ and the total photoproduction cross section result of Ξ^- in the reaction $\gamma p \rightarrow K^+K^+(X)$ using the CLAS $g11$ data set [39]. The total photoproduction cross section increases from 2 nb to 11 nb with increasing photon energy from 2.8 GeV to 3.8 GeV in agreement with the t channel theoretical model predicted by Nakayama *et al.* [40].

Most of what we know about Cascade baryons is provided by the experiments discussed above. These experiments used either a K^- beam or a charged hyperon beam on the target. In either case, it is energetically favorable to produce Ξ states in the final state as the production beam already contains an s quark in the initial state. This implies that only one $s\bar{s}$ pair has to be created from the vacuum during the interaction to favor Ξ production and conserve strangeness.

There have been several photoproduction studies conducted to search for Cascade states using data collected from the CEBAF Large Acceptance Spectrometer (CLAS) in Hall B at Jefferson Laboratory [39, 41, 42]. The photoproduction process involves an energetic high-energy photon beam incident on the target. The photoproduction process turns out to be energetically costly for Ξ production as the incident photon beam contains no s quark in the initial state. Hence, some of the energy of the incoming photon will be used to produce kaons in the final state to achieve the condition for Ξ production.

The study of Cascade photoproduction using the $g11$ CLAS data set shows clear resonances for the $\Xi^-(1320)$ ground state and the $\Xi^-(1530)$ excited state as shown in Fig. 1.4. The mass difference of the ground state Ξ doublet and the photoproduction cross sections for the $\Xi^-(1320)$ and $\Xi^-(1530)$ were reported. Cross sections for $\Xi^-(1320)$ were determined in the photon energy range from 2.75 to 3.85 GeV. It was shown that the total photoproduction cross section increases from 2 nb to 11 nb as shown in Fig. 1.4 with increasing photon energy for the $\Xi^-(1320)$. The differential photoproduction cross section of the $\Xi^-(1530)$ in the reaction $\gamma p \to K^+K^+(X)$ was also measured for the first time in the photon energy range of $3.35 - 4.75$ GeV [39].

Another CLAS photoproduction result using the $g12$ data set published in 2018 also presents strong evidence for the existence of the $\Xi^-(1320)$ and the $\Xi^-(1530)$ states as shown in Fig. 1.5. However, there was no sign of any other higher-mass

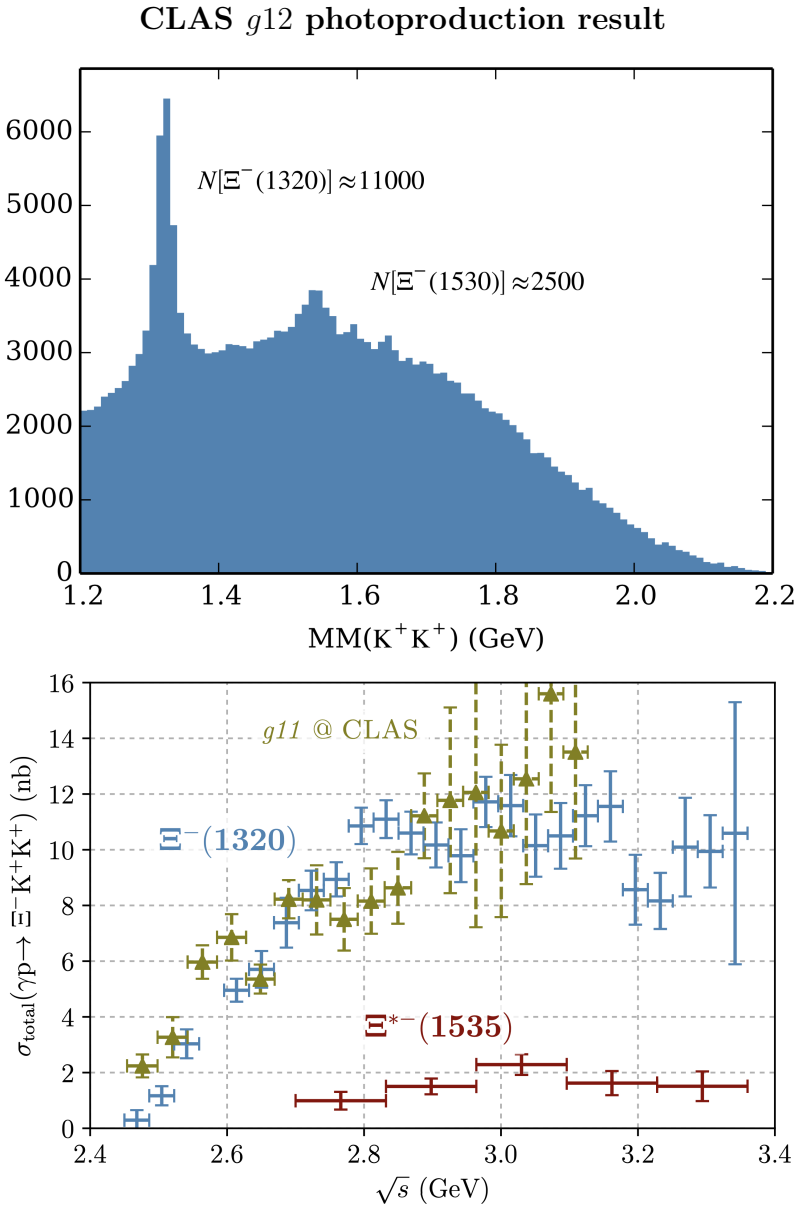

Figure 1.5: Missing mass spectra off K^+K^+ and the total photoproduction cross section result of the $\Xi^-(1320)$ and $\Xi^-(1530)$ states in the reaction $\gamma p \to K^+K^+(X)$ using the CLAS $g12$ data set [42].

Ξ^* resonances beyond the $\Xi^-(1530)$ in the missing mass spectrum. The CLAS $g12$ experiment was conducted with a higher photon energy (> 4 GeV) and flux compared to the $g11$ experiment in order to carry out a statistically significant search of higher mass Ξ states above the $\Xi^-(1530)$. The result of the $g12$ experiment was somewhat

surprising given that all the higher-mass Ξ^* states above the $\Xi^-(1530)$ were strongly suppressed. The study was only able to establish upper limits for the total cross sections for three known higher-mass Ξ^* states (at 1690, 1820, and 1950 MeV). In addition, the study presents the first-time photoproduction cross-section measurement of the $\Xi^-(1320)$ and $\Xi^-(1530)$ states at photon energies > 4 GeV. The study shows that the total cross section increases with increasing center-of-mass energies up to $\sqrt{s} = 2.8$ GeV in agreement with the previous $g11$ result and above that it levels off as shown in Fig. 1.5 to maintain constant values up to higher photon energies [42].

Photoproduction cross section results from both the $g11$ and $g12$ data sets suggested that the production mechanism for the $\Xi^-(1320)$ ground state and the $\Xi^-(1530)$ first excited state agrees with the two step t channel theoretical model through intermediate N^* and Y^* resonances of Nakayama *et al.* [40]. However, not seeing the known Ξ^* states above the $\Xi^-(1530)$ in the missing mass spectra could be an indication that the same theoretical model does not describe the photoproduction mechanism of these states.

With the recently upgraded CLAS detector for 12 GeV, known as the CLAS12 detector at Jefferson Laboratory, it is possible to further study the Ξ and Ξ^* states. This dissertation aims to study the electroproduction of experimentally under-explored Ξ hyperon production using the CLAS12 detector. The reaction $ep \to e'K^+K^+K^-(\Lambda/\Sigma^0)$ will be investigated by detecting scattered electrons either in the forward polar angle range of 5° to 35° or in the very forward polar angle range of 2.5° to 4.5°. Charged kaons will be detected within the acceptance of the CLAS12 Forward Detector system only for this study as the Central Detector tracking in the first phase data is insufficient to offer a reliable particle identification. The Λ/Σ^0 hyperons can be reconstructed using the missing mass technique to explore intermediate hyperons that decay to K^- and Λ/Σ^0.

CHAPTER 2

Experiment

2.1 The Thomas Jefferson National Accelerator

Figure 2.1: Detailed view of the Jefferson Lab CEBAF accelerator and the four experimental halls [43].

The experiment of interest in this dissertation was conducted at the Thomas Jefferson National Accelerator Facility in Newport News, VA. The Thomas Jefferson National Accelerator Facility, also known as Jefferson Lab (JLab), is home to the recently upgraded Continuous Electron Beam Accelerator Facility (CEBAF) and four experimental halls labeled as Hall A, B, C, and D. An overview of the JLab CEBAF accelerator site with four experimental halls can be seen in Fig. 2.1. CEBAF was designed to accelerate and recirculate electrons at high energies, and the four experimental halls were designed to conduct different physics experiments. The upgraded

CEBAF can accelerate electrons to energies up to 12 GeV. It provides a high-quality, high−luminosity beam of polarized electrons to different experimental halls in parallel for experimental purposes. In the experimental halls, particle detectors are designed to meet the requirements of various exciting physics programs. Our research utilizes the 11 GeV CEBAF electron beam and the new CLAS12 spectrometer situated in experimental Hall B.

2.2 CEBAF

The electron accelerator of JLab is called the Continuous Electron Beam Accelerator Facility (CEBAF). It was initially designed and built during the 1980s, and started delivering simultaneous beams to three experimental halls, A, B, and C, by the mid 1990s.

CEBAF is a world-leading and unique facility based on an innovative technology that uses superconducting radio-frequency cavities to transfer radiofrequency (RF) energy to electrons, providing the necessary acceleration gradient. It is constructed in a race−track configuration consisting of parallel north and south linear accelerators (LINACs). Each linear accelerator was initially comprised of 20 cryomodule units. Each cryomodule unit contains either five or seven superconducting radiofrequency (SRF) cavities. The north and south linear accelerators are connected to each other with the help of two recirculation arcs composed of dipole and quadrupole magnets. Dipole magnets steer the electron beam as it travels around the arc, whereas quadrupole magnets are used to focus the beam in one plane. The beam is passed through the linear accelerators up to five times before being delivered to the experimental halls. The upgrade of CEBAF included adding five new SRF cryomodule units to each linear accelerator for ten new cryomodules, as shown in Fig. 2.2. The new SRF cavities can produce four times the gradient than the pre-existing ones in

the LINACs. The upgrade also included an additional recirculation arc and an extra pass that was added in the north linear accelerator to produce the 12 GeV beam to meet experimental needs in the newly constructed experimental Hall D. With the successful completion of its upgrade, CEBAF is now capable of delivering five-pass beam with a maximum energy of 11 GeV to experimental halls, A, B, and C. In addition, the upgraded CEBAF can deliver a 5.5-pass beam with maximum energy of 12 GeV to experimental Hall D.

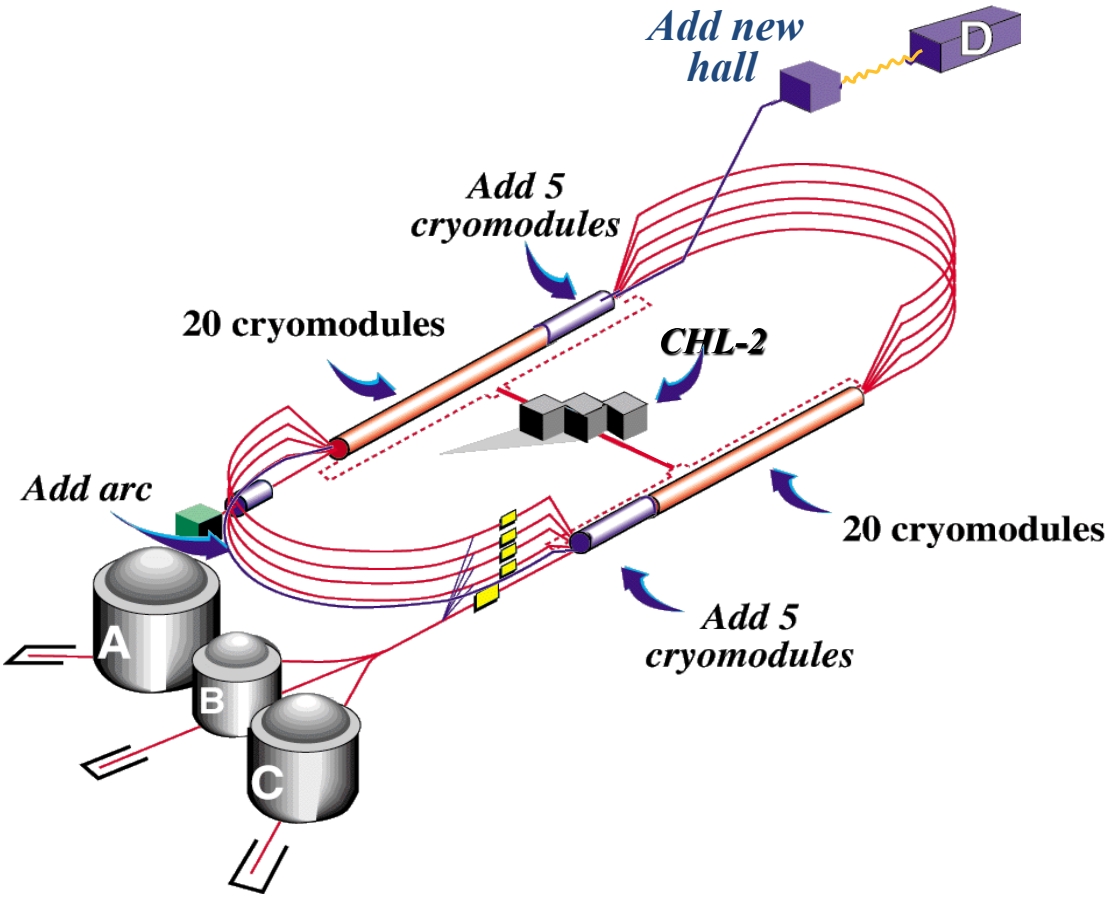

Figure 2.2: The JLab accelerator site after the 12 GeV upgrade. Image source Ref. [44].

Polarized electrons are produced in the injector by illuminating the GaAsP photocathode using circularly polarized photons from a 500 mW titanium sapphire

laser [45]. The injector is the starting point of the electron beam, where it starts its first pass through the north linear accelerator.

Simultaneous delivery of the electron beam to halls A, B, C, and D is achieved by passing the beam through RF deflecting cavities called the separators. RF separators are installed on each re-circulation arc, allowing the flexibility to simultaneously deliver beams of different energy and current to each hall. Although CEBAF can provide a beam current up to 100 μA, CLAS12 in experimental Hall B uses beam currents typically not exceeding 100 nA. The details on the structure of the CEBAF continuous electron beam and its simultaneous delivery to four halls is described in Ref. [46].

2.3 The Hall B Beamline

The extracted beam from CEBAF is delivered to experimental Hall B using the Hall B beamline system [47]. It is designed to provide the necessary controls of the electron beam by measuring and monitoring beam properties for the safe and efficient operation of CLAS12 experiments. The Hall B beamline is divided into two segments known as the "2C" and "2H" line segments. The "2C" line segment runs from the Beam Switch Yard (BSY) after CEBAF to the upstream end of experimental Hall B, and the "2H" line segment runs from the upstream end to the beam dump system in the downstream end of Hall B. The CEBAF operators have access to several quadruples, dipoles, and beam diagnostic tools installed in the upstream tunnel of the Hall B beamline to tune and deliver the beam to the CLAS12 target. Other additional monitoring components are installed along the Hall B beamline to monitor beam position, polarization, current, and halo counts to ensure safe passage of the beam. An overview of the Hall B beamline with a visual representation and a schematic of several beamline components can be seen in Fig. 2.3.

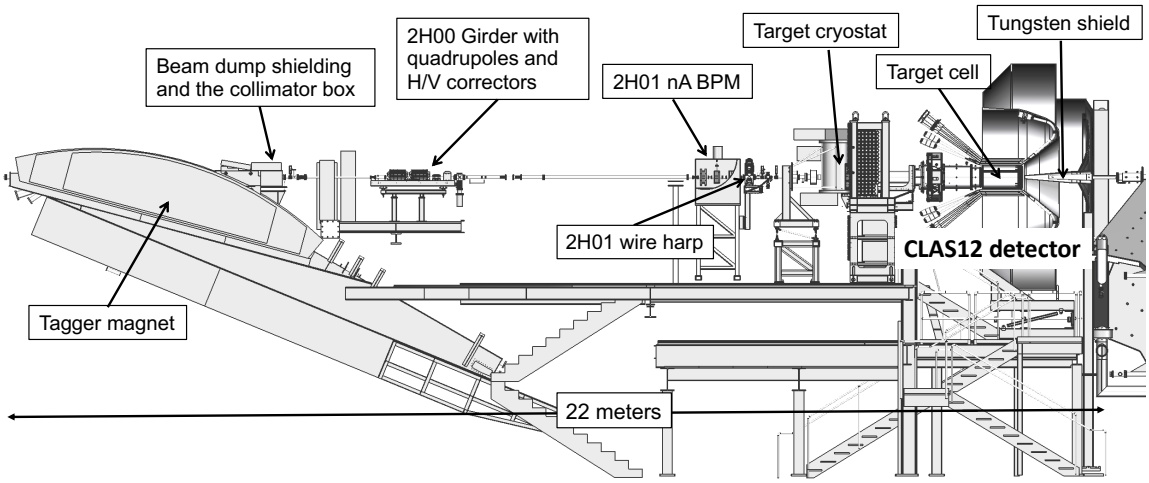

Figure 2.3: A representation and schematic of the Hall B beamline after it enters the experimental hall [47].

During typical beam operations, Hall B shift personnel monitor the beam delivery into the hall and control beamline devices using the Experimental Physics and Industrial Control System (EPICS) from the Hall B Counting House. The relevant Hall B beamline parameters used to monitor the safe passage of the beam are the Synchrotron Light Monitor (SLM), nano-amp Beam Position Monitors (BPMs), wire harps, and halo counters. The SLM consists of a photomultiplier tube (PMT) that measures the synchrotron light generated in the last dipole magnet of the 2C beamline that bends the beam into Hall B. BPMs are comprised of RF cavities to measure the beam current and relative beam position in the $x - y$ plane. Wire harps are used to measure the transverse beam profile. Wire harp scanners are devices with 25 μm tungsten wires mounted in the horizontal and vertical directions on a support fork that moves the wires into the beam at 45°. The beam halo counters are PMT-based devices located at various positions along the beamline and are mounted very close to the beam. Halo counters provide count rates for the wire harp scanners and

monitor the hall's beam-induced background. They are responsible for detecting any undesirable beam interactions due to beam dispersion in the beamline and providing feedback signals for the machine Fast Shutdown System (FSD).

Several physics experiments in Hall B require accurate beam polarization measurements. The Møller polarimeter, installed in the upstream tunnel of the Hall B beamline, is used to measure the beam polarization precisely. This device was designed, assembled, and tested by the Florida International University nuclear physics group. Beam polarization measurements are typically done weekly or following changes to the accelerator configuration.

2.4 The CEBAF Large Acceptance Spectrometer for 12 GeV

The CEBAF Large Acceptance Spectrometer for operation at 12 GeV beam energy (CLAS12) [44] is housed in experimental Hall B of Jefferson Laboratory. Figure 2.4 is the design model of the CLAS12 spectrometer and Fig. 2.5 shows a photograph of the fully installed CLAS12 spectrometer inside the hall. The CLAS12 spectrometer has been fully operational since it was commissioned in 2017.

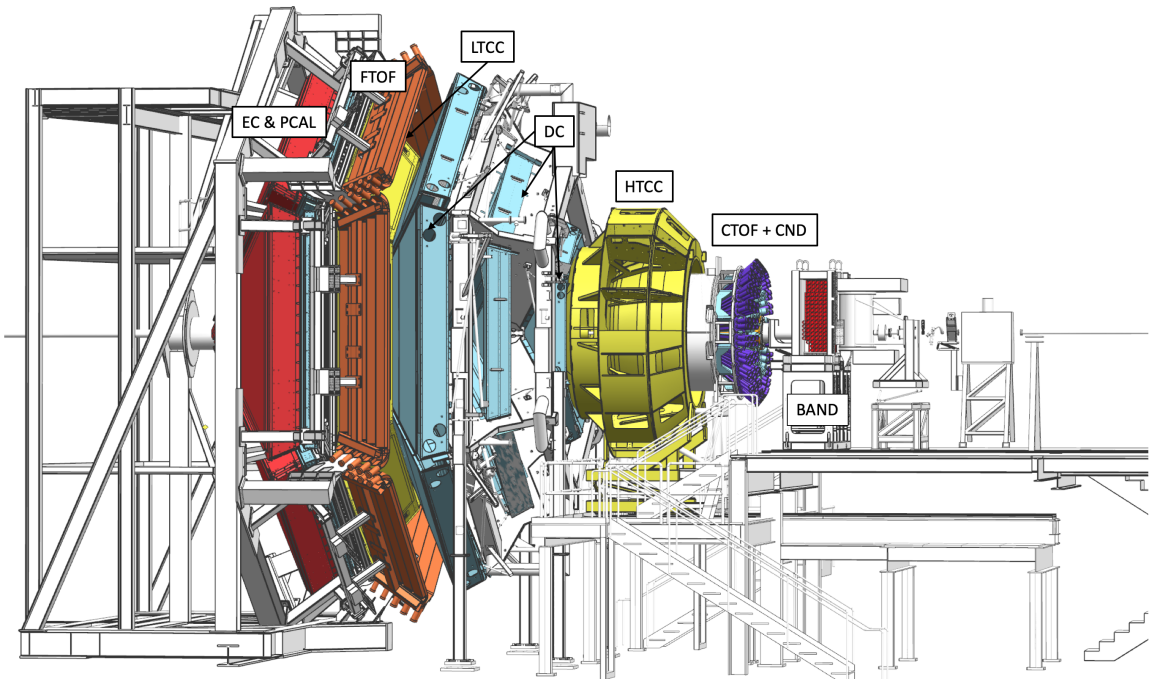

Figure 2.4: The design model of the new CLAS12 spectrometer in experimental Hall B shows both the Forward and Central Detectors and their subsystems [44]. The electron beam travels from right to left down the central axis of the spectrometer.

The CLAS12 spectrometer is designed to operate at high instantaneous luminosity of 10^{35} cm^{-2}s^{-1} using a polarized electron beam of up to 11 GeV on both polarized and unpolarized targets. The instrument detects charged and neutral particles over a solid angle of nearly 4π sr. The CLAS12 charged particle tracking is based on a newly constructed dual magnetic-field system with a six-coil superconducting torus magnet and a superconducting solenoid magnet [48]. They enable a momentum measurement utilizing tracking detectors to measure the curvature of the charged track in the field. The torus magnet provides a peak toroidal field distribution of 3.6 T around the beam axis in the azimuthal direction, which covers the forward polar-angle range from 5° to 35°. The solenoid magnet provides a 5 T solenoidal field that covers the polar angle from 35° to 125° with full azimuthal coverage. In addition to providing magnetic field for enabling momentum measurement of charged tracks, the solenoid also serves as a crucial magnetic shield. The solenoid is essential to direct the overwhelming

Møller e^+e^- background generated on the target into the Møller cone. The CLAS12 system is divided into two major parts based on its spatial coverage and different functionalities. These two major parts of the CLAS12 spectrometer are the Forward Detector (FD) and the Central Detector (CD).

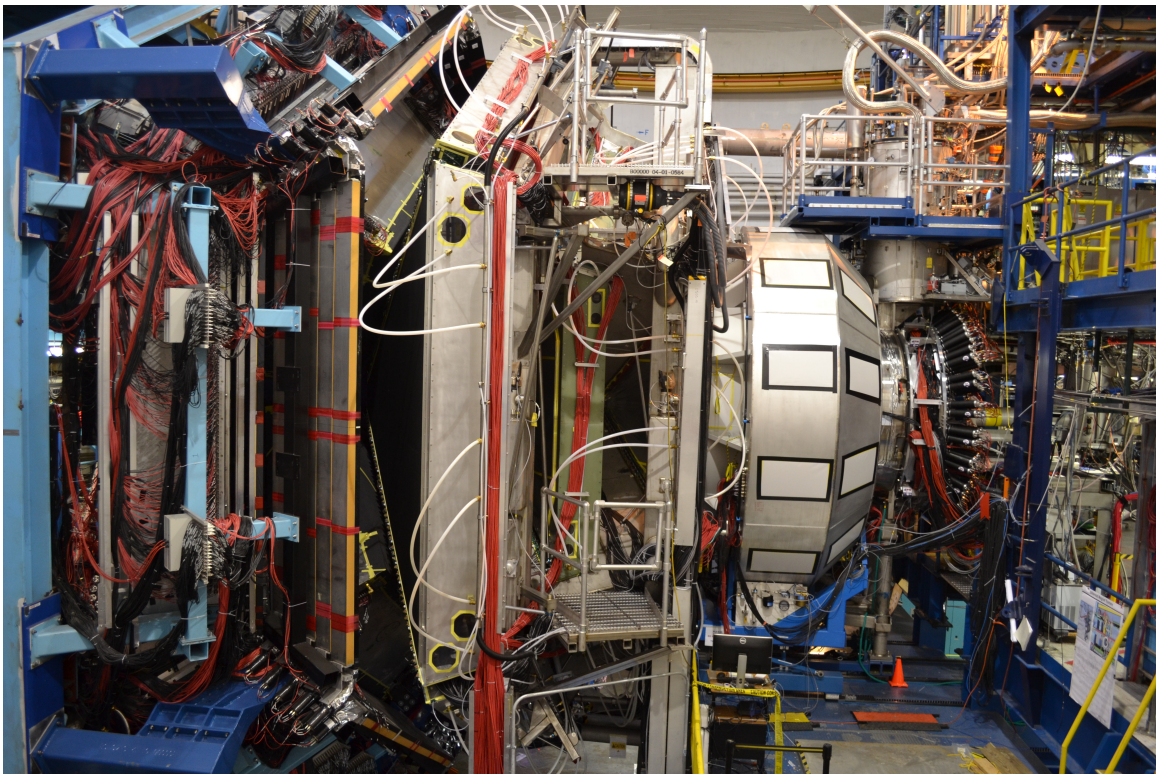

Figure 2.5: A photograph of the fully assembled CLAS12 spectrometer inside the experimental Hall B [44].

2.5 The CLAS12 Forward Detector System

The CLAS12 Forward Detector (FD) system uses several detector components of the old CLAS spectrometer. The major part of the FD is divided into six azimuthally distributed symmetric sectors. Each of the six sectors of the FD operates independently, covering one-sixth of the total azimuthal angle. The FD of CLAS12 consists of drift chambers, Cherenkov counters, time-of-flight detectors, and electromagnetic calorimeters.

2.5.1 The Drift Chamber (DC)

The CLAS12 drift chambers (DC) [49] are used to reconstruct the trajectories of charged particles to calculate the momentum and vertex information. Many layers of sense wires allow the DC to accurately reconstruct charged particles as they propagate through the torus magnetic field.

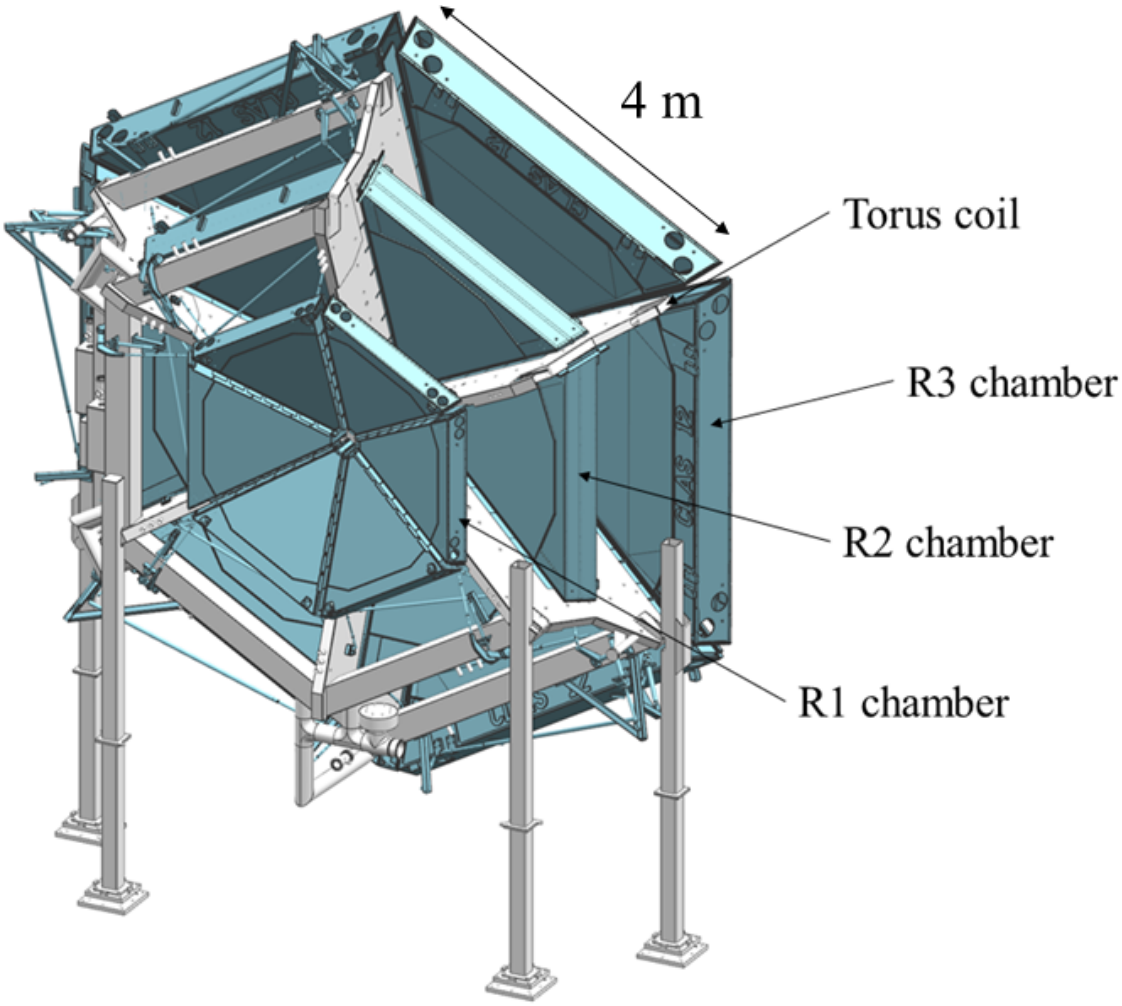

Figure 2.6: A model drawing of the CLAS12 drift chambers [49].

There are 18 planar drift chambers installed in the FD with a group of three in each of the six sectors (see Fig. 2.6). Three independent chambers in each sector are labeled region one, region two, and region three. Each chamber has sense wires

arranged in two superlayers of six layers, with the wires in the two superlayers strung with $\pm 6^{\circ}$ stereo angles. Sense wires and field wires in each layer are arranged in such a way to make a hexagonal cell structure, as shown in Fig. 2.7. There are a total of 112 sense wires in each of the six layers of a superlayer. The total number of sense wires integrated over all three regions of all six sectors is 24192. Table 2.1 briefly summarizes the design parameters used to construct the CLAS12 drift chambers.

	Region 1	**Region 2**	**Region 3**
Distance from target	2.3 m	3.5 m	4.9 m
Num. of superlayers	2	2	2
Layers/superlayer	6	6	6
Wires/layer	112	112	112
Cell radius (each SL)	0.78, 0.81 cm	1.14, 1.32 cm	1.87, 1.96 cm
Active time window	150 ns	325 - 1000 ns	750 ns

Table 2.1: Design parameters for the CLAS12 drift chambers [49]. Momentum resolution ($\frac{\delta p}{p}$) of the CLAS12 drift chambers is $\sim 1\%$.

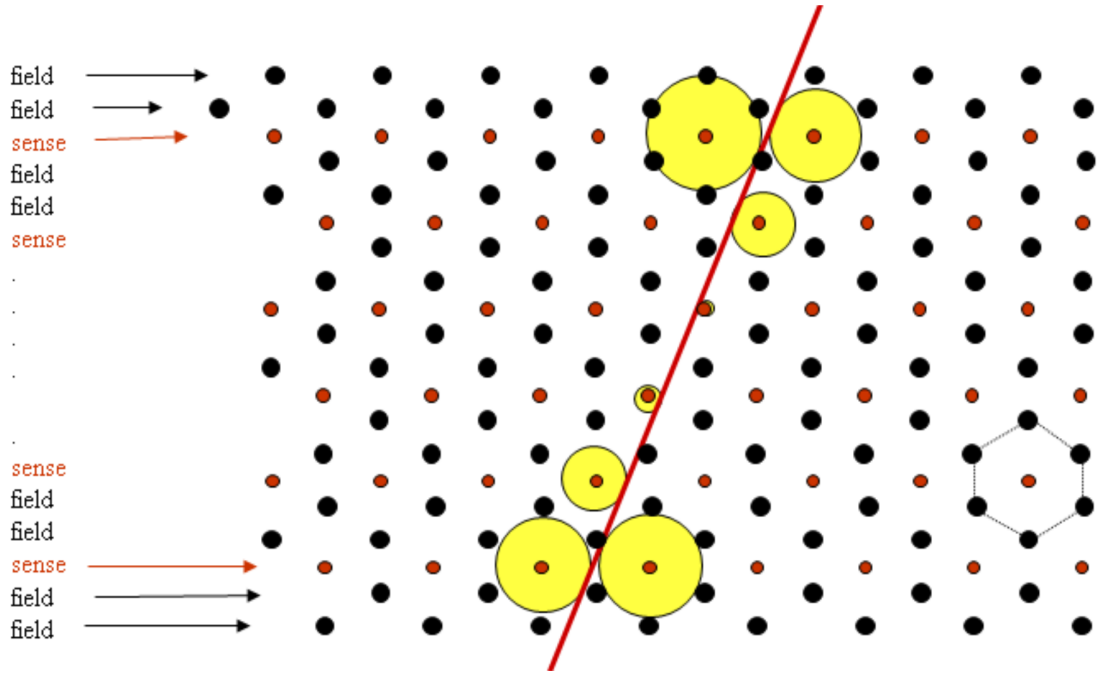

Figure 2.7: Wire layout for one superlayer of the CLAS12 drift chambers [49].

Each drift chamber is filled with a 90% argon and 10% CO_2 gas mixture. An incoming charged particle ionizes the gas mixture, and the electrons drift towards high voltage sense wires.

2.5.2 Cherenkov Counters

There are three different Cherenkov counters located downstream of the CLAS12 target to provide better particle identification of tracks reconstructed in the DC. These are the high threshold Cherenkov counter (HTCC), low threshold Cherenkov counter (LTCC), and ring imaging Cherenkov counter (RICH). Each of these Cherenkov counters is designed and constructed differently to perform particle identification for different particle species in different ranges of momenta.

Figure 2.8: Fully assembled High Threshold Cherenkov Counter [50].

The HTCC [50] is installed in front of the region one drift chambers to separate electrons with momenta below 4.9 GeV from charged pions, kaons, and protons. The HTCC is a single unit, as shown in Fig. 2.8, that operates in a dry CO_2 gas at room temperature and atmospheric pressure. In this medium, all electrons in CLAS12, with energy in the range of $1 - 10$ GeV, create Cherenkov light in the HTCC. However, the same is not true for all pions, kaons, and protons, as they have different energy thresholds to emit Cherenkov light depending on their mass.

The LTCC is used for charged pion detection at momenta greater than 3.5 GeV. The LTCC system consists of four boxes filled with heavy C_4F_{10} radiator gas. These four LTCC boxes are placed in four of the six sectors of CLAS12. The CLAS12 LTCC system is the refurbished version of the previously used Cherenkov counter in CLAS to detect electrons at low energy. The design, construction, and performance of the refurbished LTCC are described in detail in Ref. [51].

The RICH detector is installed in sector four of the FD to provide charged particle identification in the momentum range that is not accessible with LTCC and the Forward Time-of-Flight system. Details on the design, construction, and performance of the RICH detector can be found in Ref. [52]. Since the RICH reconstruction algorithm is being developed during this work, the RICH information is not employed in this analysis.

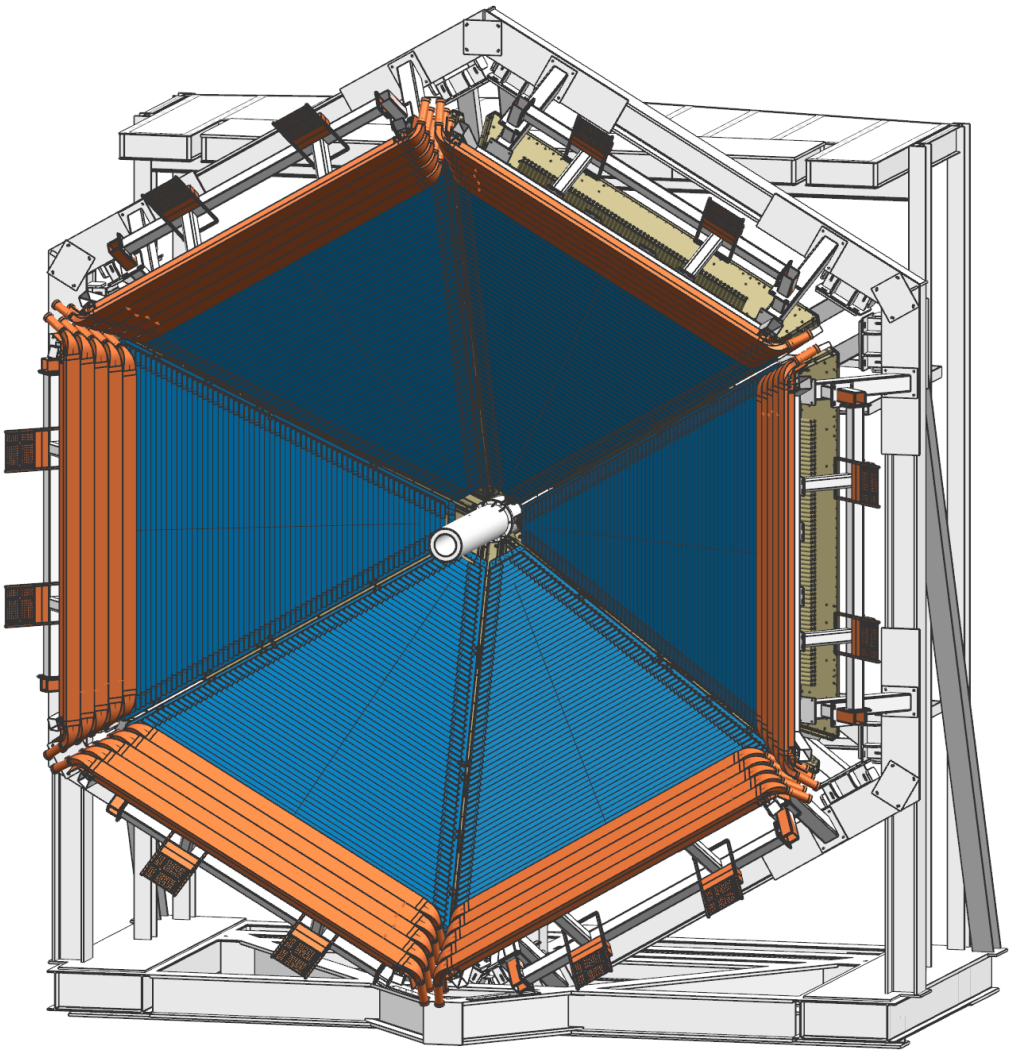

Figure 2.9: Full assembly of the Forward Time-of-Flight system showing the location of the different counters. Dark blue represents the panel-1b counters, and bright orange represents the panel-2 counters, which are positioned around the exterior of the Forward Carriage. This image does not show the panel-1a counters installed directly downstream of the panel-1b counters. The beam direction is into the page [53].

2.5.3 The Forward Time of Flight (FTOF)

The Forward Time-of-Flight (FTOF) [53] system is another major component of the FD. The FTOF system determines the flight time of charged particles that emerge from beam-target interactions. The FTOF is installed in all six sectors of the CLAS12 FD and is located approximately about seven meters downstream from the CLAS12 target. It is constructed using rectangular plastic scintillator counters of variable dimensions. A photomultiplier tube (PMT) is connected to each end of these counters. There are three arrays of scintillator counters in each of the six FD sectors of the CLAS12. Each array of the scintillator counters is referred to as the scintillator panel. Three FTOF panels in each sector of the FD are called as panel-1a, panel-1b, and panel-2 of that sector. The panel-1a and panel-1b counters cover the forward polar angle range of 5° to 35°, whereas the panel-2 counters cover a larger polar angle range from 35° to 45°. There are 23 scintillator counters in panel-1a and 5 scintillator counters in the panel-2 array. The panel-1a and panel-2 counters in the CLAS12 are the refurbished panel-1 and panel-2 TOF counters of the old CLAS spectrometer [54]. The new panel-1b array of the CLAS12 consists of 62 new scintillator counters with variable lengths from 17 cm at the smallest scattering angles to 408 cm at the largest scattering angles. The panel-1a and panel-1b arrays are mounted into two layers, as shown in Fig. 2.9, with panel-1a just upstream of the electromagnetic calorimeter and panel-1b further upstream of the panel-1a array. The time resolution of counters in panel-1b, panel-1a, and panel-2, respectively, range from 60 to 110 ps, 90 to 180 ps, and 170 to 180 ps depending on the length of counters. The momentum limits achieved for particle identification at the 4σ level of separation from FTOF timing resolution are 2.8 GeV for π/K separation, 4.8 GeV for K/p separation, and 5.4 GeV for π/p separation. Details of the FTOF construction and performance are given in Ref. [53].

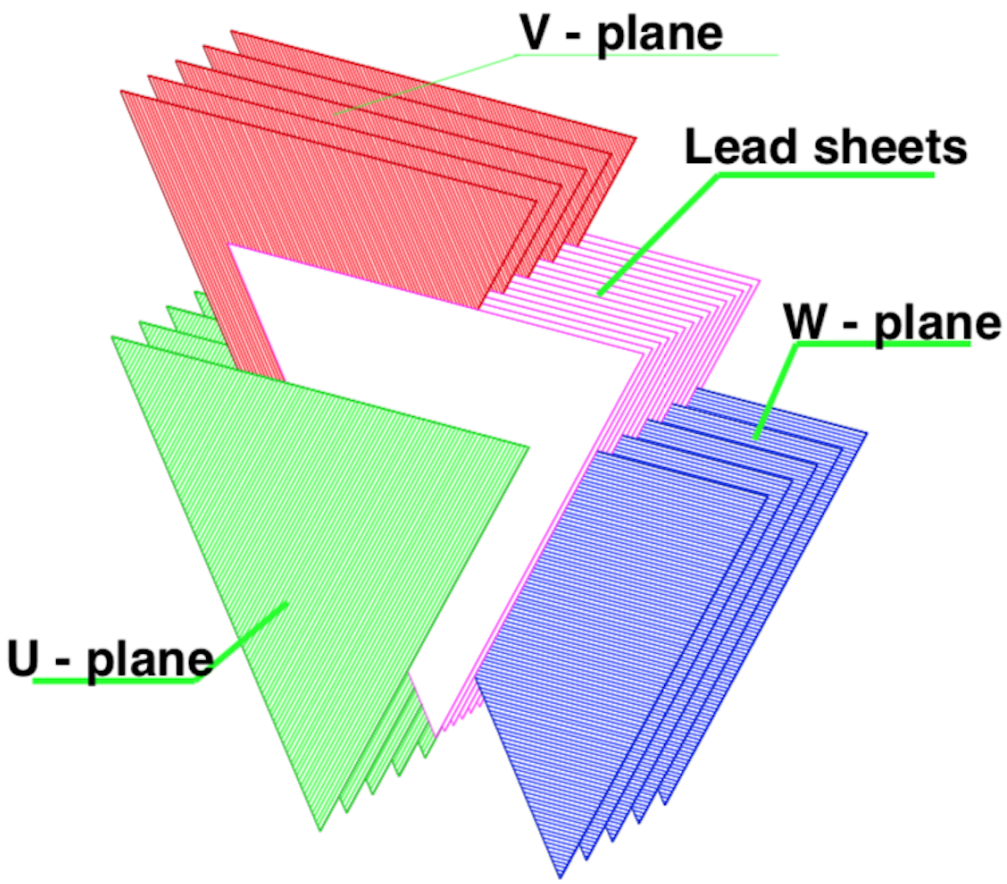

Figure 2.10: The interlacing of the CLAS12 Electromagnetic Calorimeter (ECAL) scintillator layers (U, V, and W planes) and lead sheets used to generate particle showers for electrons [55].

2.5.4 Electromagnetic Calorimeters (EC)

The CLAS12 Forward Detector Electromagnetic Calorimeter system (ECAL) uses the preexisting electromagnetic calorimeter (EC) from the CLAS spectrometer [54] and a new pre-shower calorimeter (PCAL) located in front of the EC to identify electrons, photons, and neutrons. The EC and PCAL detectors are sampling calorimeters, in which the material that measures the deposited energy is separate from the material that produces the shower. In addition to providing particle identification by measuring deposited energy, the ECAL is also used to provide primary trigger information.

The ECAL utilizes a triangular hodoscope geometry with a stereo readout, as shown in Fig. 2.10. Details of the ECAL design and construction can be found in Ref. [55].

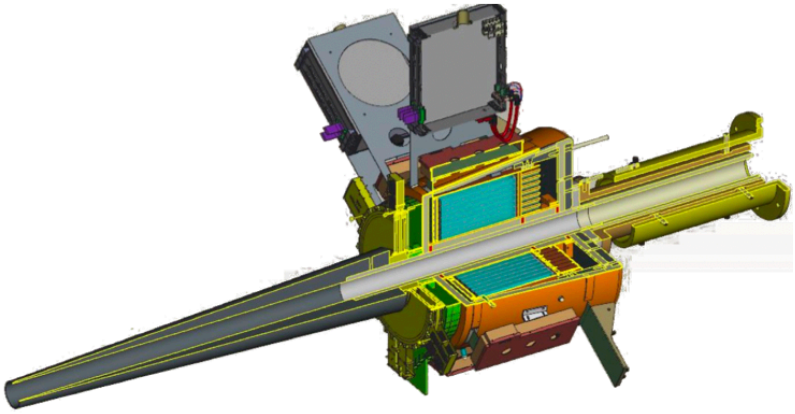

(a) Forward Tagger schematic design.

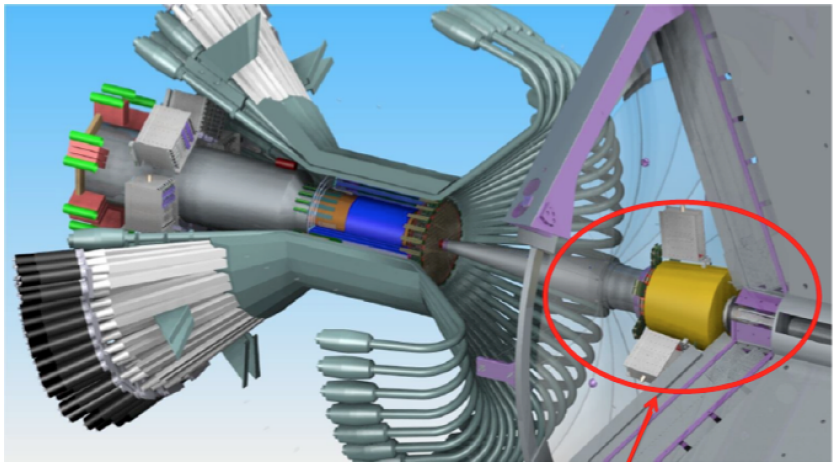

(b) Forward Tagger location downstream of the Central Detector and upstream of the torus magnet.

Figure 2.11: Fig. 2.11a shows the schematic design of the CLAS12 FT system. The FT calorimeter, depicted in cyan in Fig 2.11a, is situated approximately 180 cm from the beam target interaction point. The scintillation hodoscope shown in green and the tracker shown in yellow is situated in front of the calorimeter. A tungsten cone (gray) protects the FT from the beam's Møller electrons and other electromagnetic backgrounds such as low-energy photons. Fig. 2.11b depicts a representation of the FT setup in a red circle. These figures were taken from Refs. [44, 56].

2.5.5 The Forward Tagger (FT)

A new Forward Tagger (FT) facility was designed and installed in the CLAS12 detector system to detect electrons and photons at very forward polar angles from 2.5° to 4.5°. The kinematic coverage of the CLAS12 FT system is summarized in Table 2.2. The CLAS12 FT system provides a complementary and competitive way of conducting traditional photoproduction experiments. An electroproduction experiment employing the FT facility at extremely low photon virtuality Q^2 (quasi-real photoproduction) permits the execution of a large hadron spectroscopy program in Hall B [44].

The FT system consists of an electromagnetic calorimeter called the FT-Cal, to identify scattered electrons, measure the electromagnetic shower energy, and provide a fast trigger signal; a scintillator hodoscope, called the FT-Hodo, to distinguish electrons and high-energy photons; and a tracker, called the FT-Track, to accurately measure the electron scattering angle.

The entire FT system is installed between the HTCC and the torus magnet support, as shown in Fig. 2.11b. The front of the FT system is located at about 185 cm downstream from the nominal CLAS12 target position. The currently achieved energy resolution of the FT-Cal system is $\frac{\sigma_e}{E_e} \sim \frac{3.3\%}{\sqrt{E_e}}$, which is higher than the design value by $\sim 1-2\%$. The details of the CLAS12 FT system can be found in Ref. [56].

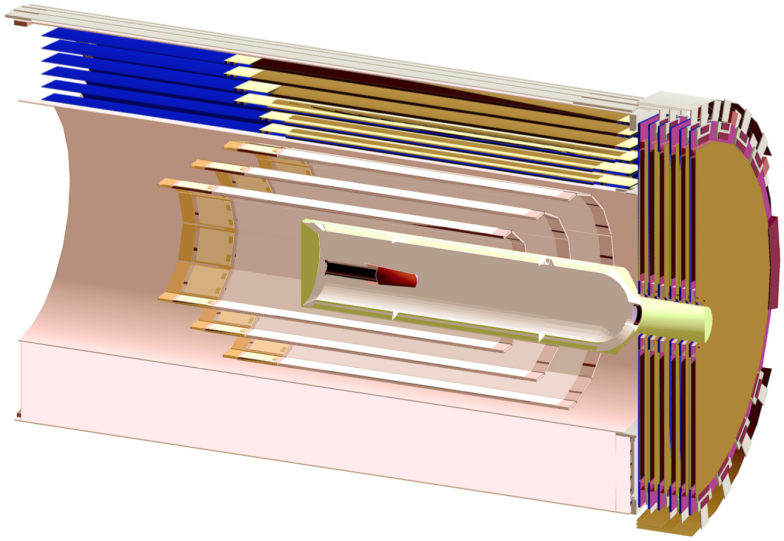

(a) The CLAS12 CVT

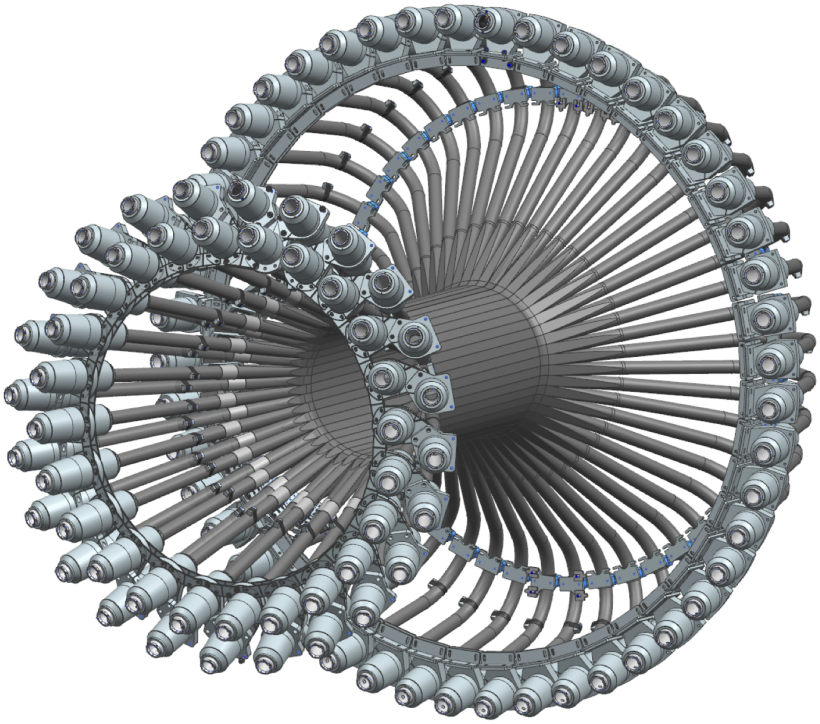

(b) The CLAS12 CTOF system

Figure 2.12: The Central Vertex Tracker schematic (in Fig. 2.12a) of the CLAS12 Central Detector system, showing the target cell and vacuum chamber from the inside, the three double layers of the Silicon Vertex Tracker (SVT), and the six layers of the Barrel Micromegas Tracker (BMT). Fig. 2.12b is the 3D view of the CLAS12 CTOF system showing 48 scintillator bars with PMTs at both ends supported by light guides [44].

FT-kinematic Coverage

Parameters	Coverage
$E_{e'}$ (GeV)	$0.5 - 4.5$
E_{γ^*} (GeV)	$6.5 - 10.5$
$\theta_{e'}$ (°)	$2.5 - 4.5$
$\phi_{e'}$ (°)	$0 - 360$
P_{γ^*} (%)	$10 - 70$
Q^2 (GeV^2)	$0.01 - 0.3$, $< Q^2 >$ 0.1
W (GeV)	$3.6 - 4.5$

Table 2.2: Kinematic coverage of the CLAS12 FT system. Full details can be found in Ref. [57].

2.6 The CLAS12 Central Detector System

Low momentum particles scattered from the target at polar angles from 35° to 125° beyond the acceptance range of the FD are detected in the CLAS12 Central Detector (CD) system. The 5 T solenoid magnet on the CD encloses multi-system detectors based on a silicon tracker and micromegas (MMs) for central tracking (see Fig. 2.12a), a Central Time-of-Flight system (CTOF) (see Fig. 2.12b) for particle identification, and a Central Neutron Detector (CND) for neutral particle detection. The solenoid provides the magnetic field for the momentum determination of charged particles traversing the tracking system.

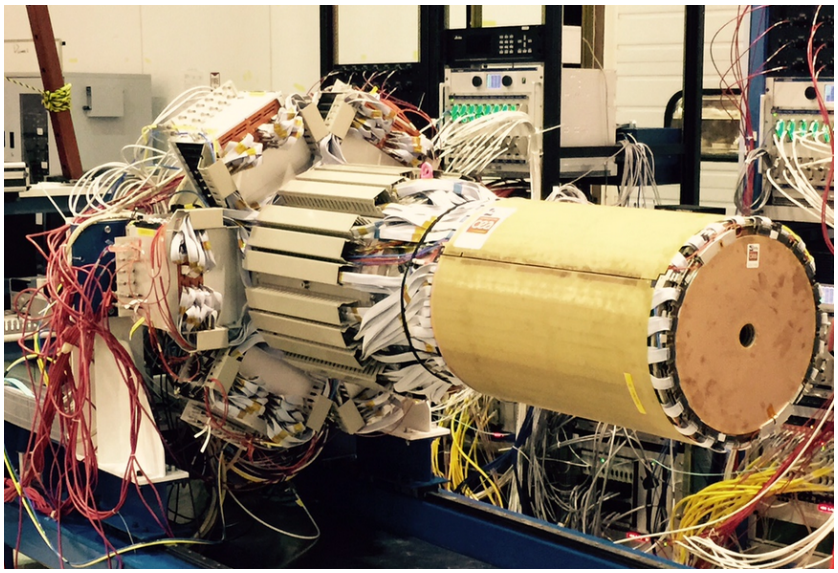

(a)

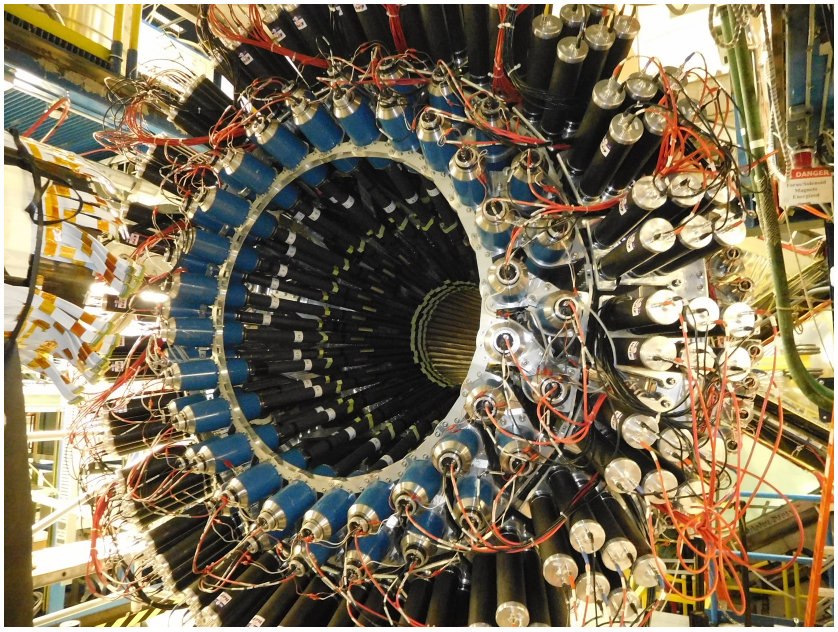

(b)

Figure 2.13: Fig. 2.13a is the fully assembled Central Vertex Tracker (SVT, BMT, and FMT) (see Fig. 2.12a as well) of the CLAS12 Central Detector. On the outside, the BMT and FMT are visible. The electron beam passes through a circular opening in the center of the FMT. The SVT is encapsulated and concealed. Fig. 2.13b shows the fully assembled CLAS12 Central Detector system. The CVT tracking system is fully inserted inside the superconducting solenoid magnet in Fig. 2.13b. Image source Ref. [44].

The tracking system of the CD is known as the Central Vertex Tracker (CVT) which is shown in Fig. 2.12a with the target cell and vacuum chamber from inside. The CVT comprises a Barrel Micromegas Tracker (BMT), a Silicon Vertex Tracker (SVT), and a Forward Micromegas Tracker (FMT). The BMT contains three layers of strips along the beamline and three layers of circular readout strips around the beamline. The SVT of the CVT system consists of three regions with 10, 14, and 18 double-sided modules of silicon sensors. The FMT consists of six circular disks of Micromegas detector installed in the forward region at about 35 cm downstream of the centre of the target. The BMT and FMT together form the Micromegas Vertex Tracker (MVT) system and the MVT together with the SVT complete the CVT system. Figure 2.13a shows the fully assembled CVT of the CLAS12 CD. The entire CVT system measures the momentum and determines the vertex of charged particles scattered from the target. Details of the SVT and MVT (BMT plus FMT) can be found, respectively, in Ref. [58] and [59].

The CTOF system is used to identify low-energy (0.3 to 1.25 GeV) charged particles emerging from the target with time-of-flight measurements. The CTOF system includes 48 plastic scintillators with PMT readout at both ends supported by focusing light guides, as shown in Fig. 2.12b. The CTOF system is designed to provide time resolution of 80 ps for charged particle identification in the CLAS12 Central Detector. Details of the CTOF are described in Ref. [60].

The CND system is installed in the outermost region of the CLAS12 CD system. It consists of three radial layers of scintillators just outside the circumference of the CTOF system. Three layers of scintillators are coupled at their downstream ends with U-turn light guides and at their upstream ends by read-out PMTs, as shown in Fig. 2.13b, with the help of approximately one meter long light guides. The primary purpose of the CLAS12 CND system is to identify 0.2-1 GeV neutrons in the CD

with neutron momentum resolution σ_p/p within 10% [61]. Details of the components of the CND and its performance is reported in Ref. [62].

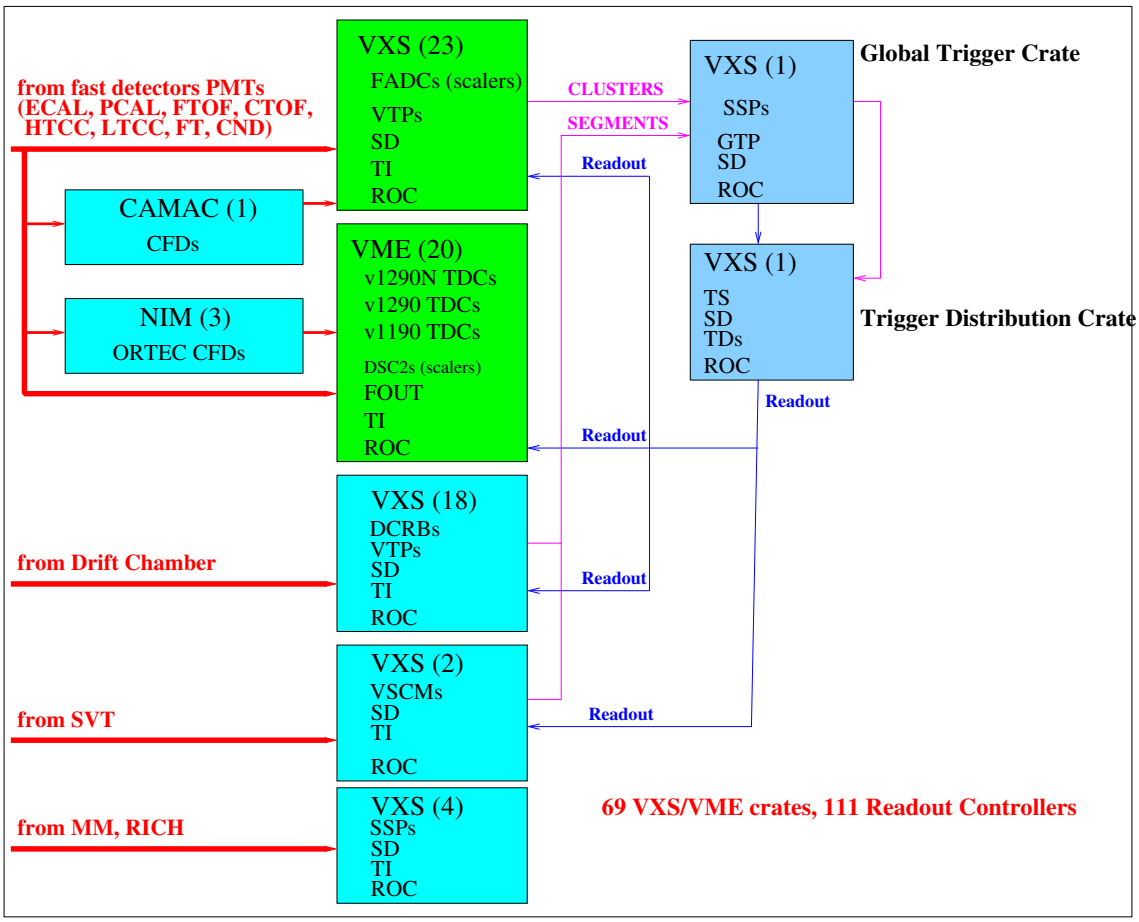

Figure 2.14: Full diagram of the CLAS12 Data Acquisition system [63].

2.7 Triggering and Data Acquisition

As described in the previous sections, CLAS12 comprises multiple detector subsystems. Each subsystem has to satisfy a series of criteria to register electronic signals in the data acquisition system.

The analog signals from the interaction of particles with the materials are recorded by the readout electronics. These analog signals are converted into digital signals using Analog-to-Digital converters (ADCs) and Time-to-Digital convert-

ers (TDCs). These ADC and TDC signals are then streamed to the network-based CLAS12 data acquisition system (DAQ) system, which organizes and transfers the recorded information to the tape storage and is also used to form the trigger. In addition to recording detector signals and forming triggers, the CLAS12 DAQ system is also used to monitor data quality in real time during beam operation. The robust data acquisition system of the CLAS12 detector can operate at trigger rates of up to 20 kHz and data rates of up to 1 GB/s with a livetime of $> 90\%$ [63]. The schematic of the CLAS12 DAQ system is illustrated in Fig. 2.14.

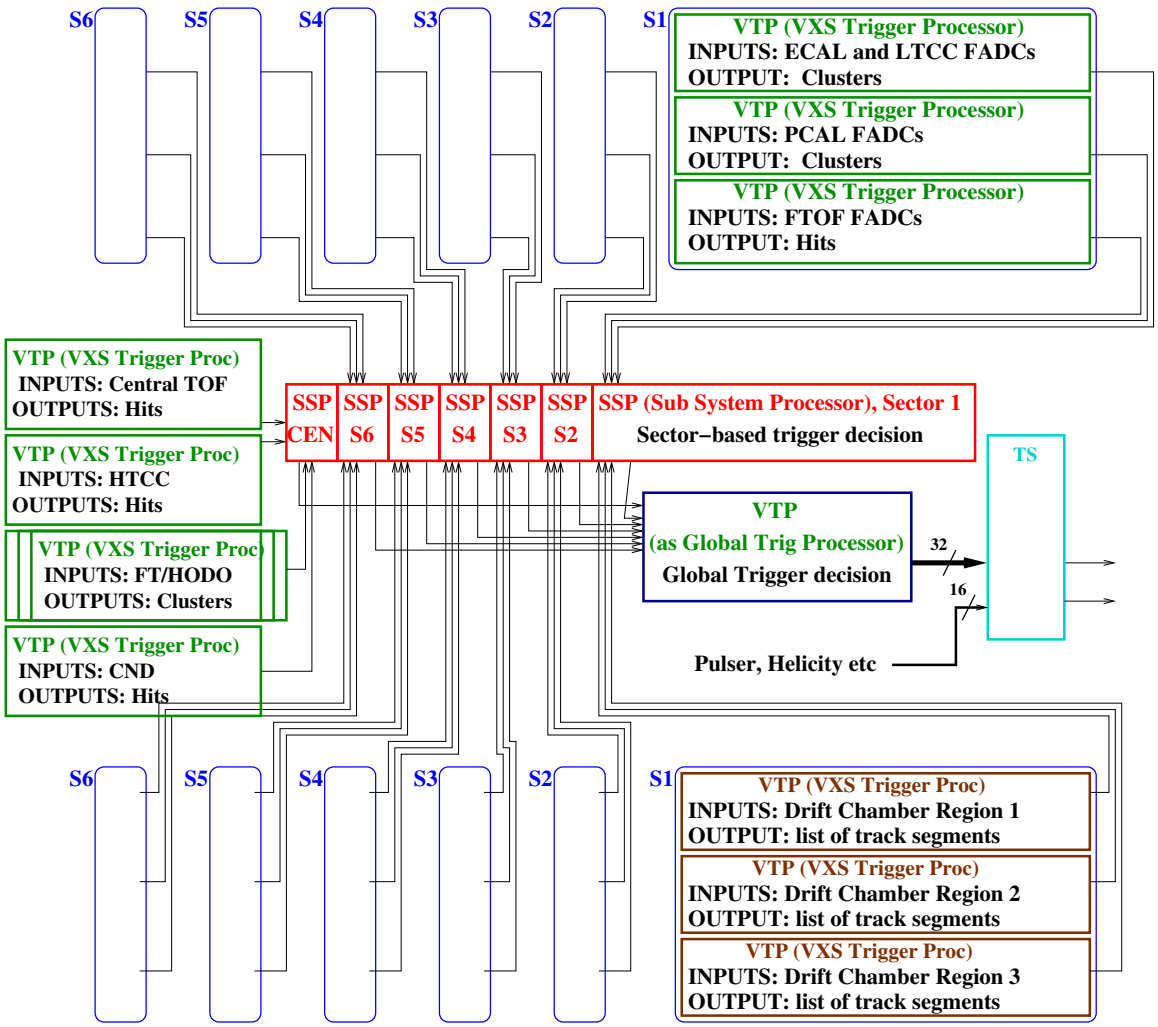

Figure 2.15: Full diagram of the CLAS12 Trigger System that is designed as a three-stage pipeline-style system as described in Ref. [64]. Flash ADC Boards (FADCs) and Drift Chamber Readout Boards (DCRBs) provide input information to the trigger system at the pre-trigger level; data processing from different detector components is performed in stage one, stage two handles timing vs. detector geometry matching for all detector components in all six FD sectors, and finally, 32 unique trigger decisions are sent to the Trigger Supervisor (TS) in the third stage.

The trigger system defines the criteria that decide when to start recording detector signals in the DAQ system. The trigger system provides logical trigger signals to the DAQ during beam operation at the CLAS12 nominal luminosity of 10^{35} cm^{-2}s^{-1}. The trigger system is versatile and efficient at isolating information required by several physics experiments on an event-by-event basis. The CLAS12 subsystems responsible

for providing information for the trigger system are the HTCC, DC, FTOF, ECAL, CTOF, CND, and FT. The details on the CLAS12 trigger system are in Refs. [64,65]. These triggers are designed to work in three distinctive stages. In the first stage, the trigger system receives information from the Drift Chamber Readout Boards (DCRBs) to perform data processing. The second triggering stage involves matching hit timing with the detector geometry of different subsets of detectors for both the FD and CD. In the third stage, the trigger system logically decides to keep or discard the event by analyzing information from the previous two stages. The schematic diagram of the CLAS12 trigger system is shown in Fig. 2.15.

```
"name": "REC::Particle",
"group": 300,
"item" : 31,
"info": "Reconstructed Particle Information",
"entries": [
    {"name":"pid",      "type":"I", "info":"particle id in LUND conventions"},
    {"name":"px",       "type":"F", "info":"x component of the momentum (GeV)"},
    {"name":"py",       "type":"F", "info":"y component of the momentum (GeV)"},
    {"name":"pz",       "type":"F", "info":"z component of the momentum (GeV)"},
    {"name":"vx",       "type":"F", "info":"x component of the vertex (cm)"},
    {"name":"vy",       "type":"F", "info":"y component of the vertex (cm)"},
    {"name":"vz",       "type":"F", "info":"z component of the vertex (cm)"},
    {"name":"vt",       "type":"F", "info":"RF and z corrected vertex time (ns)"},
    {"name":"charge",   "type":"B", "info":"particle charge"},
    {"name":"beta",     "type":"F", "info":"particle beta measured by TOF"},
    {"name":"chi2pid",  "type":"F", "info":"Chi2 of assigned PID"},
    {"name":"status",   "type":"S", "info":"particle status (represents detector collection it passed)"}
]
```

Figure 2.16: The contents of the CLAS12 Event Builder REC::Particle bank.

2.8 Raw Data Processing and Event Reconstruction

A large amount of raw experimental data collected from the ADC and TDC signals is converted into meaningful physics information, such as particle identification (PID), particle four momenta, reaction vertices, etc. with the help of the CLAS12 offline event reconstruction software [44]. The event reconstruction software has been designed

and developed based on a service-oriented architecture called the CLAS Analysis and Reconstruction Architecture (CLARA), which allows the processing of the data-stream in an organized way with different micro-services. During event reconstruction, each micro-service receives an input data-stream from the previous micro-service, processes it, outputs information into dedicated data structures called "banks", and passes the processed data to the next micro-service in the data-flow path [66].

One major CLAS12 data processing micro-service used in the final stage of the event reconstruction process is called the CLAS12 Event Builder. The CLAS12 Event Builder collects and analyzes global event information such as the RF time and beam helicity, and correlates information from the sub-detectors into particles, executes particle identification schemes, and outputs all necessary information for physics analysis into standardized and persistent data bank structures. The output data structures of the CLAS12 Event Builder are High Performance Output (HIPO) banks, whose names are prefixed with "REC". These data banks comprise commonly known Data Summary Tapes (DSTs). Reference [67] provides details on the structure of the CLAS12 DSTs. The list of Event Builder HIPO banks includes, REC::Event, REC::Particle, REC::Calorimeter, REC::Scintillator, REC::Cherenkov, REC::Track, REC::Traj, REC::CovMat, and REC::VertDoca. One can easily find the full structure of all these banks in the event.json file from the Jefferson Lab GitHub page under the CLAS12 offline software repository in Ref. [68].

The REC::Particle bank is organized with separate rows for each reconstructed particle and columns representing information such as PID, momenta, vertex, charge, timing, and status for each particle. The REC::Particle bank's contents are displayed in Fig. 2.16. Detailed detector responses for each track in the REC::Particle bank are accessible via a mapping schema that links the track index to each individual detector response bank. Follow Ref. [69] for more details on how the particles are

created in the CLAS12 Event Builder and how to correlate information across the different banks.

CHAPTER 3

Data Sets and Event Selection

3.1 CLAS12 Run-Group A

3.1.1 Experimental Conditions

CLAS12 Run-Group A (RG-A) was the first group of CLAS12 experiments that began production data taking during the spring of 2018. The RG-A experiments shared the same experimental setup such as target, beam current, magnetic field, etc., with common detector settings. The RG-A science program includes 13 experiments developed by the CLAS Collaboration and approved by Jefferson Lab's Program Advisory Committee (PAC). The scientific goal of these experiments is to explore the structure of the proton in its ground and excited states, as well as 3D imaging of the proton and gluonic excitations, in order to understand how the constituent parts of the proton are bound by the strong force and to shed light on the origin of hadron mass. Studies presented in this project are just one subset of the Very Strange physics program ($E12-11-005A$), which is a part of the MesonEx program ($E12-11-005$) of RG-A.

To satisfy the physics goals of the RG-A experiments, the experimental run conditions were developed to configure the electron beam, target, magnetic field settings, DAQ, and the trigger system. A summary of the RG-A run conditions is listed below and summarized in Table 3.1. The details on the RG-A run conditions can also be found in the general RG-A Phase 1 analysis note for the CLAS12 first publications in Ref. [70].

- Electron beam energy: Longitudinally polarized electron beam with beam energy at 10.6 GeV and 10.2 GeV.

- Beam Current: Beam current ranges from 5 nA to 75 nA.
- Target: 5 cm unpolarized liquid-hydrogen (LH_2) target.
- Torus Magnet: Full torus field with electrons inbending and outbending magnetic field configurations.
- Solenoid: Full 5 T solenoid field.
- Forward Tagger on for quasi-real photoproduction studies.
- Luminosity: L=10^{35} $cm^{-2}s^{-1}$.

3.1.2 Data Set

The data analyzed for this analysis corresponds to three RG-A data sets taken during different run periods with varying beam energies and torus polarity. These three data sets are Fall 2018 inbending, Fall 2018 outbending, and Spring 2019 inbending. Inbending and outbending torus polarities bend negatively charged particles towards and away from the beamline, respectively. Both the inbending and outbending Fall 2018 data sets were taken with a 10.6 GeV electron beam energy. The Spring 2019 data set was taken with slightly lower 10.2 GeV electron beam energy with inbending torus polarity setting only. The total accumulated charge incident on the target corresponding to these three different data sets is 37.06 mC, 34.08 mC, and 50.53 mC, respectively, for Fall 2018 inbending, Fall 2018 outbending, and Spring 2019 inbending. These values correspond to total live-time gated Faraday cup charge summed over all good runs used in this analysis. The list of good runs from the different RG-A run periods analyzed for this study is summarized in the appendix **A.1**. The list of good runs for different RG-A run periods was compiled by Rafayel Paremuzyan by checking the Faraday cup charge normalized counts for J/ψ analysis and by browsing and checking the shift summaries from the logbook recorded during the data taking for outlier runs. CLAS12mon, an online monitoring tool [71] developed by Andrey

Analyzed RG-A Data Summary

Expt. condition	Fall 2018 out-bending	Fall 2018 in-bending	Spring 2019 in-bending
Beam (GeV)	10.604	10.604	10.199
Current (nA)	$40 - 55$	$40 - 55$	50
Target	LH_2	LH_2	LH_2
Torus field	$+100\%$	-100%	-100%
Solenoid field	-100%	-100%	-100%
Run range	$5422 - 5666$	$4804 - 5019$	$6616 - 6783$
Number of good runs used	156	147	114
Beam charge on target (mC)	34.0826	37.0594	50.5319

Table 3.1: Summary of the experimental conditions for the three different RG-A data sets analyzed.

Kim, is very useful to browse and check the status of the run during the data taking. To calculate the beam charge, a Python library developed by Maurik Holtrop to access the Run Control Database [72] (RCDB) and add MYA data (MYA is an EPICS-based archiving system) such as beam charge is used. The script provides both the livetime corrected and uncorrected beam charge. The Python library is available in GitHub (see Ref. [73]).

3.2 Event Selection

The main focus of this analysis is the reaction $ep \to e'K^+K^+K^-(\Lambda/\Sigma^0)$, where we are especially interested in searching for intermediate doubly-strange excited hyperons in the reaction $ep \to e'K^+K^+\Xi^{*-}$ that decay through ΛK^- and $\Sigma^0 K^-$. First we

performed a preliminary investigation of the reaction $ep \rightarrow e'K^+K^+(X)$ by detecting the e' and two K^+ in each event to search for the signature of electroproduced higher-mass doubly-strange excited hyperons as missing particles. The preliminary study does not show any signature of the missing higher-mass excited hyperons other than $\Xi^{*-}(1530)$ in the reaction $ep \rightarrow e'K^+K^+(X)$. Therefore, we decided to investigate the exclusive reaction

$$ep \rightarrow e'K^+K^+\Xi^{*-}$$
$$\hookrightarrow K^-(\Lambda/\Sigma^0),$$

by detecting an additional K^- in the event to search for excited intermediate hyperons (Ξ^{*-}) that decay to ΛK^- and $\Sigma^0 K^-$. Requiring an additional K^- in the event suppresses the majority of the non-strange background events and helps to single out electroproduced Ξ^{*-} resonances if there are any. The two topologies studied for the reaction used only the Forward Detector of the CLAS12 spectrometer to detect the final state charged kaons (K^+, K^+, and K^-) with trigger electrons detected either in the Forward Detector or in the Forward Tagger. The first topology with the trigger electron and all three charged kaons detected in the Forward Detector studied high Q^2 electroproduction process of the reaction of interest. The second topology with the trigger electron detected in the Forward Tagger studied the quasi-real photoproduction process of the reaction.

A general data filtering was performed on the available data based on pre-assigned particle identification (PID). Filtered data files analyzed for this analysis correspond to the so-called "skim-14" and "skim-11" skims. The "skim-14" files contain events with an electron in the Forward Detector and at least one K^+ detected in either the CD or FD. Similarly, the "skim-11" filtered files consist of events with at least one electron detected in the Forward Tagger with one or more K^+ tracks de-

tected either in the CD or FD. The java code for "skim-11" and "skim-14" is included in Ref. [74]. Final data filtering was performed starting initially from the "skim-14" and "skim-11" files to select events with at least two K^+ and one K^- in the FD with an electron in either the FD or FT. The topologies with an electron in either the FT or in the FD are analyzed separately as these processes address two different production mechanisms for the same reaction.

The next section describes the particle identification criteria imposed by the CLAS12 Event Builder and a few additional cuts implemented on electrons and charged kaons to improve particle identification for this analysis. Various cuts on top of the Event Builder cuts were implemented on an event-by-event basis to reduce the background of events other than $ep \rightarrow e'K^+K^+K^-(\Lambda/\Sigma^0)$.

3.3 Particle Identification (PID)

The CLAS12 Event Builder assigns the first layer of particle identification by associating detector responses from various CLAS12 subsystems to particles through an identification protocol. The magnetic field will deflect particles in polar angle, either making their curvature inbending or outbending with respect to the beamline based on the torus polarity. The direction of curvature of the track in the toroidal magnetic field is analyzed to assign the charge of the particle track. The Event Builder initially provides $e^-/e^+(11/-11)$ for charged particles in the Forward Detectors based on the DC, HTCC, ECAL, and FTOF response. The Event Builder then allocates $d/p/K^\pm/\pi^\pm(45/2212/\pm321/\pm211)$ to charged particles with Time-of-Flight hits that do not meet the e^+/e^- criterion based on minimizing the time difference between the particle vertex time and the event start time. For each PID assignment by the Event Builder, a quality factor known as chi2pid is computed that indicates the accuracy of the Event Builder PID assignment for the track. The chi2pid for e^-/e^+ is assigned

based on the number of σ from the expected e^-/e^+ ECAL sampling fraction, which will be discussed later in detail. Similarly, the chi2pid for charged hadrons is assigned as the number of σ from the expected vertex time for a given PID assumption (i.e. $\frac{\Delta t}{\sigma}$). The CLAS12 Event Builder also stores the particle track status, which indicates whether the track was reconstructed in the Central or Forward Detector. It also carries information that tells us about the detector responses such as scintillator, calorimeter, Cherenkov, etc. associated with the track. The status assignment used by the Event Builder for a particle track is given by,

status = 1000* FT +2000* FD +4000* CD +100* N_{scint} +10* N_{cal} +1* N_{cher},

where,

- FT/FD/CD are 1 if that detector subsystem contributed to the PID, else 0
- N_{scint} is the number of scintillator responses
- N_{cal} is the number of calorimeter responses
- N_{cher} is the number of Cherenkov responses.

All the information from the Event Builder is output to dedicated data structures, called HIPO banks, for further physics analysis. The identification schema described for electrons and charged kaons in the following sections detail the final particle selection criteria used in this analysis.

3.3.1 Electron Identification in the Forward Detector

For charged particle tracks in the Forward Detector, the Event Builder first assigns e^-/e^+ PID based on certain requirements from the DC, FTOF, HTCC, and ECAL detectors. First, the Event Builder looks for a charged track of the correct curvature in the DC that has a matched hit in the FTOF. Second, it looks for a minimum of two photoelectrons detected in the HTCC by the Cherenkov light created by that track. The HTCC separates electrons from negative pions to a pion momentum of

4.9 GeV. An electron will produce more photoelectrons in the HTCC than pions of the same velocity due to their lower momenta. The distribution of photoelectrons for the negative tracks in sector one after applying the number of photoelectrons cut ($N_{phe} > 2$) is shown in Fig. 3.1.

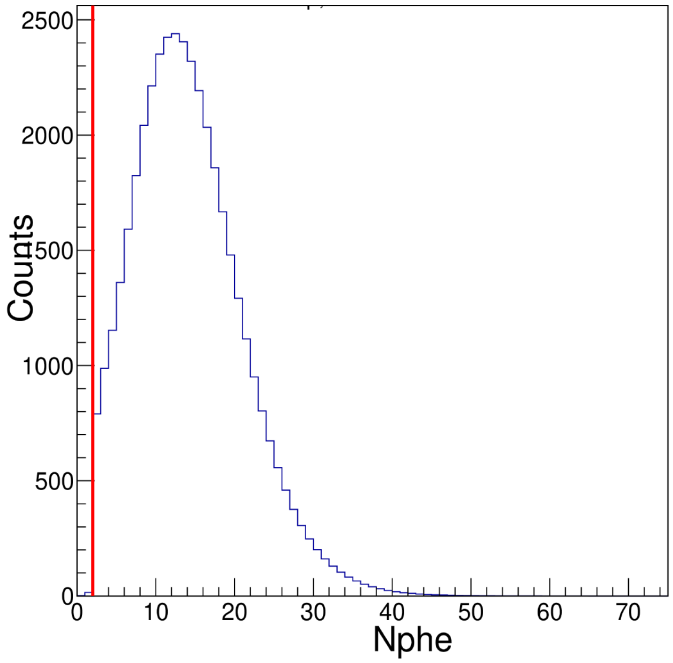

Figure 3.1: Number of photoelectrons (N_{phe}) reconstructed in the HTCC for electron tracks in sector one. The vertical red line at $N_{phe} = 2$ indicates the position of the number of photoelectrons cut implemented by the Event Builder to assign electron ID in the Forward Detector. When selecting electrons in the Forward Detector with the Event Builder PID, this cut is automatically imposed.

Electrons traveling through the calorimeter develop an extended electromagnetic shower and deposit significant energy. Minimum-ionizing pions, on the other hand, deposit smaller and nearly constant amounts of energy compared to electrons. Thus, the third criterion for electron identification in the Forward Detector is a minimum of 60 MeV of energy deposited in the PCAL. The energy deposition in EC vs. the energy in the PCAL is shown in Fig. 3.2.

In addition to the three criteria explained above, a sampling fraction cut is also implemented in the Event Builder to clean up electron identification in the

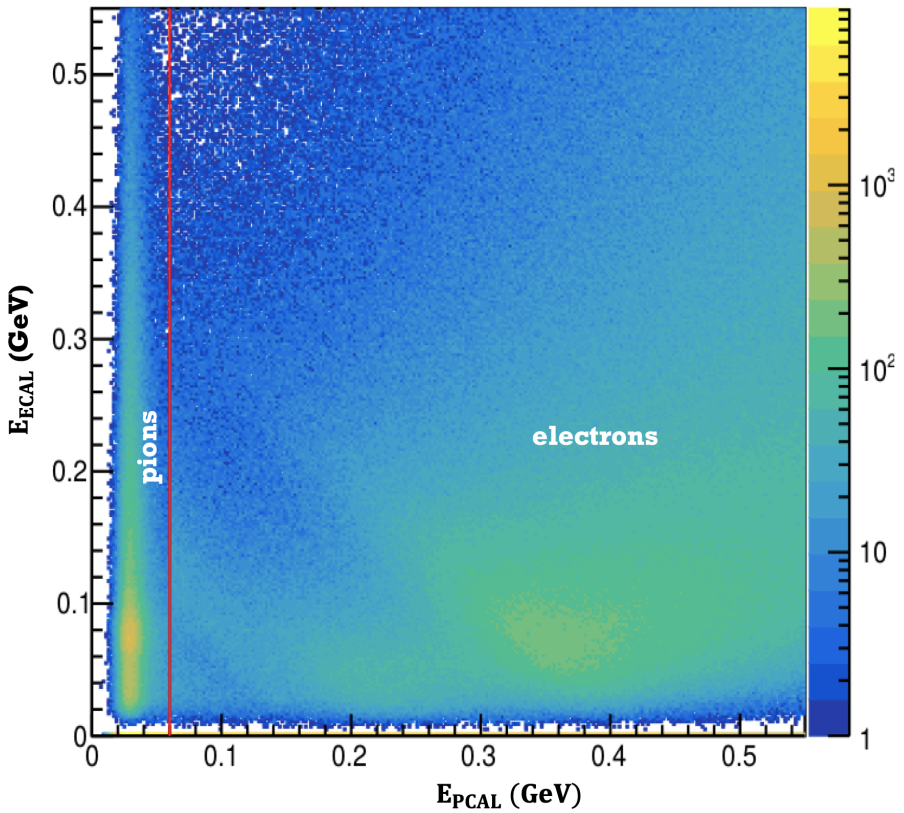

Figure 3.2: Energy deposited in the EC (EC_{in} + EC_{out}) vs. energy deposited in the PCAL. The red line at 60 MeV represents the minimum energy deposited cut implemented by the Event Builder to assign electron ID in the Forward Detector sector one. The band below the 60 MeV red line corresponds to pions. When using the Event Builder PID to choose electrons in the Forward Detector, this cut is automatically enforced.

Forward Detector. The sampling fraction is momentum dependent and given by $SF = E(det)/p$, where p is the momentum of the electron track determined from the DC tracking and $E(det)$ is the sum of the cluster energy detected by the EC and PCAL. The mean and width of the sampling fraction are parameterized as a function of the total energy deposited by the particle track in the ECAL. For the electron track, the momentum-dependent sampling fraction cut implemented by the Event Builder is $\pm 5\sigma$. The Event Builder's calorimeter sampling fraction for sector one electrons with the $\pm 5\sigma$ cut is shown in Fig. 3.3. When selecting electrons in the Forward Detector with the Event Builder PID, this cut is automatically imposed.

The details on the sampling fraction parameterization are available in the CLAS12 Event Builder page in Ref. [69].

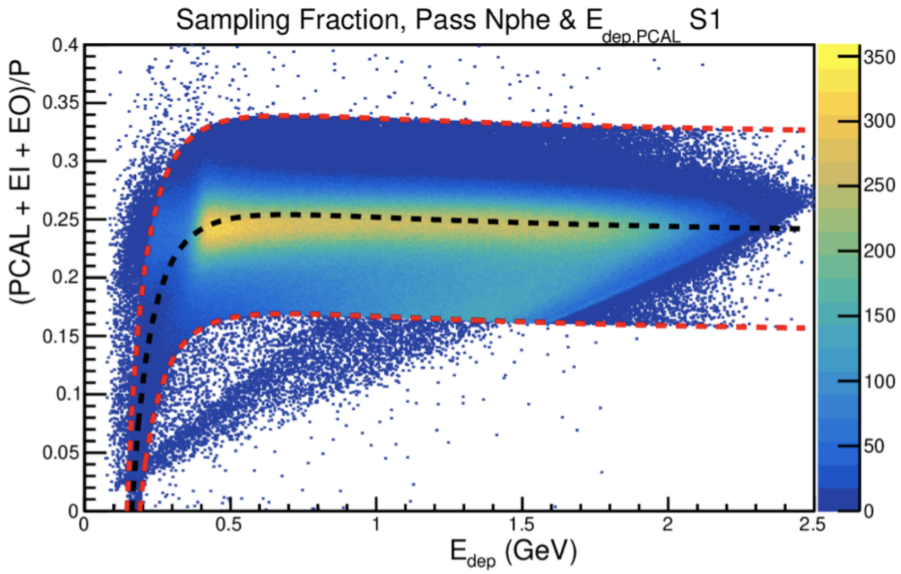

Figure 3.3: An example of the momentum-dependent calorimeter sampling fraction cut ($\pm 5\sigma$) implemented by the CLAS12 Event Builder. The plot is the ratio of the sum of energy deposited in the forward calorimeter layers to track momentum vs. deposited energy in the pre-shower calorimeter for sector one electrons. The electron tracks have N_{phe} and minimum PCAL energy cuts applied. The black dashed line corresponds to the mean sampling fraction, and the red dashed lines correspond to the $\pm 5\sigma$ width implemented by the CLAS12 Event Builder. Using the Event Builder PID to choose electrons in the Forward Detector also insures that this cut is automatically enforced in the PID assignment.

In addition to all these criteria required by the Event Builder, some additional PID refinement cuts were implemented post Event Builder to select good electrons in the FD for this analysis. A $z-$vertex cut (coordinate along the beamline) of -10 cm to 1 cm on the electron track candidate was implemented to ensure that scattered electrons come from the target region. A hard cut of $1 < P_{e'} < E_{beam}$ (GeV) on the momentum of the trigger electron was applied to remove the contamination from low momentum accidental electrons coming from outside of the target region created with different processes such as pair production, Compton scattering, ionization, multiple

scattering, etc. A polar angle cut of $5^\circ < \theta_{e'} < 35^\circ$ was applied for the trigger electron to ensure electrons were detected within the angular region covered by the FD. The minimum-ionizing pions are easy to identify as discussed earlier and are easily removed with the PCAL minimum energy deposition cut implemented by the Event Builder. However, there is contamination from the heavily-ionizing pions at higher momentum that overlap the signal region for electrons. To remove the contamination of heavily-ionizing pions in the electron sample with pion momentum above the HTCC threshold of 4.9 GeV, a calorimeter "diagonal cut" was applied for electrons with momenta greater than 4.5 GeV. The calorimeter diagonal cut is defined based on deposited energy by electrons in different parts of the calorimeter. This cut is not implemented in the Event Builder PID assignment in this preliminary pass of the data processing. This preliminary pass of the data is referred to as the pass-1 data processing. The post Event Builder diagonal cut implemented in our analysis is given by the black diagonal line $E_{inner}/p < 0.2 - E_{PCAL}/p$ as shown in Fig. 3.4. The detailed study of the post Event Builder diagonal cut for particles using pass-1 data was performed by Stefan Diehl and documented in the CLAS12 centralized software wikipage [75]. There is a plan to include this cut in the Event Builder during the next pass of the data processing. Additionally, geometrical fiducial cuts from the preliminary studies on the drift chamber volume were also applied to exclude events in regions where the acceptance is low and not well understood. The study of the drift chamber fiducial volume cut was performed by Stefan Diehl and Aron Kripko using preliminary pass-1 data, and the details can be found from the CLAS12 Run Group A wikipage [76]. Table 3.2 summarizes the various cuts applied to select electrons in the Forward Detector.

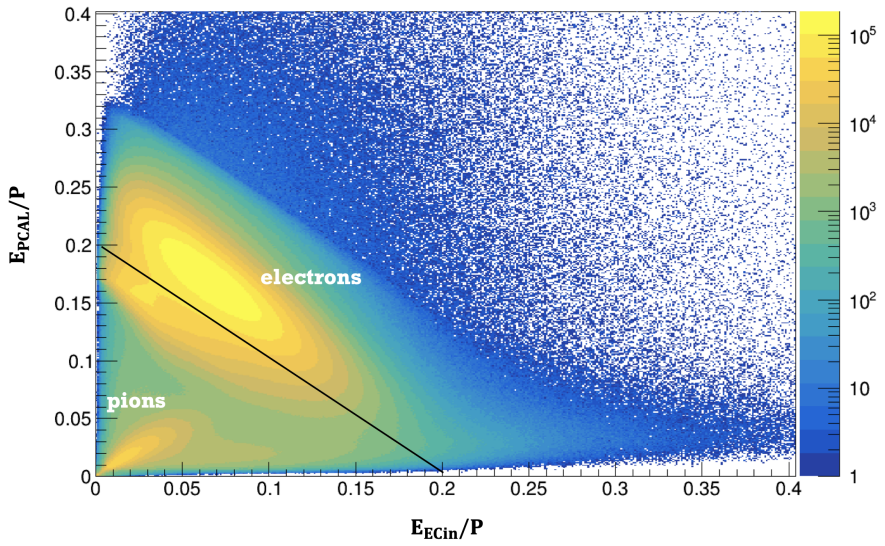

Figure 3.4: Calorimeter diagonal cut used for electrons with momentum greater than 4.5 GeV. As shown in the figure, the black diagonal line cut separates two distinct distributions corresponding to true electrons and heavily-ionizing pions misidentified as electrons. The minimum-ionizing pions are shown by the band below 0.06 and the band appears due to the minimum-ionizing energy deposition by low momentum pions. The details of the study can be found in the CLAS12 centralized software wikipage [75].

3.3.2 Electron Identification in the Forward Tagger

The Forward Tagger can only differentiate charged particles from neutral particles. The CLAS12 Event Builder assigns two possible particle identifications (electron or photon) for tracks in the Forward Tagger based on the response from the Forward Tagger hodoscope. Electrons and photons both produce indistinguishable electromagnetic showers inside the calorimeter. However, electrons are identified by observing a hit in the hodoscope and matching that hit with the response from the Forward Tagger calorimeter.

There is no standard fiducial volume cut developed for the Forward Tagger electron. In this analysis, a lab polar angle cut of $2.5° < \theta_{e'} < 4.5°$ for electrons in the Forward Tagger was applied. This polar angle cut matches the actual location of the

Forward Tagger in the laboratory phase space with respect to the center of the target. In addition, an electron energy cut of $1 < E_{e'} < 4.5$ GeV was applied following the MesonEx trigger to select high-energy, quasi-real photons for the experiment. The Forward Tagger electrons with energy lower than 1 GeV were not included in our data sample as most of those electrons are low momentum accidental background electrons. The vertex information for the electron detected in the Forward Tagger is not available in the pass-1 data, hence, no vertex cut was applied for the Forward Tagger electron. Table 3.2 summarizes the various cuts applied to select electrons in the Forward Tagger.

Electrons interacting with the calorimeter initiate electromagnetic showers. If by any chance the electromagnetic shower is not fully contained within the detector, this leads to an incomplete energy measurement that must be corrected. To address this issue, a Forward Tagger electron energy correction was developed by using the reaction $ep \rightarrow e'p\pi^+\pi^-$ with the scattered electron detected in the Forward Tagger. The final state proton and charged pions were detected in the Forward Detector. With accurate knowledge of the incoming electron beam energy and the mass of the proton target, the electron's energy in the FT can be reconstructed assuming the final state proton and pion energies are accurately reconstructed in the FD. The FT-detected electron energy can then be corrected to match the missing energy determined by the FD-detected proton and pions. The electron energy correction for the Forward Tagger was derived by graduate students from Florida International University and the University of York. The effect of the Forward Tagger electron energy correction on the missing mass spectrum $MM(e'K^+K^+K^-)$ for the reaction $ep \rightarrow e'K^+K^+K^-X$ is shown in Fig. 3.5.

Electron selection cuts in FT and FD

Cuts	FT electron	FD electron
Track charge	-1	-1
Track status	$1000 \leq \lvert status \rvert < 2000$	$2000 \leq \lvert status \rvert < 4000$
$\theta_{e'}$ cut	$2.5^\circ < \theta_{e'} < 4.5^\circ$	$5^\circ < \theta_{e'} < 35^\circ$
Momentum cut	$1.0 < P_{e'} < 4.5$ GeV	$1.0 < P_{e'} < E_b$ GeV
z-vertex cut	N/A	$-10 < v_{e'}^z < 1$ cm
$N_{e'}$	1	1
Electron energy correction	Applied	N/A
PCAL minimum energy cut	N/A	60 MeV
ECAL sampling fraction cut	N/A	$\pm 5\sigma$
Calorimeter diagonal cut	N/A	$E_{inner}/p < 0.2 - E_{PCAL}/p$
DC fiducial cut	N/A	Applied
N_{phe} cut	N/A	2

Table 3.2: Summary table showing different cuts applied to select electrons in the FT and FD.

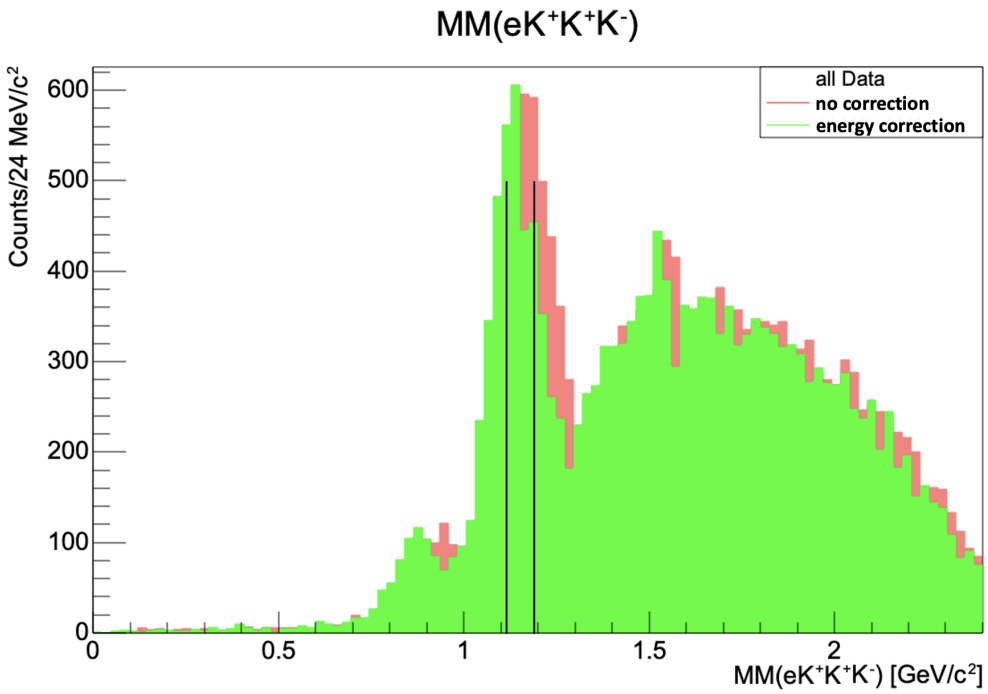

Figure 3.5: The effect of Forward Tagger electron energy correction on $MM(e'K^+K^+K^-)$ from the reaction $ep \to e'K^+K^+K^-X$. Two black lines are drawn at the nominal mass values of the Λ and Σ^0 at 1.115 GeV and 1.192 GeV, respectively. The missing mass distribution shifts towards the nominal mass values of the Λ and Σ^0 after correcting the electron's energy in the Forward Tagger.

3.3.3 Charged Kaon Identification

Charged kaons (two K^+ and one K^-) detected in the Forward Detector are initially selected from the Event Builder information. To improve kaon identification in the reaction $ep \to e'K^+K^+K^-X$, additional post Event Builder cuts implemented in the analysis include a Forward Detector polar angle cut, momentum cut, β cut, z-vertex cut, momentum-dependent vertex time cut, and DC fiducial cut. The cuts applied to improve charged kaon identification are summarized in Table 3.3.

Figure 3.6 shows an example of β vs. p plots for all positively and negatively charged hadrons detected in the Forward Detector with a hit in the FTOF system.

Charged Kaon Selection Cuts in FD

Cuts	K^+	K^-
Track charge	$+1$	-1
Track status	$2000 \leq \lvert status \rvert < 4000$	$2000 \leq \lvert status \rvert < 4000$
chi2pid cut	< 5.0	< 5.0
FD θ cut	$5^\circ < \theta_{K^+} < 35^\circ$	$5^\circ < \theta_{K^-} < 35^\circ$
Momentum cut	$0.4 < P_{K^+} < E_b$ GeV	$0.4 < P_{K^-} < E_b$ GeV
z-vertex cut	$-10 < v^z_{K^+} < 1$ cm	$-10 < v^z_{K^-} < 1$ cm
β cut	$0.4 < \beta_{K^+} < 1.05$	$0.4 < \beta_{K^-} < 1.05$
DC fiducial cut for hadron	Applied	Applied
$\delta \mathrm{vt}_{meas-calc}$ cut	Applied	Applied

Table 3.3: Summary table showing different cuts applied to select charged kaons in the FD.

The fractional velocity β for each particle is defined as the velocity divided by the speed of light. The velocity for each charged particle is calculated using the time-of-flight and path length of the particle from the primary interaction vertex to the scintillator hit position in the FTOF system. Three clear bands in the β vs. momentum plot for positively charged particles correspond to pions, kaons, and protons, as labeled. In addition, there is a faint band of deuterons in the β vs. momentum plot of positive particles. These deuterons are created due to the interaction of incident electrons with the aluminium end windows of the CLAS12 LH_2 target. Similarly, there are three bands in the β vs. momentum plot for negatively charged particles corresponding to pions, kaons, and anti-protons, as labeled. Electron PID was not included while making these plots. There is a clear separation of the different particle types at low momentum. As the momentum increases, the particle velocity approaches the speed of light, the bands merge, and particle ID becomes less certain.

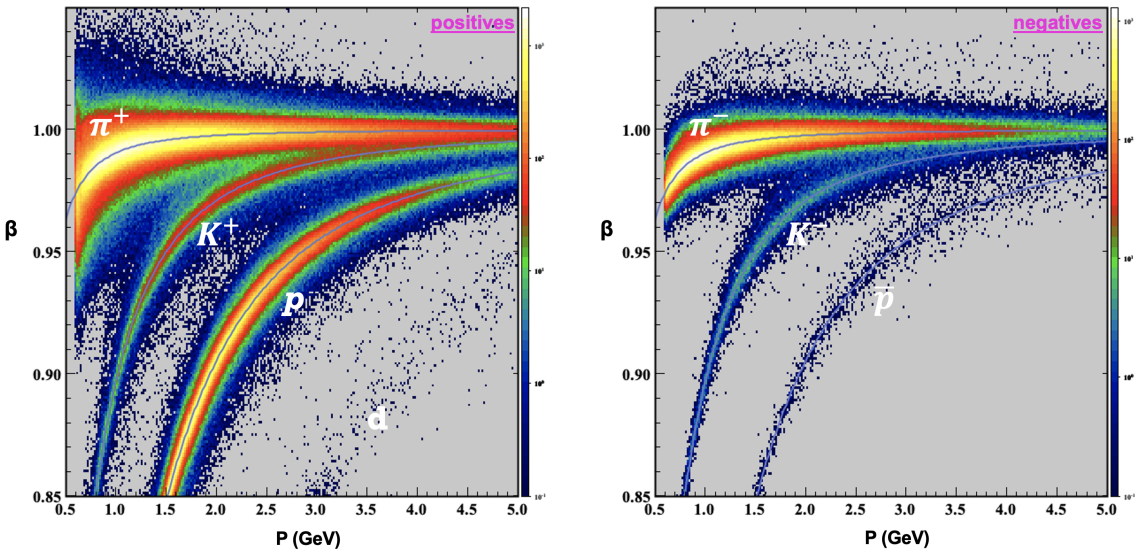

Figure 3.6: Example of β vs. p plots for all positively charged and negatively charged hadrons in FTOF.

One can calculate the mass of charged particles using β and the momentum from tracking using the formula, $M^2_{calc} = p^2_h * \left(\frac{1-\beta^2_h}{\beta^2_h}\right)$. Figure 3.7 shows an example of the calculated time-of-flight mass squared, M^2_{calc}, for all positively and negatively charged hadrons hitting the FTOF using particle momentum determined from the Forward Detector tracking and speed, β, measured using the time-of-flight and path length information. For a particle with a total travel time of T along a well-determined trajectory of path length L, the speed is determined with the formula $\beta = \frac{L}{cT}$, where c is the speed of light. The resolution of the FTOF limits the precision to which T is determined in the experiment, which eventually will affect the β measurement. Hence, one can observe in particle physics experiments a value of β greater than one, as shown in the β vs. p plot in Fig. 3.6. Such instrumental resolution is also responsible for the negative value of the square of the mass, as shown in Fig. 3.7.

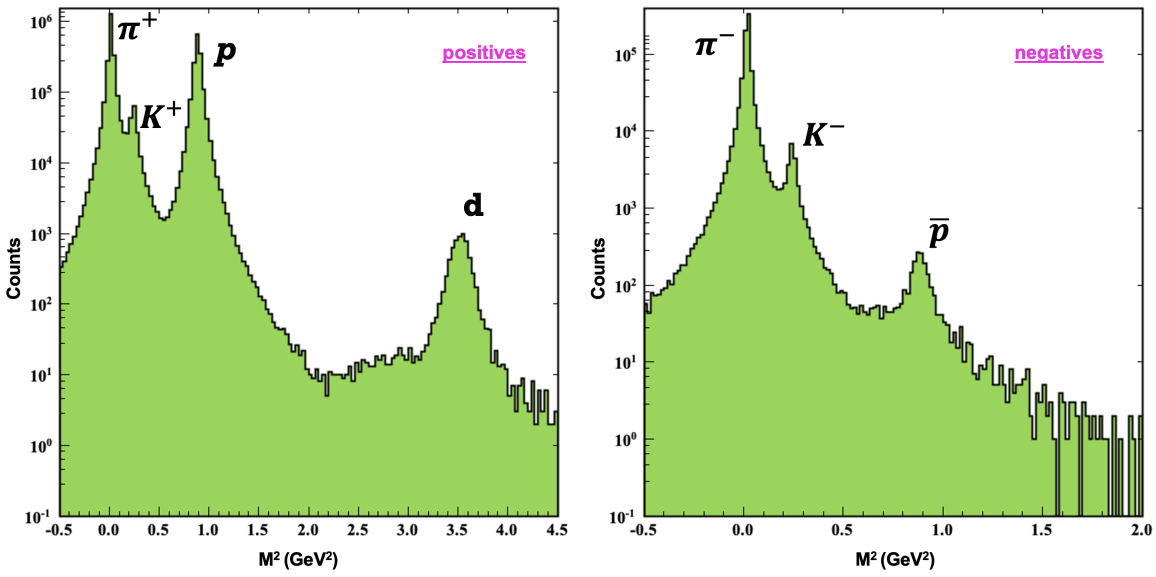

Figure 3.7: Example of time-of-flight mass squared calculated using β and p from forward tracking for all positively charged (left) and negatively charged (right) hadrons in CLAS12.

3.3.3.1 Target z-Vertex Cut

The target z-vertex cut removes events with vertices reconstructed outside the target cell volume. The decay of the intermediate hyperon, Ξ^{*-}, in the reaction of interest, $ep \rightarrow e'K^+K^+\Xi^{*-}$, is a strong decay, implying that the scattered electron, two K^+, and one K^- in each event should originate from the target region. The center of the 5-cm-long target used for this experiment is located at -3 cm along the z axis in the global CLAS12 coordinate system. The z-vertex cut applied to select the target region for electrons and charged kaons detected in the Forward Detector is shown in Fig. 3.8. Due to the vertex resolution in the available pass-1 data, there is a longer vertex cut (around 11 cm) than the target's length.

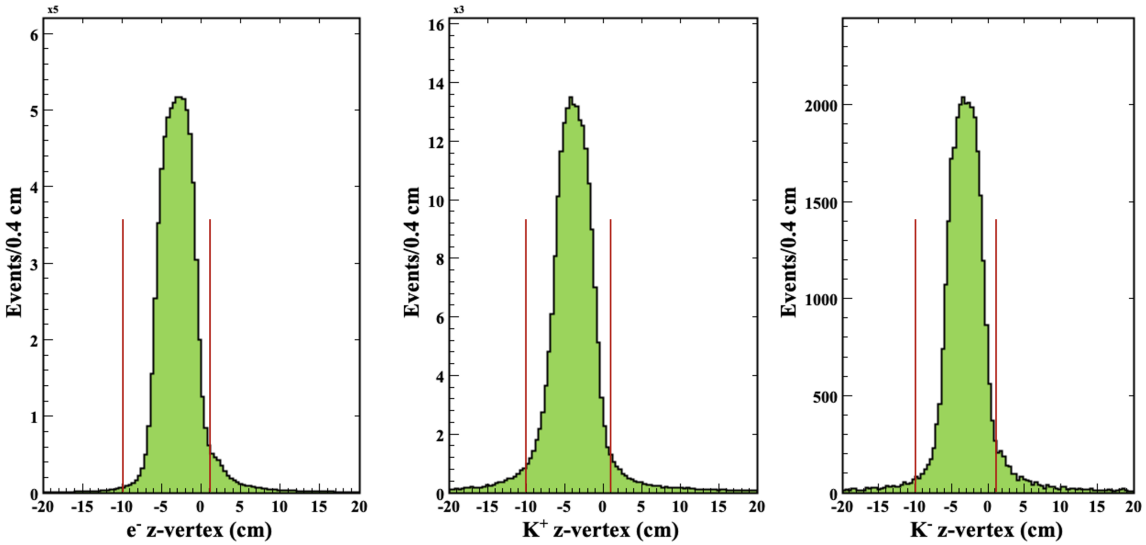

Figure 3.8: Distribution of the z-vertex position of electrons and charged kaons in all six sectors. Wider vertex cuts from -10 cm to 1 cm than the length of the target were placed to include the physical region of the target due to the vertex resolution.

3.3.3.2 Momentum Dependent Vertex Time Cut

For the charged kaons in each event, the time difference between the measured and computed vertex time was calculated using:

$$\delta vt_{K^{\pm}} = TOF_{K^{\pm}} * \left(1 - \sqrt{\frac{p^2_{K^{\pm}} + M^2_{calc}}{p^2_{K^{\pm}} + M^2_{K^{\pm}}}}\right), \tag{3.1}$$

where M_{calc} is calculated using particle momentum (p) and β from the tracking defined by,

$$M^2_{calc} = p^2_{K^{\pm}} * \left(\frac{1 - \beta^2_{K^{\pm}}}{\beta^2_{K^{\pm}}}\right). \tag{3.2}$$

The time-of-flight for charged kaons ($TOF_{K^{\pm}}$) in the formula for $\delta vt_{K^{\pm}}$ was computed using the track-dependent vertex time and the FTOF hit time for each kaon track on an event-by-event basis using,

$$TOF_{K^{\pm}} = FTOF^{hit-time}_{K^{\pm}} - t^{v_z}_{K^{\pm}}, \tag{3.3}$$

where $t^{v_z}_{K^{\pm}}$ is the corrected event start time (STT) propagated to the individual particle vertex for each $K^{\pm}$ track using the formula,

$$t^{v_z}_{K^{\pm}} = STT + \left(\frac{v^z_{K^{\pm}}}{c * \beta_{K^{\pm}}}\right). \tag{3.4}$$

Figure 3.9 shows the time difference between the measured and computed vertex time ($\delta vt_{K^{\pm}}$) as a function of particle momentum for K^+ and K^- particles. The black lines shown in the plot are the actual cut applied to improve kaon identification. These black curves were adjusted to mimic the detector resolution function leaving more room for the wider cut at lower momentum and less room for the narrow cut going from lower to higher momentum, as shown in Fig. 3.9. Equation (3.5) describes

the momentum-dependent $\delta vt_{K^{\pm}}$ cut applied for $K^{\pm}$ to remove pions misidentified as kaons by the Event Builder.

$$\delta vt_{K^{\pm}} = |0.05 + e^{(-p+\frac{0.4}{p})}|. \tag{3.5}$$

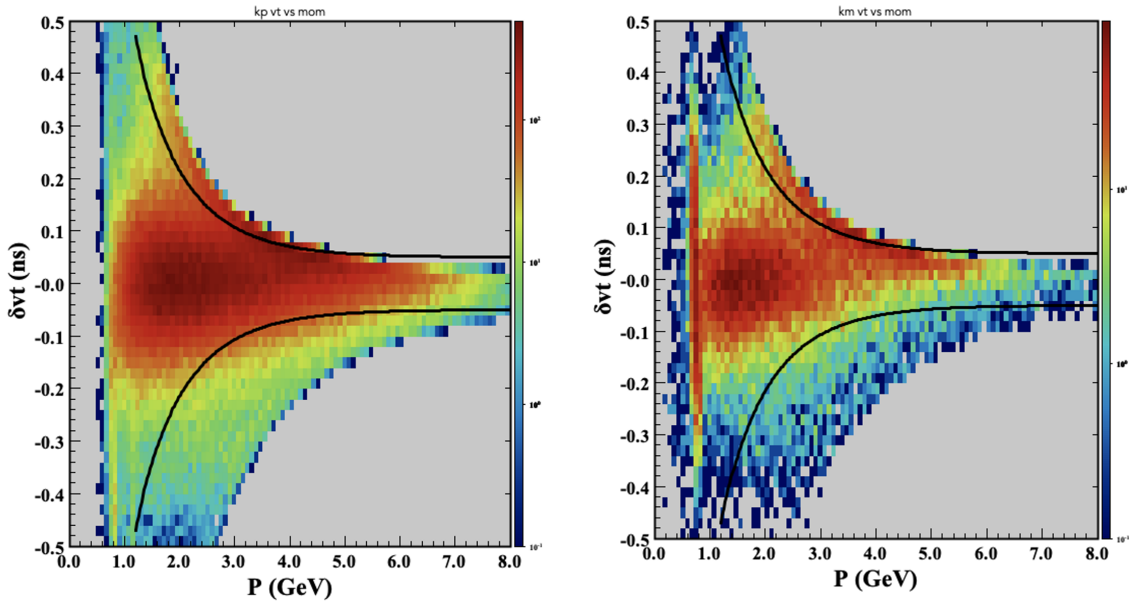

Figure 3.9: The time difference between the measured and computed vertex time for K^+ (left) and K^- (right) as a function of momentum. The black curves in each plot show the cut applied to clean up kaon selection. The plots include only kaons that were pre-assigned a kaon ID by the Event Builder.

3.3.3.3 Fiducial Volume Cuts

We need to remove tracks where the particle momentum vector points toward the edges of the active region of the detector, such as near the region where the torus coils are located. The detection efficiency in such regions cannot be accurately determined. Furthermore, the detection efficiency near the edges of the active region of the detectors such as drift chambers and calorimeters is problematic as it changes very rapidly. Therefore, the drift chamber fiducial volume cuts were applied for electrons and charged kaons in the Forward Detector to select the region where the efficiency

is relatively flat. The preliminary drift chamber fiducial cuts for CLAS12 were developed by Aron Kripko and Stefan Diehl. The detailed procedure on how the drift chamber fiducial cuts for electrons and hadrons were developed, including a discussion on the exact parameterizations, can be found in the CLAS12 RG-A analysis overview and procedures note [76].

3.4 Reaction Reconstruction

3.4.1 Missing Mass Technique

We used the missing mass technique to study the reactions $ep \rightarrow e'K^+K^+(X)$ and $ep \rightarrow e'K^+K^+K^-(Y)$. In both cases, we know the energy of an incoming electron beam and the status of the proton target, which is at rest. In the first case, we look for missing final-state particles by detecting the scattered electron and two positively charged kaons in the final state in each event. The missing final-state particles (X) that we are interested to explore in the missing mass off of $e'K^+K^+$ are doubly-strange Ξ^{*-} particles. In the second case, an additional negatively charged kaon will be detected to study the missing final-state particles. The missing final-state particles (Y) we are interested in exploring in the missing mass off of $e'K^+K^+K^-$ are Λ and Σ^0, which are the decay products of the intermediate Ξ^{*-} in the missing mass off of $e'K^+K^+$ through $K^-\Lambda$ and $K^-\Sigma^0$. Figures 3.10 to 3.21 show the kinematics (Q^2, W, Q^2 vs. W, and virtual photon energy (E_γ)) of the scattered electron detected in the FD and FT and scatterplots of p vs. θ, p vs. ϕ, and θ vs. ϕ of detected final state particles (e', K^+s, and K^-) for the Ξ^{*-} data sample from the different data sets. The z-vertex distributions (v_z) and θ vs. v_z scatterplots from the different data sets when the scattered electron is detected in the FD are also shown.

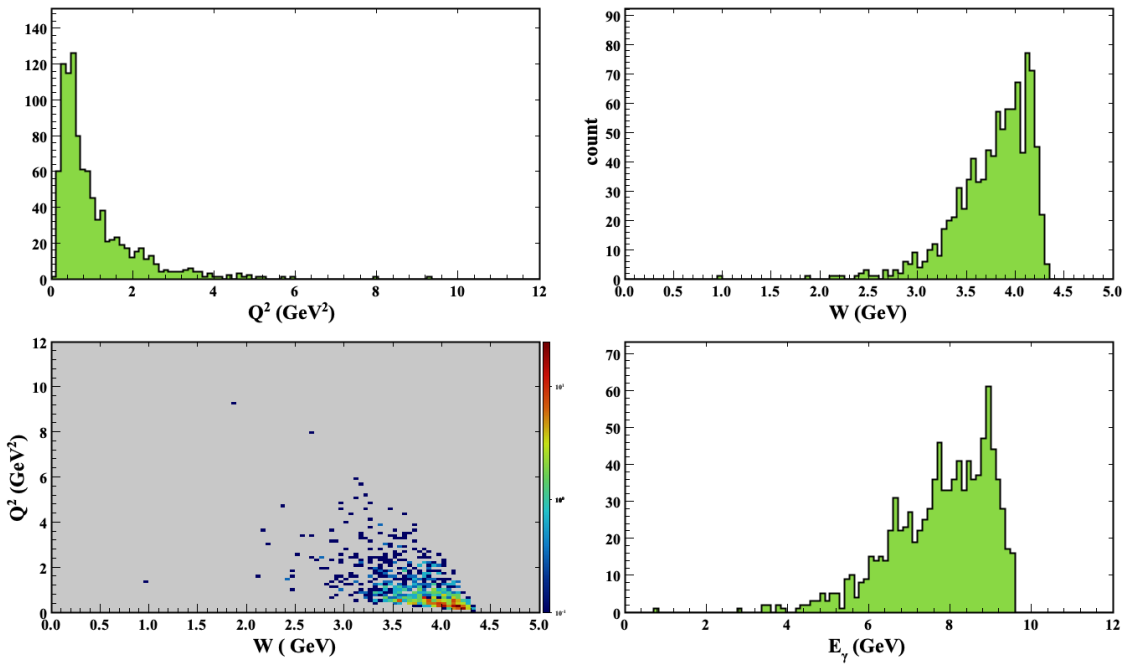

(a) Fall 2018 outbending FD-e.

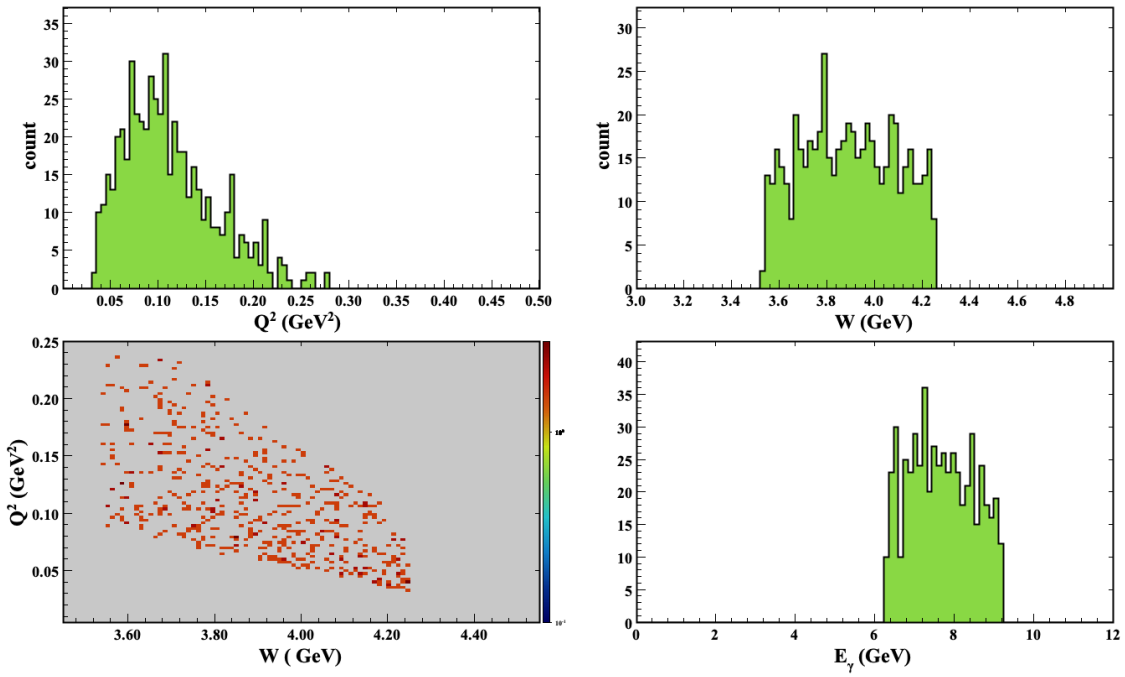

(b) Fall 2018 outbending FT-e.

Figure 3.10: The electron kinematics for the Fall 2018 outbending Ξ^{*-} data sample: Q^2 GeV^2 (upper left), W GeV (upper right), Q^2 vs. W (lower left), and virtual photon energy E_γ (GeV) (lower right). The set of plots in Fig. 3.10a (top) and 3.10b (bottom) correspond to the FT-e and FD-e, respectively.

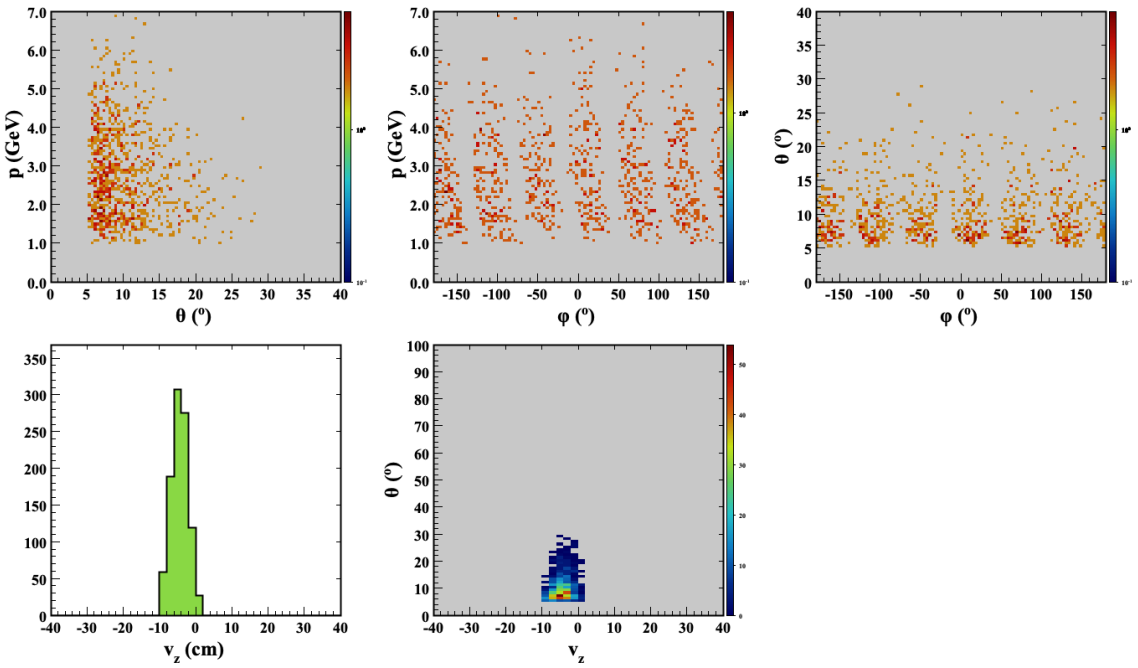

(a) FD-e in Ξ^{*-} data sample (Fall 2018 outbending FD-e).

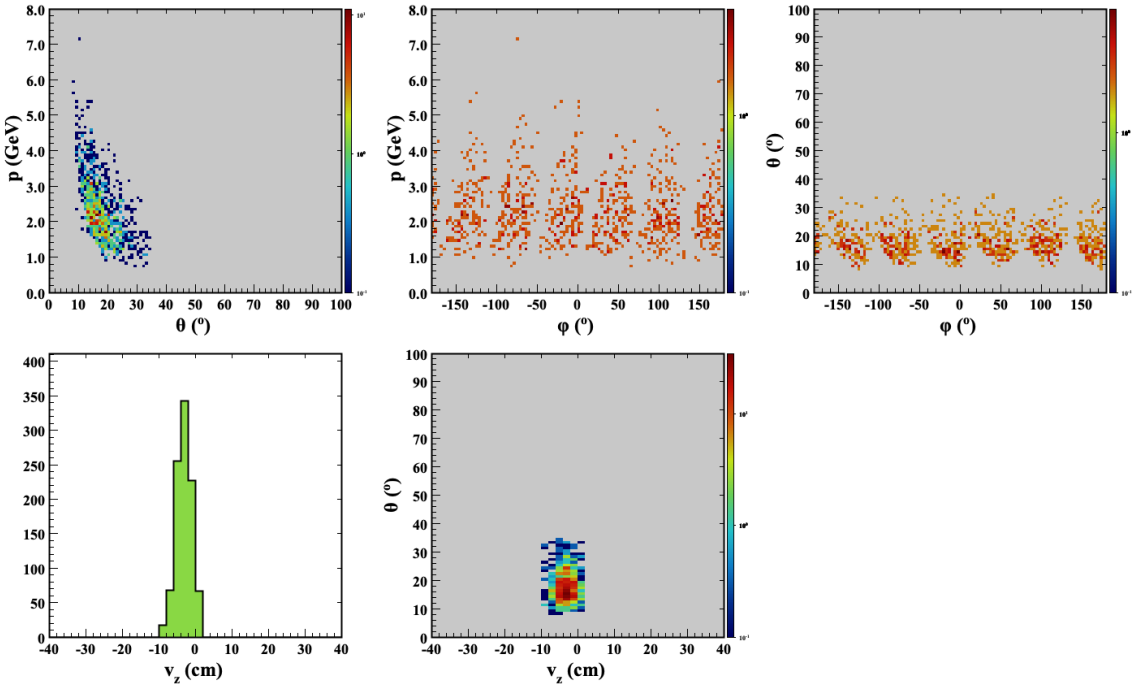

(b) Fast K^+ in Ξ^{*-} data sample (Fall 2018 outbending FD-e).

Figure 3.11: Final state FD-e (Fig. 3.11a) and fast moving K^+ (Fig. 3.11b) distributions: p (GeV) vs. θ° (upper left), p (GeV) vs. ϕ° (upper middle), θ° vs. ϕ° (upper right), v_z (cm) (lower left), and θ° vs. v_z (cm) (lower middle) for the Fall 2018 outbending Ξ^{*-} data sample when the electron is detected in the FD.

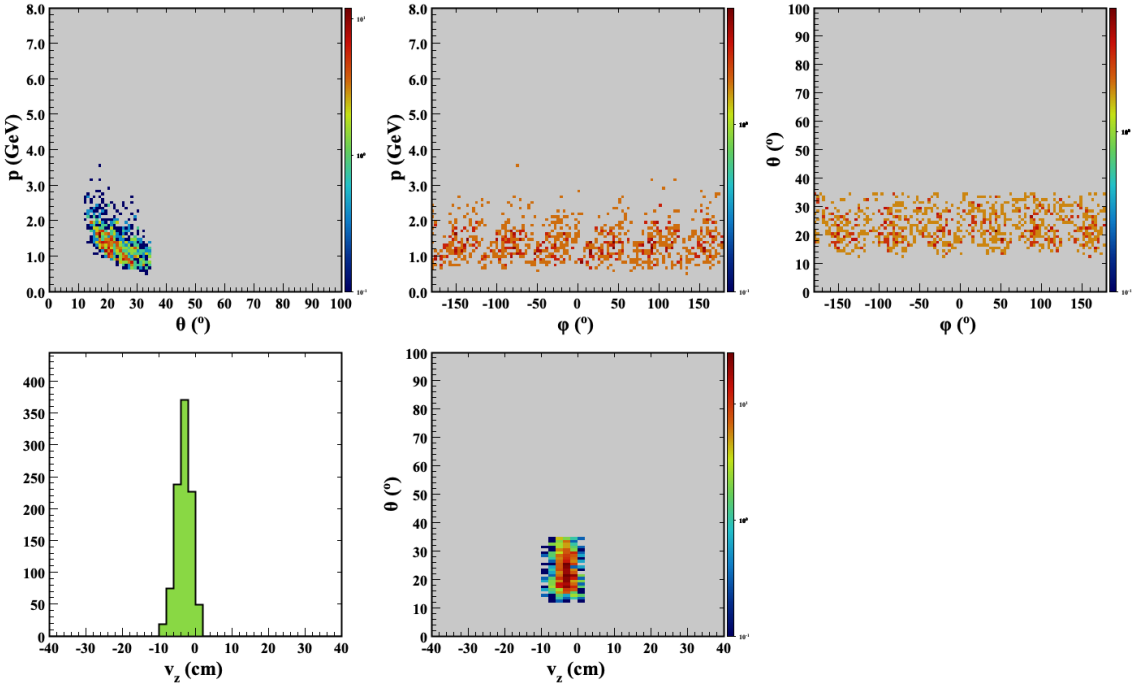

(a) Slow K^+ in Ξ^{*-} data sample (Fall 2018 outbending FD-e).

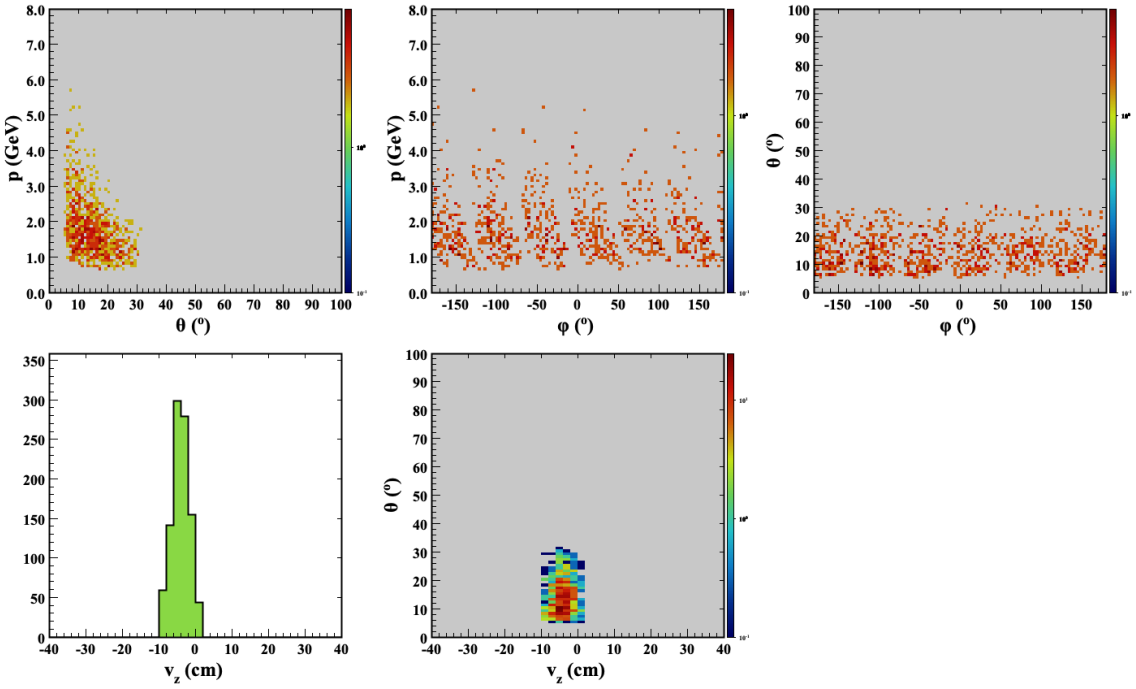

(b) K^- in Ξ^{*-} data sample (Fall 2018 outbending FD-e).

Figure 3.12: Final state slow moving K^+ (Fig. 3.12a) and K^- (Fig. 3.12b) distributions: p (GeV) vs. θ° (upper left), p (GeV) vs. ϕ° (upper middle), θ° vs. ϕ° (upper right), v_z (cm) (lower left), and θ° vs. v_z (cm) (lower middle) for the Fall 2018 outbending Ξ^{*-} data sample when the electron is detected in the FD.

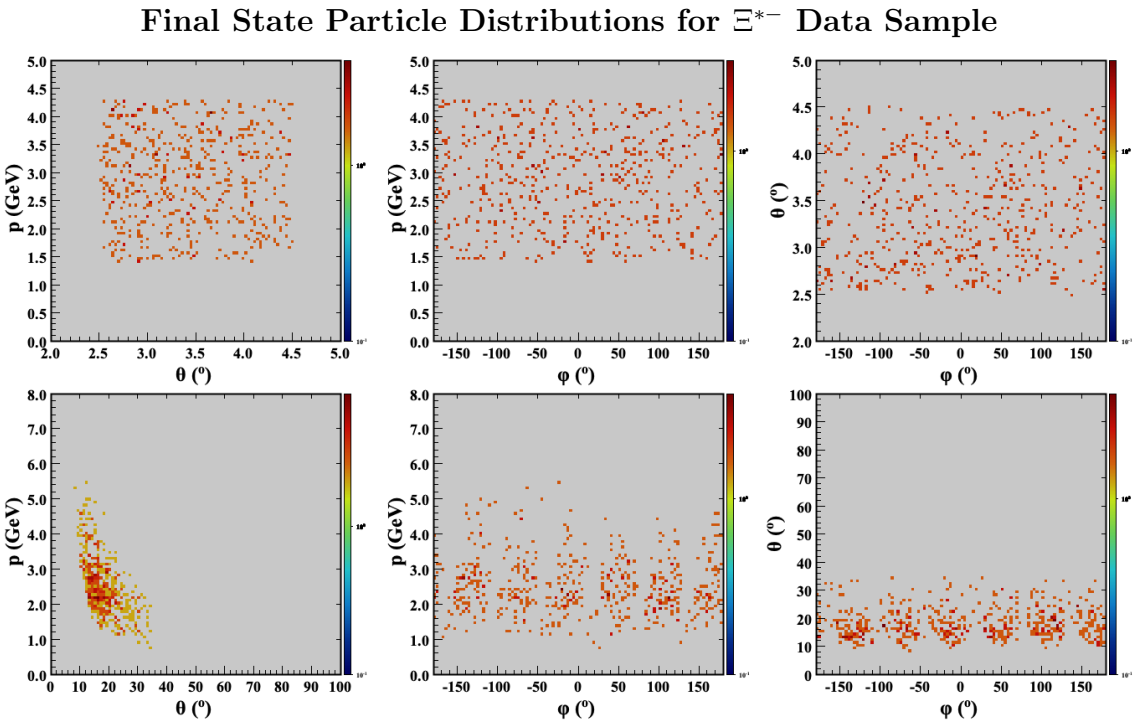

(a) FT-e (top row) and fast K^+ (bottom row) distributions (Fall 2018 out FT-e).

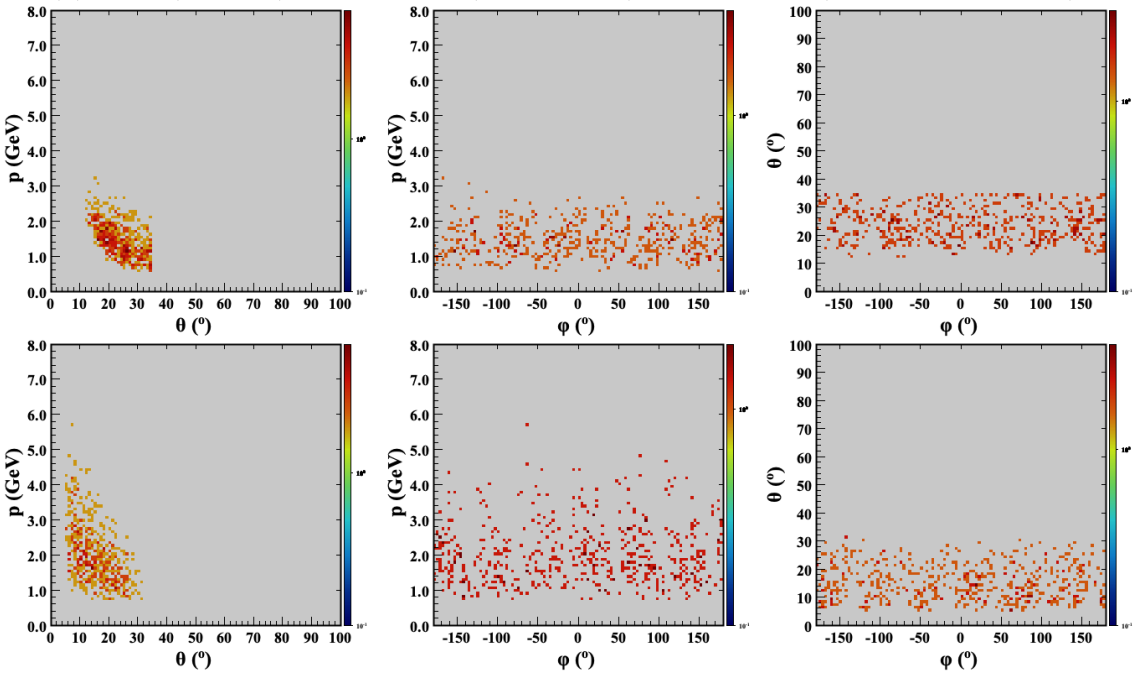

(b) Slow K^+ (top row) and K^- (bottom row) distributions (Fall 2018 out FT-e).

Figure 3.13: Final state FT-e (top row Fig. 3.13a), fast moving K^+ (bottom row Fig. 3.13a), slow moving K^+ (top row Fig. 3.13b), and K^- (bottom row Fig. 3.13b) distributions: the set of plots in each row correspond to p (GeV) vs. θ°, p (GeV) vs. ϕ°, and θ° vs. ϕ° from left to right for the different final state particles for the Fall 2018 outbending Ξ^{*-} data sample when the electron is detected in the FT.

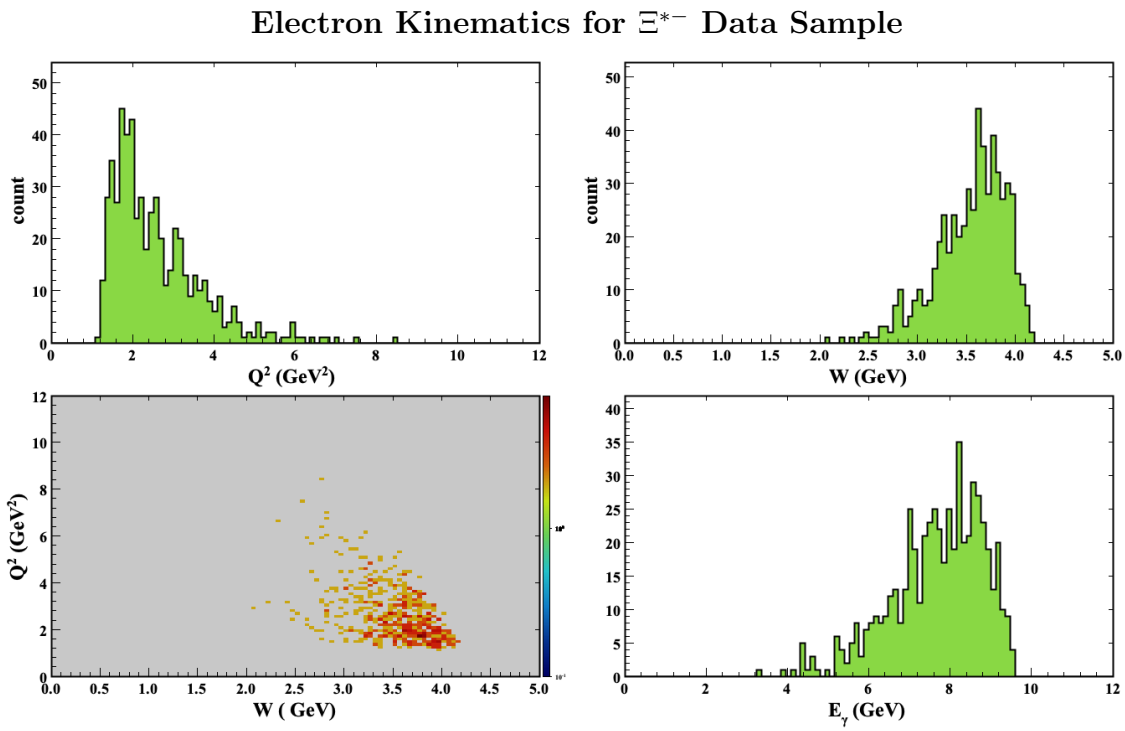

(a) Fall 2018 inbending FD-e.

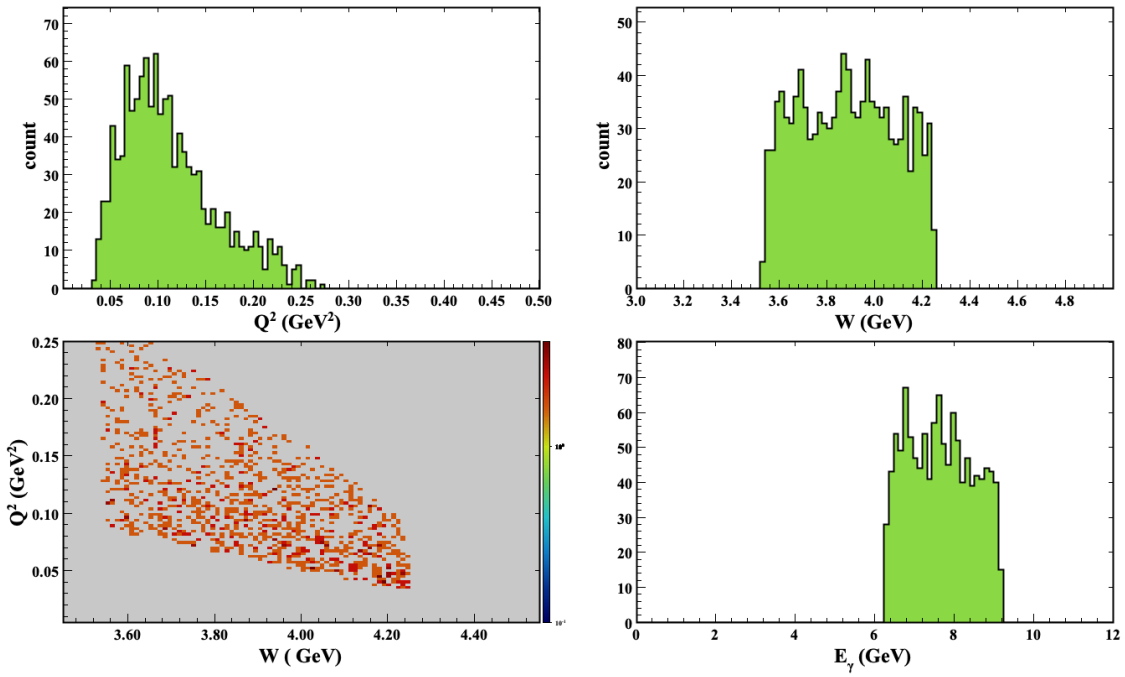

(b) Fall 2018 inbending FT-e.

Figure 3.14: Same as Fig. 3.10 but for the Fall 2018 inbending data set.

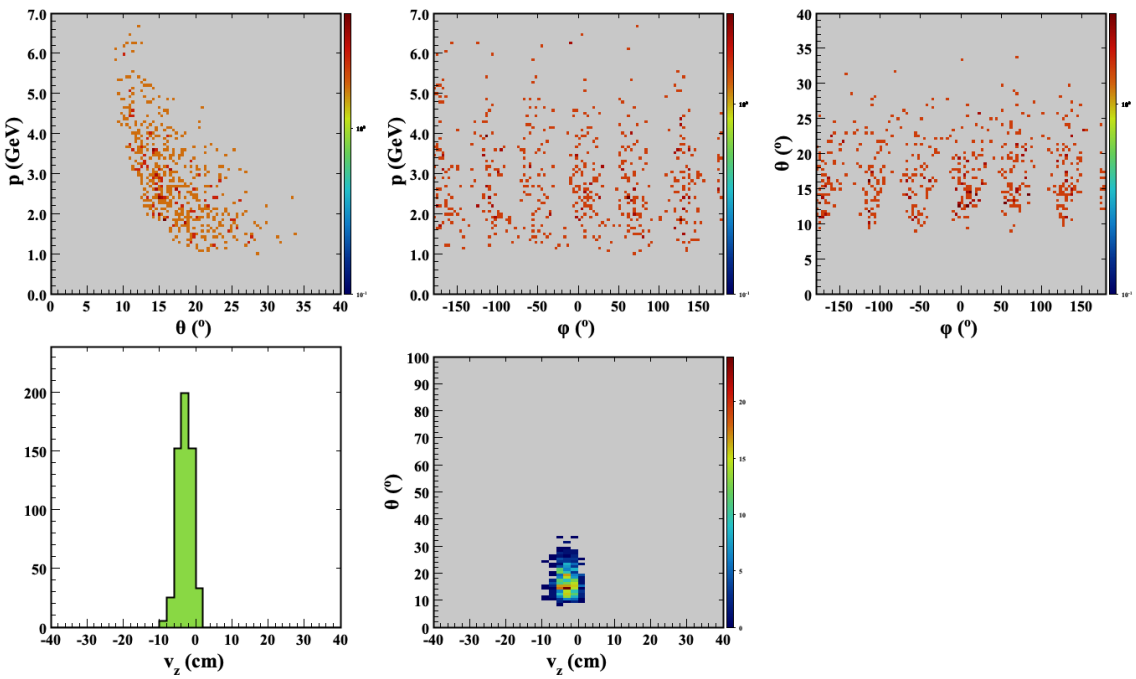

(a) FD-e in Ξ^{*-} data sample (Fall 2018 inbending FD-e).

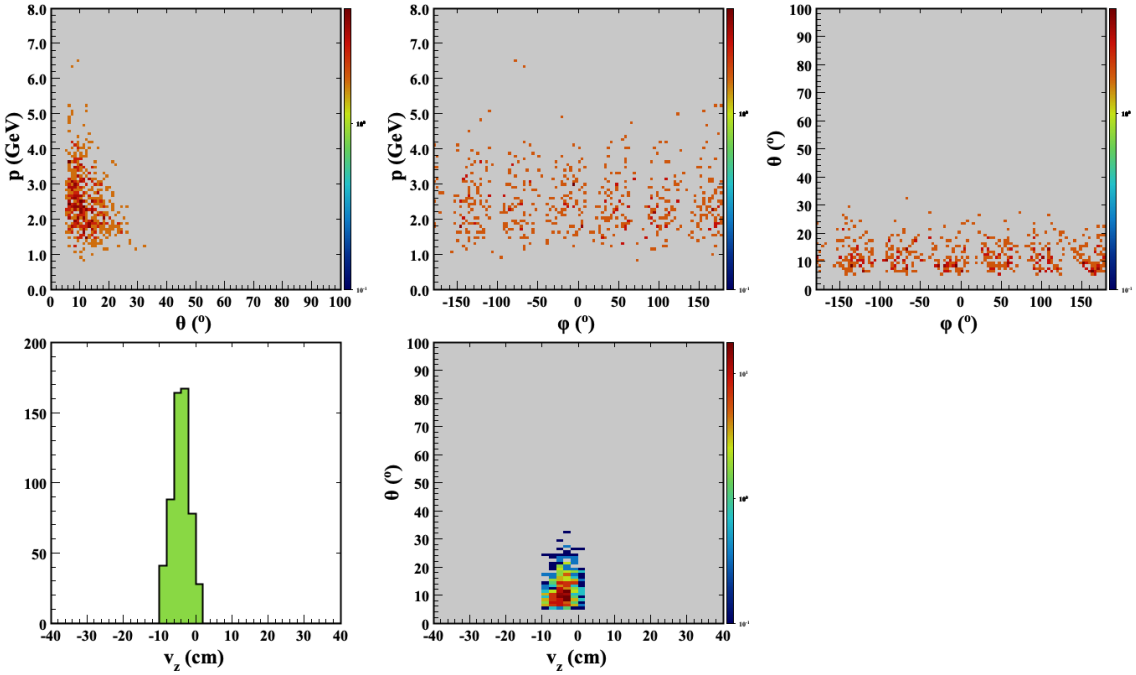

(b) Fast K^+ in Ξ^{*-} data sample (Fall 2018 inbending FD-e).

Figure 3.15: Same as Fig. 3.11 but for the Fall 2018 inbending data set.

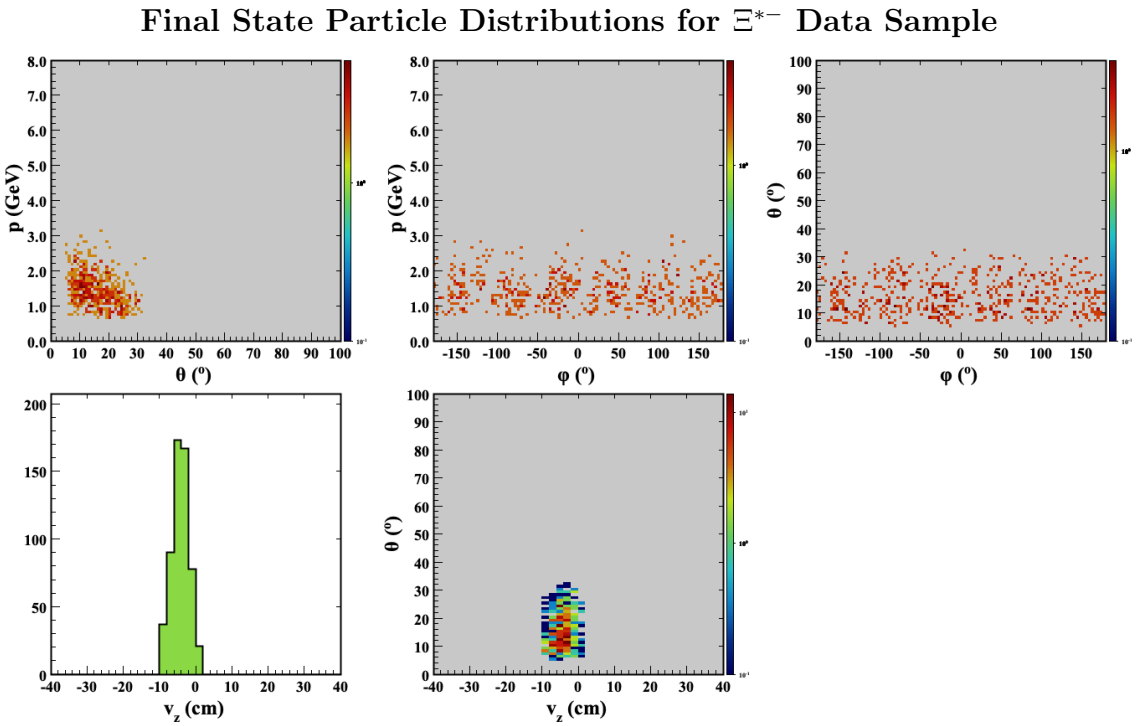

(a) Slow K^+ in Ξ^{*-} data sample (Fall 2018 inbending FD-e).

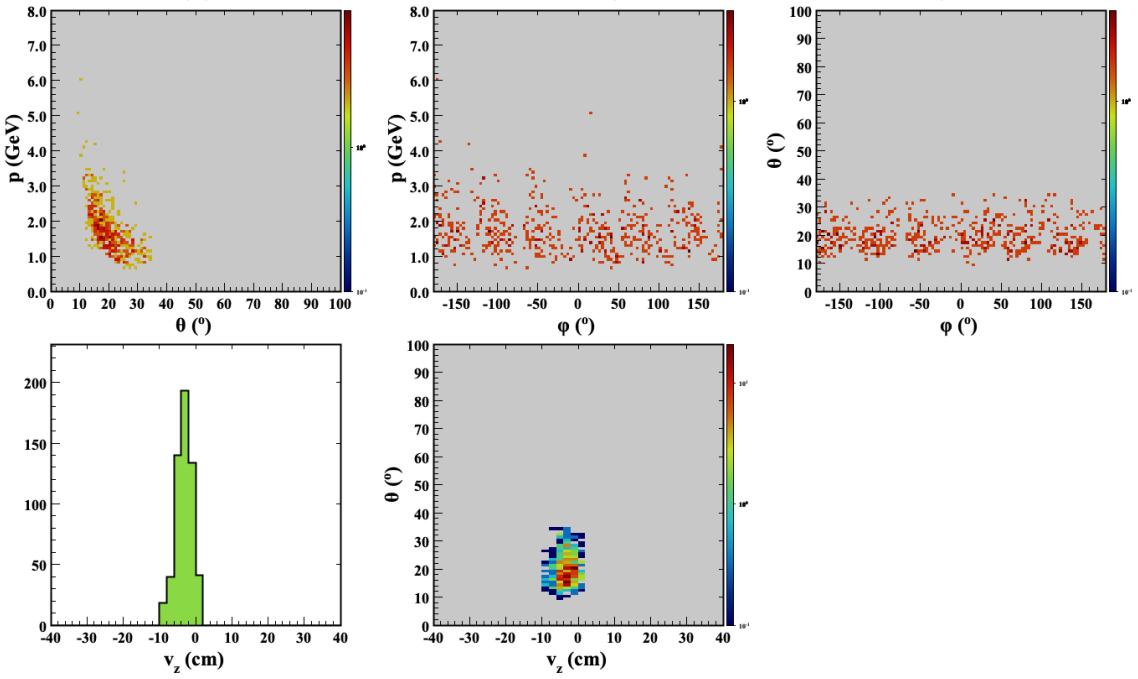

(b) K^- in Ξ^{*-} data sample (Fall 2018 inbending FD-e).

Figure 3.16: Same as Fig. 3.12 but for the Fall 2018 inbending data set.

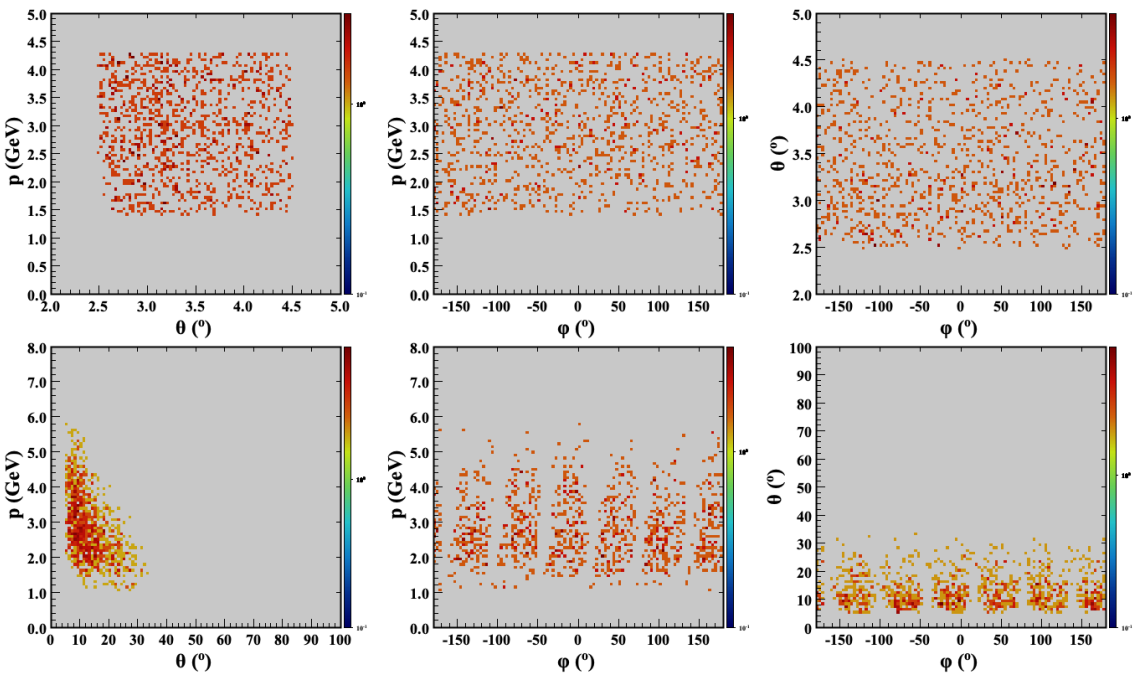

(a) FT-e (top row) and fast K^+ (bottom row) distributions (Fall 2018 in FT-e).

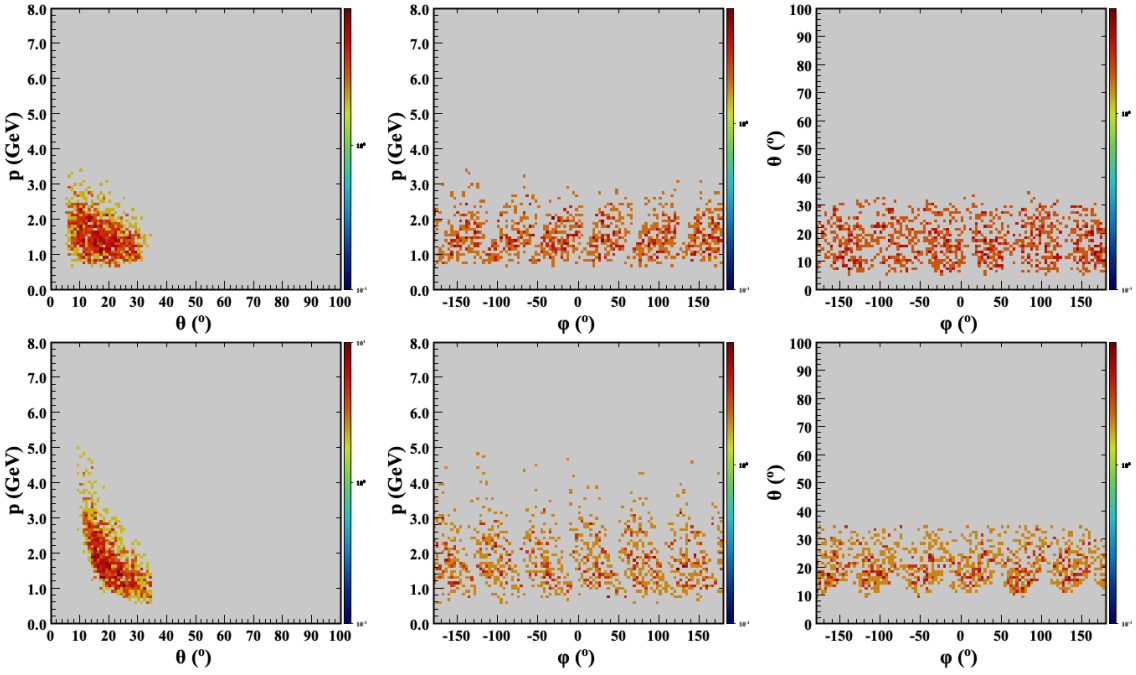

(b) Slow K^+ (top row) and K^- (bottom row) distributions (Fall 2018 in FT-e).

Figure 3.17: Same as Fig. 3.13 but for the Fall 2018 inbending data set.

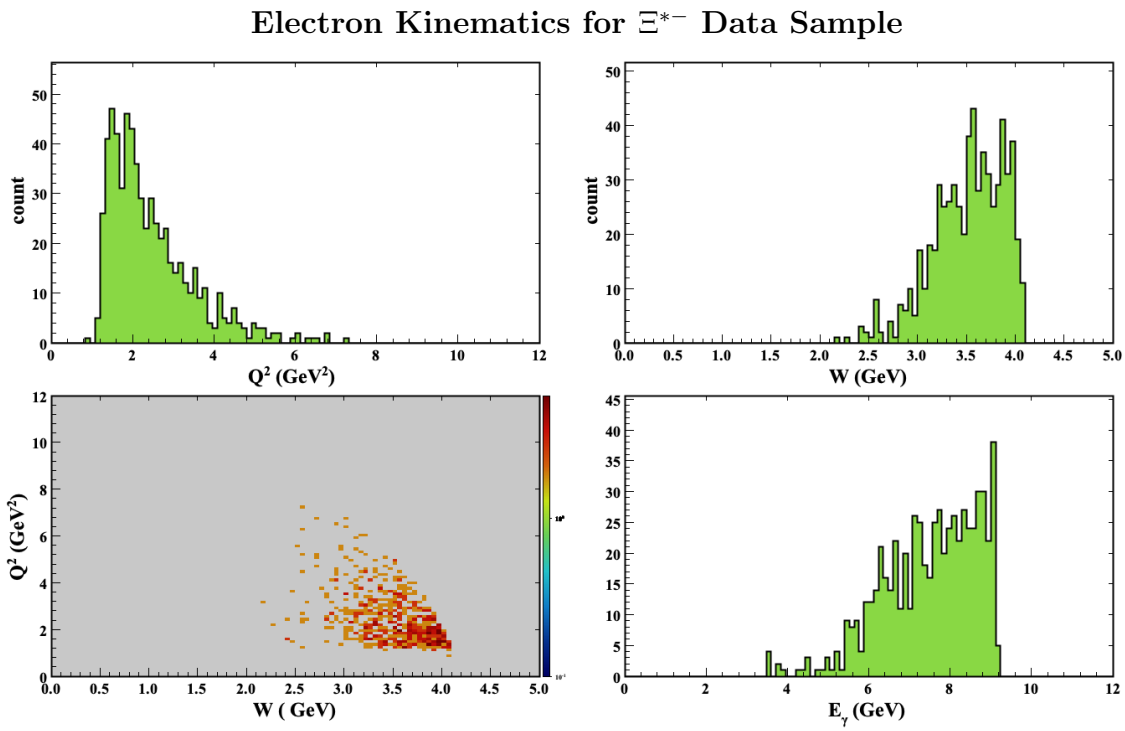

(a) Spring 2019 inbending FD-e.

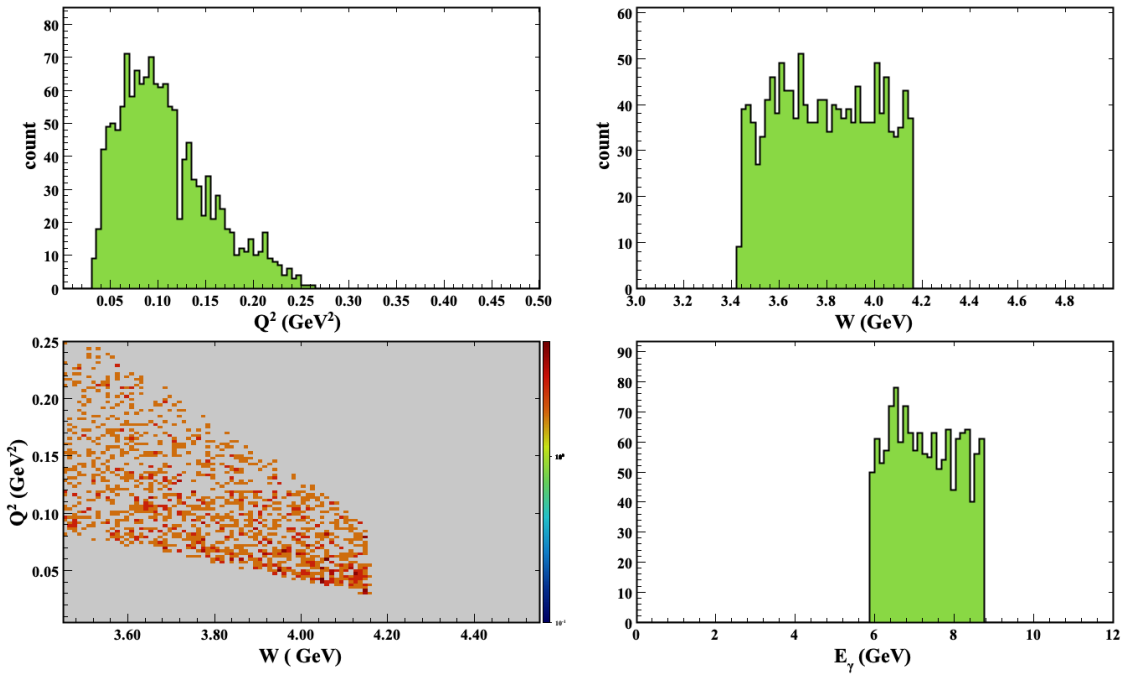

(b) Spring 2019 inbending FT-e.

Figure 3.18: Same as Fig. 3.10 but for the Spring 2019 inbending data set.

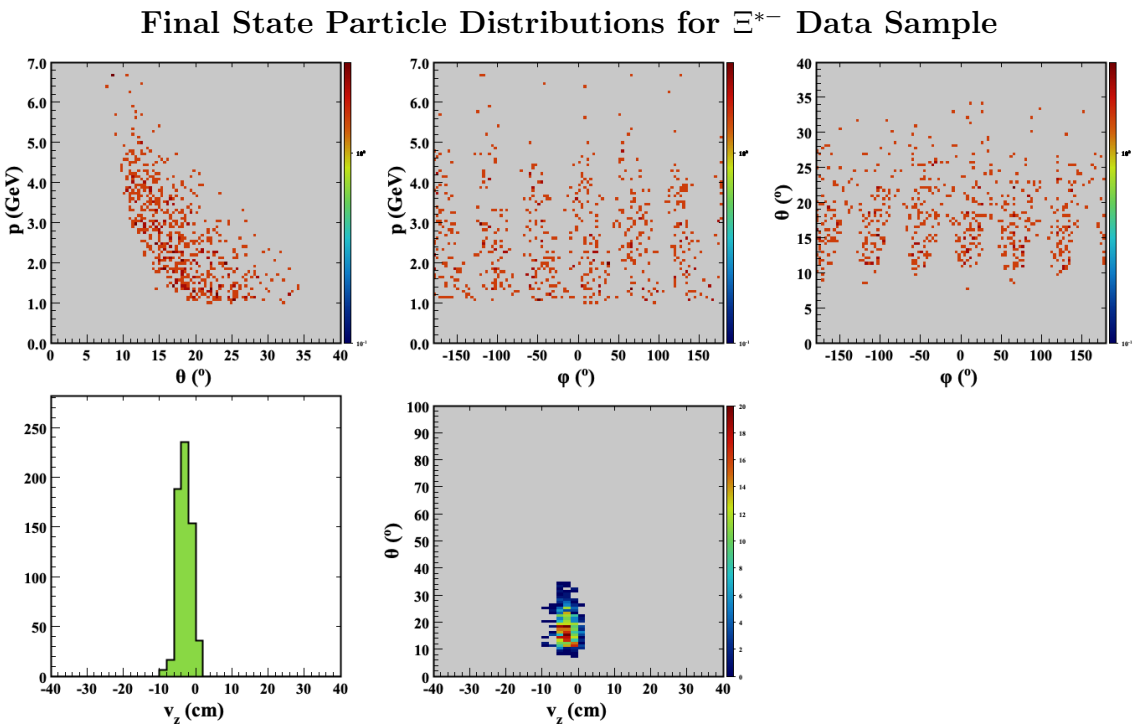

(a) FD-e in Ξ^{*-} data sample (Spring 2019 inbending FD-e).

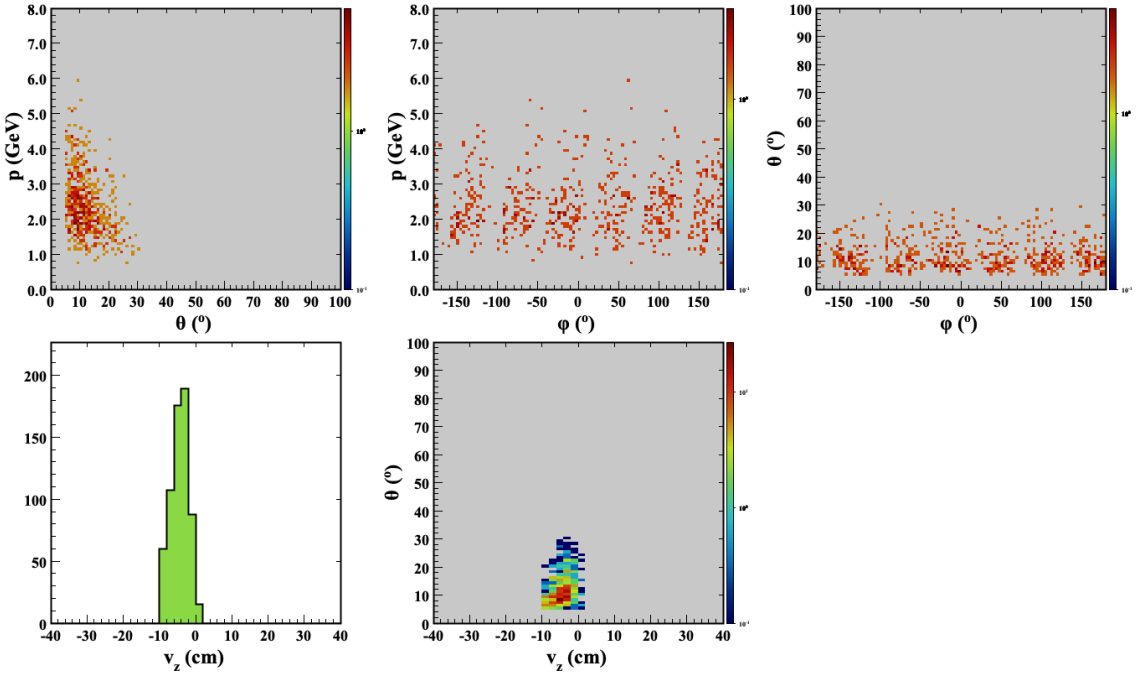

(b) Fast K^+ in Ξ^{*-} data sample (Spring 2019 inbending FD-e).

Figure 3.19: Same as Fig. 3.11 but for the Spring 2019 inbending data set.

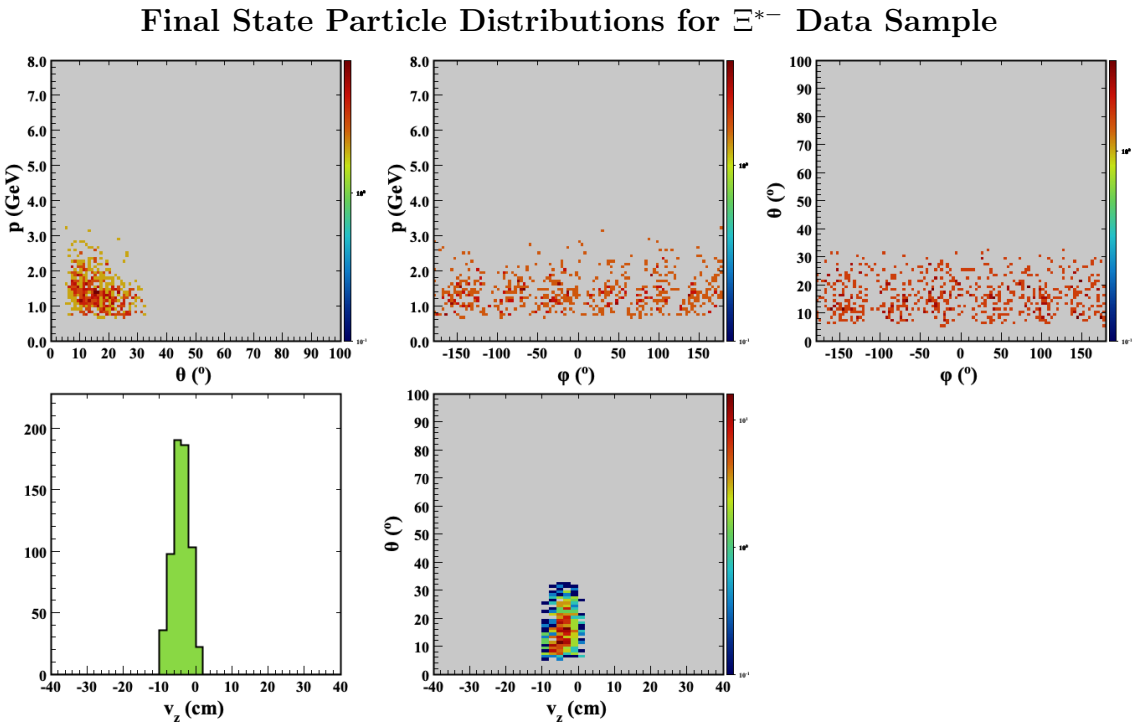

(a) Slow K^+ in Ξ^{*-} data sample (Spring 2019 inbending FD-e).

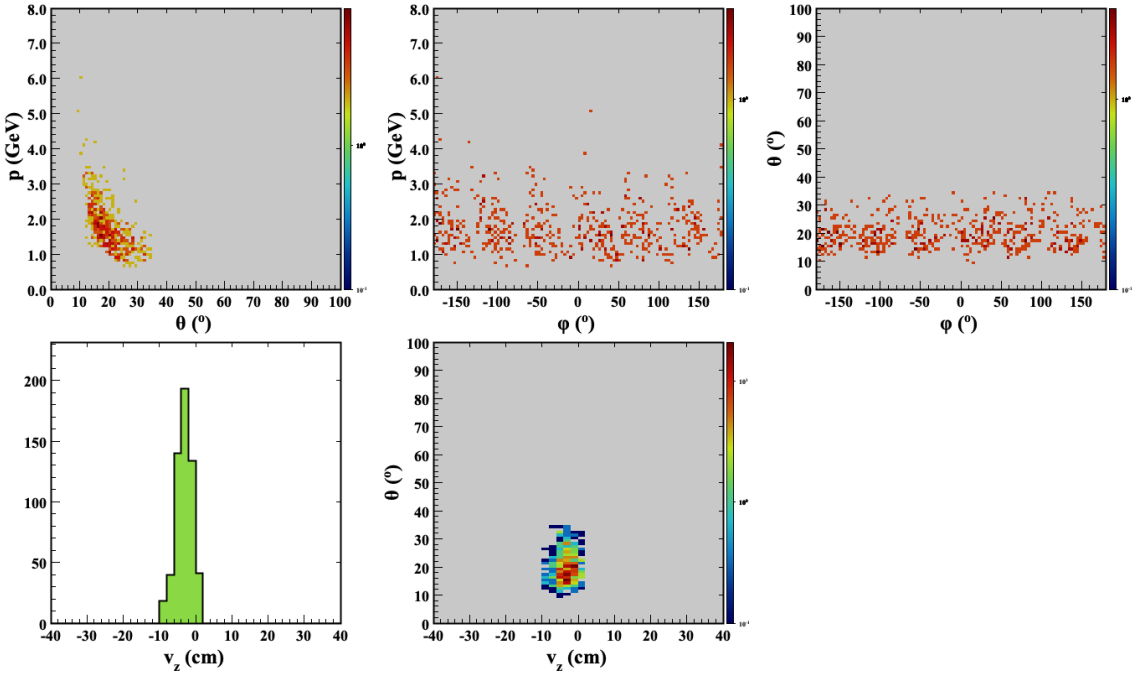

(b) K^- in Ξ^{*-} data sample (Spring 2019 inbending FD-e).

Figure 3.20: Same as Fig. 3.16 but for the Spring 2019 inbending data set.

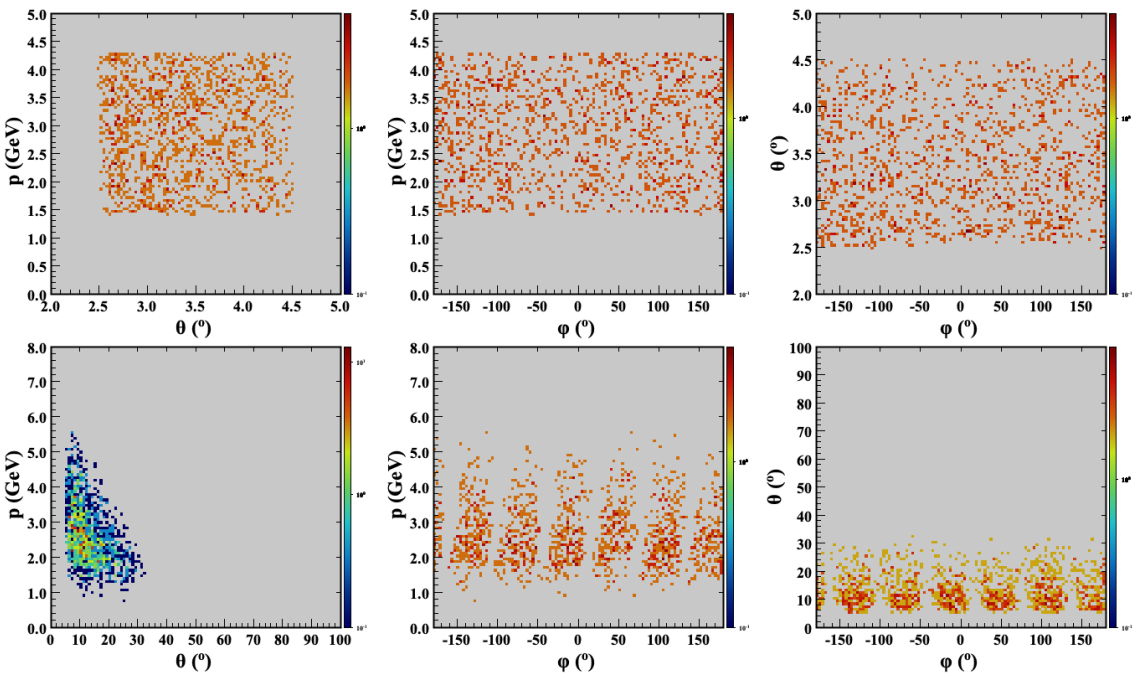

(a) FT-e (top row) and fast K^+ (bottom row) distributions (Spring 2019 in FT-e).

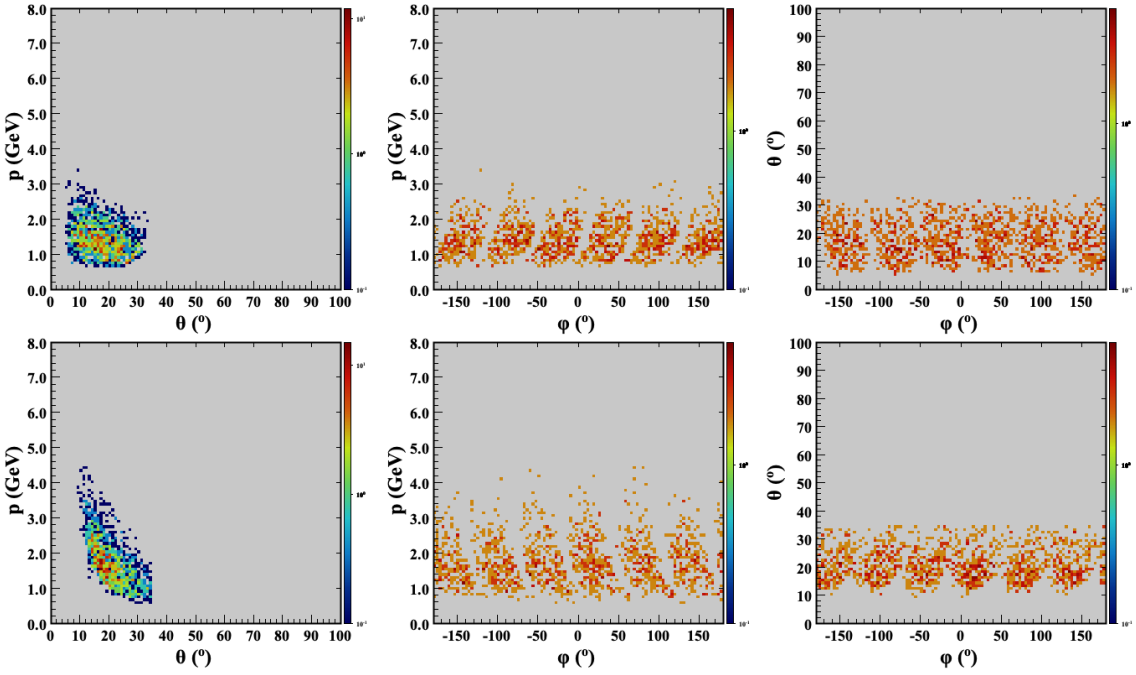

(b) Slow K^+ (top row) and K^- (bottom row) distributions (Spring 2019 in FT-e).

Figure 3.21: Same as Fig. 3.13 but for the Spring 2019 inbending data set.

The missing mass technique utilizes the conservation of four-momentum to determine the four-momenta of the missing final-state particles by using the knowledge of the incident electron beam energy and the proton mass in the initial state and the detected particle four-momenta in the final state. For example, in the reaction, $ep \rightarrow e'K^+K^+K^-(Y)$, the four-momenta of the missing final-state particles (Y) can be obtained by applying the conservation of energy and momentum as

$$P_Y = P_{beam} + P_{target} - P_{e'} - P_{K^+} - P_{K^+} - P_{K^-}, \tag{3.6}$$

where P_Y is the four-momentum vector of Y. Since we are interested to reconstruct intermediate Ξ^{*-} in the reaction $ep \rightarrow e'K^+K^+\Xi^{*-}$ in which the Ξ^{*-} decays through $K^-\Lambda$ and $K^-\Sigma^0$, P_Y can be identified as the reconstructed momentum vector of the ground state Λ and Σ^0. Thus, if Ξ^{*-} states are produced in the reaction $ep \rightarrow e'K^+K^+(\Xi^{*-})$, one can expect to observe two resonances at the Λ mass (1.1157 GeV) and the Σ^0 mass (1.1926 GeV) in the missing mass off of $e'K^+K^+K^-$ as a result of Ξ^{*-} decay. The advantage of utilizing the missing mass technique while searching for Λ and Σ^0 resonances is that it eventually allows you to explore intermediate Ξ^{*-} hyperon without detecting all decay particles of Ξ^{*-}. By selecting the Λ and Σ^0 hyperons in the missing mass off of $e'K^+K^+K^-$, one can look for intermediate Ξ^{*-} resonances in the missing mass off of $e'K^+K^+$ that decay strongly to $K^-\Lambda$ and $K^-\Sigma^0$. Figure 3.22 shows a possible diagram for the electroproduction of the Ξ^{*-} states through decay of an intermediate hyperon resonance (Y^*) produced in a t-channel process. This diagram is relevant for only heavier Ξ^{*-} states such as $\Xi(1690)$, $\Xi(1820)$, etc. that decay to K^-Y. Low mass Ξ states such as $\Xi(1320)$ and $\Xi(1530)$ that do not decay to K^-Y do not follow this production diagram.

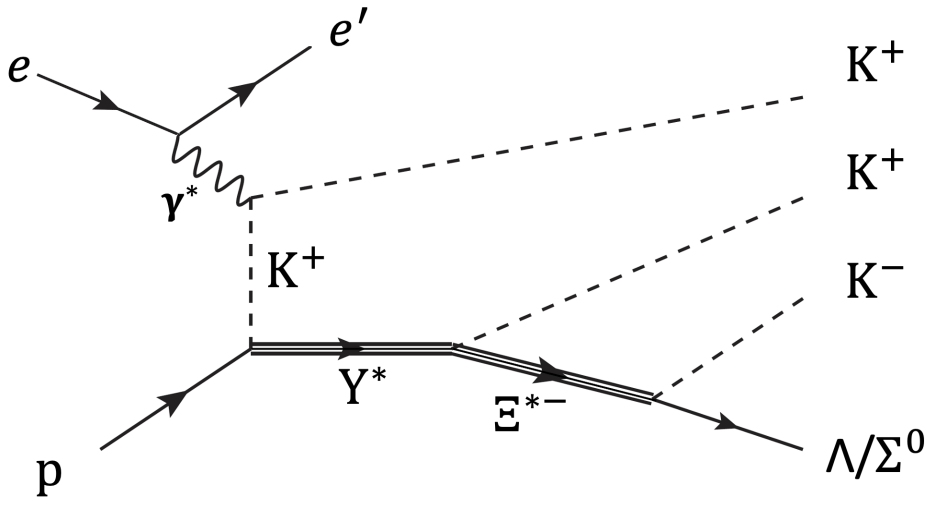

Figure 3.22: Diagram showing an electroproduction of Ξ^{*-} states in a possible t-channel production mechanism predicted by Ref. [40] for an electroproduction process. This diagram is applicable for heavier Ξ^{*-} states above 1530 MeV mass that decay to K^-Y.

3.4.2 Features of the Missing Mass Spectrum

Figure 3.23 shows observed features of the missing mass distributions off of $e'K^+K^+$ using pass-1 data when a scattered electron and two positively charged kaons are detected in the final state. The missing mass distribution shows the first-ever observed resonance of the octet ground state Cascade $\Xi^-(1320)$ using electroproduction data. The missing mass resolution with scattered electrons detected in the Forward Detector is better compared to the case with scattered electrons detected in the Forward Tagger because the Forward Detector momentum resolution is better than the Forward Tagger energy resolution. Evidence of the decuplet ground state Cascade $\Xi^-(1530)$ (a peak with FD-e resolution and a shoulder with FT-e resolution) is also present in the missing mass distribution. Within the Forward Detector acceptance

of the CLAS12 spectrometer, no statistically significant resonances corresponding to the known Ξ^* states above the $\Xi^{*-}(1530)$ mass were observed in the missing mass off of $e'K^+K^+$, which triggered us to detect an additional K^- in the event. Since the main goal of this research is to extensively search for the higher-mass Ξ^{*-} states that are accessible with the upgraded 10.6 GeV CEBAF electron beam energy, we decided to search for the Λ and Σ^0 hyperons in the missing mass off of $e'K^+K^+K^-$ in the exclusive reaction $ep \rightarrow e'K^+K^+K^-(\Lambda/\Sigma^0)$ by looking at data events that have at least e', K^+, K^+, and K^- detected.

Missing Mass Distribution off of $e'K^+K^+$

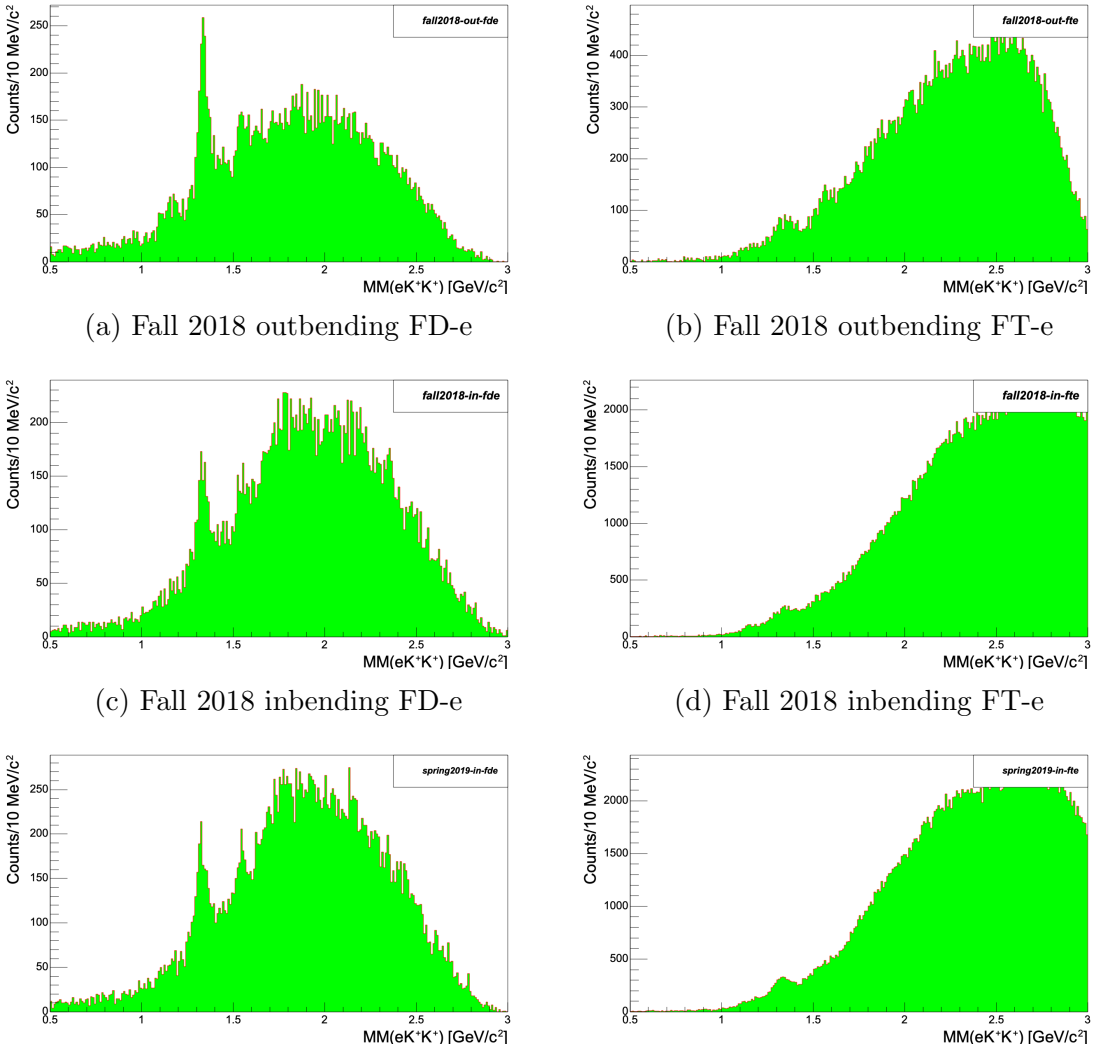

(a) Fall 2018 outbending FD-e

(b) Fall 2018 outbending FT-e

(c) Fall 2018 inbending FD-e

(d) Fall 2018 inbending FT-e

(e) Spring 2019 inbending FD-e

(f) Spring 2019 inbending FT-e

Figure 3.23: Missing mass distribution off of $e'K^+K^+$ in the system $ep \rightarrow e'K^+K^+(X)$, where $e'K^+K^+$ tracks are detected. The three plots in the first column correspond to the three different RG-A data sets (Fall 2018 outbending, Fall 2018 inbending, and Spring 2019 inbending) when the scattered electron is detected in the Forward Detector. The three plots in the second column correspond to scattered electrons detected in the Forward Tagger. None of these plots show clear evidence of higher-mass Ξ^{*-} states in the missing mass spectra.

The analysis to search for Ξ^{*-} states in the exclusive reaction $ep \rightarrow e'K^+K^+K^-(\Lambda/\Sigma^0)$ must remove various physics background reactions. The major physics background contamination on our $e'K^+K^+K^-$ events for the Ξ^{*-} data sample can come from the physics processes such as ϕN^* production where the ϕ meson can decay to K^+K^- and N^* decay to $K^+(\Lambda/\Sigma^0)$ giving the same final state particles. Careful investigation of various mass spectra formed by different combinations of the detected particles of $e'K^+K^+K^-$ events showed a clear $\phi(1020)$ meson resonance in the K^+K^- invariant mass spectrum. Such events are removed in our Ξ^{*-} data sample for further analysis by only taking events with K^+K^- invariant mass above 1.08 GeV as shown in Fig. 3.24.

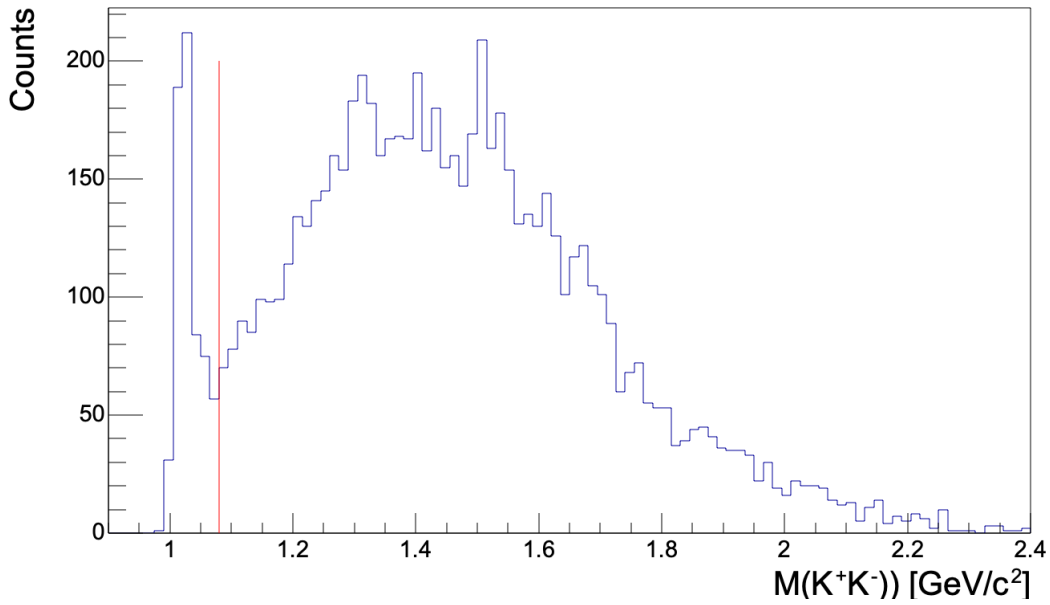

Figure 3.24: Invariant mass of K^+K^- showing a clean resonance of electroproduced $\phi(1020)$ mesons at 1.02 GeV when $e'K^+K^+K^-$ tracks are detected. This plot is made using the Fall 2018 inbending data set with an electron detected in the FT. All of the data sets we are analyzing show $\phi(1020)$ mesons when $e'K^+K^+K^-$ tracks are detected. These $\phi(1020)$ meson events are removed in our Ξ^{*-} data sample from all data sets by applying a cut at 1.08 GeV.

Figure 3.25 shows observed features of the missing mass distributions off of $e'K^+K^+K^-$ with at least e', K^+, K^+, and K^- tracks detected in the final state. Clear evidence of Λ and Σ^0 hyperons is observed in the missing mass off of $e'K^+K^+K^-$ in the $ep \rightarrow e'K^+K^+K^-(Y)$ system. The mass resolution for the Λ and Σ^0 in the missing mass spectrum is such that the two hyperons resonances are indistinguishable no matter where the scattered electrons are detected. Later in this section we summarize the Λ and Σ^0 mass resolution obtained from the fit in the pass-1 data (see Table 3.4). Quantitatively, the mass resolution worsens by a factor of $1-2$ when the scattered electron is detected in the Forward Tagger. Relatively bad mass resolution observed in the missing mass distribution for the case of FT-e compared to FD-e is simply due to relatively bad momentum resolution of the FT-e compared to FD-e. The momentum information of the FT-e comes from the FT-e energy measurement only. The energy of the FT-e is directly measured by using the FT-calorimeter. Hence, the energy resolution of the FT-e is determined by the FT-calorimeter instrumental resolution at measuring the electron energy. On the other hand, the momentum resolution of the electron detected in the Forward Detector is determined by using the response from the DCs, and the instrumental resolution of the DCs is better at determining the momenta of the particles than the FT-calorimeter at measuring the energy. When an electron is detected in the Forward Tagger, the missing mass distribution has a relatively high background compared to when an electron is detected in the Forward Detector. The Forward Tagger sees more electromagnetic background and accidental electrons than the Forward Detector as it is installed near the target.

The $MM(e'K^+K^+)$ vs. $MM(e'K^+K^+K^-)$ scatterplots of Fig. 3.26 do not show clear evidence of the electroproduction of any specific higher-mass Ξ^{*-} states from the currently available statistics of the pass-1 data in the FD acceptance.

In principle, using charged kaons detected in the CD would significantly increase the statistics. It is highly likely that the Ξ^{*-} production favors the topologies in CLAS12 in which at least one kaon in the final state is detected in the CD. However, the missing mass plots with at least one of the charged kaons detected in the CD and the electron in the FD in the pass-1 data are dominated by the high particle-misidentification background. Similar missing mass plots with the scattered electron detected in the FT are much more affected by the particle-misidentification background, and similar missing mass studies have not advanced so much with the pass-1 data due to the poor energy resolution of the FT-Cal. The preliminary missing mass plots and missing mass scatterplots (see Appendix **A.2**, Figs. 1 to 9) do not show clear evidence of the Λ/Σ^0 hyperon peak if at least one of the charged kaons is detected in the Central Detector. The issues in the central tracking and worse timing resolution that lead to particle misidentification and poor CD momentum resolution, as well as the misalignment of the CLAS12 subsystems (FD, CD, and FT) with respect to the target in the pass-1 data, are some important reasons why this analysis confines kaons to be detected in the limited FD acceptance only.

Missing Mass Distribution off of $e'K^+K^+K^-$

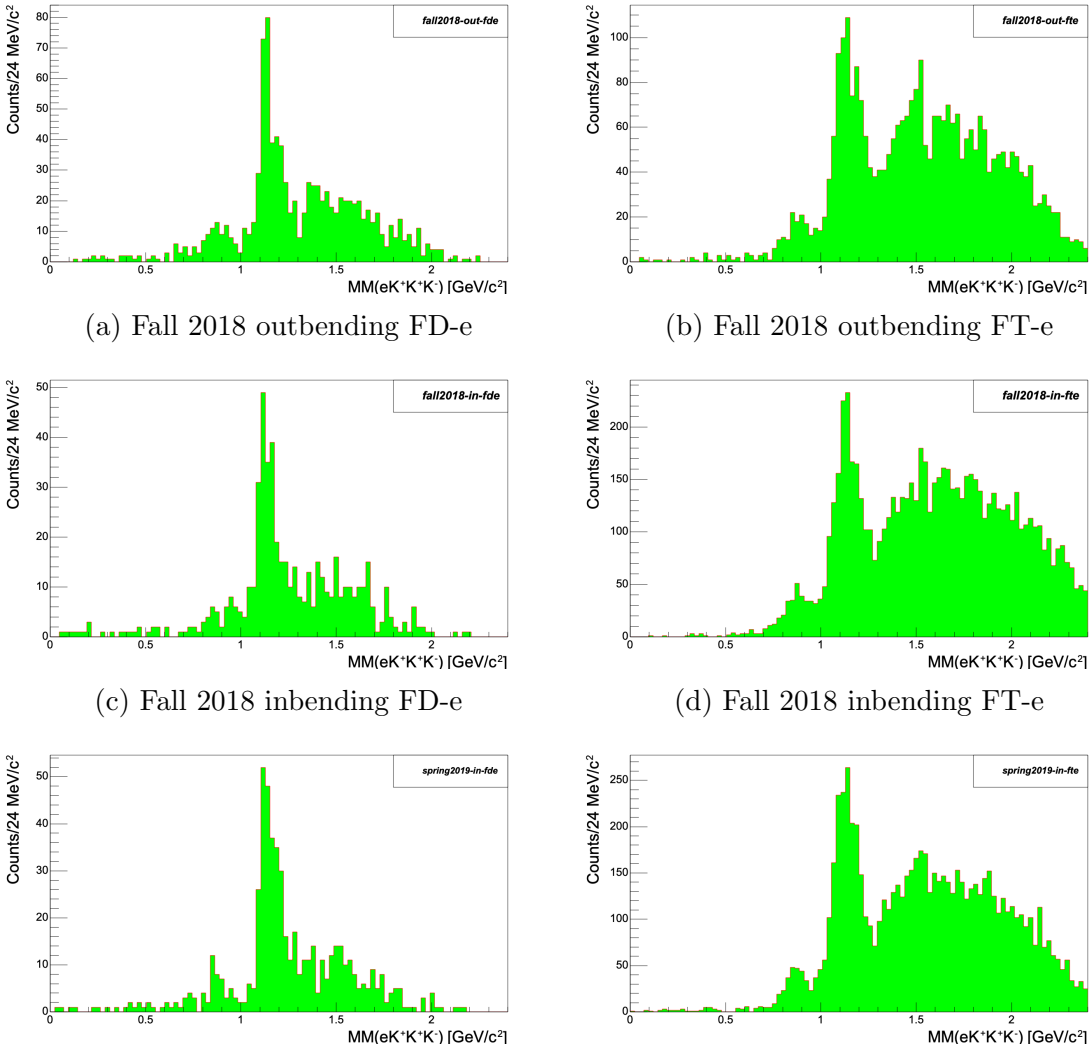

(a) Fall 2018 outbending FD-e

(b) Fall 2018 outbending FT-e

(c) Fall 2018 inbending FD-e

(d) Fall 2018 inbending FT-e

(e) Spring 2019 inbending FD-e

(f) Spring 2019 inbending FT-e

Figure 3.25: Missing mass distribution off of $e'K^+K^+K^-$ after applying all cuts to clean up electrons and charged kaon identification. The three plots in the first column correspond to three RG-A data sets (Fall 2018 outbending, Fall 2018 inbending, and Spring 2019 inbending) when the scattered electron is detected in the Forward Detector. The three plots in the second column correspond to scattered electrons detected in the Forward Tagger. The background from particle misidentification causes a non-physical resonance to appear below 1 GeV.

Missing Mass Distribution Scatterplots

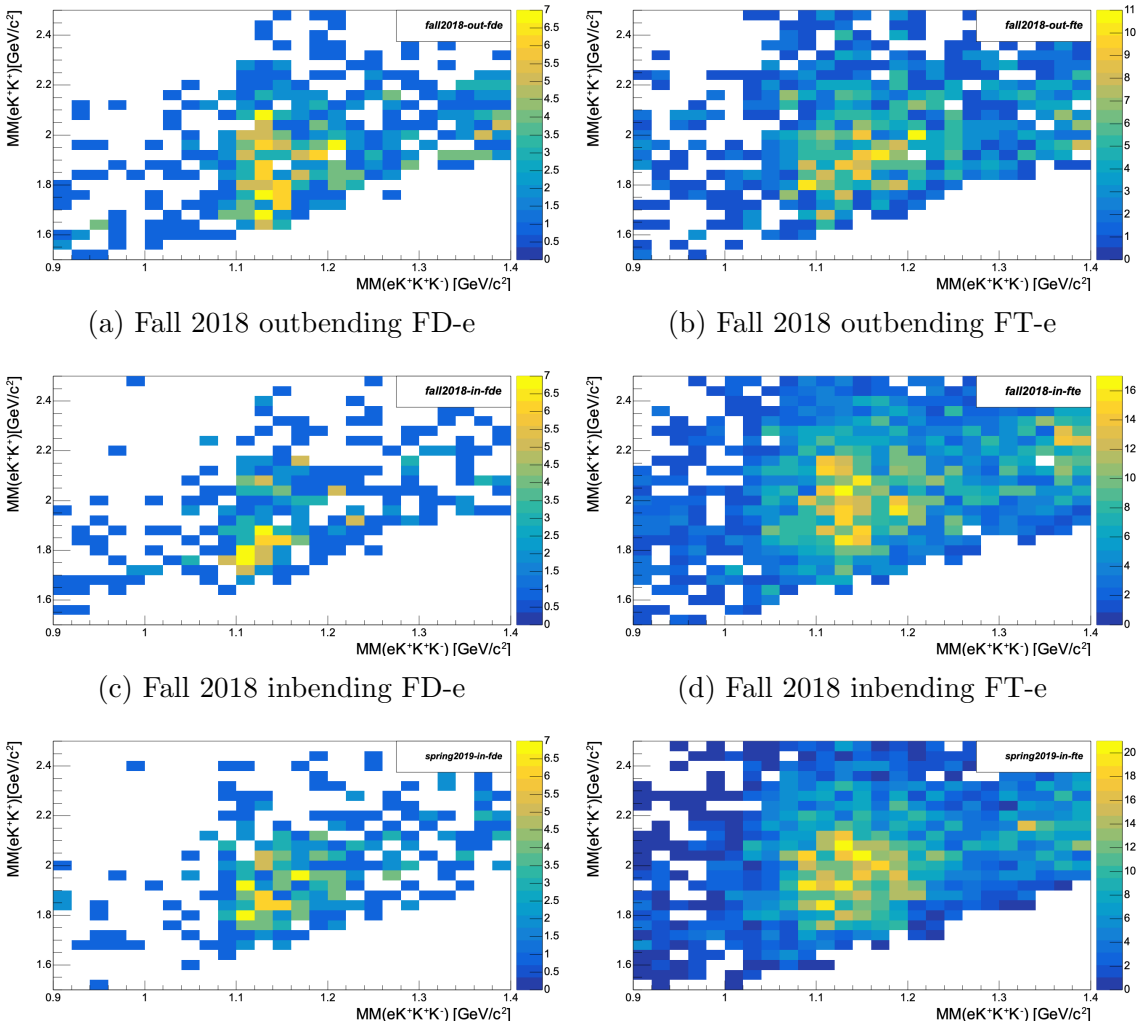

(a) Fall 2018 outbending FD-e

(b) Fall 2018 outbending FT-e

(c) Fall 2018 inbending FD-e

(d) Fall 2018 inbending FT-e

(e) Spring 2019 inbending FD-e

(f) Spring 2019 inbending FT-e

Figure 3.26: Scatterplots showing $MM(e'K^+K^+K^-)$ along the x axis and $MM(e'K^+K^+)$ along the y axis for the three RG-A data sets. The first column corresponds to the case when the scattered electron is detected in the Forward Detector, and the second column corresponds to the case when the scattered electron is detected in the Forward Tagger.

3.5 Reconstruction of Ξ^{*-} Hyperons in the Reaction $ep \rightarrow e'K^+K^+\Xi^{*-} \rightarrow e'K^+K^+K^-(Y)$

The missing mass distributions off of $e'K^+K^+K^-$ reported in this analysis show evidence of smeared ground state Λ and Σ^0 hyperons in all available RG-A data sets. The data events corresponding to the Λ and Σ^0 region in the missing mass off of $e'K^+K^+K^-$ constitute our Ξ^{*-} data sample. Using this data sample we can simply combine reconstructed Λ/Σ^0 from the missing mass off of $e'K^+K^+K^-$ with the detected K^- to search for intermediate Ξ^{*-} states that decay to $K^-\Lambda$ or $K^-\Sigma^0$. In order to select the Λ/Σ^0 events in the missing mass distribution, the Λ and Σ^0 peaks were fit with Gaussian distributions and a linear function was used to represent the background. We then identified the Λ and Σ^0 events in the missing mass of the $e'K^+K^+K^-$ system by applying a cut of $\mu_\Lambda - 3\sigma_\Lambda$ to $\mu_{\Sigma^0} + 3\sigma_{\Sigma^0}$ with parameters taken from the fit. Figure 3.27a shows an example of the cut applied to select the Λ and Σ^0 region in the missing mass distribution for the Fall 2018 outbending data set with scattered electrons detected in the FT. A similar plot showing the Λ and Σ^0 selection for the Fall 2018 outbending data set with scattered electrons in the FD is shown in Fig 3.28a. Table 3.5 summarizes the cuts on the $MM(e'K^+K^+K^-)$ distribution implemented on the different data sets to select the Λ and Σ^0 events.

The missing mass off of $e'K^+K^+$ after applying the cut on $MM(e'K^+K^+K^-)$ to select the Λ and Σ^0 region, as explained above, does not show any statistically significant signal for Ξ^{*-} production. To estimate the shape of the background in the expected Ξ^{*-} signal region and to further clean up the background possibly present in the $MM(e'K^+K^+)$ distribution, we used sideband background events from the missing mass off of the $e'K^+K^+K^-$ system to plot $MM(e'K^+K^+)$. The sideband background events were normalized in such a way that the total number of background

events in the Λ and Σ^0 region from $\mu_\Lambda - 3 * \sigma_\Lambda$ to $\mu_{\Sigma^0} + 3 * \sigma_\Lambda$ was equivalent to the sum of the background events from the upper and lower sidebands. The magenta areas in Fig. 3.27b correspond to the normalized sideband events selected in the $MM(e'K^+K^+K^-)$ missing mass to estimate the background shape in the missing mass off of $e'K^+K^+$ for the Fall 2018 outbending data set with the scattered electron detected in the FT. A similar plot showing the normalized sideband region for the Fall 2018 outbending data set with scattered electrons in the FD is shown in Fig 3.28b. Table 3.6 summarizes the cuts implemented on $MM(e'K^+K^+K^-)$ for the different data sets analyzed to select the sideband regions. The green histogram in the middle plot of Fig 3.32 corresponds to the actual $MM(e'K^+K^+)$ distribution from the normalized sideband events corresponding to the magenta areas in Fig 3.28b for the Fall 2018 outbending data set with a FT-electron. Similar plots from the other available data sets are presented in Fig. 3.29 to Fig. 3.34.

The estimated shape of the background from the normalized sideband background events is then subtracted in the final $MM(e'K^+K^+)$ distribution. This same procedure was applied separately for all three RG-A data sets with separate plots for scattered electrons in the Forward Tagger or the Forward Detector. The missing mass distributions with different cuts and from the sideband events are shown for the different data sets in Fig. 3.29 to Fig. 3.34.

$MM(e'K^+K^+K^-)$ **Using RG-A Fall 2018 Outbending FT-e**

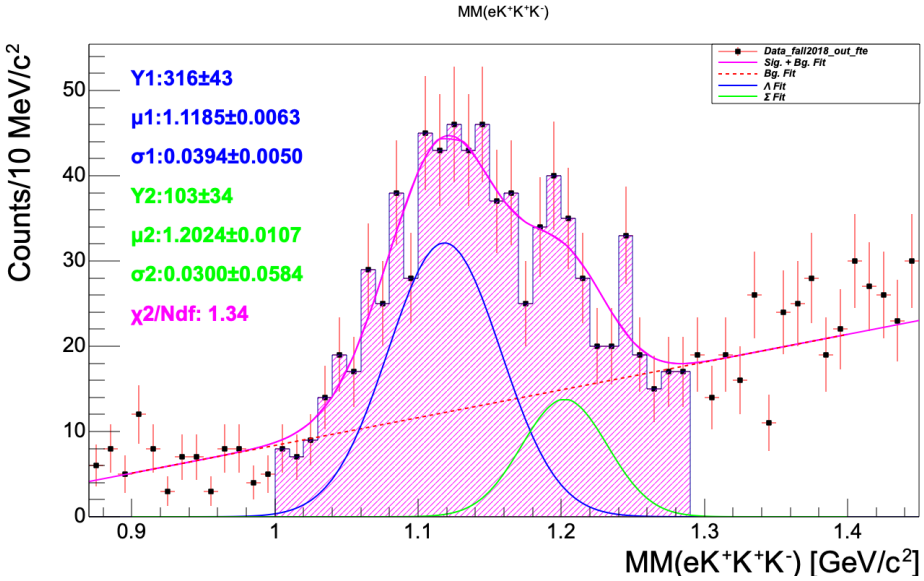

(a) Λ/Σ^0 region

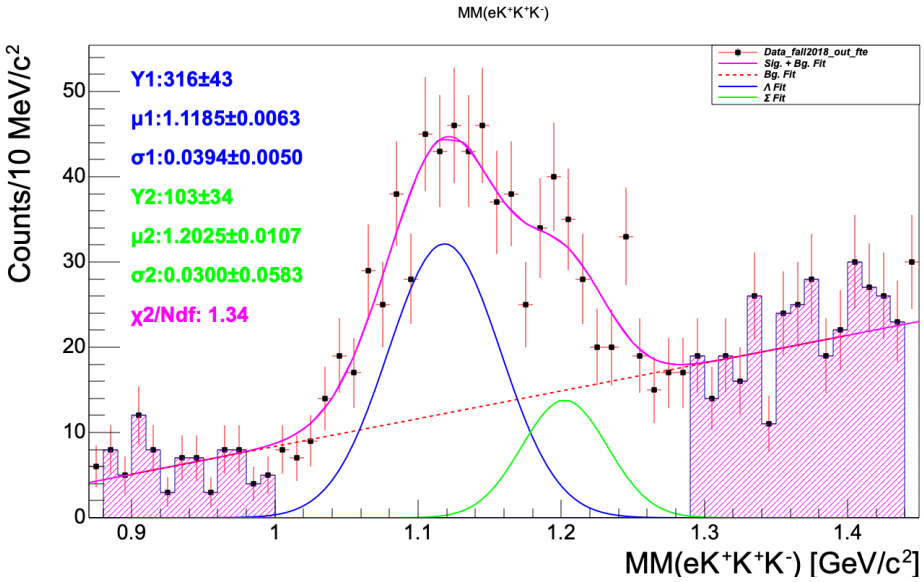

(b) Normalized sideband region

Figure 3.27: The missing mass off of the $e'K^+K^+K^-$ system using the Fall 2018 outbending data set with the scattered electron detected in the FT. The shaded region in Fig. 3.27a corresponds to the Λ/Σ^0 signal region, and the shaded region in Fig. 3.27b corresponds to the normalized sideband region such that the total number of background events from the signal region is approximately equal to the sum of the background events from the upper and lower sideband regions.

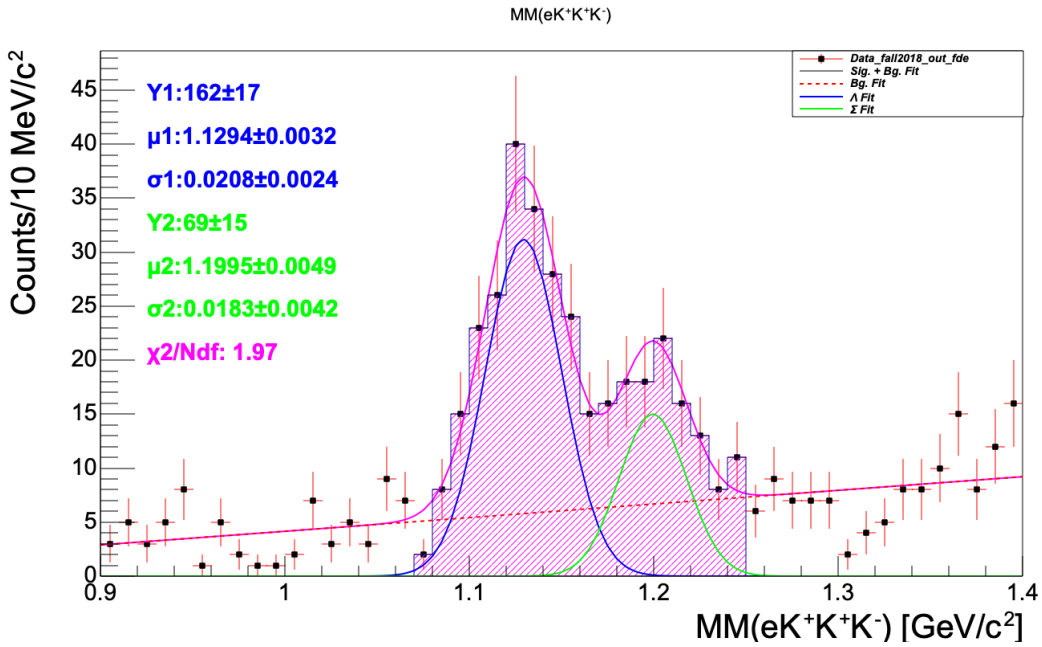

(a) Λ/Σ^0 region

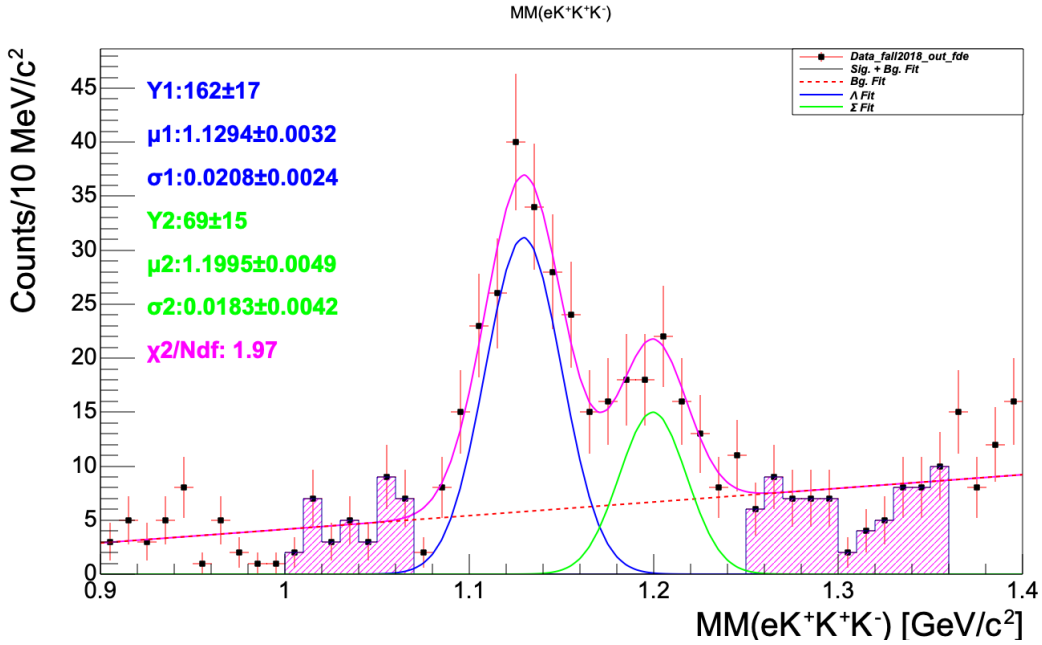

(b) Normalized sideband region

Figure 3.28: Same as Fig 3.27 but for the RG-A Fall 2018 outbending data set with the scattered electron detected in the FD.

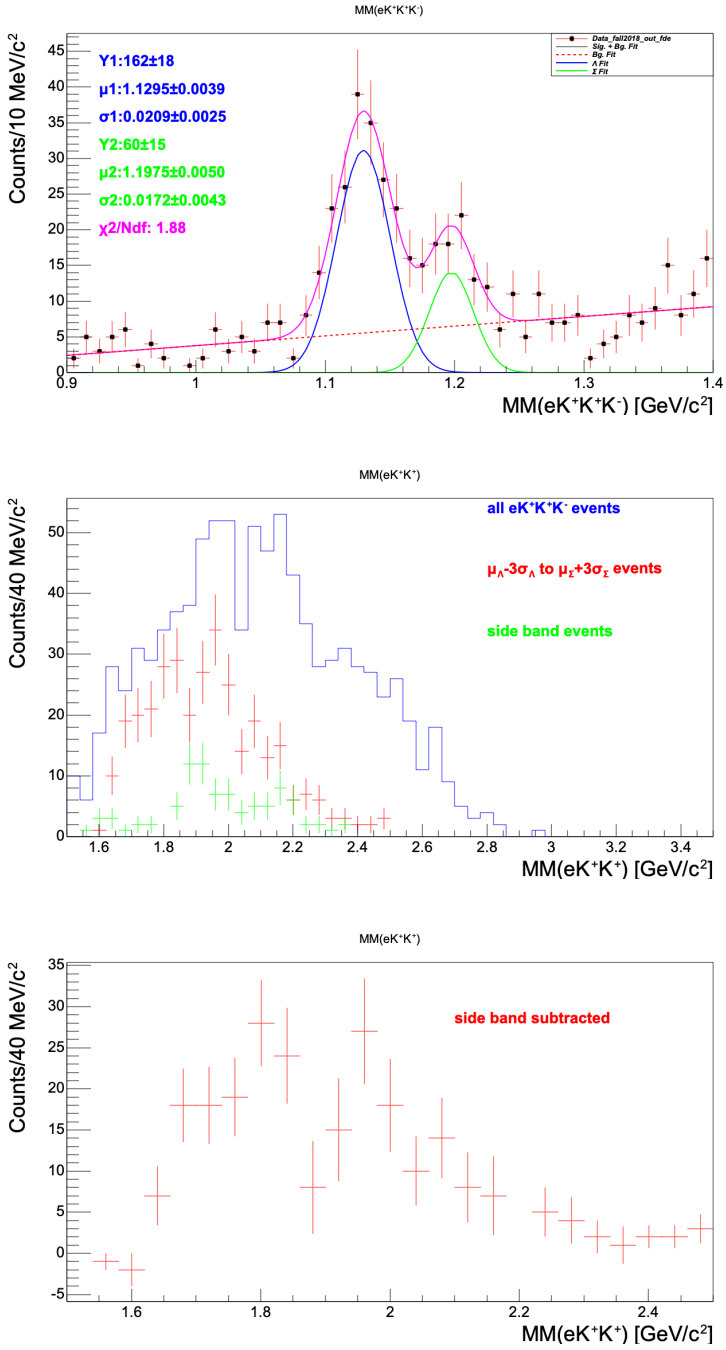

Figure 3.29: Different missing mass distributions from the RG-A Fall 2018 outbending data set with the electron detected in the Forward Detector. The top plot shows the global fit (magenta) with a double Gaussian function (blue for the Λ signal and green for the Σ^0 signal) plus a linear background (red) function. The middle plot shows the different $MM(e'K^+K^+)$ distributions from selecting different regions in the $MM(e'K^+K^+K^-)$ distribution. The bottom plot is the background-subtracted $MM(e'K^+K^+)$ distribution.

Missing m Mass Distribution Using RG-A Fall 2018 Inbending FD-e

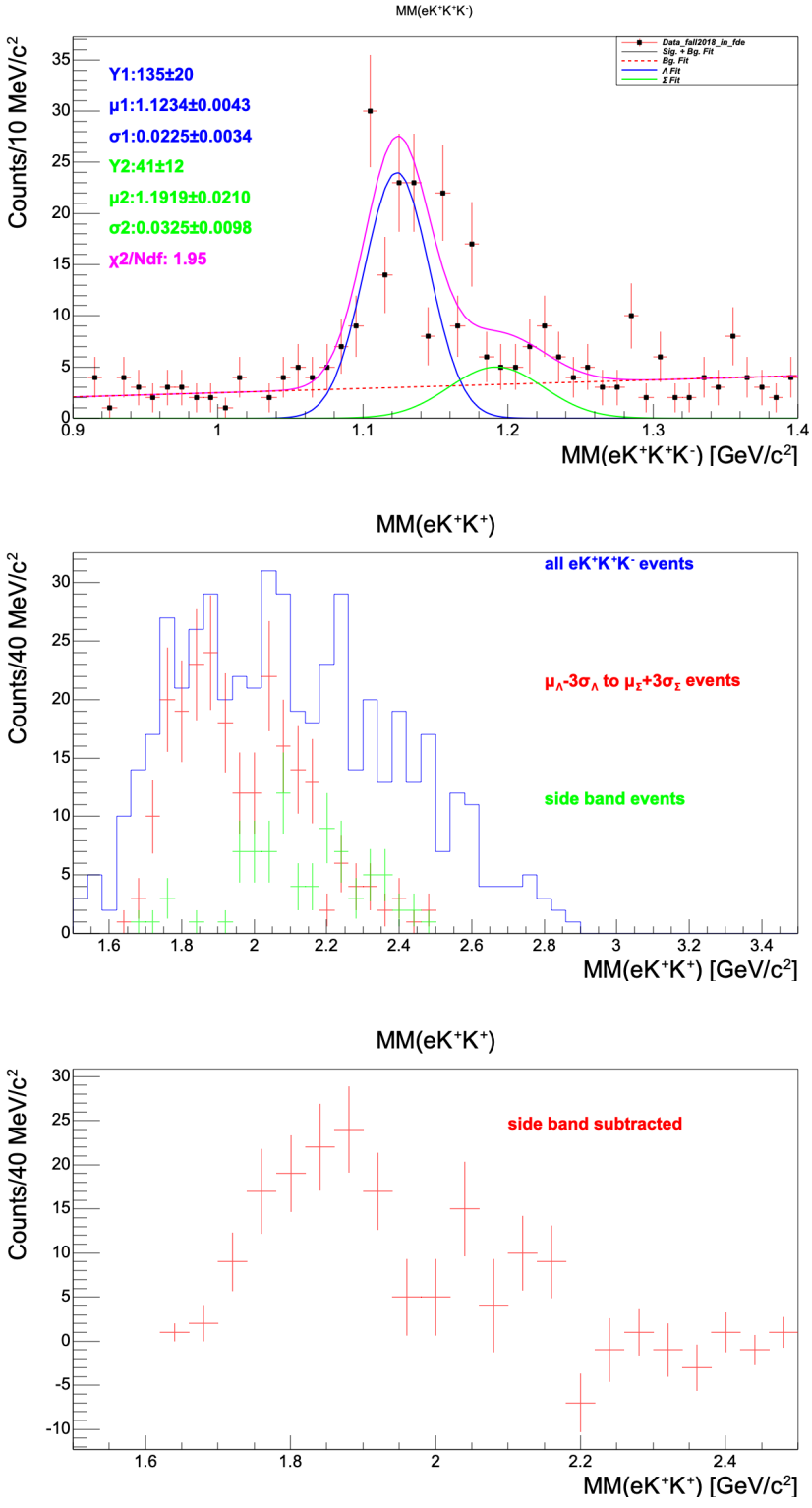

Figure 3.30: Same as 3.29 but for the RG-A Fall 2018 inbending data set with the FD electron.

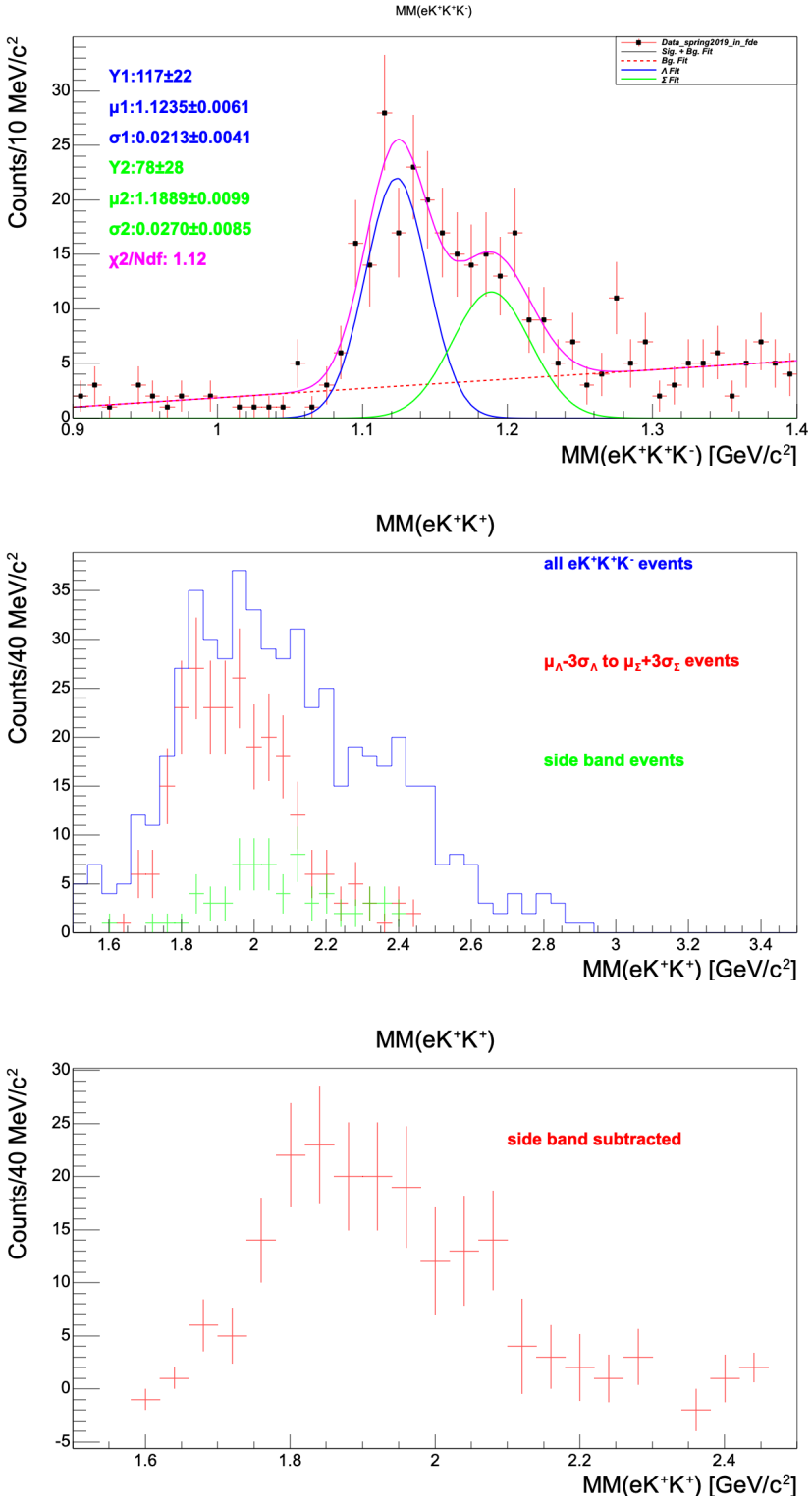

Figure 3.31: Same as 3.29 but for the RG-A Spring 2019 inbending data set with the FD electron.

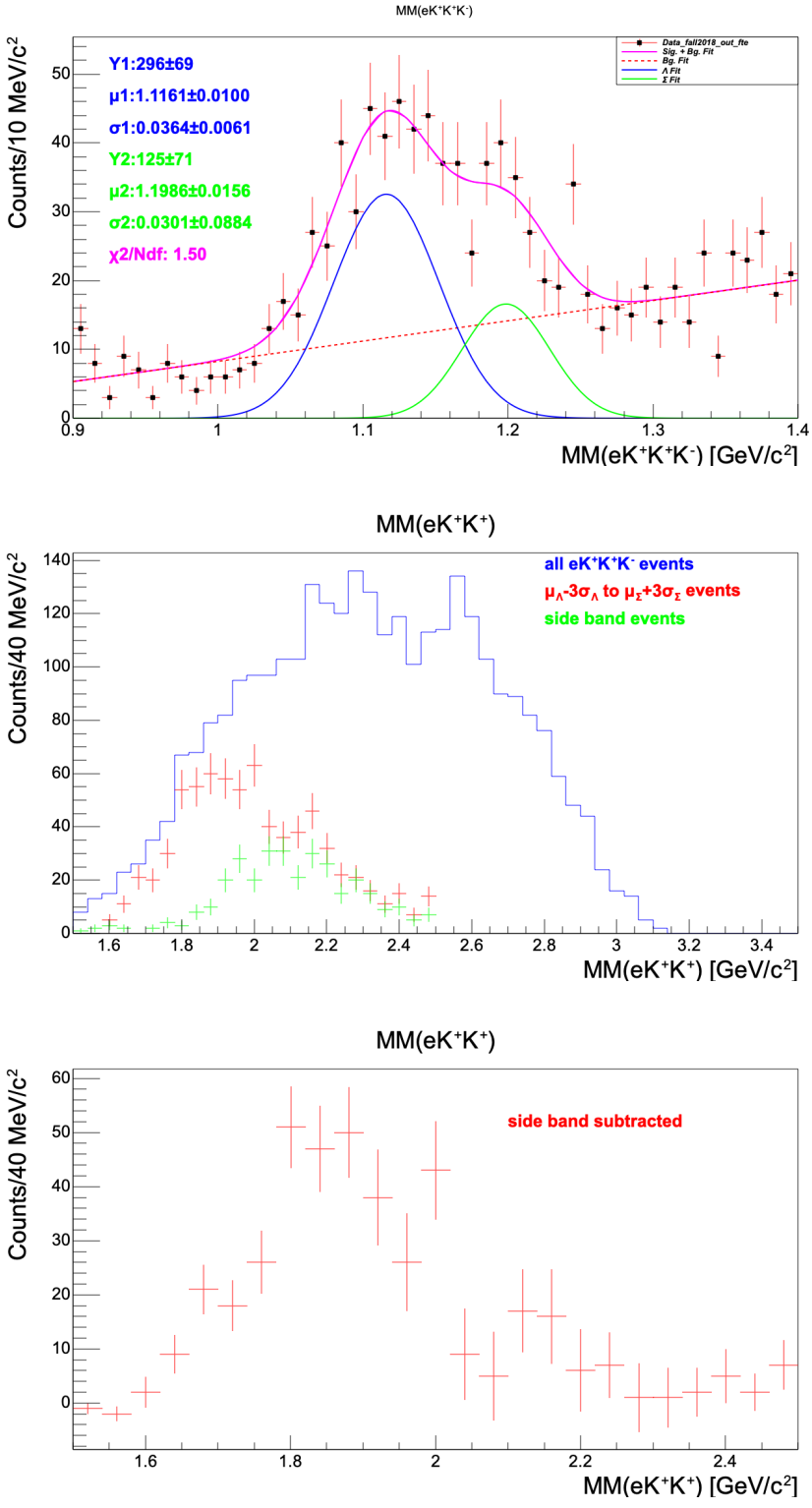

Figure 3.32: Same as 3.29 but for the RG-A Fall 2018 outbending data set with the FT electron.

Missing Mass Distribution Using RG-A Fall 2018 Inbending FT-e

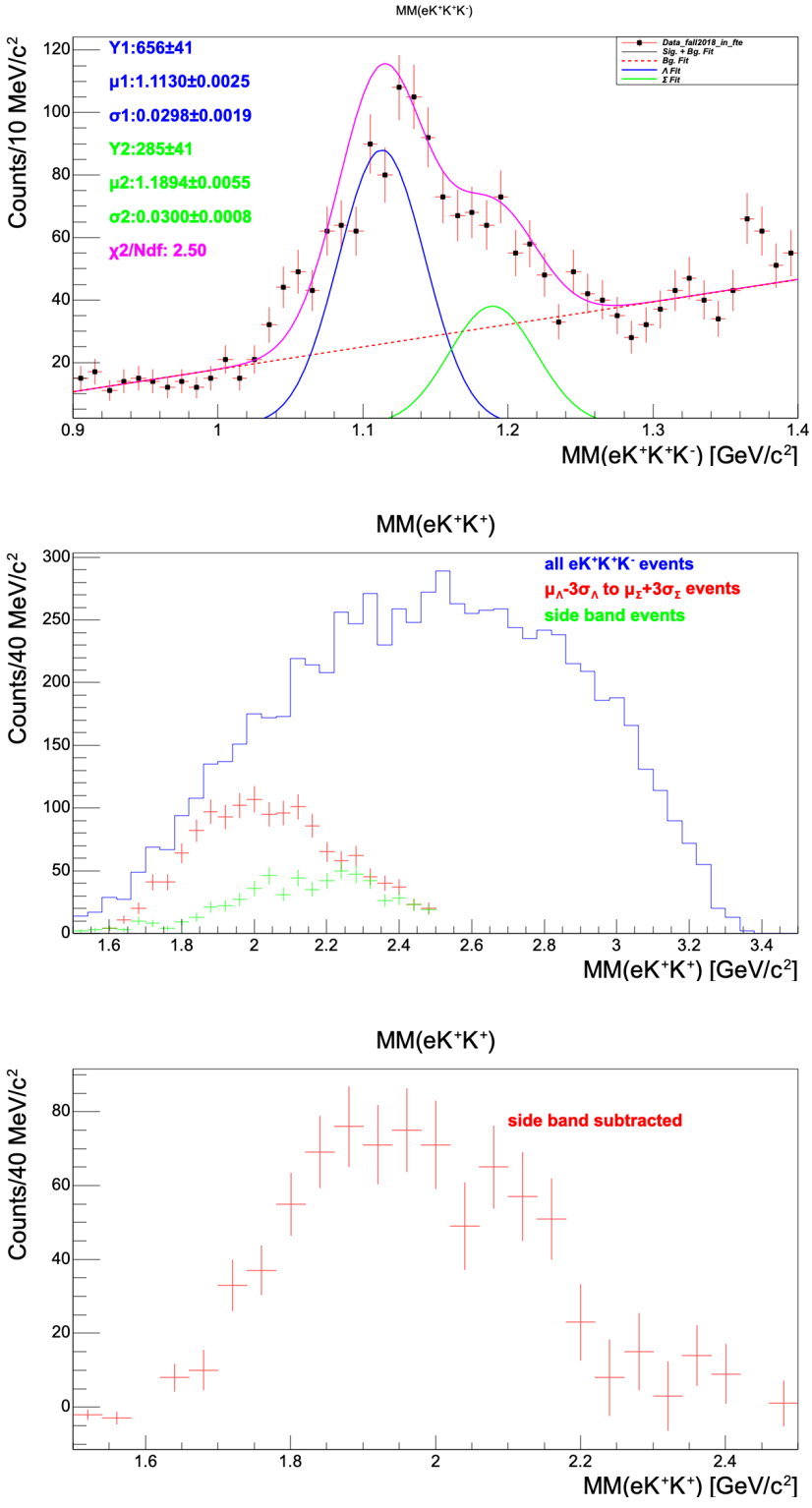

Figure 3.33: Same as 3.29 but for the RG-A Fall 2018 inbending data set with the FT electron.

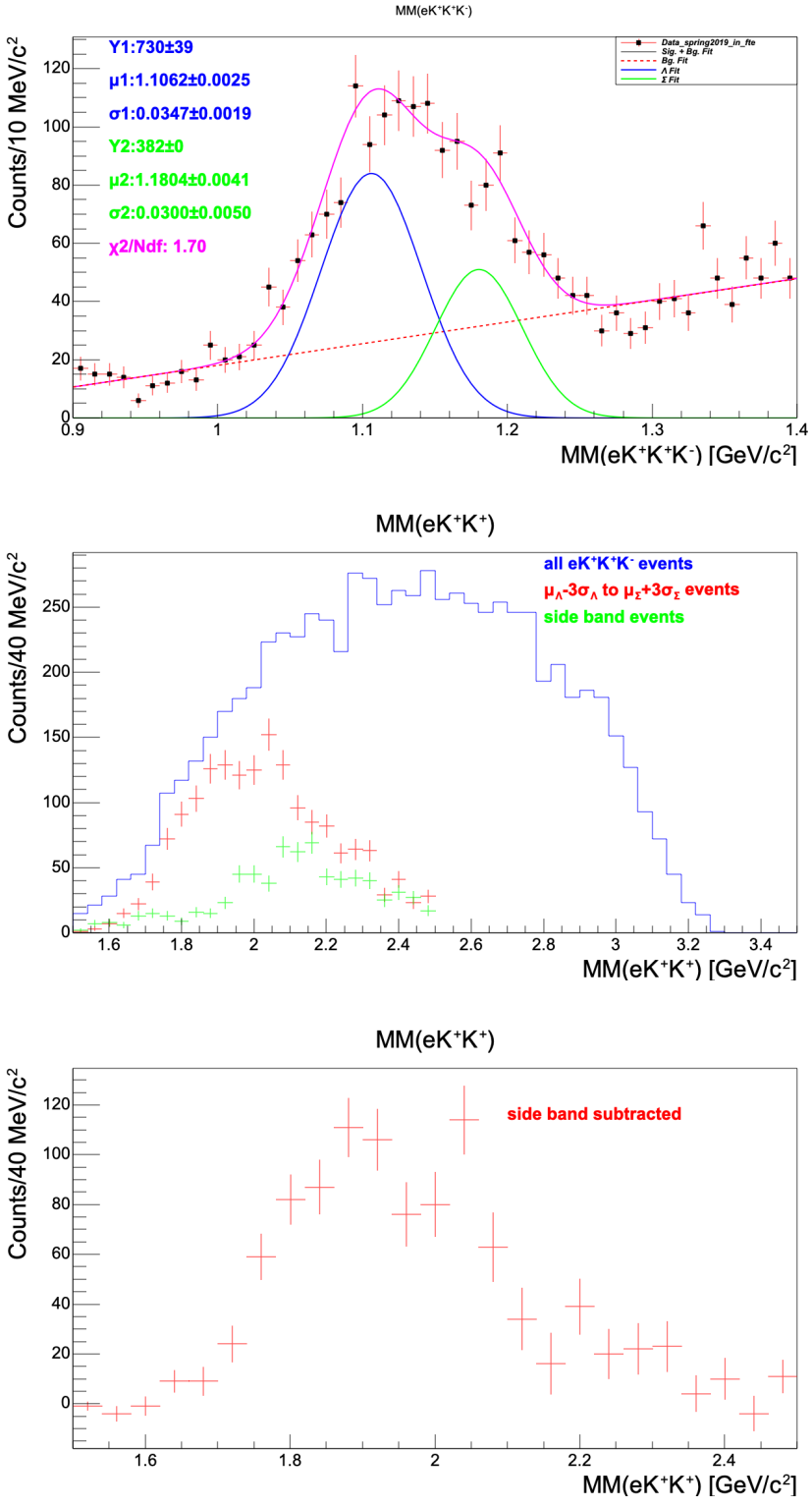

Figure 3.34: Same as 3.29 but for the RG-A Spring 2019 inbending data set with the FT electron.

Fit Results of the $MM(e'K^+K^+K^-)$ Distributions

Data set	μ_Λ (GeV)	σ_Λ (GeV)	Λ Yield	μ_{Σ^0} (GeV)	σ_{Σ^0} (GeV)	Σ^0 Yield
Fall 2018 outbending FT-e	1.116± 0.010	0.036± 0.006	296 ± 69	1.199± 0.016	0.030± 0.088	125 ± 71
Fall 2018 inbending FT-e	1.113± 0.003	0.029± 0.002	656 ± 41	1.189± 0.005	0.030± 0.001	285 ± 41
Spring 2019 inbending FT-e	1.106± 0.002	0.035± 0.002	730 ± 39	1.1804± 0.004	0.030± 0.005	382 ± 40
Fall 2018 outbending FD-e	1.129± 0.004	0.021± 0.003	162 ± 18	1.197± 0.005	0.017± 0.004	60±15
Fall 2018 inbending FD-e	1.123± 0.004	0.023± 0.003	135 ± 20	1.192± 0.021	0.032± 0.010	41±12
Spring 2019 inbending FD-e	1.123± 0.006	0.021± 0.004	117 ± 22	1.189± 0.010	0.027± 0.008	78±28

Table 3.4: Summary table showing fit results and Λ/Σ^0 yields from the missing mass distribution, $MM(e'K^+K^+K^-)$, for the different data sets analyzed.

Cut Summary on The $MM(e'K^+K^+K^-)$ to Select Λ/Σ^0

Data set	Λ/Σ^0 selection cut ($\mu_\Lambda - 3\sigma_\Lambda$ to $\mu_{\Sigma^0} + 3\sigma_{\Sigma^0}$) on MM
Fall 2018 outbending FT-e	$1.00 \leq MM \leq 1.29$ GeV
Fall 2018 inbending FT-e	$1.02 \leq MM \leq 1.28$ GeV
Spring 2019 inbending FT-e	$1.01 \leq MM \leq 1.27$ GeV
Fall 2018 outbending FD-e	$1.07 \leq MM \leq 1.25$ GeV
Fall 2018 inbending FD-e	$1.02 \leq MM \leq 1.28$ GeV
Spring 2019 inbending FD-e	$1.05 \leq MM \leq 1.29$ GeV

Table 3.5: Summary table showing the cuts applied in the missing mass distribution $MM(e'K^+K^+K^-)$ to select Λ/Σ^0 events for the different data sets.

Cut Summary on the $MM(e'K^+K^+K^-)$ to Select Normalized Sideband Events

Data set	Normalized sideband event selection cut on MM
Fall 2018 outbending FT-e	l-sb: [0.88, 1.00) GeV; u-sb: (1.29, 1.44] GeV
Fall 2018 inbending FT-e	l-sb: [0.84, 1.02) GeV; u-sb: (1.28, 1.40] GeV
Spring 2019 inbending FT-e	l-sb: [0.78, 1.01) GeV; u-sb: (1.27, 1.39] GeV
Fall 2018 outbending FD-e	l-sb: [1.00, 1.07) GeV; u-sb: (1.25, 1.36] GeV
Fall 2018 inbending FD-e	l-sb: [0.97, 1.05) GeV; u-sb: (1.29, 1.44] GeV
Spring 2019 inbending FD-e	l-sb: [0.96, 1.06) GeV; u-sb: (1.27, 1.38] GeV

Table 3.6: Summary table showing the cuts applied in the missing mass distribution $MM(e'K^+K^+K^-)$ to select normalized sideband events for the different data sets.

3.6 Four-Momentum Transfer Q^2 for Ξ^{*-} Data Sample

The Q^2 coverage for which $K^+K^+K^-$ events are detected with scattered electrons in the Forward Tagger after applying the cuts listed in Table 3.2 span the range of $0.02 - 0.25$ GeV^2 as shown in Fig. 3.35 for both outbending and inbending torus field configurations. The torus polarity setting has no effect on the electron going in the Forward Tagger, but it impacts the distribution of charged kaons going in the Forward Detector, resulting in different detection acceptance. For the same reason, inbending and outbending torus field settings have different Q^2 coverage, as shown in Fig. 3.35, when a scattered electron is detected in the Forward Detector.

The CLAS12 acceptance for electrons in the Forward Detector with inbending torus configuration is such that it cannot detect electrons with low Q^2 kinematics, as shown in Fig. 3.35. Electrons with low Q^2 kinematics curl into the beam pipe in the inbending torus configuration. On the other hand, the Forward Detector can detect electrons with low Q^2 kinematics in the outbending torus configuration as the magnetic field is such that it curls electrons towards the Forward Detector acceptance. Hence, the outbending torus field setting, which bends negatively charged particles outward with respect to the beam pipe, is favorable for our case to detect $K^+K^+K^-$ tracks in coincidence with the trigger electron in the Forward Detector as it results in accessing lower Q^2, which eventually provides us a higher virtual photon flux.

The two-dimensional scatterplot of four-momentum transfer Q^2 vs. the missing mass off of $e'K^+K^+K^-$ in Fig. 3.36 shows general features of the different data sets in terms of the Λ, Σ^0 reconstruction from the missing mass technique with different Q^2 coverage. For the FT-e Q^2 kinematics, the majority of reconstructed Λ/Σ^0 events, which constitute our Ξ^{*-} data sample of interest, lies in the Q^2 range from $0.033 - 0.13$ GeV^2 as shown in the red rectangles in the plots from the right column of

Fig. 3.35. For the FD-e Q^2 kinematics, the majority of reconstructed Λ/Σ^0 events are observed from the missing mass technique in the Q^2 range from $1.28-2.88$ GeV^2 and $0.16-1.28$ GeV^2, respectively, for the inbending and outbending torus field configurations as shown in the red rectangles in plots from left column of Fig. 3.35.

Q^2 Coverage for $e'K^+K^+K^-$ Tracks Detected

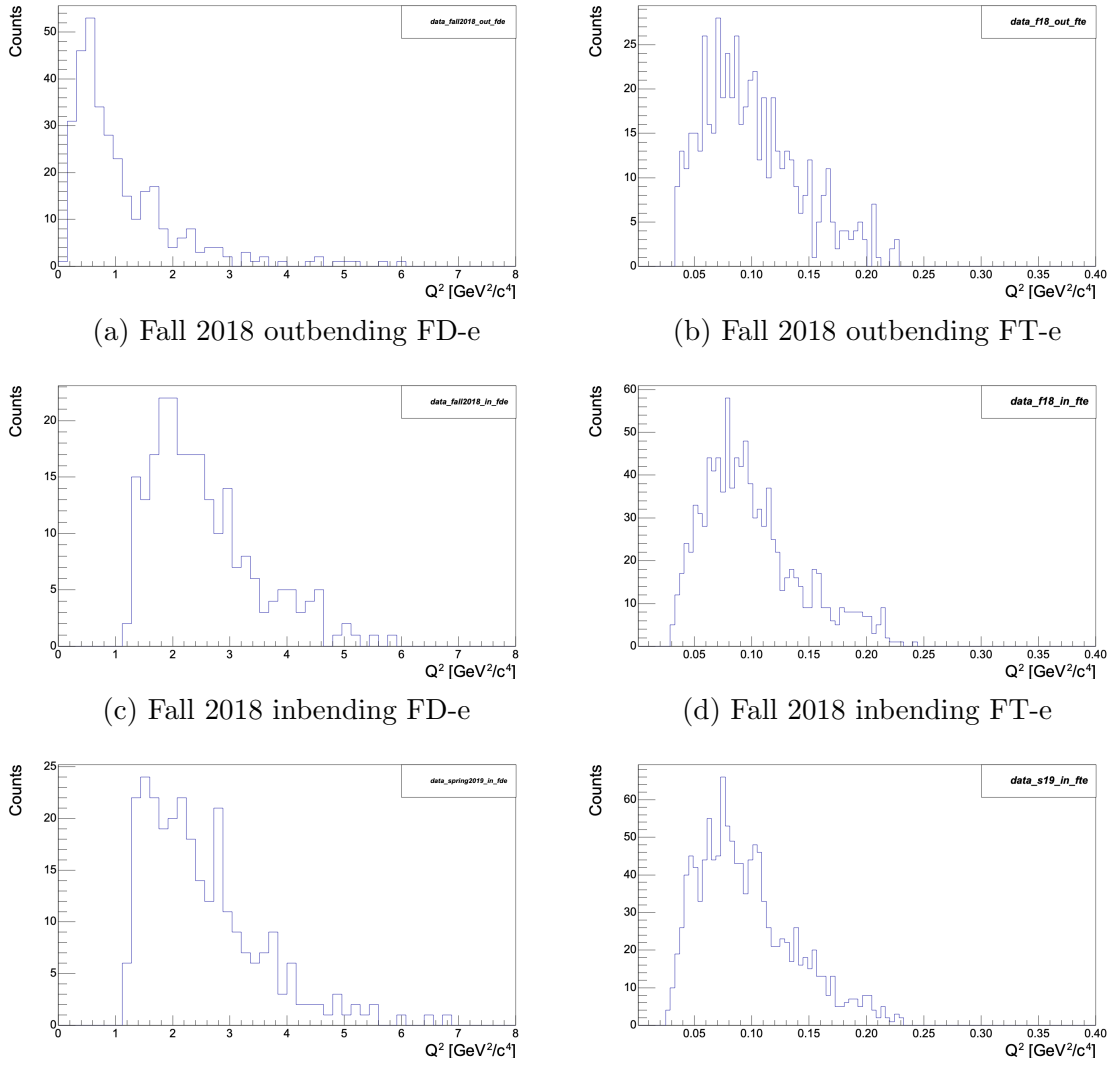

(a) Fall 2018 outbending FD-e

(b) Fall 2018 outbending FT-e

(c) Fall 2018 inbending FD-e

(d) Fall 2018 inbending FT-e

(e) Spring 2019 inbending FD-e

(f) Spring 2019 inbending FT-e

Figure 3.35: Different Q^2 coverage from the different data sets with different torus polarity settings for which $K^+K^+K^-$ tracks are detected with scattered electrons either in the Forward Detector (left column) or in the Forward Tagger (right column).

Q^2 vs. Missing Mass off of $e'K^+K^+K^-$

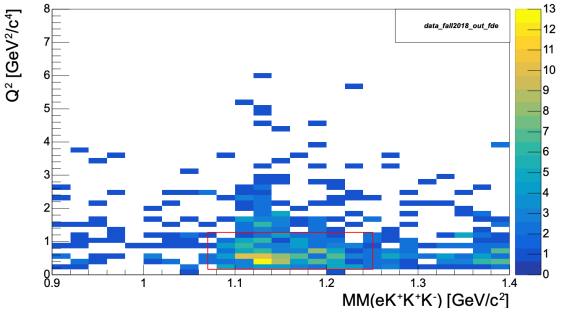

(a) Fall18 out FD-e Q^2 : $[0.16, 1.28]$ GeV^2

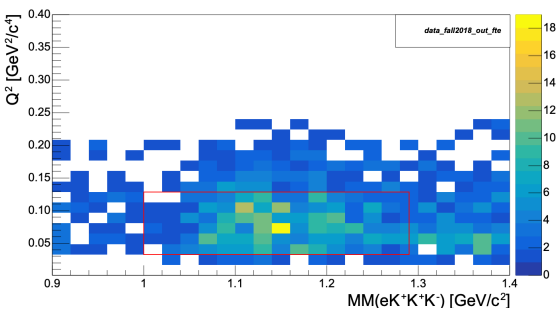

(b) Fall18 out FT-e Q^2 : $[0.03, 0.13]$ GeV^2

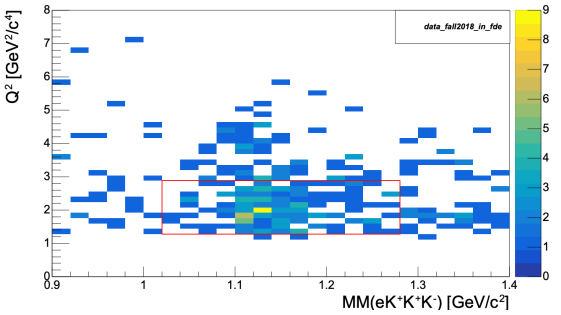

(c) Fall18 in FD-e Q^2 : $[1.28, 1.88]$ GeV^2

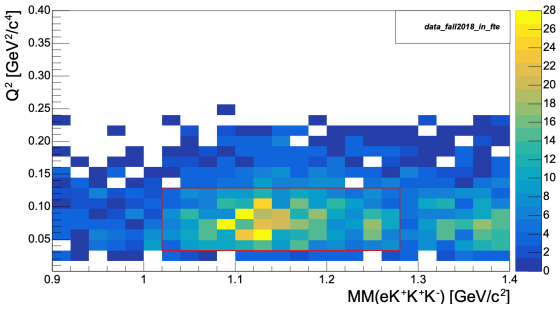

(d) Fall18 in FT-e Q^2 : $[0.03, 0.13]$ GeV^2

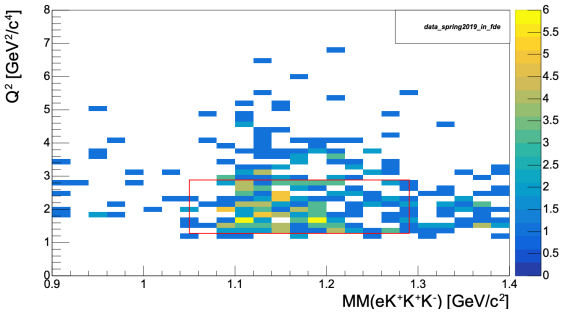

(e) Spring19 in FD-e Q^2 : $[1.28, 1.88]$ GeV^2

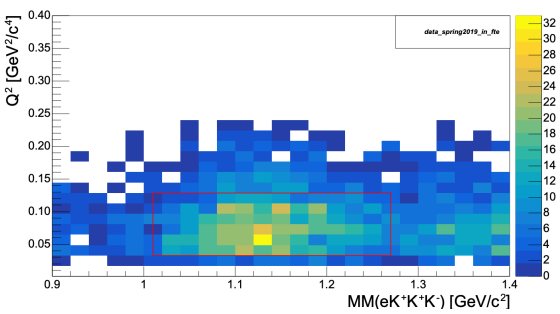

(f) Spring19 in FT-e Q^2 : $[0.03, 0.13]$ GeV^2

Figure 3.36: Two dimensional scatter plot showing Q^2 coverage with respect to the missing mass off of $e'K^+K^+K^-$ form the different data sets with different torus field polarity for which $K^+K^+K^-$ events are detected with the scattered electron either in the Forward Detector (left column) or in the Forward Tagger (right column). Because of the torus polarity, the majority of our events are above and below $Q^2 = 1$ GeV^2 with inbending and outbending polarity, respectively, for the FD-e case. This analysis concentrates on the Q^2 coverage from several data sets, which are specified in the caption and shown by the red rectangle drawn in each figure.

CHAPTER 4

CLAS12 Monte Carlo Simulation

The experimental data distributions are the result of the physical distributions modified by the detector response function. Simulated data with a proper theoretical model can be tuned to reproduce the detector response function in Monte Carlo (MC) studies. In particle physics experiments, Monte Carlo simulations are used to understand the detector's imperfections (i.e. limited geometrical coverage, detection inefficiencies, resolution biases, etc.) and the physical processes that can affect the ability to reconstruct a track. In our case, we are specifically interested in understanding the detector efficiency and acceptance to reconstruct the reaction $ep \rightarrow e'K^+K^+K^-(\Lambda/\Sigma^0)$ from the simulation. Once we measure the detector efficiency and acceptance, we can correct any inefficiencies that are present in the real data. The detector efficiency, ϵ, and its uncertainty, $\delta\epsilon$, are defined as

$$\epsilon = \frac{N_{rec}}{N_{gen}}, \tag{4.1}$$

$$\delta\epsilon = \sqrt{\frac{(1-\epsilon)\epsilon}{N_{gen}}}, \tag{4.2}$$

where N_{rec} and N_{gen} are the total number of reconstructed and generated events in the Monte Carlo study.

The CLAS12 detector simulations use a c++ framework called GEMC to simulate events through the CLAS12 detector. The GEMC framework [77] uses the GEant4 simulation toolkit to simulate the passage of particles through the CLAS12 detector by considering the physical location and composition of its different components. The entire CLAS12 geometry has been developed by users using GEant4 tools and implemented in the GEMC framework. All physical processes such as

pair production, Compton scattering, ionization, multiple scattering, bremsstrahlung, electron-positron annihilation, hadron interactions, etc. that can occur by the passage of particles through matter are also accounted for in GEMC while simulating the interaction of particles through the CLAS12 detector.

4.1 Monte Carlo Smearing to Reproduce Data Resolution

The MC missing-mass resolution is better than the data missing-mass resolution, in spite of the fact that every effort was made to account for all physical processes in the simulation. It is therefore necessary to smear the MC distributions to match the data distributions. The ground state $\Xi^-(1320)$ resonance in the $MM(e'K^+K^+)$ is visible for all RG-A data sets. The mass resolution of the $\Xi^-(1320)$ in the missing mass of the $ep \to e'K^+K^+(X)$ system with charged kaons and scattered electrons detected in the FD is better than charged kaons detected in the FD and scattered electrons in the FT as shown in Fig. 4.1, which shows the $\Xi^-(1320)$ missing-mass resolution from the fit for two different cases (FT-e and FD-e) using the RG-A Fall 2018 outbending data set.

$\Xi^-(1320)$ Mass Resolution in the $MM(e'K^+K^+)$ Distribution

$\Xi^-(1320)$	Electron detected in the FD	Electron detected in the FT
μ (GeV)	1.3383 ± 0.0015	1.3344 ± 0.0051
σ (GeV)	0.0244 ± 0.0015	0.0482 ± 0.0071

Table 4.1: Summary table showing the fit parameters of reconstructed $\Xi^-(1320)$ in the $MM(e'K^+K^+)$ missing mass distribution using the RG-A Fall 2018 outbending data when a scattered electron is detected either in the FD or in the FT with kaons detected in the FD.

$\Xi^-(1320)$ **Fit from the RG-A Fall 2018 Outbending Data**

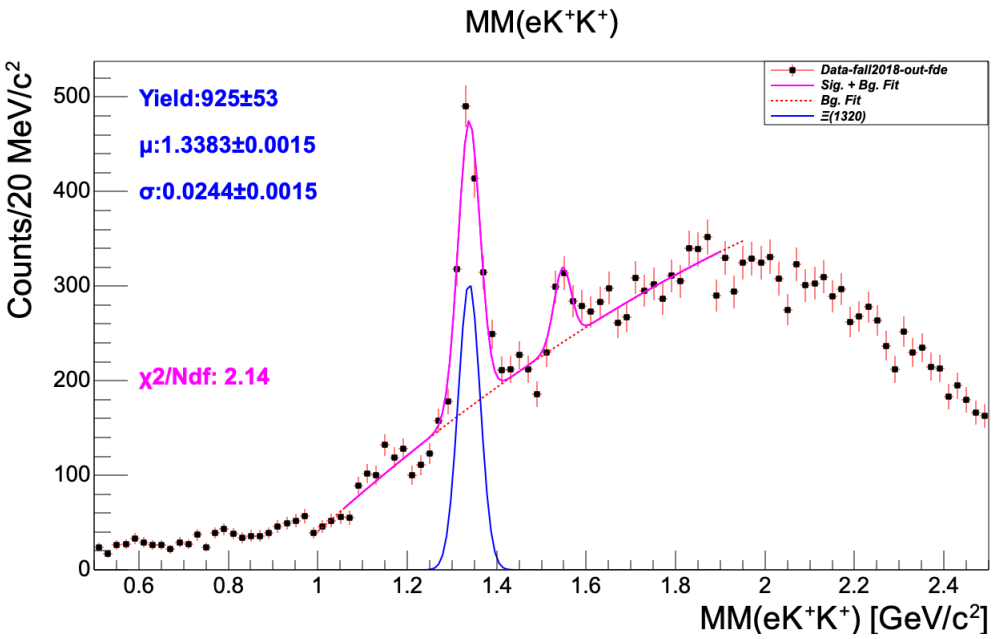

(a) Electron in the FD.

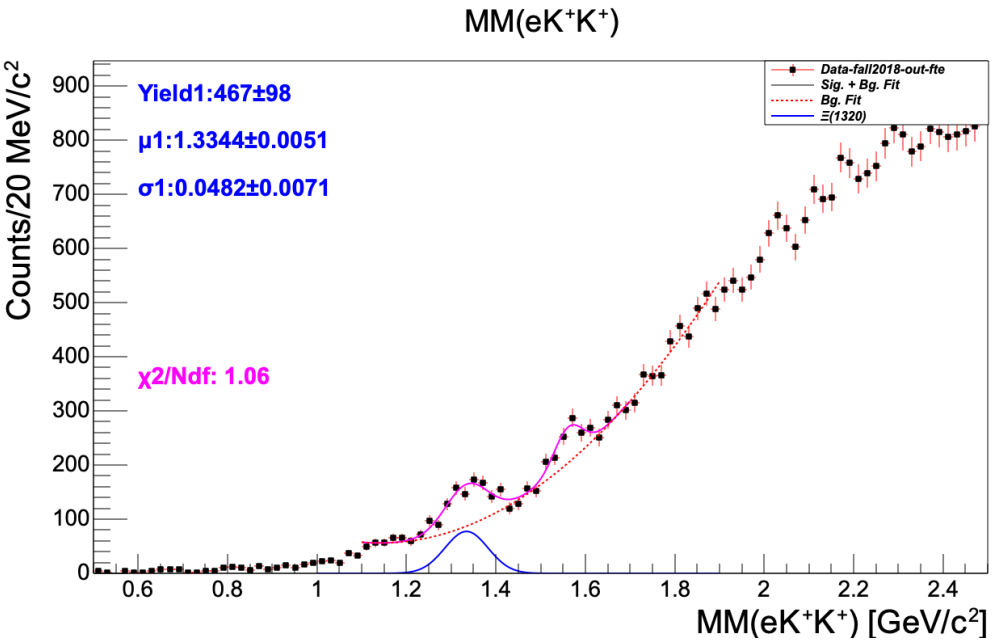

(b) Electron in the FT.

Figure 4.1: Plot showing fit parameters and fit functions for the missing mass distribution off of $e'K^+K^+$ using the RG-A Fall 2018 outbending data set with the scattered electron detected either in the FD (top) or in FT (bottom). The magenta line is the global fit function, which is the sum of a double Gaussian fit function to represent the octet ground state $\Xi^-(1320)$ (blue) and decuplet ground state $\Xi^-(1530)$ plus a third-order polynomial function (red) to represent the background. The result of the fit is summarized in Table 4.1.

In order to ensure the MC simulation reproduces the data missing mass distributions, the CLAS12 GEMC simulations of the ground state $\Xi^-(1320)$ were performed first to match the resolution of the ground state $\Xi^-(1320)$ resonance in the missing mass off of $e'K^+K^+$. The exclusive reaction $ep \rightarrow e'K^+K^+\Xi(1320) \rightarrow e'K^+K^+\pi^-\Lambda$ was simulated with a phase space generator and the $\Xi^-(1320)$ was reconstructed using the missing mass technique by detecting at least two K^+ tracks in addition to the e' track in the FD acceptance. The 4.4.2 GEMC software and CLAS12 geometry tag was used to run the $\Xi^-(1320)$ simulation and all other simulations discussed later in this analysis. The details of the GEMC source code and CLAS12 geometry used in the 4.4.2 GEMC tag is stored in the Jefferson Lab gemc GitHub page under the clas12Tags repository in Ref. [78]. The reconstructed $\Xi^-(1320)$ mass resolution in the missing mass distribution from the data and MC were then compared. To find the correct MC resolution that reproduces the data resolution, the change in the $\Xi^-(1320)$ mass resolution by applying different momentum smearing factors ($\frac{\Delta p}{p}$) to the momentum of reconstructed particles in the MC was studied. First, the MC smearing factor for FD-particles was determined by matching the $\Xi^-(1320)$ mass resolution in the $MM(e'K^+K^+)$ from data and MC by detecting the scattered electron and two K^+ in the FD. Second, the MC smearing factor for FD-particles derived in the first step was used to derive the MC smearing factor for the FT-electron. The same technique of matching the $\Xi^-(1320)$ mass resolution from data and MC in the $MM(e'K^+K^+)$ was used by fixing the MC smearing factor from the first step for K^+s detected in the FD and varying the MC smearing factors for scattered electrons detected in the FT.

Momentum Smearing Factor Derived Using $\Xi^-(1320)$ in Data vs. MC

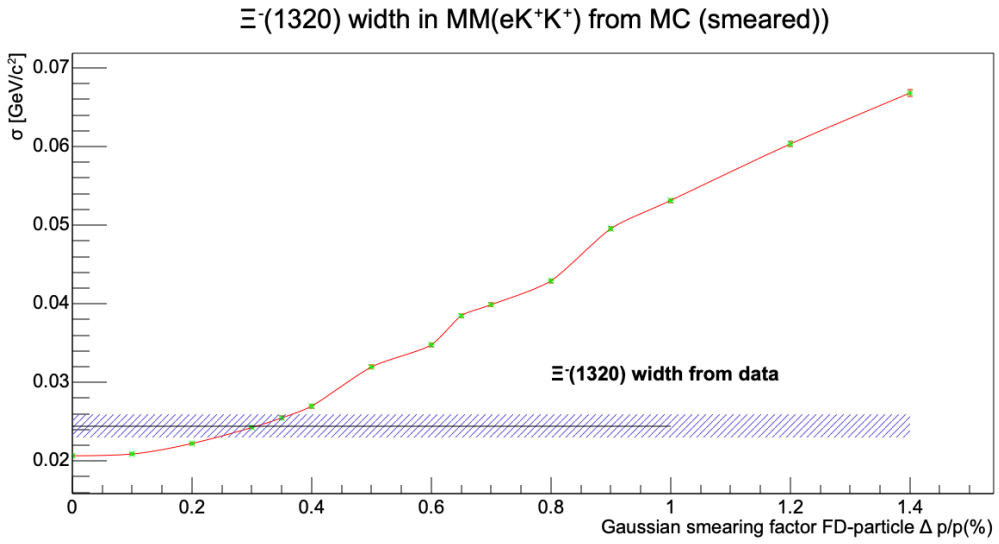

(a) MC smearing factor ($\frac{\Delta p}{p}$) optimization for FD-particles.

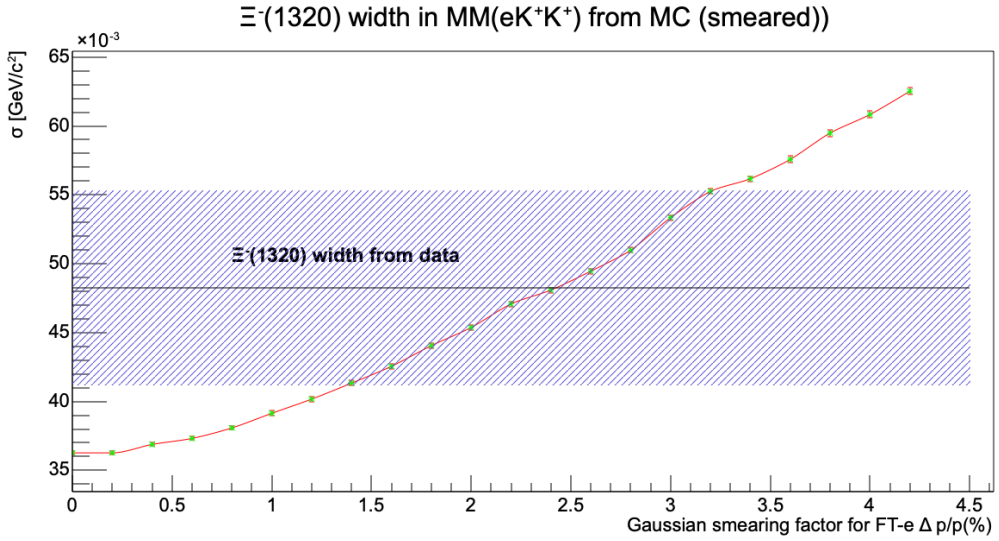

(b) MC smearing factor ($\frac{\Delta p}{p}$) optimization for FT-electron.

Figure 4.2: Plot showing the $\Xi^-(1320)$ mass resolution (width) of $MM(e'K^+K^+)$ from the RG-A Fall 2018 outbending data and MC with different MC smearing factors as a function of the momentum smearing factor for particles. The top plot is for the electron detected in the FD, and the bottom plot is for the electron detected in the FT. The black horizontal line in each plot shows the $\Xi^-(1320)$ width of the Gaussian fit as summarized in Table 4.1 for the RG-A Fall 2018 outbending data with a blue band representing the uncertainty range on the width for the two different cases. A momentum smearing factor of 0.3% has been fixed from the top plot for FD-kaons to derive the momentum smearing factor for FT-electron in the bottom plot.

Figure 4.2 shows the mass resolution of the reconstructed $\Xi^-(1320)$ from MC simulation in the missing mass spectrum as a function of the momentum smearing factor ($\frac{\Delta p}{p}$) for the FD-electron and for the FT-electron cases. We can see that the mass resolution of the $\Xi^-(1320)$ changes with different smearing factors. The simulation reproduces the observed data mass resolution of the $\Xi^-(1320)$ state in the missing mass spectrum at $(0.30 \pm 0.05)\%$ momentum smearing factor for the forward detected particles. Hence, the simulation with 0.30% momentum smearing for the FD particles will provide a fair estimate of the CLAS12 FD resolution. We used the upper limit of the momentum smearing factor, 0.35%, for FD-kaons to derive the momentum smearing factor for FT-electrons. We repeated the same MC study by detecting scattered electrons in the FT rather than in the FD. Charged kaons are still detected in the FD, so we fixed their momentum smearing factor at 0.35% and measured the missing mass resolution as a function of the FT-electron momentum smearing factor, as shown in Fig. 4.2b.

The missing mass resolution as a function of the FT-electron momentum smearing factor shows that the best match between data and MC, in this case, can be achieved at a momentum smearing factor of $(2.5 \pm 1)\%$ for the FT-electron in addition to 0.35% for the FD-kaons. We considered the worst-case scenario and chose the upper limit of these momentum smearing factors (0.35% for FD-particles and 3.5% for FT-particles) in our simulations for the excited states to determine the experimental mass resolution even though these momentum smearing factors were derived comparing the resolution of the ground state Cascade in the simulation and data. The effect of the different momentum smearing factors while determining the experimental mass resolution of the $\Xi^{*-}(1820)$ state and eventually the upper limit cross-section estimate was studied to provide an associated systematic uncertainty.

4.2 $\Xi^{*-}(1820)$ Experimental Mass Resolution

The mass resolution of the reconstructed $\Xi^{*-}(1820)$ in the missing mass off of $e'K^+K^+$ was inferred from the Monte Carlo simulations after checking that they were consistent with the data. The generated events for the reaction $ep \rightarrow e'K^+K^+\Xi^{*-} \rightarrow e'K^+K^+K^-\Lambda/\Sigma^0$ with an intrinsic $\Xi^{*-}(1820)$ width of 24 MeV from the Particle Data Group (PDG) were simulated independently for the scattered electron reconstructed either in the FT or in the FD using CLAS12 GEMC. The resulting missing mass distribution off of $e'K^+K^+$ after applying the MC momentum smearing was then fitted with a Gaussian function as shown in Fig. 4.3. The width of that Gaussian fit is what was used as the mass resolution for the $\Xi^{*-}(1820)$ in the missing mass distribution to work with a similar reaction topology using real data where no statistically significant $\Xi^{*-}(1820)$ signal was observed. Table 4.2 summarizes the expected mass resolution of the $\Xi^{*-}(1820)$ in the data derived from the MC simulation with appropriate momentum smearing.

$\Xi^{*-}(1820)$ **Experimental Mass Resolution**

Electron detected in	Expected $\Xi^{*-}(1820)$ width
FD	46.96 ± 0.61 MeV
FT	55.22 ± 0.31 MeV

Table 4.2: Summary table showing the expected mass resolution of the reconstructed $\Xi^{*-}(1820)$ in the $MM(e'K^+K^+)$ missing mass distribution when a scattered electron is detected either in the FD or in the FT with kaons detected in the FD. The expected mass resolution was derived using a MC smearing study as explained in the Sections 4.1 and 4.2.

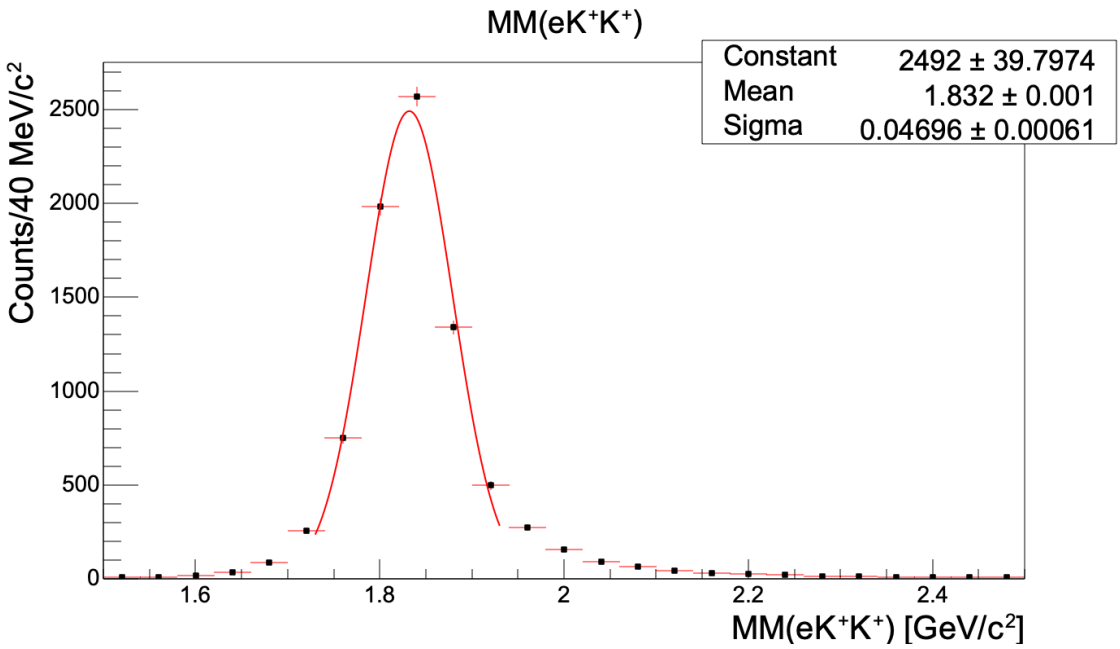

(a) Electron detected in the FD.

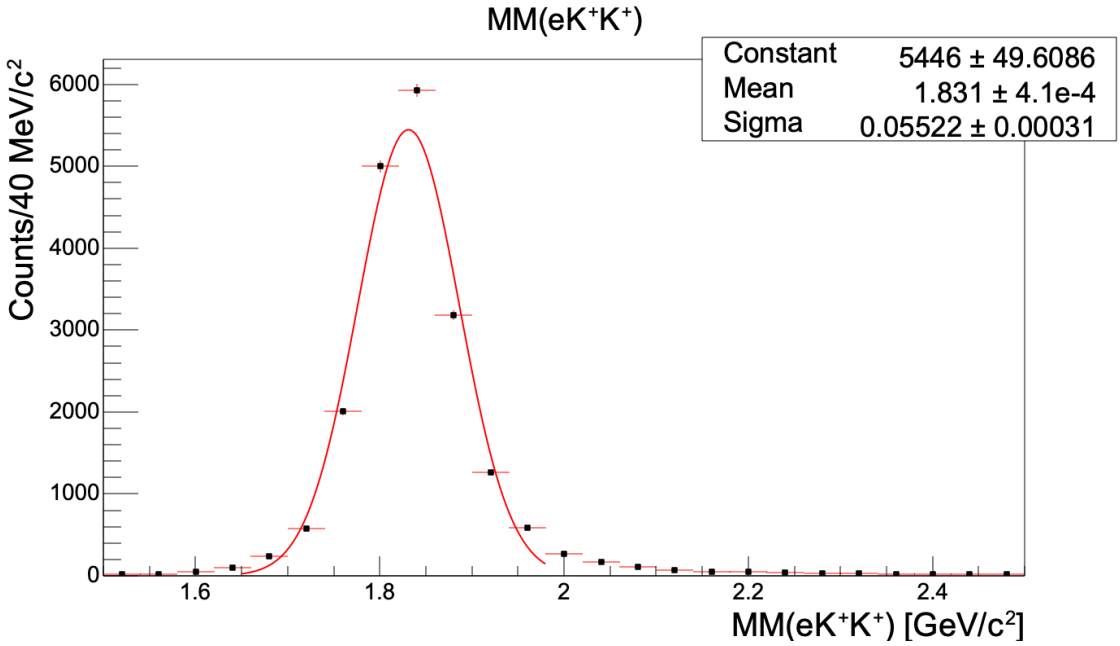

(b) Electron detected in the FT.

Figure 4.3: Plot showing the $\Xi(1820)$ mass resolution from MC in $MM(e'K^+K^+)$ for the $ep \rightarrow e'K^+K^+\Xi^{*-}(1820) \rightarrow e'K^+K^+K^-(\Lambda/\Sigma^0)$ process with the scattered electron detected in the FD (top plot) or in the FT (bottom plot). The normally distributed Gaussian smearing factor of 0.3% for the momentum of FD-particles and that of 3.5% for the momentum of FT-detected electron (derived in Section 4.1) has been applied to make sure that the missing mass distribution from the MC simulation matches that from the real data.

4.3 Mass-Dependent Detection Efficiency of Ξ^{*-} in the Reaction $ep \rightarrow e'K^+K^+\Xi^{*-} \rightarrow e'K^+K^+K^-(\Lambda/\Sigma^0)$

The CLAS12-elSpectro phase space Monte Carlo generator [79] was used to generate the reactions, $ep \rightarrow e'K^+K^+\Xi^{*-} \rightarrow e'K^+K^+K^-(\Lambda)$, and $ep \rightarrow e'K^+K^+\Xi^{*-} \rightarrow e'K^+K^+K^-(\Sigma^0)$ in different electron scattering kinematics in phase space, where flat mass distributions of the intermediate doubly strange excited Cascade Ξ^{*-} were generated and allowed to decay through $K^-\Lambda$ and $K^-\Sigma^0$, respectively. The main purpose of generating flat mass distributions for the intermediate Ξ^{*-}s was to study the mass-dependent detection efficiency of the CLAS12 detector in the excited state Cascade mass range from above 1.6 GeV. To differentiate the electroproduction (high Q^2, i.e. > 0.5 GeV^2) and the quasi-real photoproduction (low Q^2) processes, the electron scattering phase space was restricted in such a way that the polar scattering angle of the generated electron was greater than 5° in the former case, and in the range of 2.5° to 4.5° in the latter case. These two processes were simulated separately by repeating the same steps for scattered electrons in the two different electron scattering angle ranges. While running the simulation, background merging was performed by merging simulated data with real data from a random CLAS12 trigger to accurately mimic possible beam and electronic backgrounds from different physical processes in the simulation that are present in the real data that affects the charged track reconstruction efficiency [80].

Particle tracks behave differently in response to different torus polarity settings resulting in different detection efficiencies. The same Monte Carlo steps were repeated for high Q^2 and low Q^2 processes for the different torus polarities to understand their effect on the CLAS12 acceptance and to calculate the detection efficiency for our reactions of interest.

The generated and reconstructed missing mass distributions from the MC simulation study to calculate the detection efficiency as a function of missing mass $MM(ep \to e'K^+K^+X)$ in the exclusive process $ep \to e'K^+K^+(\Xi^{*-}) \to e'K^+K^+K^-$ (Λ/Σ^0) are shown in Figs. 4.4 to 4.9 for the different run configurations. The reconstruction efficiency for different missing mass bins was calculated independently using Eq. (4.1) for the different run configurations. The reconstruction efficiency as a function of missing mass in these figures corresponds to the CLAS12 Forward Detector reconstruction efficiency as the final state particles are detected in the Forward Detector geometrical coverage only. Table 4.3 summarizes the reconstruction efficiencies in the Forward Detector geometrical acceptance for different data configurations for a 40 MeV Ξ^{*-} missing mass bin from 1.82 GeV to 1.86 GeV. The efficiency as a function of Q^2 for various missing mass bins is briefly illustrated in Section 4.4.

Efficiency as a Function of Mass (Fall 2018 Outbending FT-e)

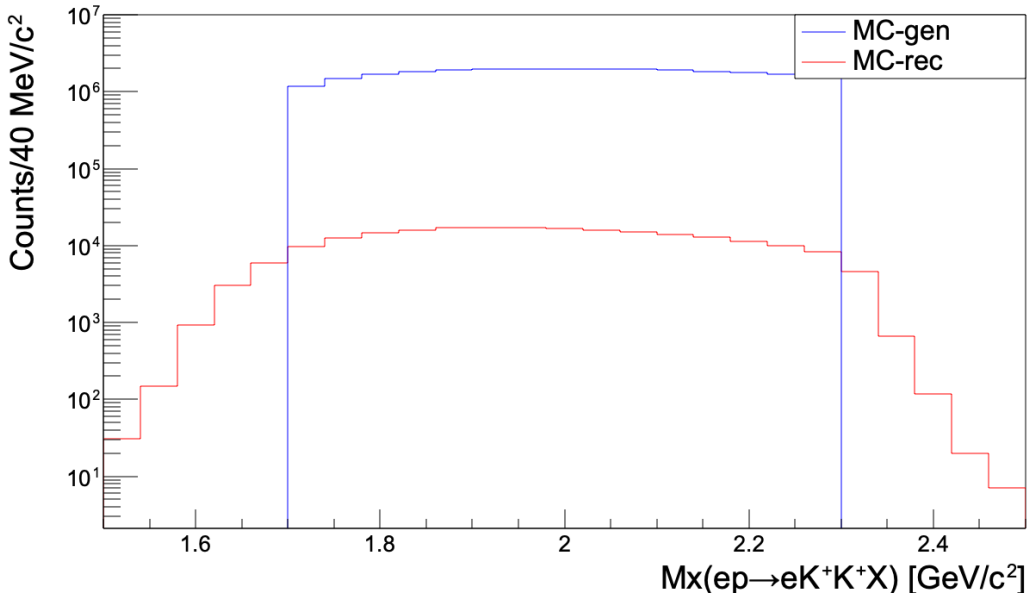

(a) MC Generated (blue) ≈ 26.7M vs. Reconstructed (red) ≈ 223K events.

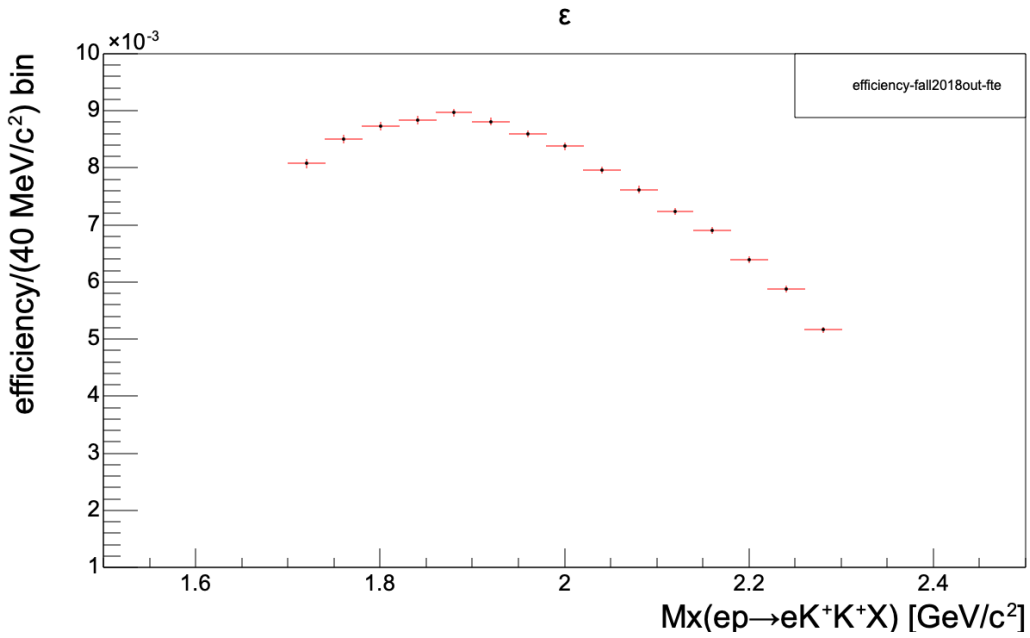

(b) Efficiency

Figure 4.4: Efficiency as a function of missing mass (bottom), $MM(e'K^+K^+)$, for the Fall 2018 outbending torus configuration where $e'K^+K^+K^-$ tracks are detected with the e' in the Forward Tagger and charged kaons in the Forward Detector. The top plot shows the generated flat Ξ^{-*} mass distribution (blue histogram) in the phase space, and the corresponding reconstructed mass distribution (red histogram) from the GEMC simulation.

Efficiency as a Function of Mass (Fall 2018 Inbending FT-e)

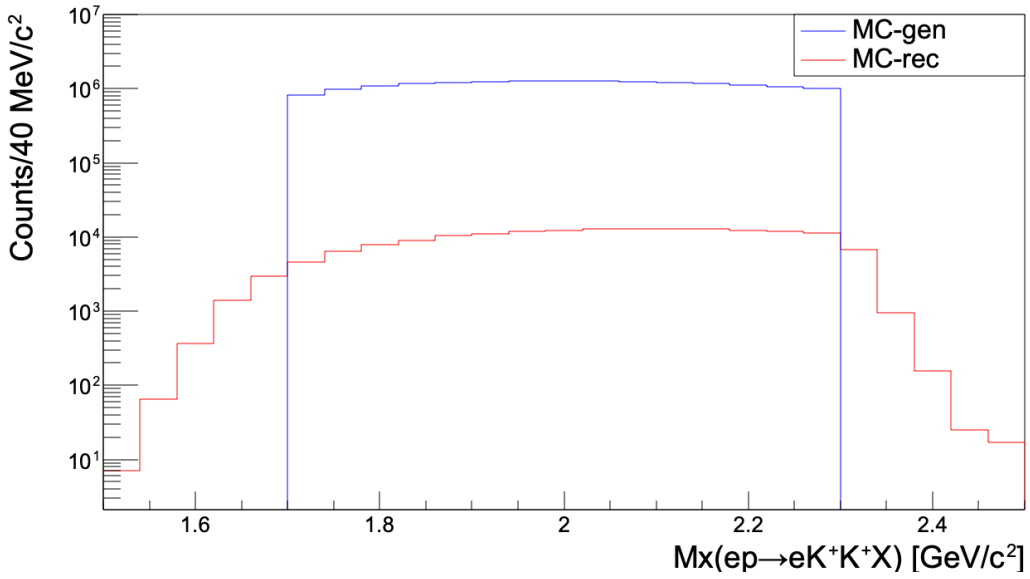

(a) MC Generated (blue) ≈ 17.1M vs. Reconstructed (red) ≈ 173K events.

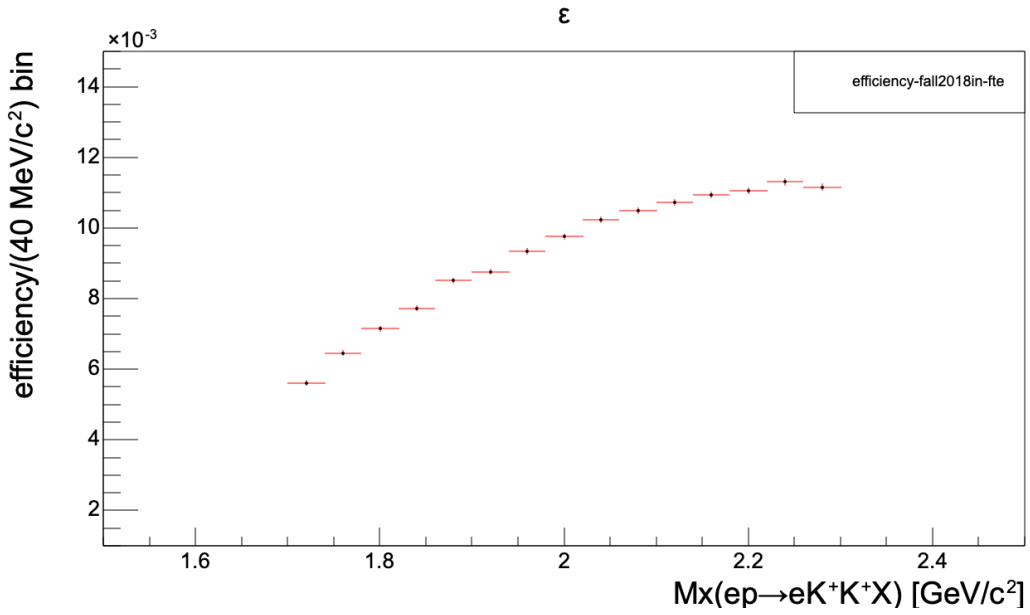

(b) Efficiency

Figure 4.5: Same as Fig. 4.4 but for the RG-A Fall 2018 inbending MC simulation configuration.

Efficiency as a Function of Mass (Spring2019 Inbending FT-e)

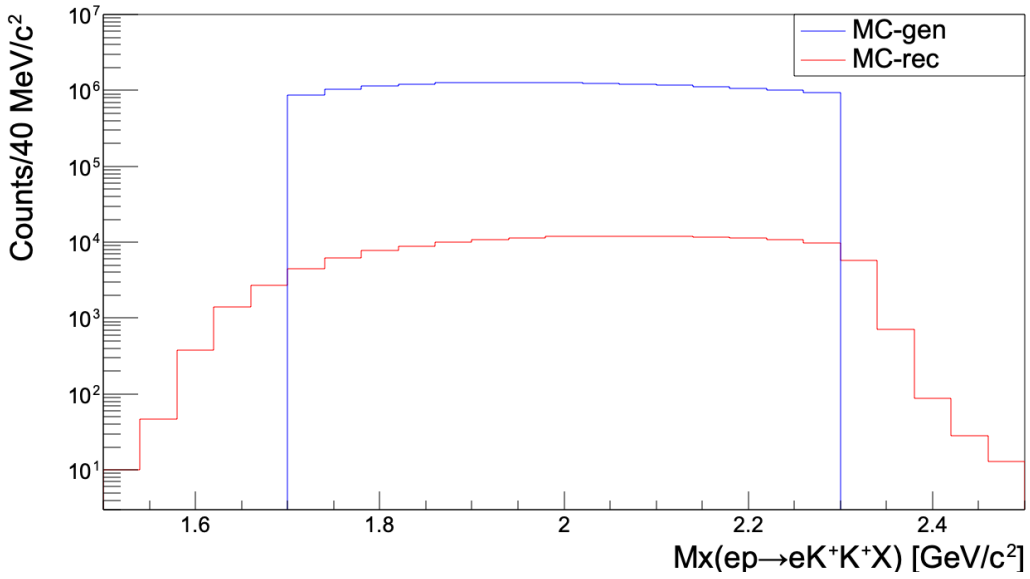

(a) MC Generated (blue) ≈ 17M vs. Reconstructed (red) 162K events.

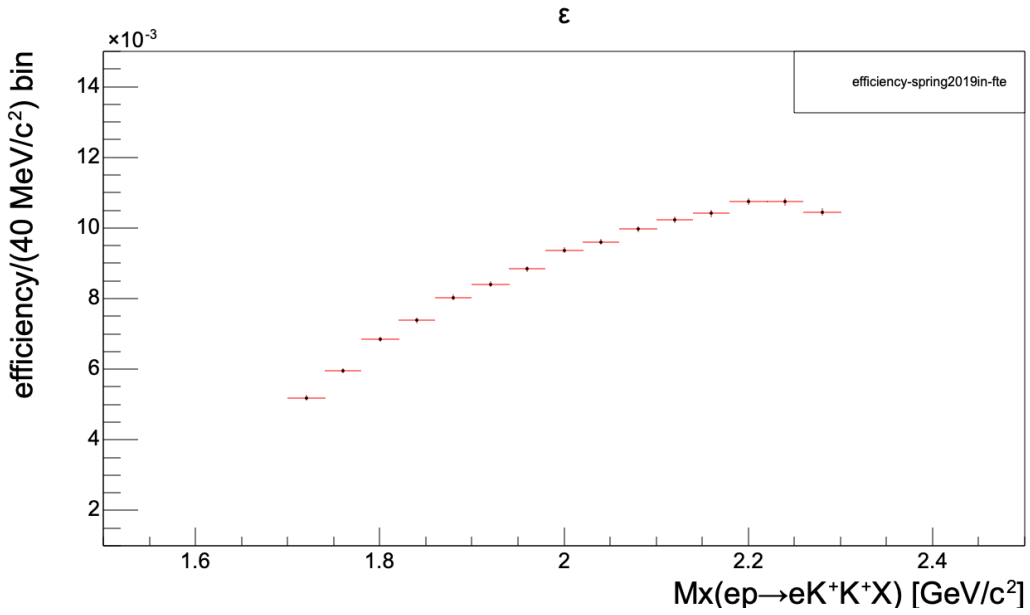

(b) Efficiency

Figure 4.6: Same as Fig. 4.4 but for the RG-A Spring 2019 inbending MC simulation configuration.

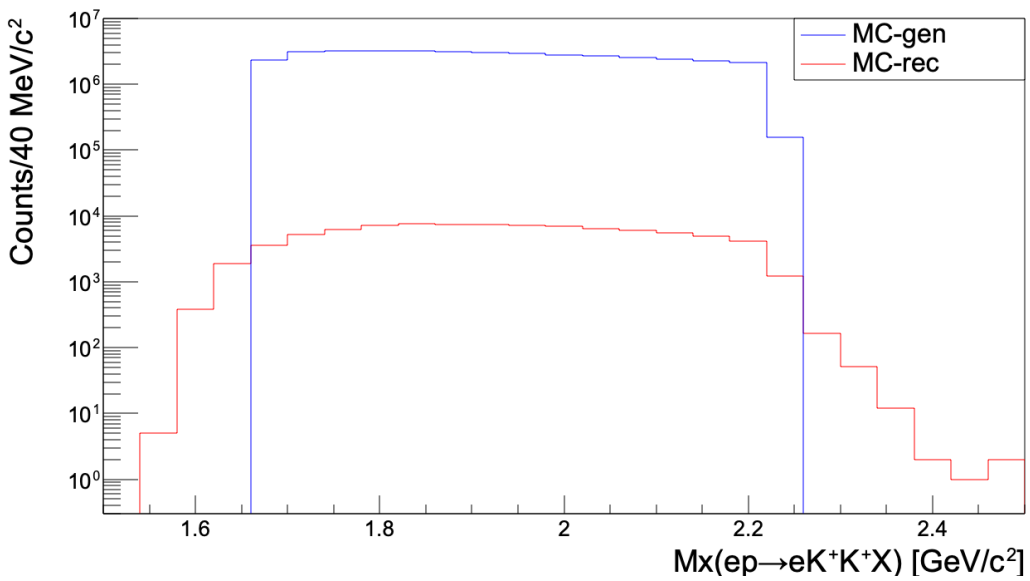

(a) MC Generated (blue) ≈ 33M vs. Reconstructed (red) ≈ 80K events.

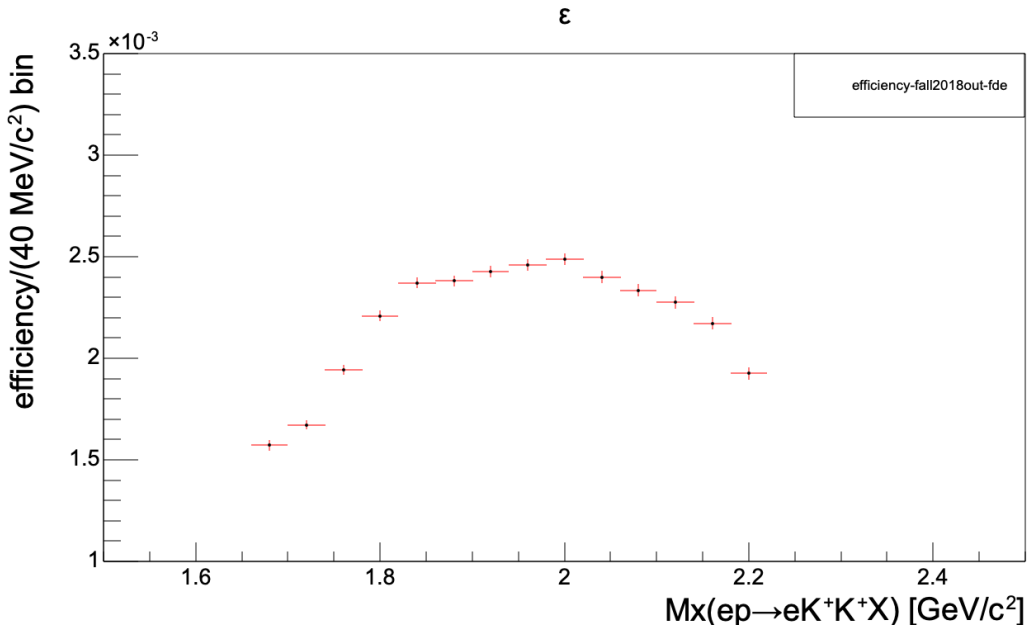

(b) Efficiency

Figure 4.7: Efficiency as a function of missing mass (bottom), $MM(e'K^+K^+)$, for the Fall 2018 outbending torus configuration where $e'K^+K^+K^-$ tracks are detected with the e' and charged kaons from the Forward Detector. The top plot shows the generated flat Ξ^{-*} mass distribution in the phase space (blue histogram) with the corresponding reconstructed missing mass distribution (red histogram) from the GEMC simulation.

Efficiency as a Function of Mass (Fall2018 Inbending FD-e)

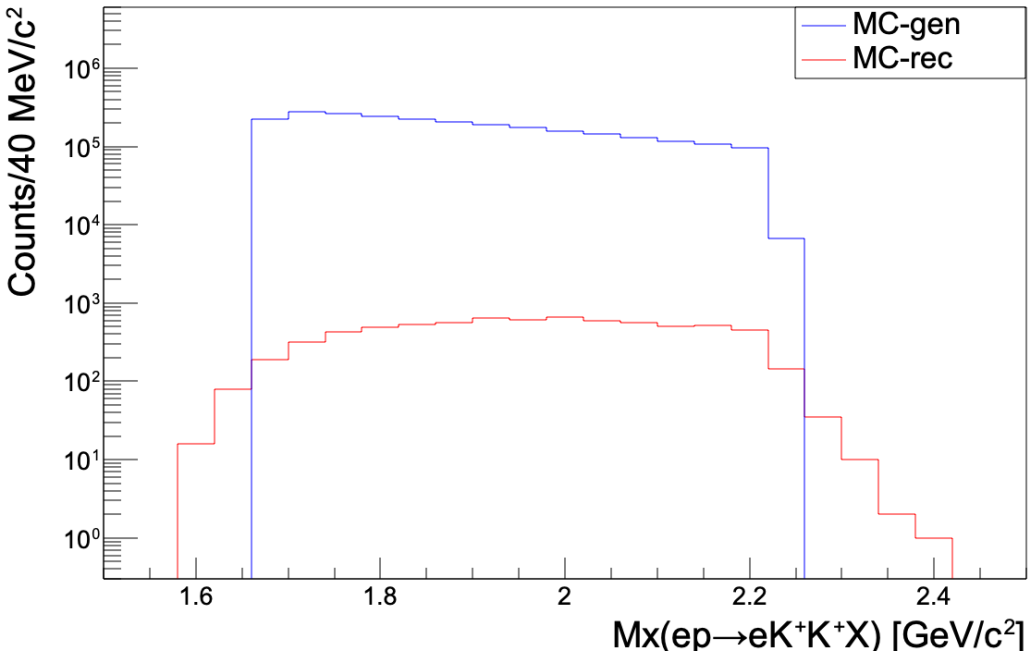

(a) MC Generated (blue) ≈ 2.6M vs. Reconstructed (red) ≈ 7K events.

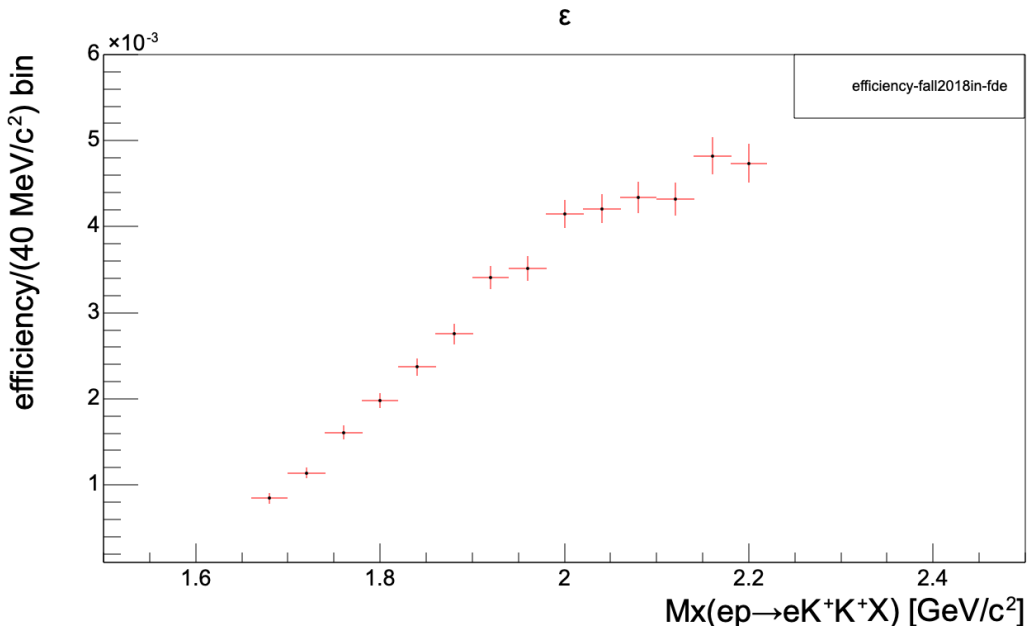

(b) Efficiency

Figure 4.8: Same as Fig. 4.7 but for the RG-A Fall 2018 inbending MC simulation configuration.

Efficiency as a Function of Mass (Spring 2019 Intbending FD-e)

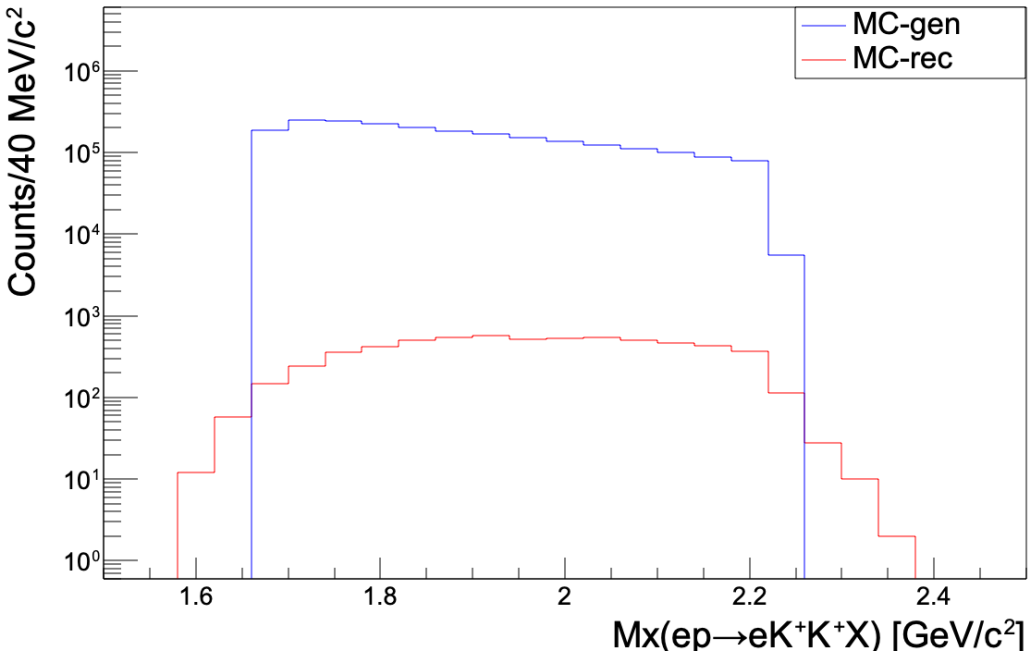

(a) MC Generated (blue) ≈ 2.3M vs. Reconstructed (red) ≈ 6K events.

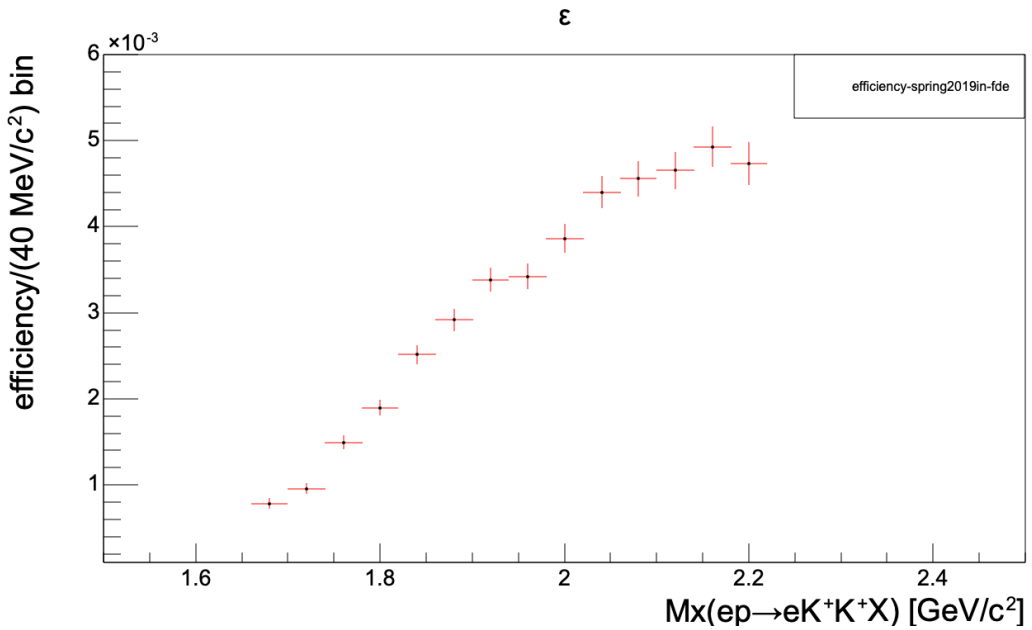

(b) Efficiency

Figure 4.9: Same as Fig. 4.7 but for the RG-A Spring 2019 inbending MC simulation configuration.

Efficiency summary for the $\Xi^{*-}(1820)$ reconstruction

Data set	Q^2-bin	MM-bin	$N_{gen.}$	$N_{rec.}$	Efficiency
Fall18 out FT-e	[0.03 : 0.13] GeV^2	[1.82 : 1.86] GeV	1807903	15980	0.00884 $\pm$ 0.00007
Fall18 in FT-e	[0.03 : 0.13] GeV^2	[1.82 : 1.86] GeV	1169460	9038	0.00773 $\pm$ 0.00008
Spring19 in FT-e	[0.03 : 0.13] GeV^2	[1.82 : 1.86] GeV	1209929	8935	0.00739 $\pm$ 0.00008
Fall18 out FD-e	[0.16 : 1.28] GeV^2	[1.82 : 1.86] GeV	2766758	6758	0.00244 $\pm$ 0.00003
Fall18 in FD-e	[1.28 : 1.88] GeV^2	[1.82 : 1.86] GeV	226012	536	0.00237 $\pm$ 0.00009
Spring19 in FD-e	[1.28 : 1.88] GeV^2	[1.82 : 1.86] GeV	201998	508	0.00252 $\pm$ 0.00011

Table 4.3: The reaction $ep \rightarrow e'K^+K^+\Xi^{*-}(1820) \rightarrow e'K^+K^+K^-(\Lambda/\Sigma^0)$ reconstruction efficiency for the different data configurations in the CLAS12-FD phase space acceptance derived using GEANT4 based MC simulation.

4.4 Q^2-Dependent Reconstruction Efficiency

We investigated the variation of reaction reconstruction efficiency with four-momentum transfer Q^2 for each intermediate Ξ^{*-} missing mass bin from the previous section. Figures 4.10 to 4.15 shows the Q^2-dependent reaction reconstruction efficiency for the different missing mass bins of Ξ^{*-} for the different run configurations.

The reaction reconstruction efficiency decreases with increasing momentum transfer Q^2 when the scattered electron is detected in the Forward Tagger. The decrease in efficiency with increasing Q^2 in the FT-e scattering kinematics is more noticeable for the outbending torus field configuration as shown in Fig. 4.10. On the other hand, the decrease in efficiency with increasing values of Q^2 in the FT-e scattering kinematics is very small with inbending torus field configuration and it remains constant as shown in Figs. 4.11 and 4.12 in the Q^2 range from $0.033 - 0.13$ GeV^2, where the majority of the reconstructed Λ/Σ^0 events were observed in the missing mass off of $e'K^+K^+K^-$ contributing to the Ξ^{*-} data sample as discussed in Section 3.6.

Q^2-Dependent Reconstruction Efficiency (Fall 2018 Outbending FT-e)

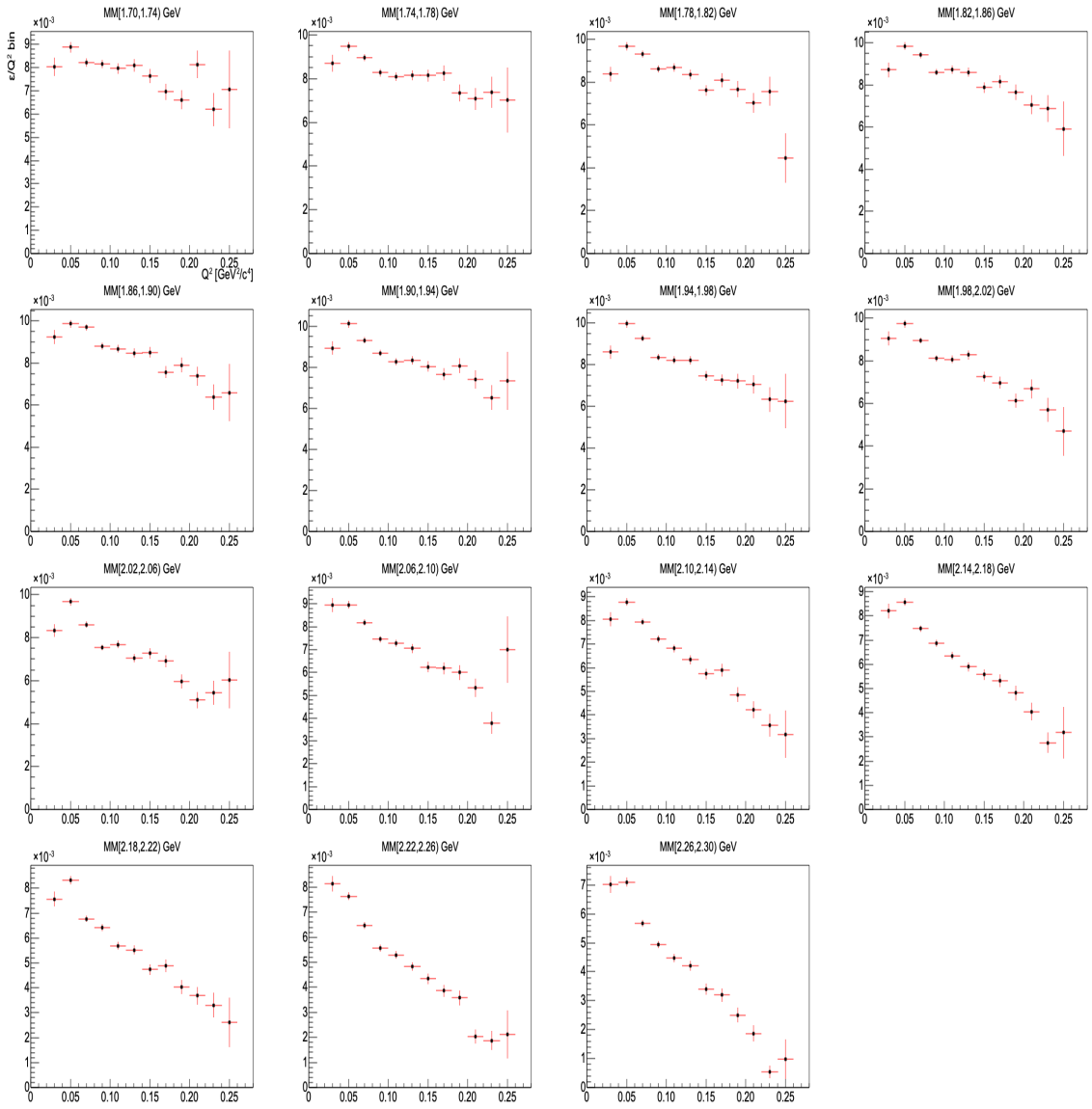

Figure 4.10: Reaction $ep \rightarrow e'K^+K^+(\Xi^{*-}) \rightarrow e'K^+K^+K^-(\Lambda/\Sigma^0)$ reconstruction efficiency as a function of momentum transfer Q^2 for different Ξ^{*-} missing mass bins for the Fall 2018 outbending run configuration with electron detected in the Forward Tagger.

Q^2-Dependent Reconstruction Efficiency (Fall 2018 Inbending FT-e)

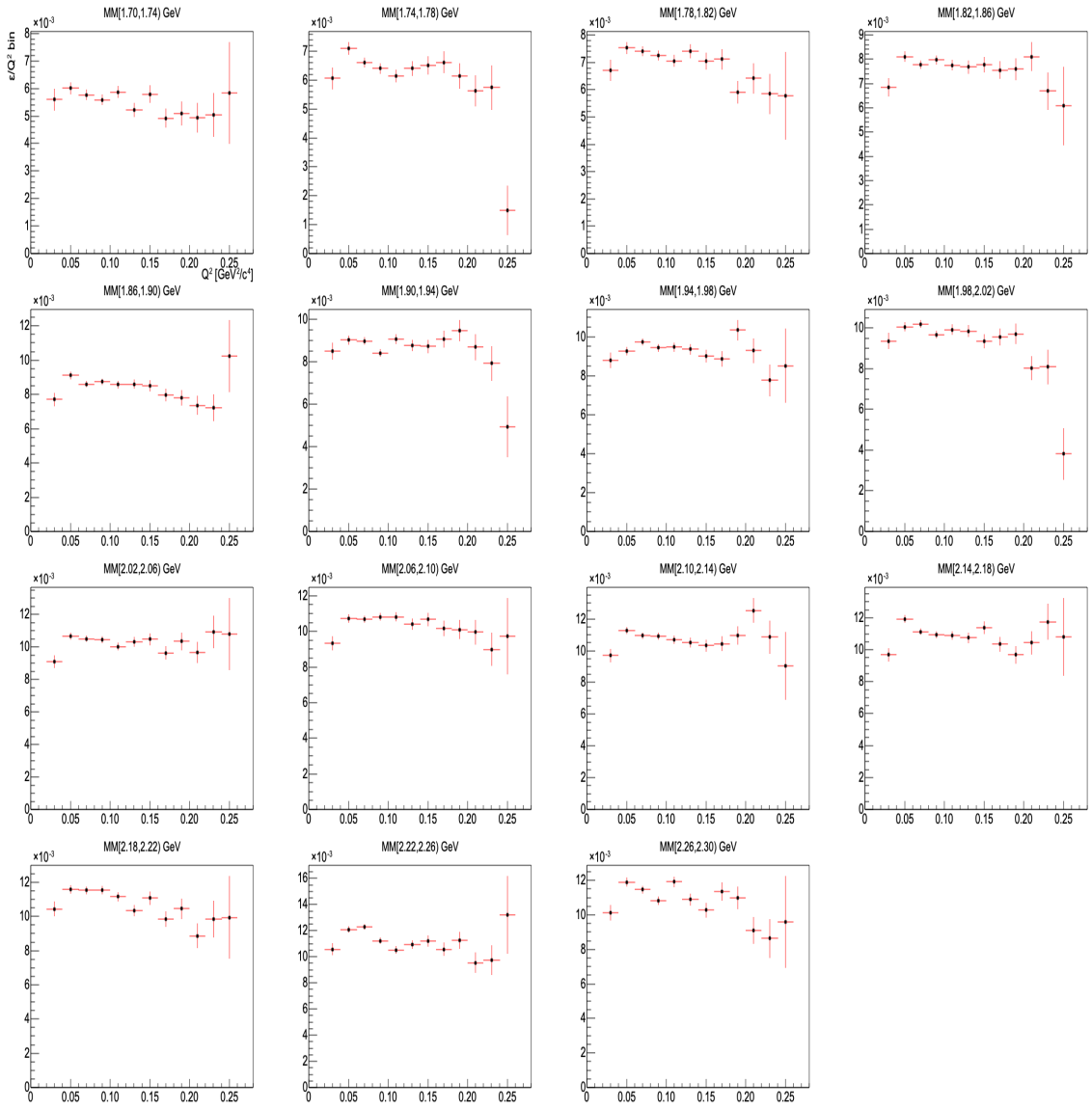

Figure 4.11: Same as Fig. 4.10 but for the RG-A Fall 2018 inbending MC simulation configuration.

Q^2-Dependent Reconstruction Efficiency (Spring 2019 Inbending FT-e)

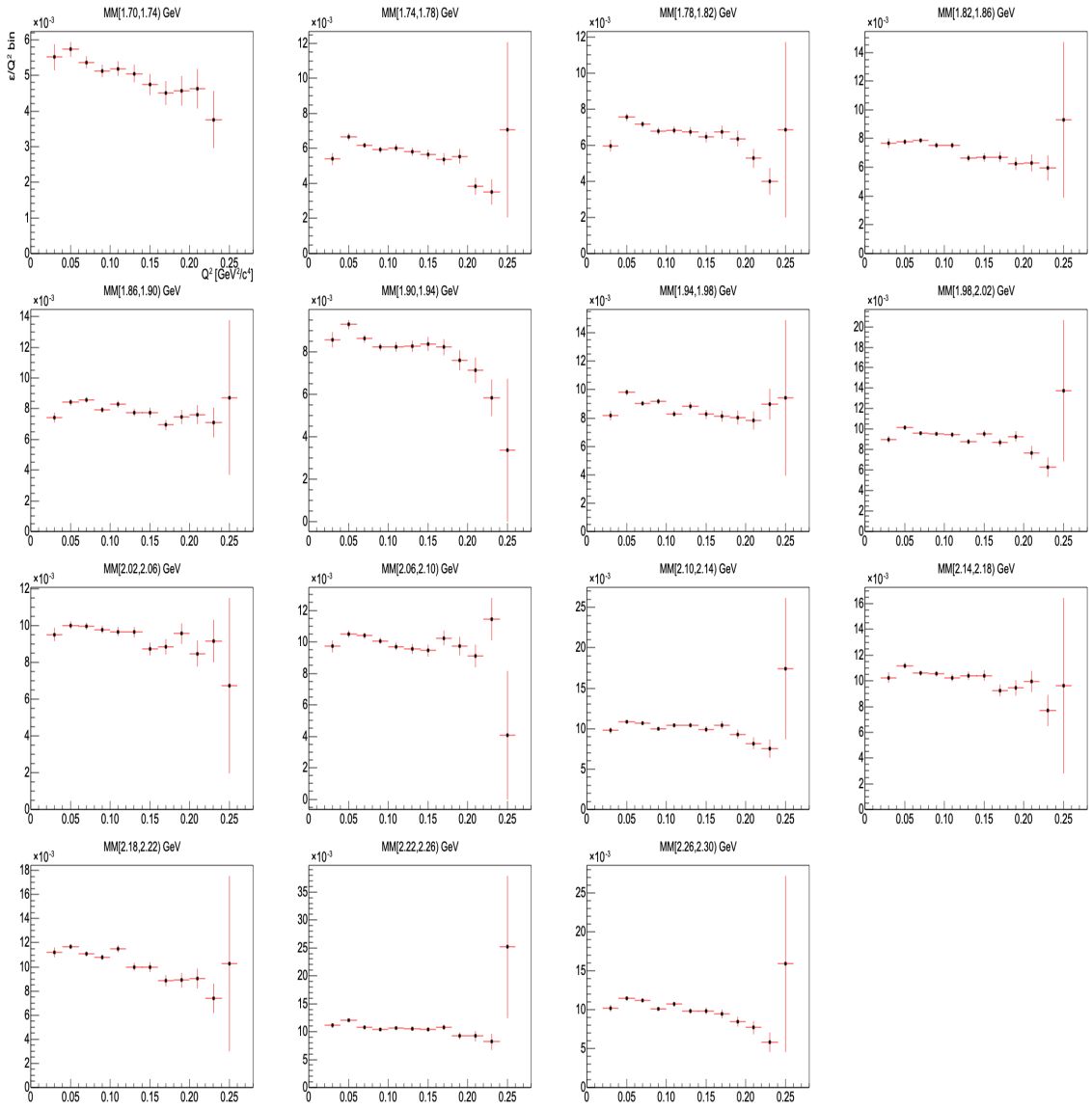

Figure 4.12: Same as Fig. 4.10 but for the RG-A Spring 2019 inbending MC simulation configuration.

Q^2-Dependent Reconstruction Efficiency (Fall 2018 Outbending FD-e)

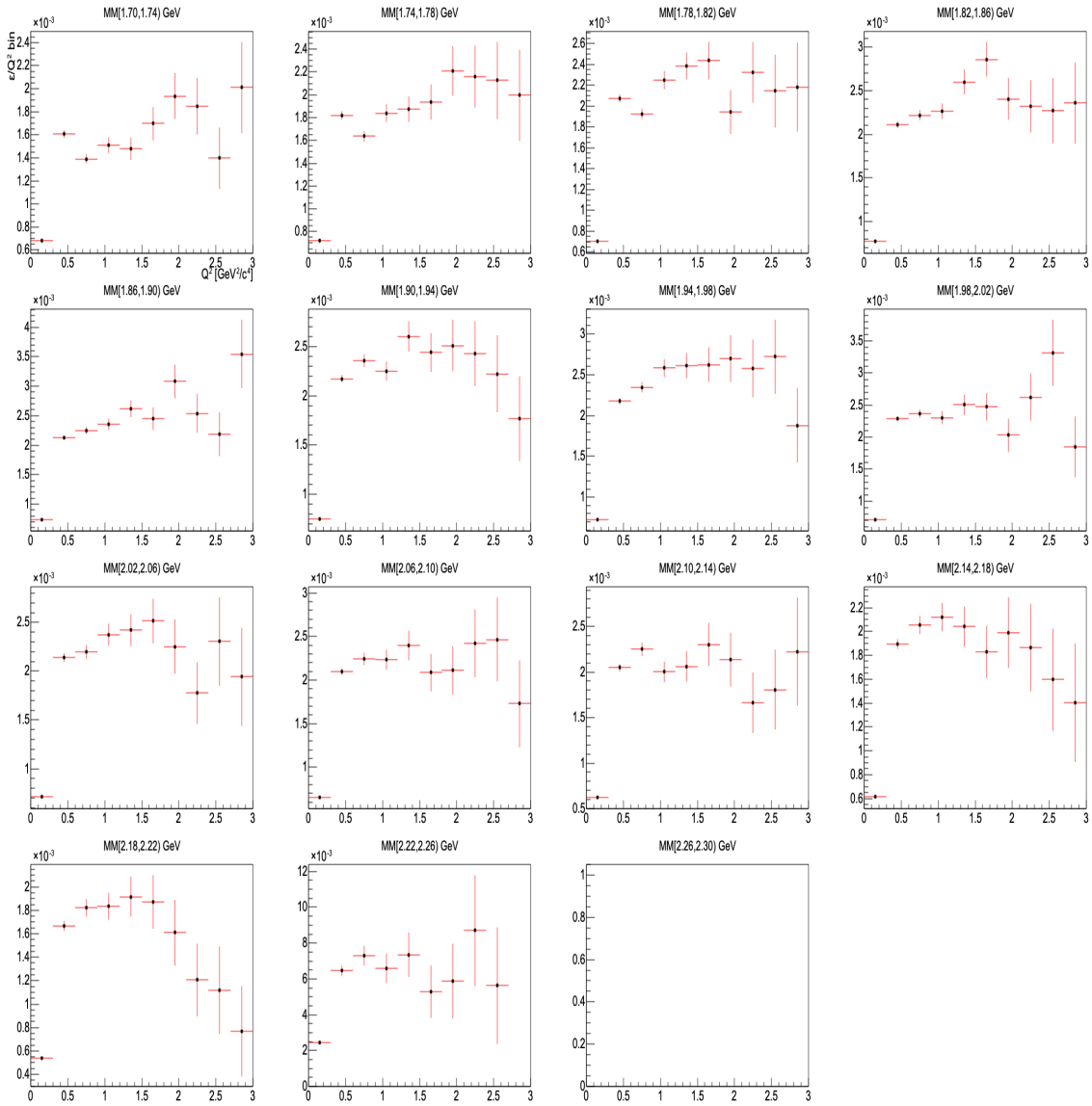

Figure 4.13: Reaction $ep \rightarrow e'K^+K^+(\Xi^{*-}) \rightarrow e'K^+K^+K^-(\Lambda/\Sigma^0)$ reconstruction efficiency as a function of momentum transfer Q^2 for different Ξ^{*-} missing mass bins for the Fall 2018 outbending run configuration with electron detected in the Forward Detector.

Q^2-Dependent Reconstruction Efficiency (Fall 2018 Inbending FD-e)

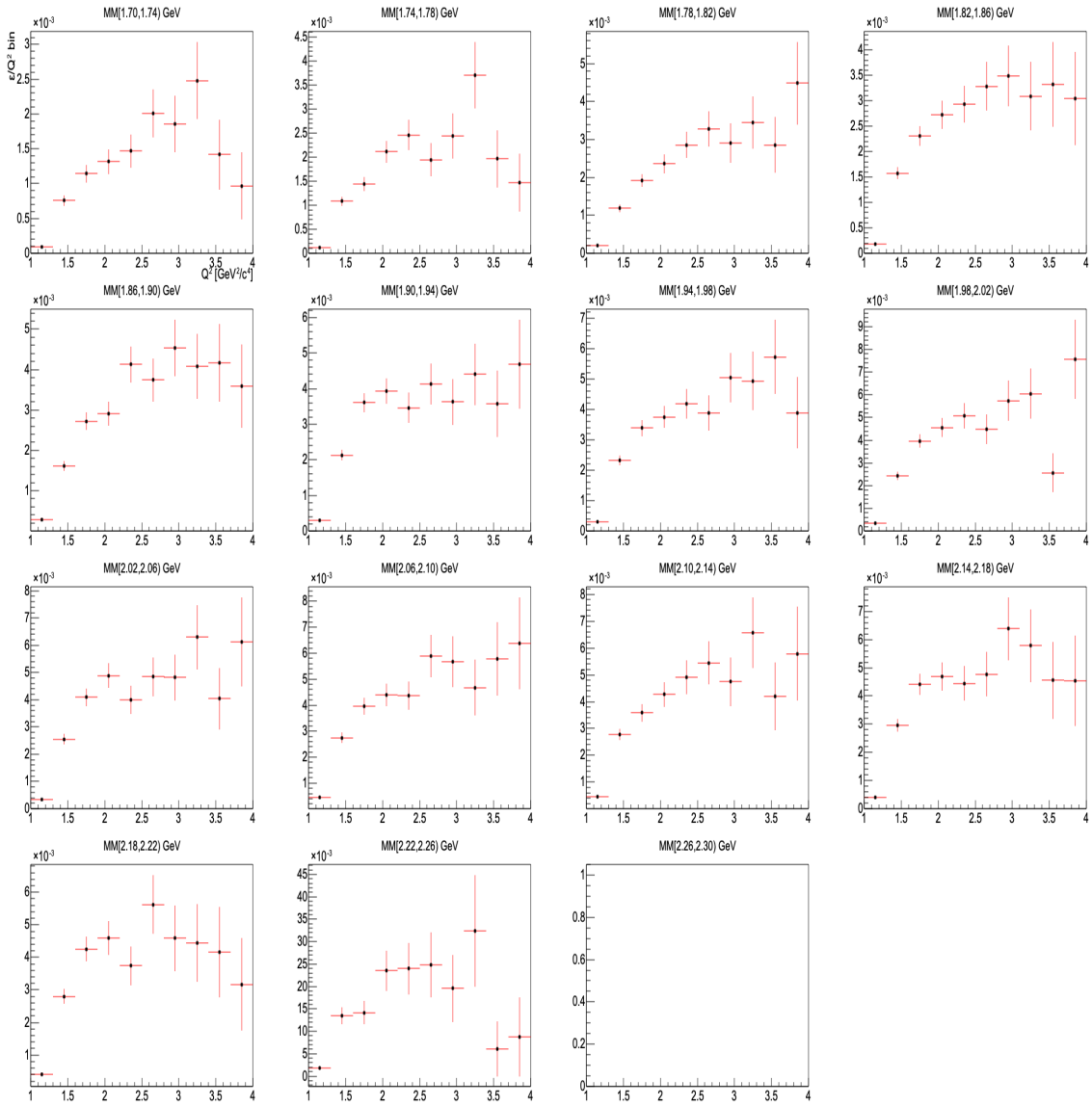

Figure 4.14: Same as Fig. 4.13 but for the RG-A Fall 2018 inbending MC simulation configuration.

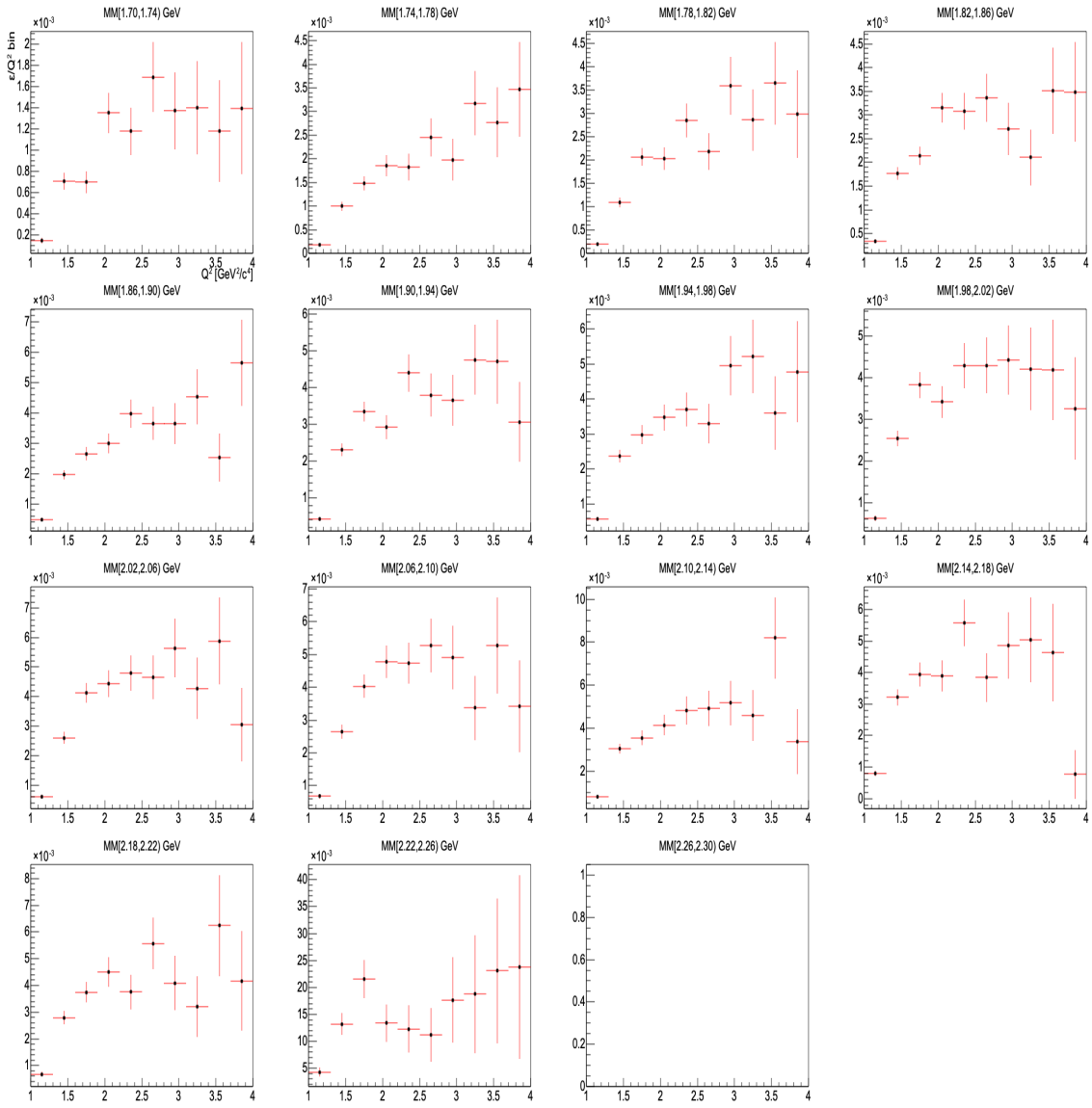

Figure 4.15: Same as Fig. 4.13 but for the RG-A Spring 2019 inbending MC simulation configuration.

4.5 Quality Control of Simulations

The event generator used in this analysis is a phase space event generator, which simply generates intermediate Cascade state in the phase space without implement-

ing any theoretical production model. The generator then decays the intermediate Cascade to the final state K^- and Λ/Σ^0 particles by conserving their four-momenta in the phase space. Therefore, it is very important to make sure that the geometrical acceptance of the detector to reconstruct the reaction of interest matches in between the MC simulation and experimental data. This can be done by comparing the final-state particle momentum and angular distributions in simulation and the experimental data. Since the final Ξ^{*-} data sample for this analysis is highly limited by statistics, an alternative approach of comparing the Q^2 distributions from data and MC was implemented rather than comparing the momentum and angular distributions of different final-state particles. Figure 4.16 shows an example of the Q^2 distribution comparison made for the Ξ^{*-} data sample and simulation result for the Fall 2018 inbending configuration when the scattered electron is detected in the FT to judge how realistic is the simulation to reproduce the data. The different histograms shown in the comparison plot are such that the total integral of each histogram is normalized to one so that the overall shapes can be compared. Similar comparisons were performed for the rest of the data sets analyzed with respective simulations and ensured that the Q^2 distribution from the simulation perfectly matches with that from the experimental data.

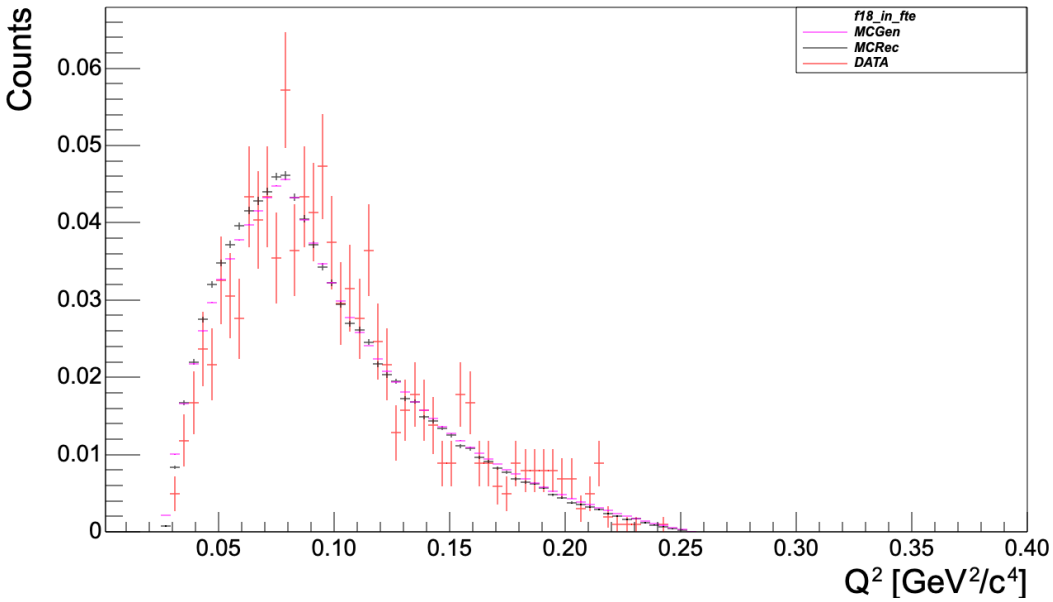

Figure 4.16: Example showing the overall shape of the Q^2 distribution comparison between MC generated (magenta) events, MC reconstructed (black) events, and the experimental Ξ^{*-} data sample (red) from the Fall 2018 inbending data set with the electron detected in the FT. The total integral of each histogram is normalized to one.

The plots that are shown in Figures 4.17 to 4.28 are the scattered electron kinematic plots (Q^2, W, Q^2 vs. W and E_γ), scatterplots (p vs. θ, p vs. ϕ, and θ vs. ϕ of the reconstructed final state e', K^+s, and K^-), and z-vertex plots from the MC simulation study for the different RG-A run period configurations. These sets of plots are helpful to understand the geometrical acceptance of the detector to reconstruct the reaction $ep \rightarrow e'K^+K^+(\Xi^{*-}) \rightarrow e'K^+K^+K^-(\Lambda/\Sigma^0)$ from the MC simulation and compare the observed acceptance of the Ξ^{*-} data sample from the experimental data. A similar set of plots from the RG-A experiments corresponding to the Ξ^{*-} data sample from the different data sets was discussed in Section 3.4.1.

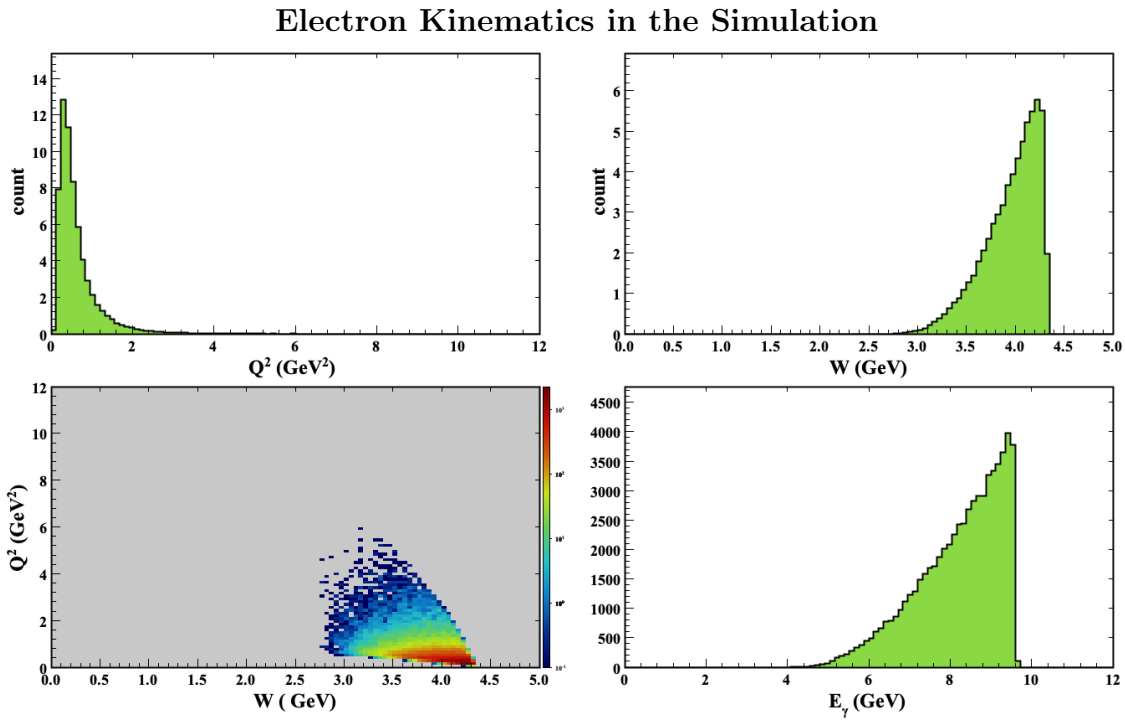

(a) Fall 2018 outbending FD-e.

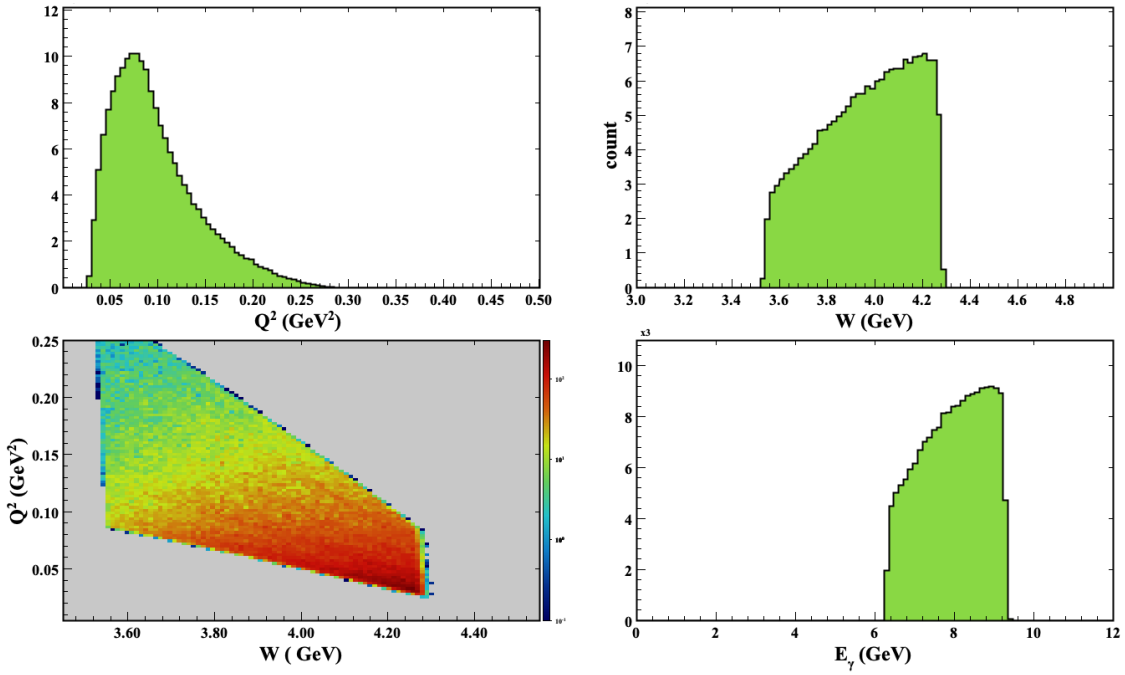

(b) Fall 2018 outbending FT-e.

Figure 4.17: The electron kinematics for the Fall 2018 outbending MC simulation configuration: Q^2 GeV^2 (upper left), W GeV (upper right), Q^2 vs. W (lower left), and virtual photon energy E_γ (GeV) (lower right). The set of plots in Fig. 4.17a (top) and 4.17b (bottom) correspond to the FT-e and FD-e, respectively.

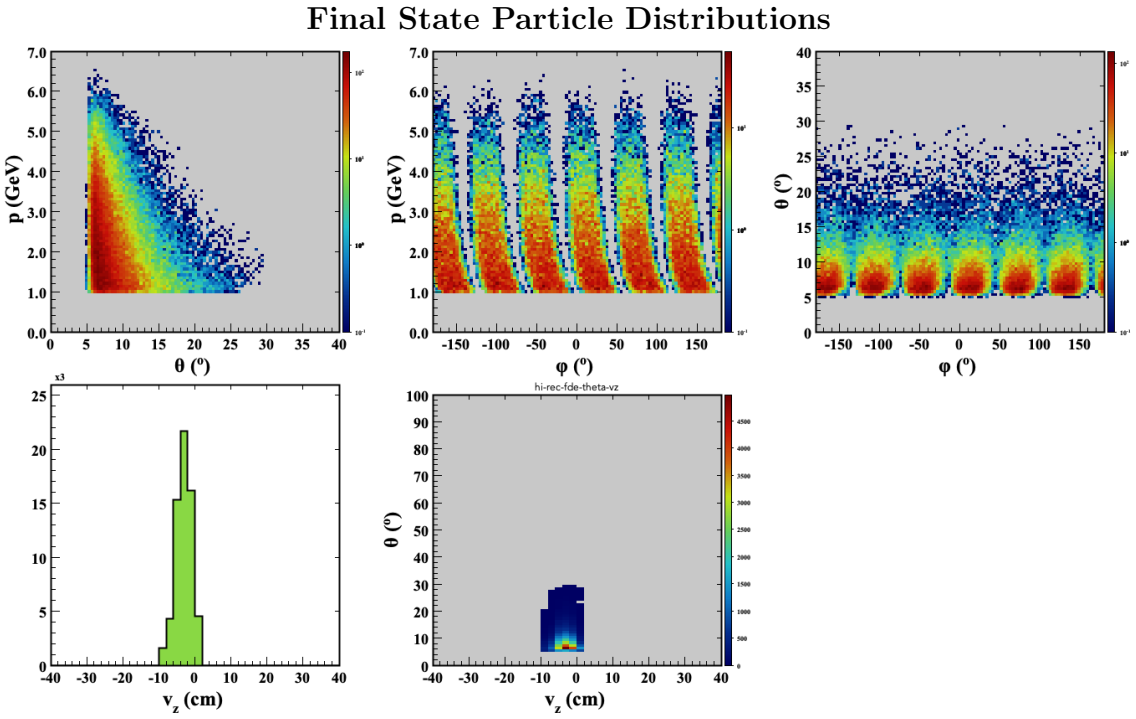

(a) FD-e (Fall 2018 outbending MC configuration).

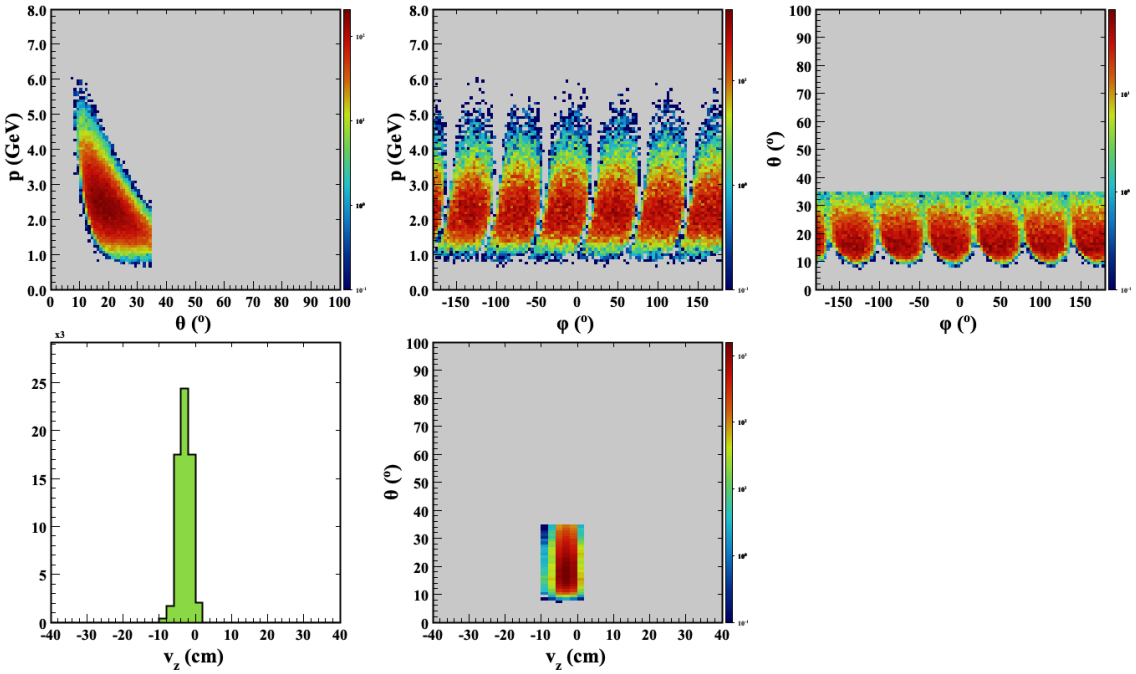

(b) Fast K^+ (Fall 2018 outbending MC configuration).

Figure 4.18: Final state FD-e (Fig. 4.18a) and fast moving K^+ (Fig. 4.18b) distributions: p (GeV) vs. θ° (upper left), p (GeV) vs. ϕ° (upper middle), θ° vs. ϕ° (upper right), v_z (cm) (lower left), and θ° vs. v_z (cm) (lower middle) for the Fall 2018 outbending MC simulation configuration when the electron is detected in the FD.

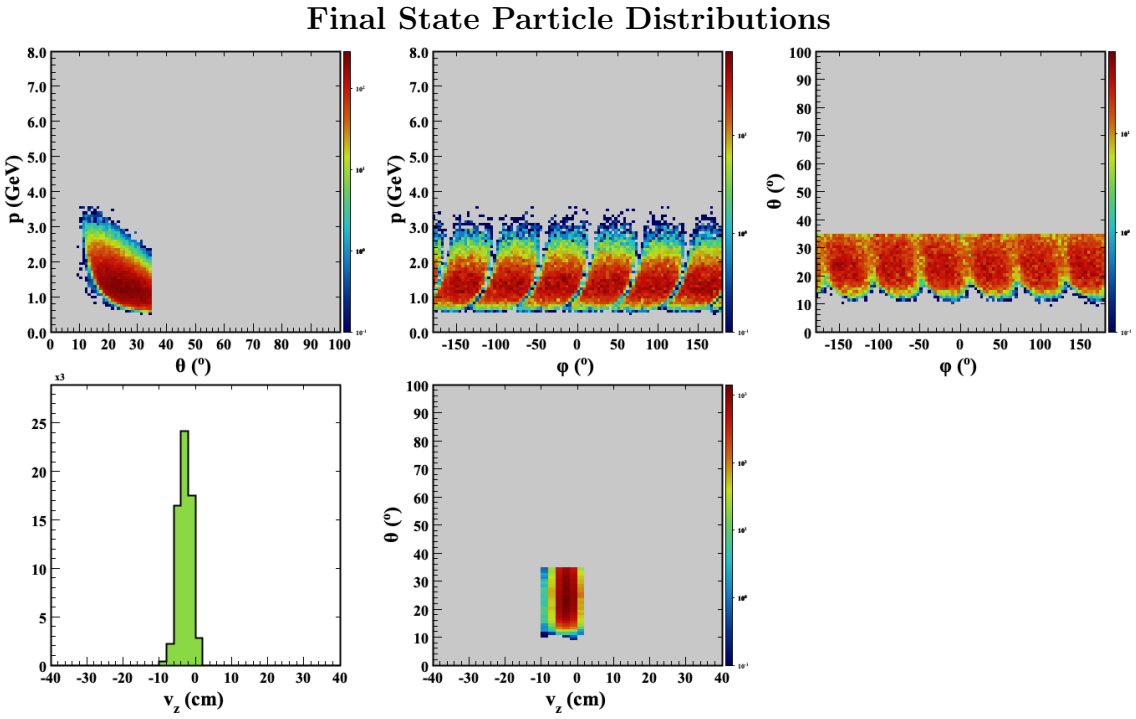

(a) Slow K^+ (Fall 2018 outbending MC configuration).

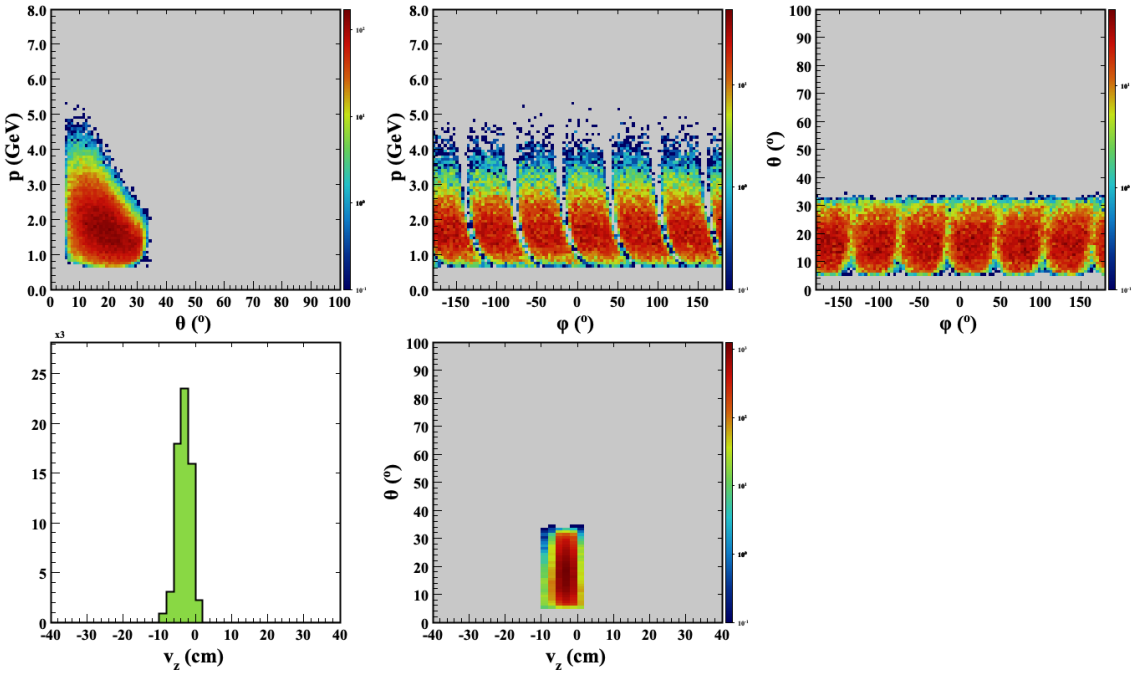

(b) K^- (Fall 2018 outbending MC configuration).

Figure 4.19: Final state slow moving K^+ (Fig. 4.19a) and K^- (Fig. 4.19b) distributions: p (GeV) vs. θ° (upper left), p (GeV) vs. ϕ° (upper middle), θ° vs. ϕ° (upper right), v_z (cm) (lower left), and θ° vs. v_z (cm) (lower middle) for the Fall 2018 outbending MC simulation configuration when the electron is detected in the FD.

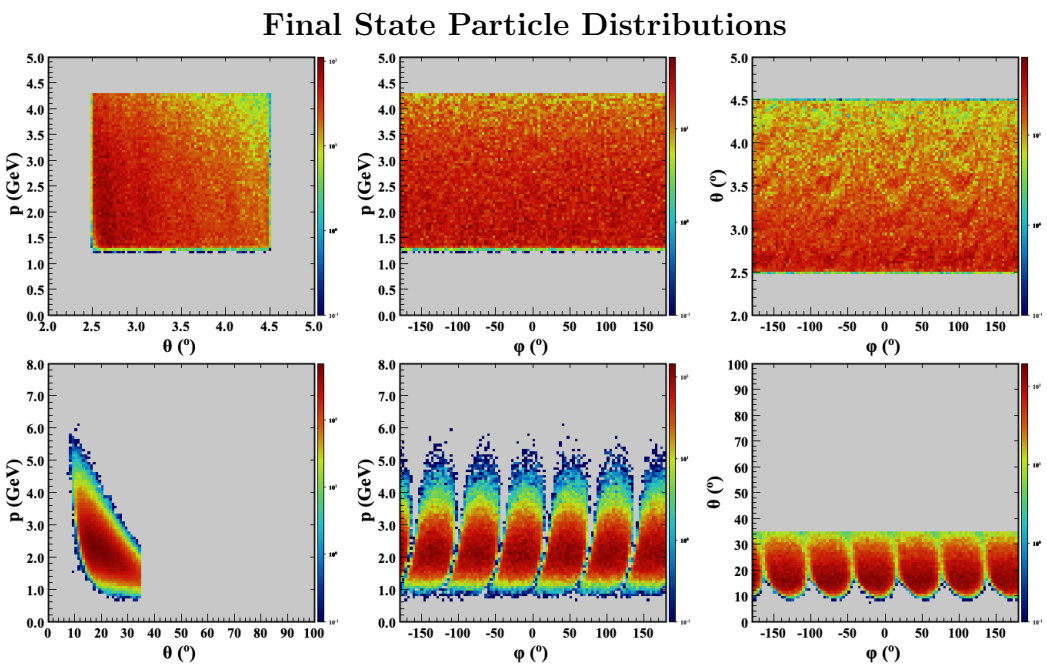

(a) FT-e (top row) and fast K^+ (bottom row) distributions (Fall 2018 out MC configuration).

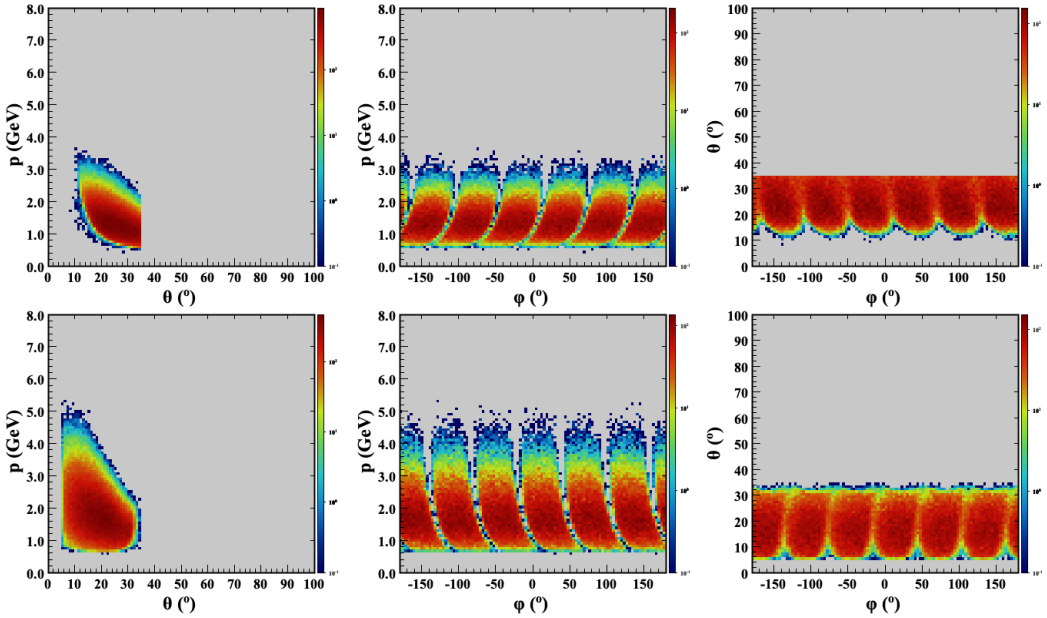

(b) Slow K^+ (top row) and K^- (bottom row) distributions (Fall 2018 out MC configuration).

Figure 4.20: Final state FT-e (top row Fig. 4.20a), fast moving K^+ (bottom row Fig. 4.20a), slow moving K^+ (top row Fig. 4.20b), and K^- (bottom row Fig. 4.20b) distributions: the set of plots in each row correspond to p (GeV) vs. θ°, p (GeV) vs. ϕ°, and θ° vs. ϕ° from left to right for the different final state particles for the Fall 2018 outbending MC simulation configuration when the electron is detected in the FT.

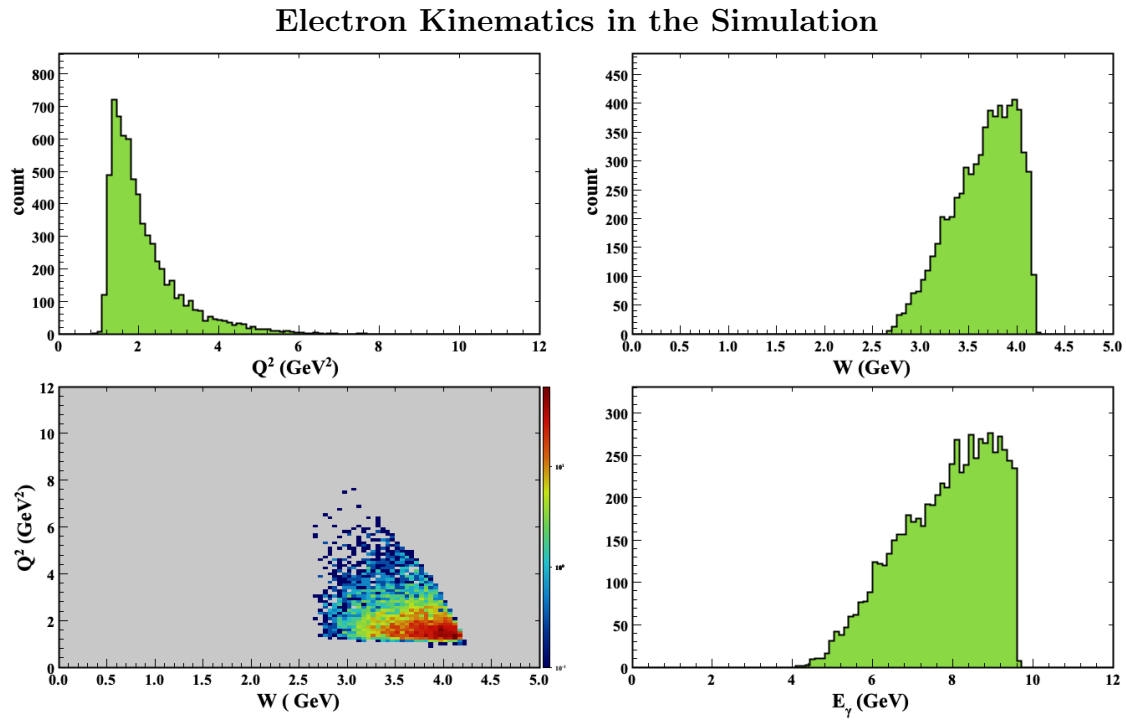

(a) Fall 2018 inbending FD-e.

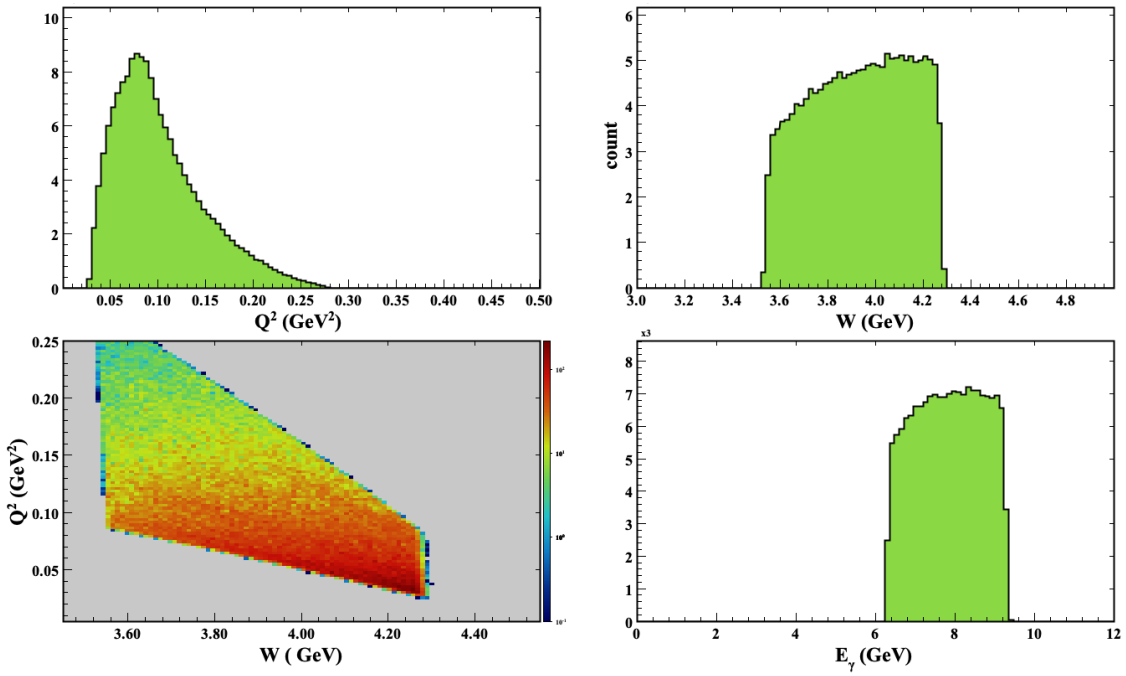

(b) Fall 2018 inbending FT-e.

Figure 4.21: Same as Fig. 4.17 but for the RG-A Fall 2018 inbending MC simulation configuration.

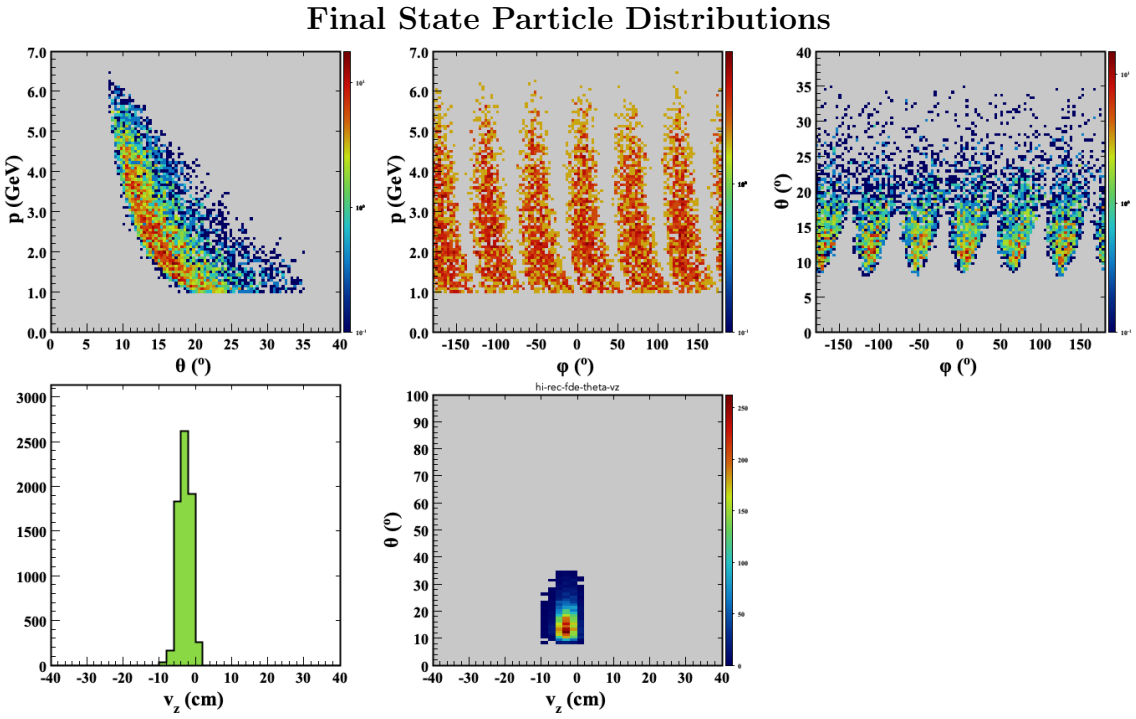

(a) FD-e (Fall 2018 inbending MC configuration).

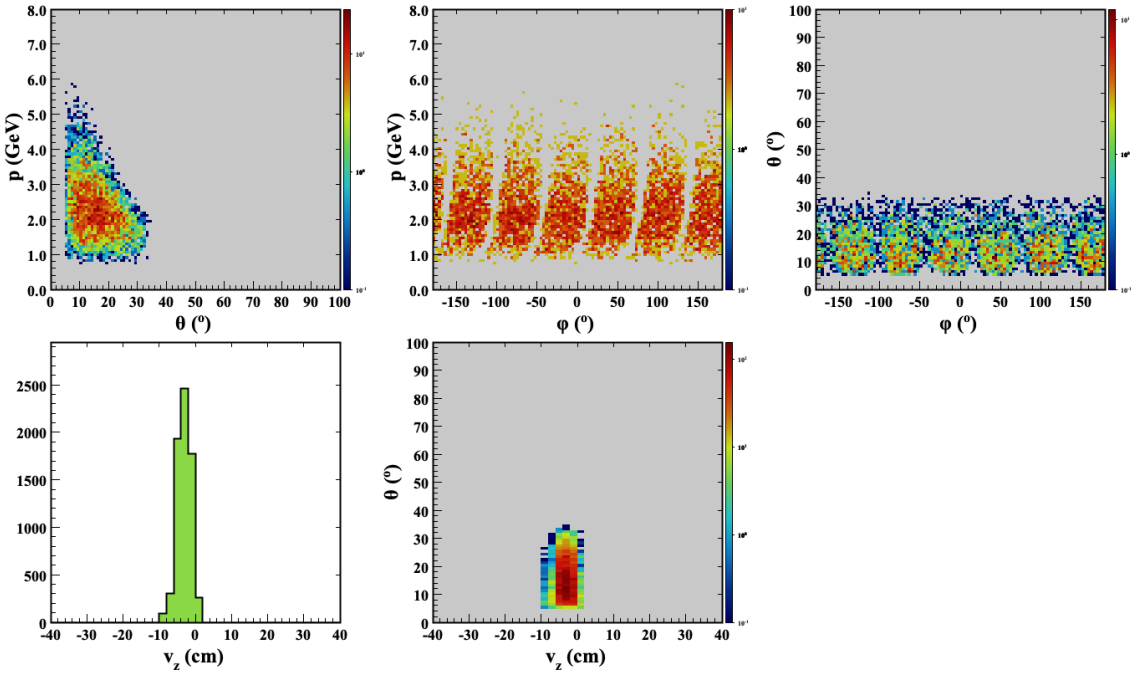

(b) Fast K^+ (Fall 2018 inbending MC configuration).

Figure 4.22: Same as Fig. 4.18 but for the RG-A Fall 2018 inbending MC simulation configuration.

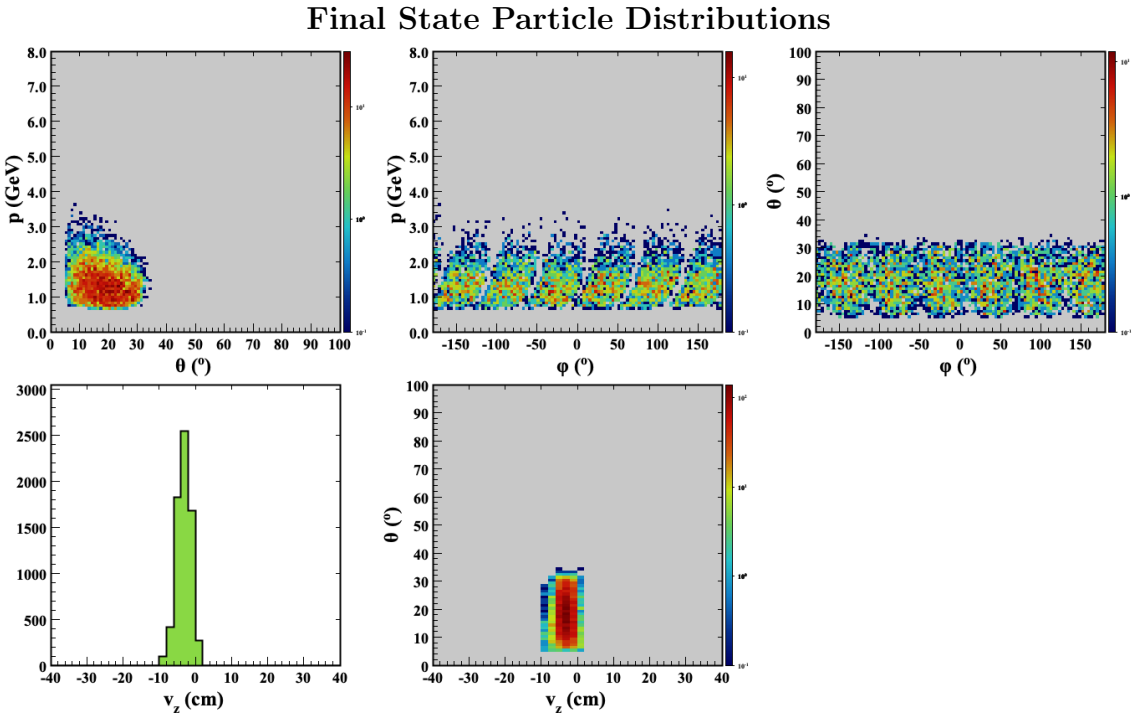

(a) Slow K^+ (Fall 2018 inbending MC configuration).

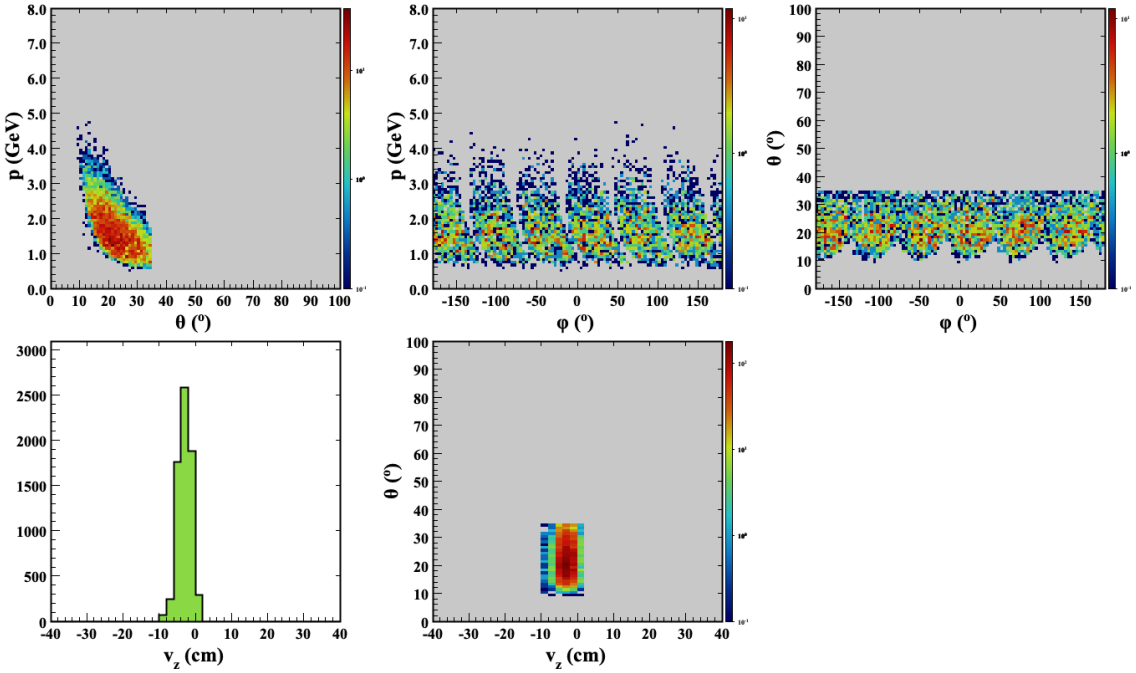

(b) K^- (Fall 2018 inbending MC configuration).

Figure 4.23: Same as Fig. 4.19 but for the RG-A Fall 2018 inbending MC simulation configuration.

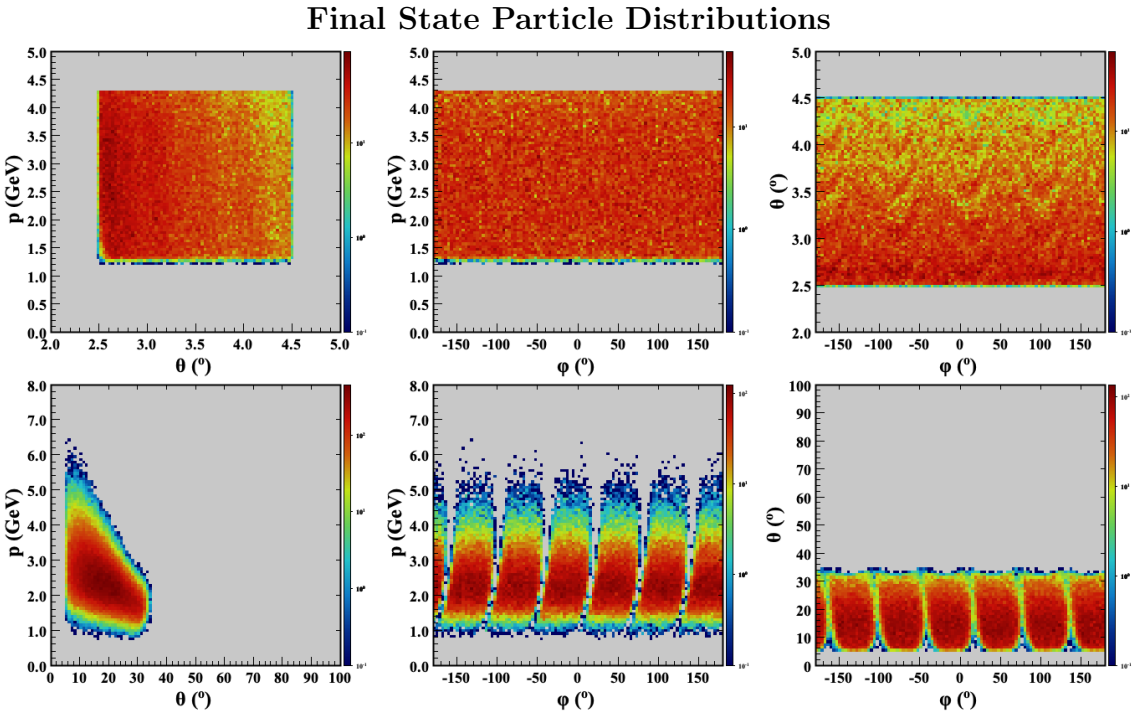

(a) FT-e (top row) and fast K^+ (bottom row) distributions (Fall 2018 inbending MC configuration).

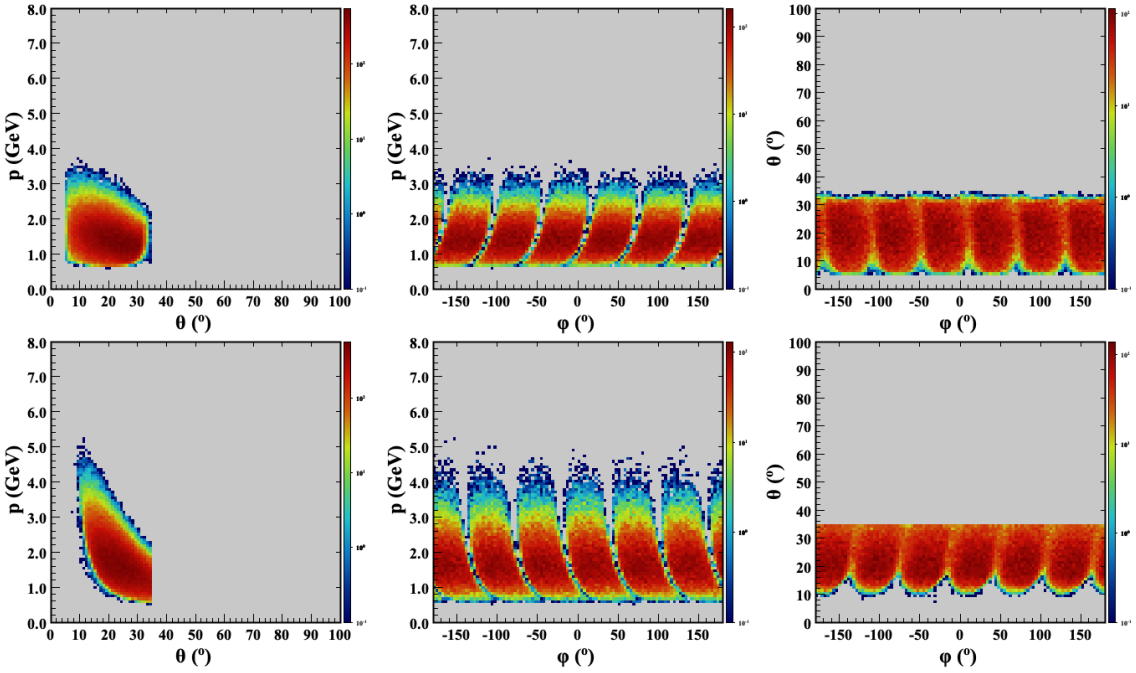

(b) Slow K^+ (top row) and K^- (bottom row) distributions (Fall 2018 inbending MC configuration).

Figure 4.24: Same as Fig. 4.20 but for the RG-A Fall 2018 inbending MC simulation configuration.

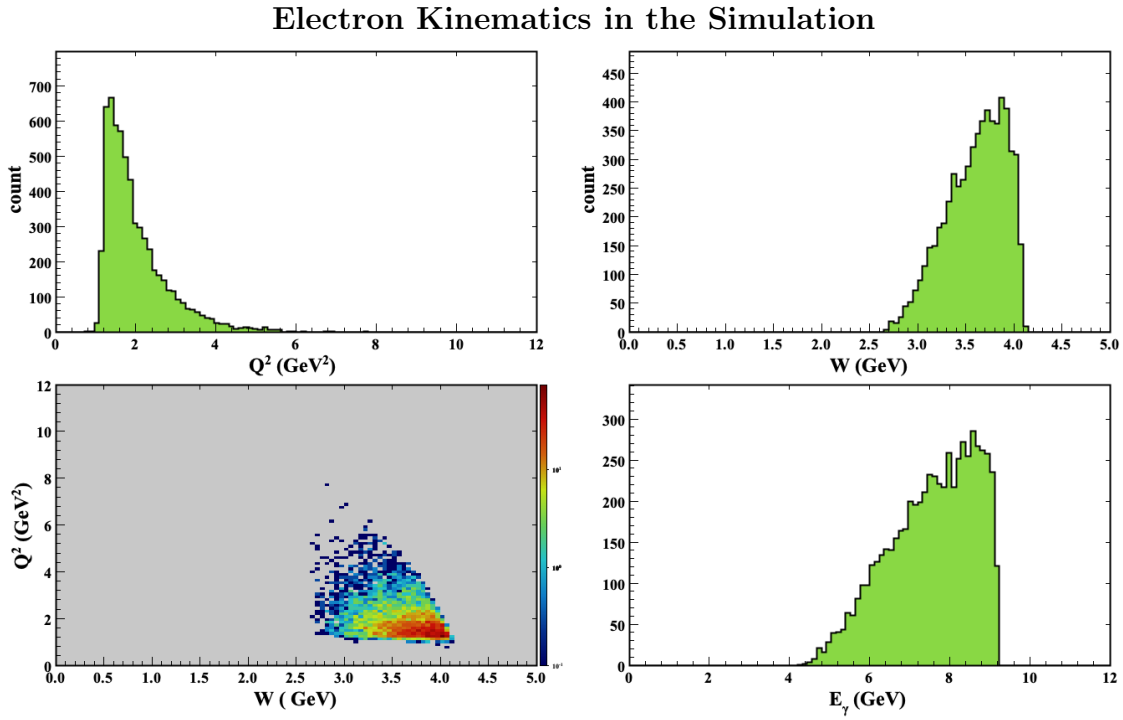

(a) Spring 2019 inbending FD-e.

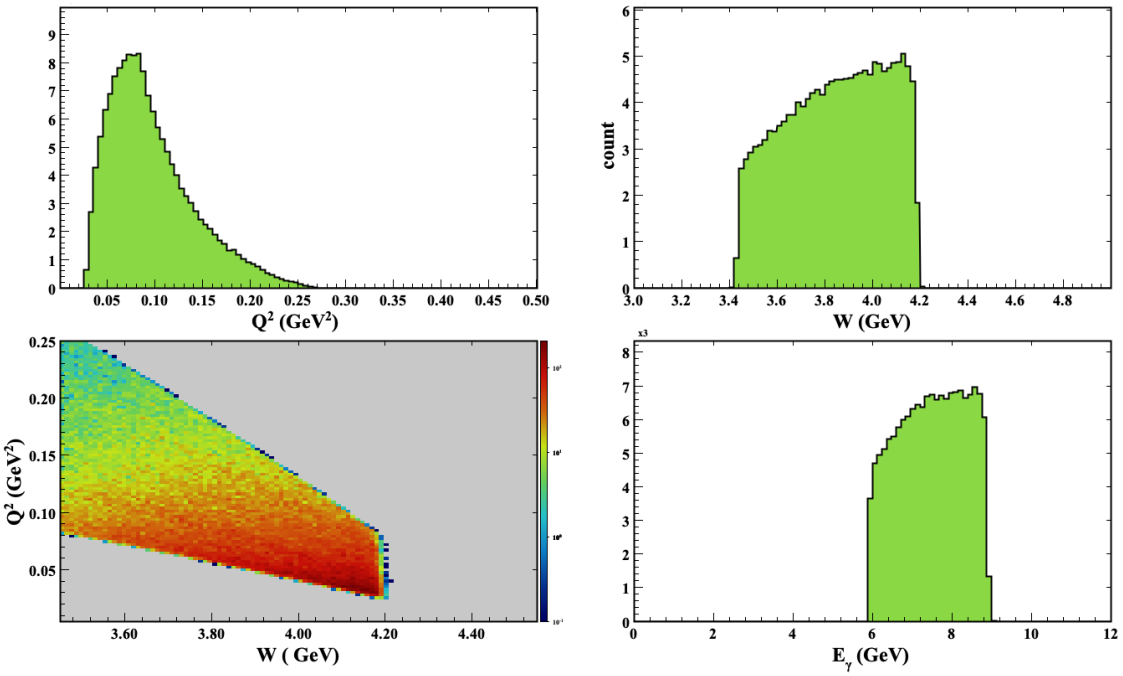

(b) Spring 2019 inbending FT-e.

Figure 4.25: Same as Fig. 4.17 but for the RG-A Spring 2019 inbending MC simulation configuration.

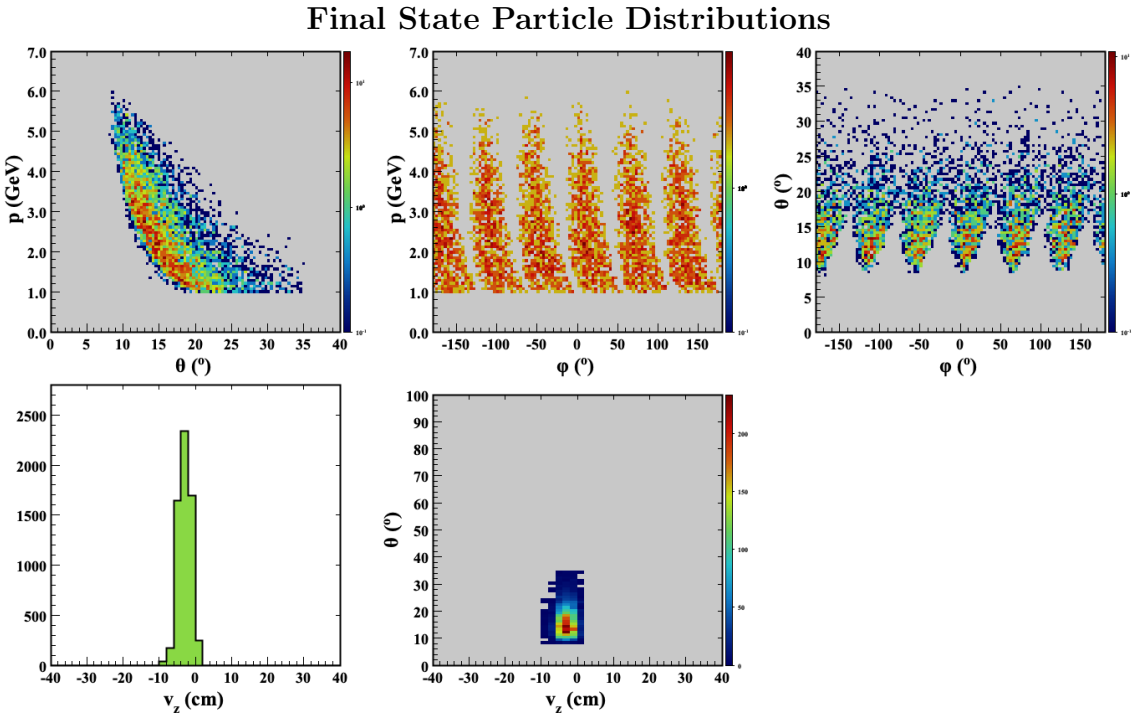

(a) FD-e (Spring 2019 inbending MC configuration).

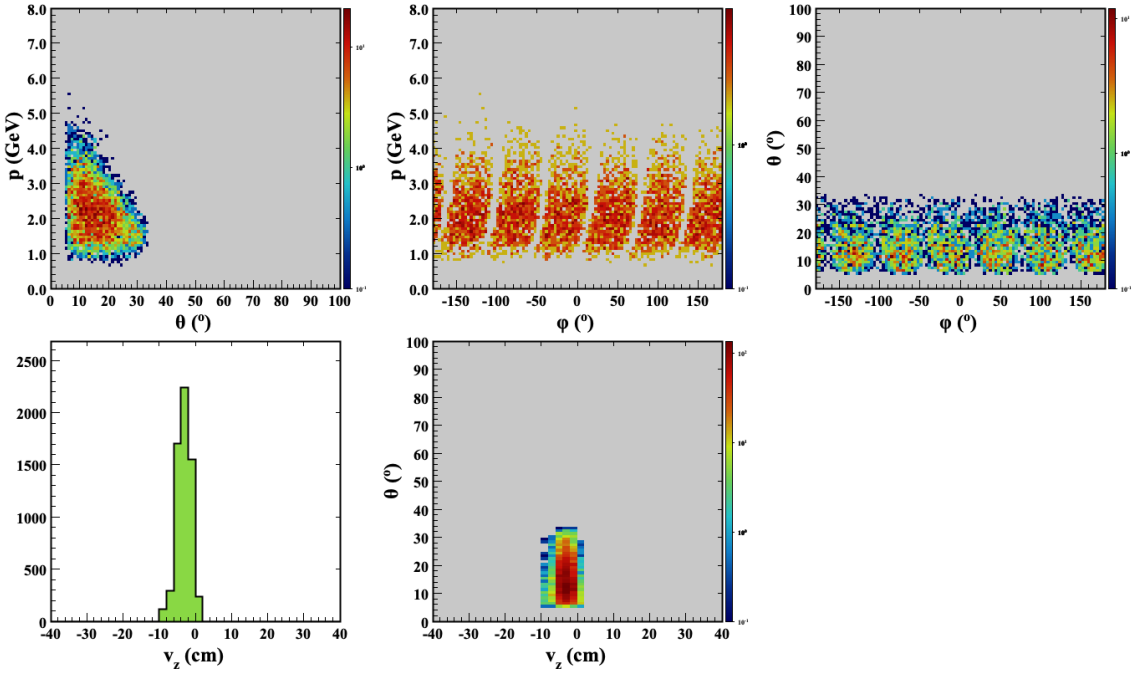

(b) Fast K^+ (Spring 2019 inbending MC configuration).

Figure 4.26: Same as Fig. 4.18 but for the RG-A Spring 2019 inbending MC simulation configuration.

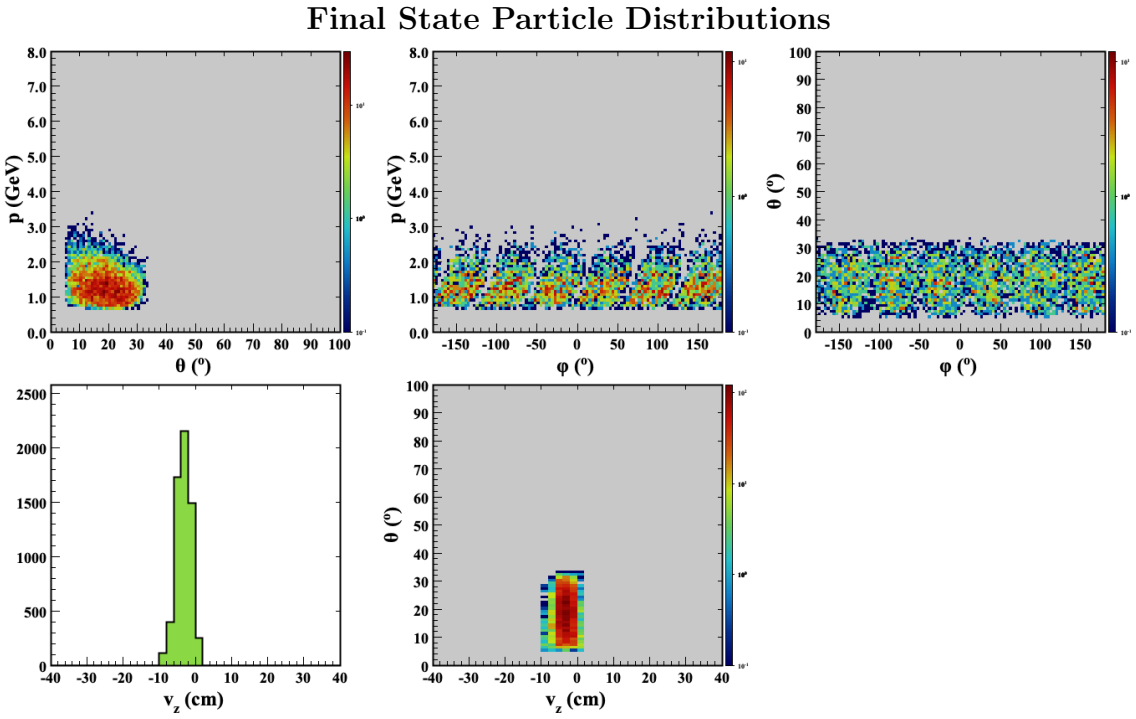

(a) Slow K^+ (Spring 2019 inbending MC configuration).

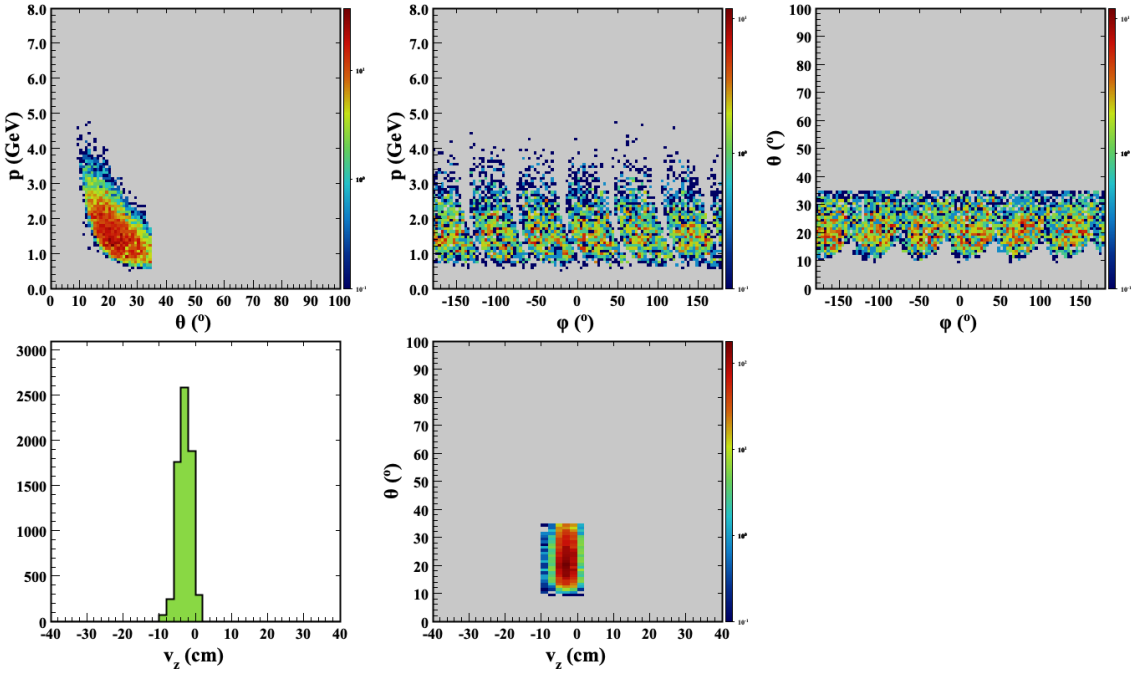

(b) K^- (Spring 2019 inbending MC configuration).

Figure 4.27: Same as Fig. 4.23 but for the RG-A Spring 2019 inbending MC simulation configuration.

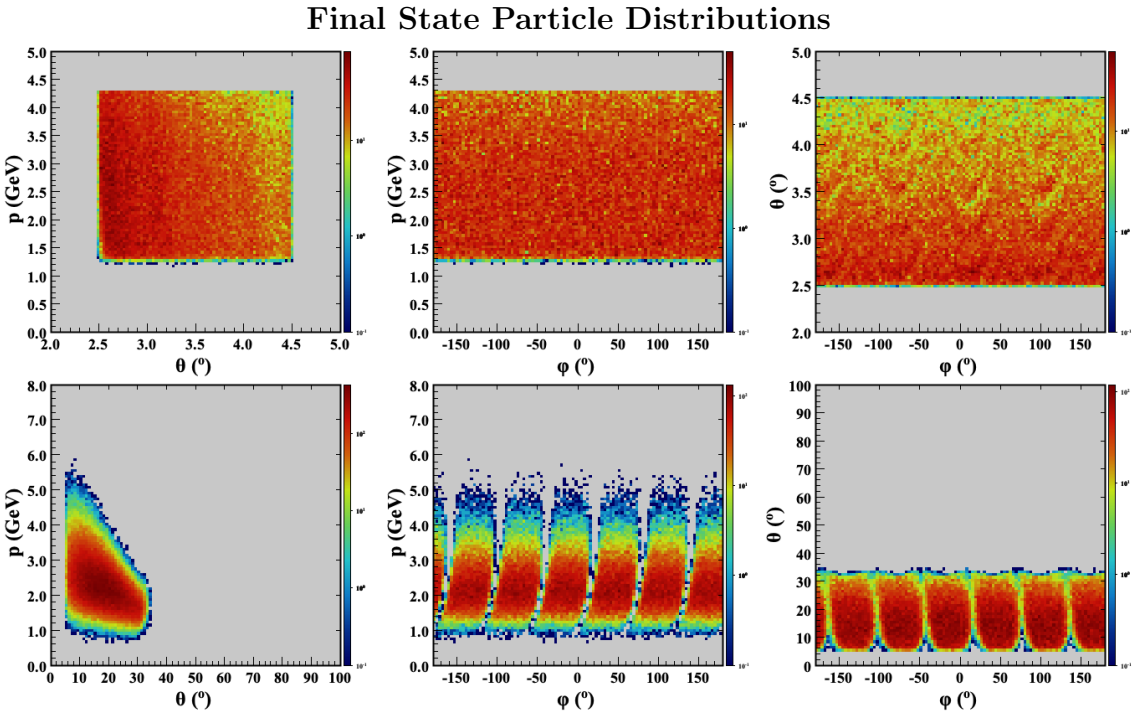

(a) FT-e (top row) and fast K^+ (bottom row) distributions (Spring 2019 inbending MC configuration).

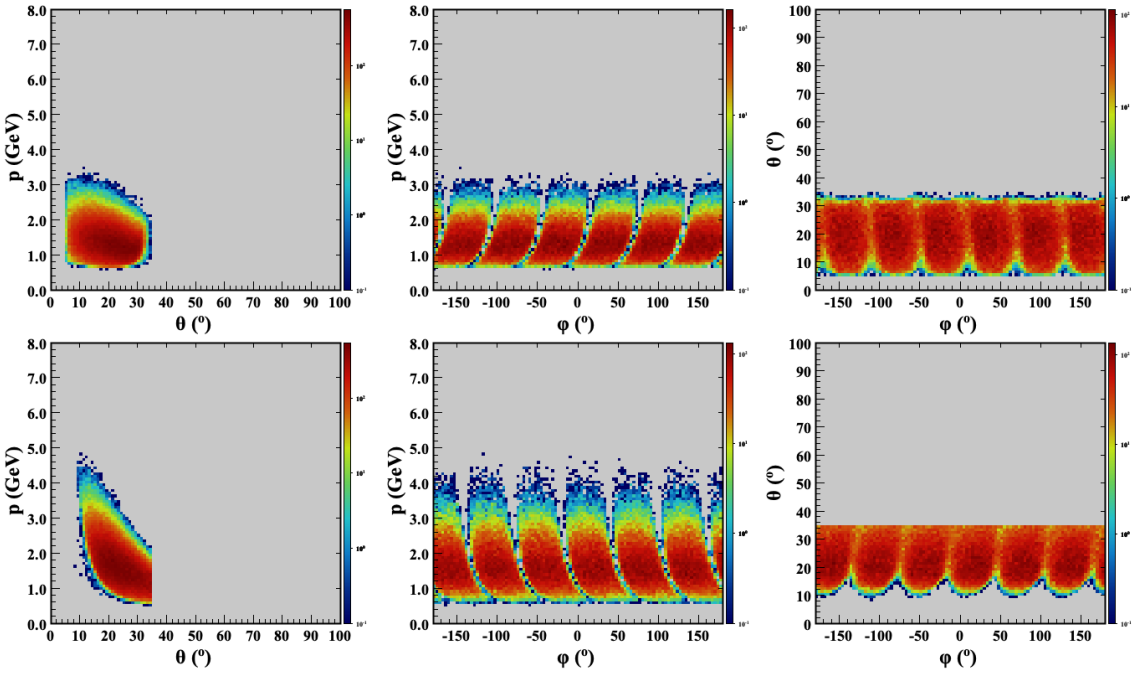

(b) Slow K^+ (top row) and K^- (bottom row) distributions (Spring 2019 inbending MC configuration).

Figure 4.28: Same as Fig. 4.20 but for the RG-A Spring 2019 inbending MC simulation configuration.

CHAPTER 5

Electroproduction Cross Section

5.1 Upper Limit Estimate on $\Xi^{*-}(1820)$ Electroproduction

For the same $K^-(\Lambda/\Sigma^0)$ decay mode, several Ξ^{*-} states were expected to be seen in the analysis of exclusive reaction $ep \to e'K^+K^+K^-(\Lambda/\Sigma^0)$ that were previously claimed in other experiments with non-zero branching ratios as documented in the PDG and summarized in Table 5.1. However, the missing mass spectrum off of $e'K^+K^+$ for Λ/Σ^0 events observed and reconstructed from the missing mass off of $e'K^+K^+K^-$ exhibits no evidence of any statistically significant Ξ^{*-} resonance. Establishing an upper limit electroproduction cross section of Ξ^{*-} states is one of the intriguing studies one may pursue in such a situation using the currently available statistics from the pass-1 RG-A data within the CLAS12 Forward Detector acceptance. Hence, in this work it was decided to establish an upper limit on the $\Xi^{*-}(1820)$ production cross section by determining the experimental mass resolution of the $\Xi^{*-}(1820)$ state, background shape, and the CLAS12 detection efficiency for the reaction of interest.

The experimental mass resolution of the $\Xi^{*-}(1820)$ state in the missing mass spectrum is inferred from the MC simulation discussed in Section 4.2. The problem with the current simulation is that it does not reproduce the data. So, the momentum of the detected particles in the simulation was smeared. The missing mass resolution changes by changing the momentum smearing factor. The observed experimental resolution of the ground state $\Xi(1320)$ in the data was used to derive the appropriate momentum smearing factor to achieve the best match between the data and simulation. With that done, the same smearing factor was used for the excited

Previously Seen Ξ^{*-} States from PDG With $K^-(\Lambda/\Sigma^0)$ Decay Mode

State	$K^-\Lambda$	$K^-\Sigma^0$
$\Xi^{*-}(1690)$	$***$ (seen)	$**$ (seen)
$\Xi^{*-}(1820)$	$***$ (large)	$**$ (small)
$\Xi^{*-}(1950)$	$**$ (seen)	N/A
$\Xi^{*-}(2030)$	$**$	$***$
$\Xi^{*-}(2120)$	$*$ (seen)	N/A
$\Xi^{*-}(2500)$	$*$	$*$

Table 5.1: Experimentally seen Ξ^{*-} states that decay to $K^-\Lambda$ or $K^-\Sigma^0$ with their non-zero branching ratios in terms of the PDG ratings. The data summarized here were taken from the 2022 edition of the review of PDG [81].

$\Xi^{*-}(1820)$ Signal Window Selection on the $MM(e'K^+K^+K^-)$

Data set	Excluded $\Xi^{*-}(1820)$ mass window to fix Bg. shape
Fall 2018 outbending FT-e	$[1.74, 1.90]$ GeV $\approx 3\sigma^{FT}_{\Xi^{*-}(1820)}$
Fall 2018 inbending FT-e	$[1.74, 1.90]$ GeV $\approx 3\sigma^{FT}_{\Xi^{*-}(1820)}$
Spring 2019 inbending FT-e	$[1.74, 1.90]$ GeV $\approx 3\sigma^{FT}_{\Xi^{*-}(1820)}$
Fall 2018 outbending FD-e	$[1.74, 1.86]$ GeV $\approx 2.5\sigma^{FD}_{\Xi^{*-}(1820)}$
Fall 2018 inbending FD-e	$[1.74, 1.86]$ GeV $\approx 2.5\sigma^{FD}_{\Xi^{*-}(1820)}$
Spring 2019 inbending FD-e	$[1.74, 1.86]$ GeV $\approx 2.5\sigma^{FD}_{\Xi^{*-}(1820)}$

Table 5.2: Summary table showing the $\approx 3\sigma$ $\Xi^{*-}(1820)$ signal range in the missing mass distribution around the nominal mass value (1.823 GeV) of the $\Xi^{*-}(1820)$. The corresponding signal mass range was excluded while fitting the data to determine the polynomial background shape.

state simulation to calculate the experimental mass resolution of the $\Xi^{*-}(1820)$ state in the $MM(e'K^+K^+)$ distribution for the $e'K^+K^+K^-$ system even though the momentum smearing factor was derived from the ground state Cascade. The results obtained for the experimental mass resolution of the $\Xi^{*-}(1820)$ state are 46.96 MeV and 55.22 MeV for scattered electrons detected in the FD and in the FT, respectively, as summarized in Table 4.2.

An excess of $\Xi^{*-}(1820)$ signal events was assumed in the missing mass spectrum hidden under a smooth background. The excess was estimated by fitting the missing mass distribution with a Gaussian function to represent a possible $\Xi^{*-}(1820)$ resonance plus a fixed-shape scaled background function to represent the background. The shape of the background function used in the fit was determined by multiple approaches.

In the first approach, the whole spectrum was fit by excluding the signal region. The signal region to exclude in the fit was determined by looking into the experimental mass resolution of the $\Xi^{*-}(1820)$ state. A mass window of $\approx \pm 3\sigma$ width was selected around the $\Xi^{*-}(1820)$ nominal mass value as shown in Fig. 5.1 as the signal region to exclude in the fit. Table 5.2 summarizes the excluded mass window range in the missing mass distribution to determine the background shape for the different data sets analyzed. Figure 5.2 shows an example of a third-order polynomial background fit to the missing mass distribution with the resulting fit parameters shown in the plot. The two plots correspond to the RG-A Fall 2018 outbending data set after excluding the $\Xi^{*-}(1820)$ mass window when a scattered electron is detected in the FD or in the FT. One major problem with implementing this technique is that the background function has a sizable uncertainty due to the poor statistics.

$\Xi^{*-}(1820)$ **Mass Window**

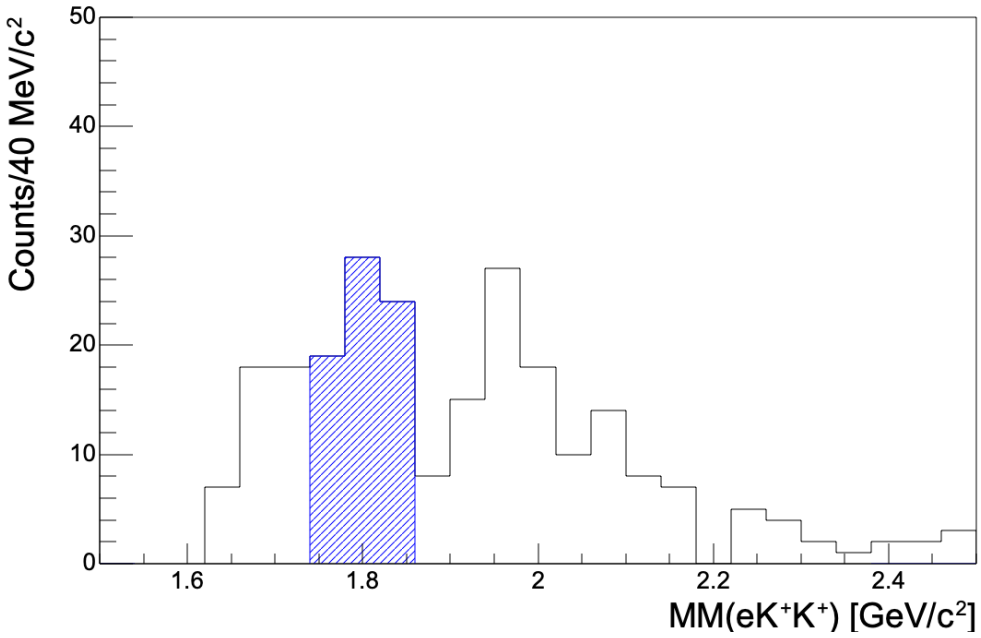

(a) Scattered electron detected in the FD.

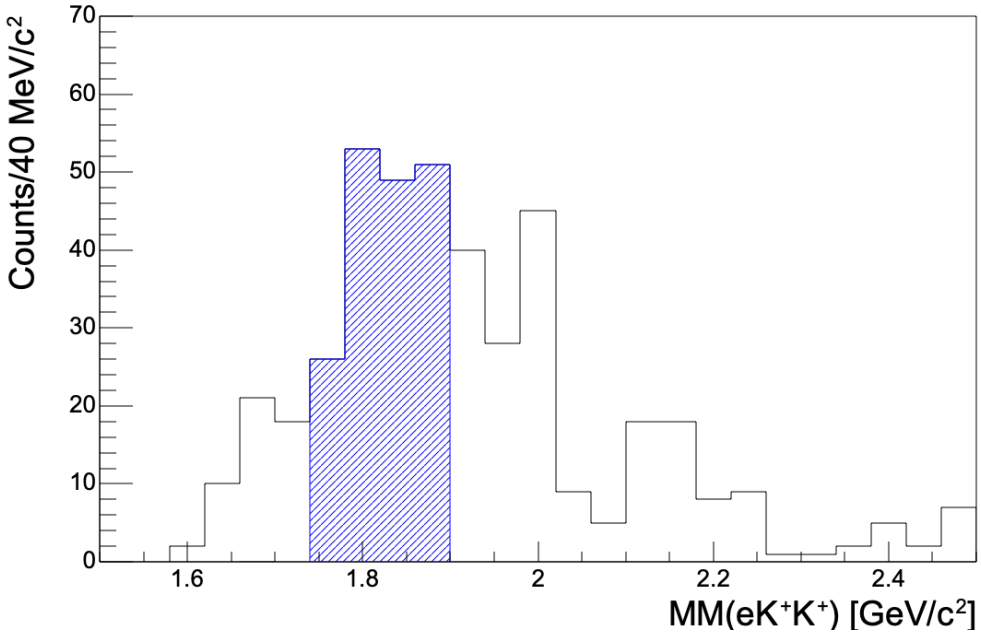

(b) Scattered electron detected in the FT.

Figure 5.1: Example plot showing the $\Xi^{*-}(1820)$ mass window in the sideband events subtracted $MM(e'K^+K^+)$ distribution from Fig. 3.29 and Fig. 3.32 for the RG-A Fall 2018 outbending data set with the scattered electron detected in the FD (top) or in the FT (bottom), respectively.

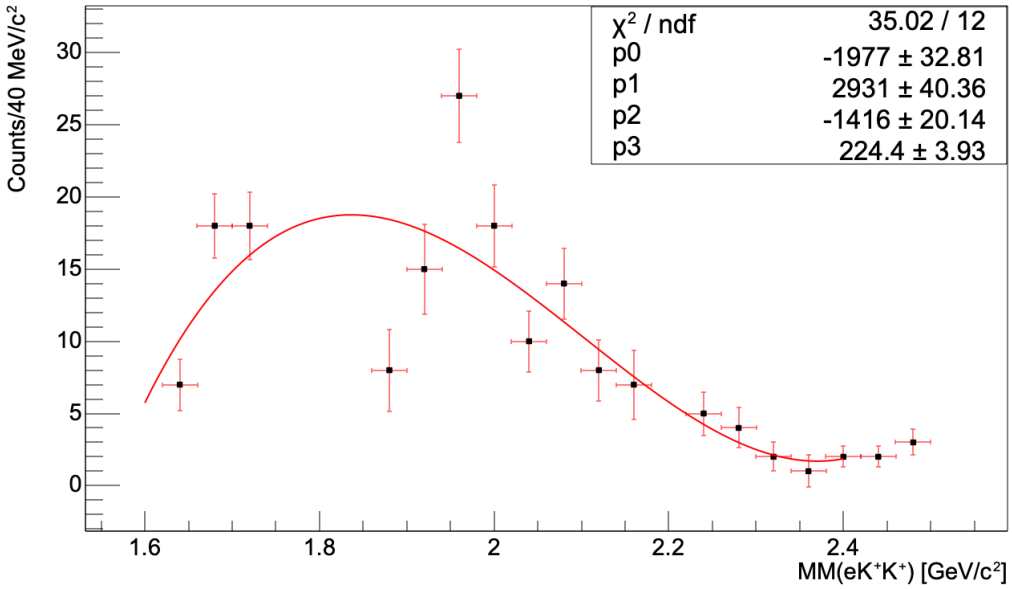

(a) Scattered electron detected in the FD.

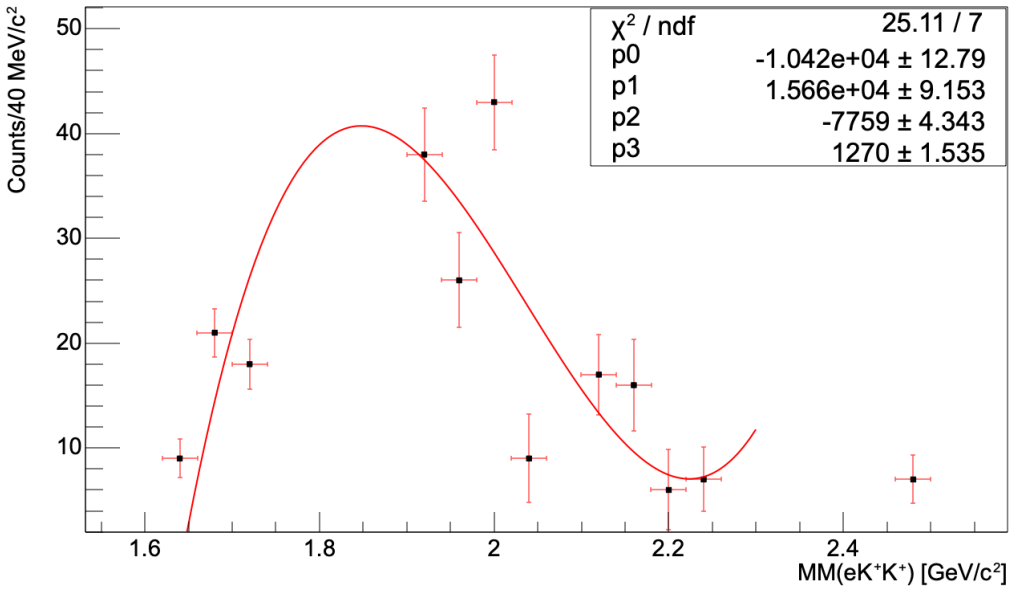

(b) Scattered electron detected in the FT.

Figure 5.2: Example plot showing the background shape from the fit and corresponding parameters determined by fitting the missing mass distribution excluding the $\Xi(1820)$ mass window shown in Fig. 5.1 for the RG-A Fall 2018 outbending data set with scattered electrons detected in the FD (top) or in the FT (bottom), respectively.

The second approach implemented to determine the background is the event mixing technique, which mixes particles from different events to form a background spectrum. In this analysis, a spectrum to define a background shape was obtained by mixing three kaons (K^+, K^+, and K^-) from different events over the $e'K^+K^+K^-$ data sample and by constraining the same missing mass selection cuts to select the Λ/Σ^0 region as summarized in Table 3.5. The kaons chosen were limited to the FD to determine the background spectrum. Mixing kaons from different events that satisfy Λ/Σ^0 selection ensures that the possible background coming predominantly from misidentified pions as kaons in the data sample is also included in the resulting background spectrum. The event mixing strategy was appealing since it allowed for the formation of a high-statistics background spectrum. Another major advantage of implementing this technique was that the analysis technique does not have to exclude the $\Xi^{*-}(1820)$ signal region to determine the background shape as implemented in the previous technique. In contrast, the event mixing technique allows the analysis to employ the complete spectrum resulting from mixing kaons from the Λ/Σ^0 region, which is the $\Xi^{*-}(1820)$ signal region. In practice, the event mixing technique provided a smooth background shape with very small error bars. Figures 5.3 and 5.4 shows the different missing mass spectra used to determine the background shape by implementing the event mixing technique using the Fall 2018 outbending data set.

Figures 5.5 to 5.7 represents the normalized background shape (blue) in the $MM(e'K^+K^+)$ distribution derived using the event mixing technique along with other background spectra resulting from other techniques for comparison for the different data sets. The background shape from the event mixing technique was normalized in such a way that the total number of background events within the Λ/Σ^0 mass region derived by integrating the background fit function from $\mu_\Lambda - 3*\sigma_\Lambda$ to $\mu_{\Sigma^0} + 3*\sigma_\Lambda$ was equivalent to the total events in the background spectrum obtained from the event

mixing technique. Comparison of the background shape from the event mixing technique and the Λ/Σ^0 signal shape determined by fit weighting of the $MM(e'K^+K^+K^-)$ spectra for the different data sets is shown in Figs. 5.8 to 5.10.

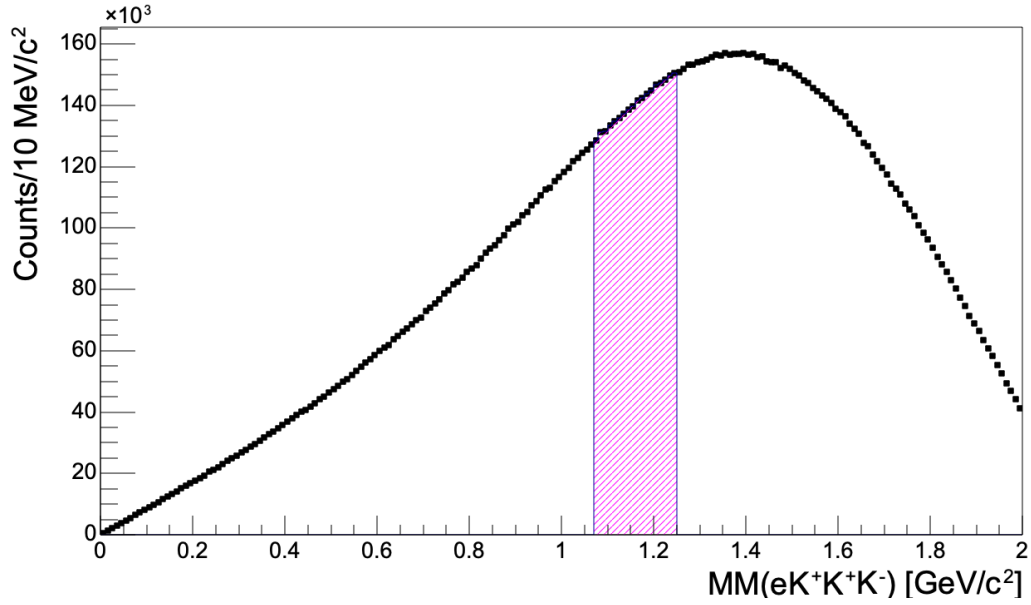

(a) $MM(e'K^+K^+K^-)$ distribution by mixing kaons from different events over the $e'K^+K^+K^-$ data sample.

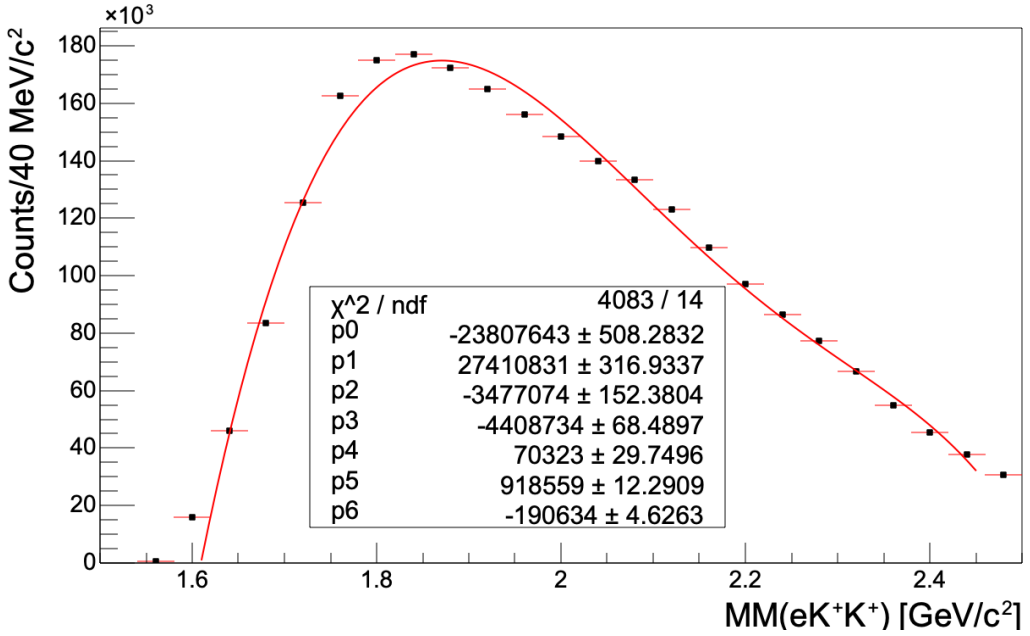

(b) BG. template for the $MM(e'K^+K^+)$ distribution using mixed events that fall in the shaded region in (a).

Figure 5.3: Missing mass distributions used to determine the background shape from the event mixing technique. Plots correspond to the Fall 2018 outbending data set with the FD-e.

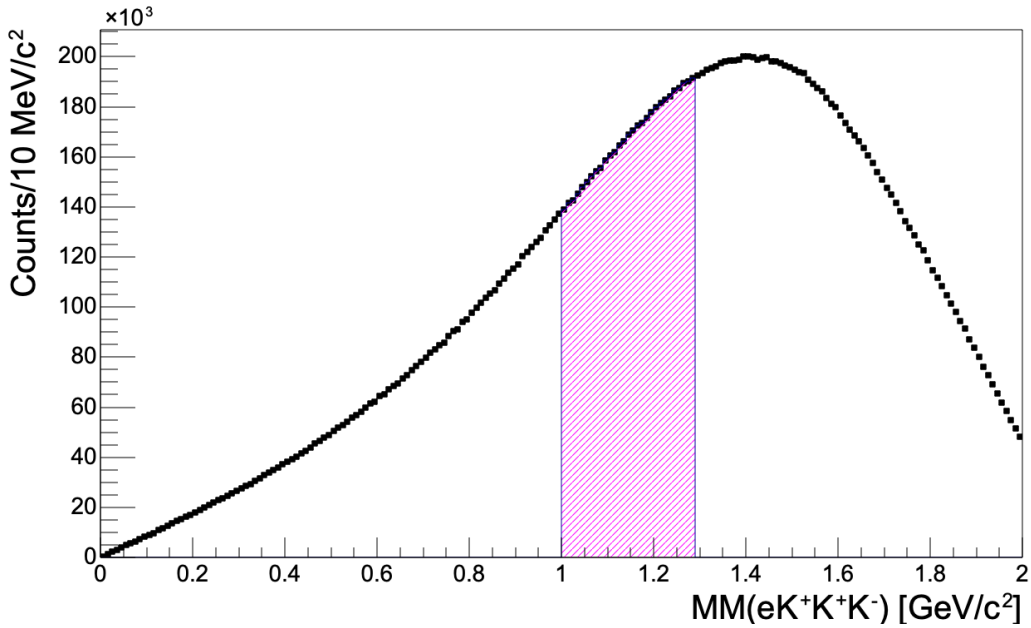

(a) $MM(e'K^+K^+K^-)$ distribution by mixing kaons from different events over the $e'K^+K^+K^-$ data sample.

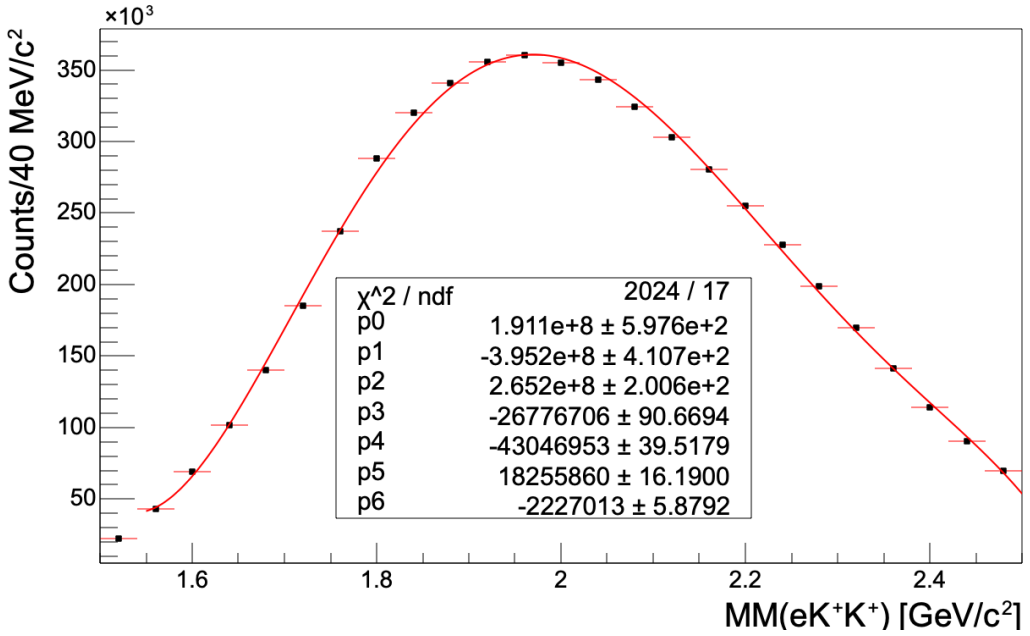

(b) BG. template for the $MM(e'K^+K^+)$ distribution using mixed events that fall in the shaded region in (a).

Figure 5.4: Missing mass distributions used to determine the background shape from the event mixing technique. Plots correspond to the Fall 2018 outbending data set with the FT-e.

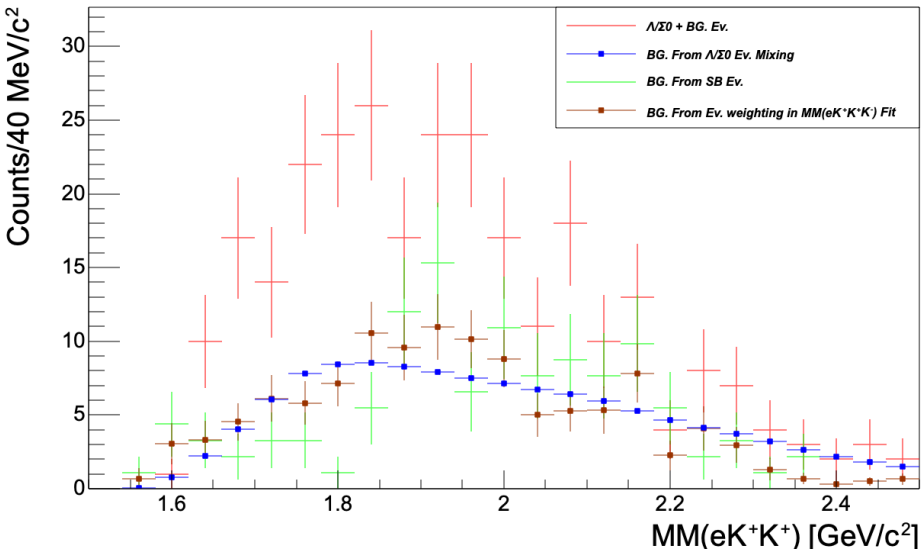

(a) Scattered electrons detected in the FD.

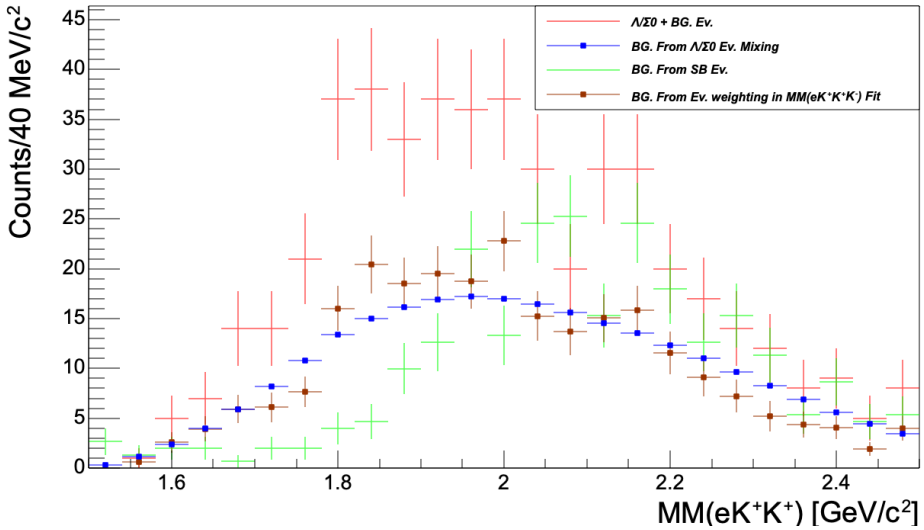

(b) Scattered electrons detected in the FT.

Figure 5.5: Comparison of the background shape in the $MM(e'K^+K^+)$ spectra (red) for the Λ/Σ^0 events selected with cuts specified in Table 3.5 in $MM(e'K^+K^+K^-)$ spectra for the Fall 2018 outbending data set. The blue, green, and brown histograms correspond to the normalized background distributions derived from the event mixing technique, the side band events, and the fit weighting technique.

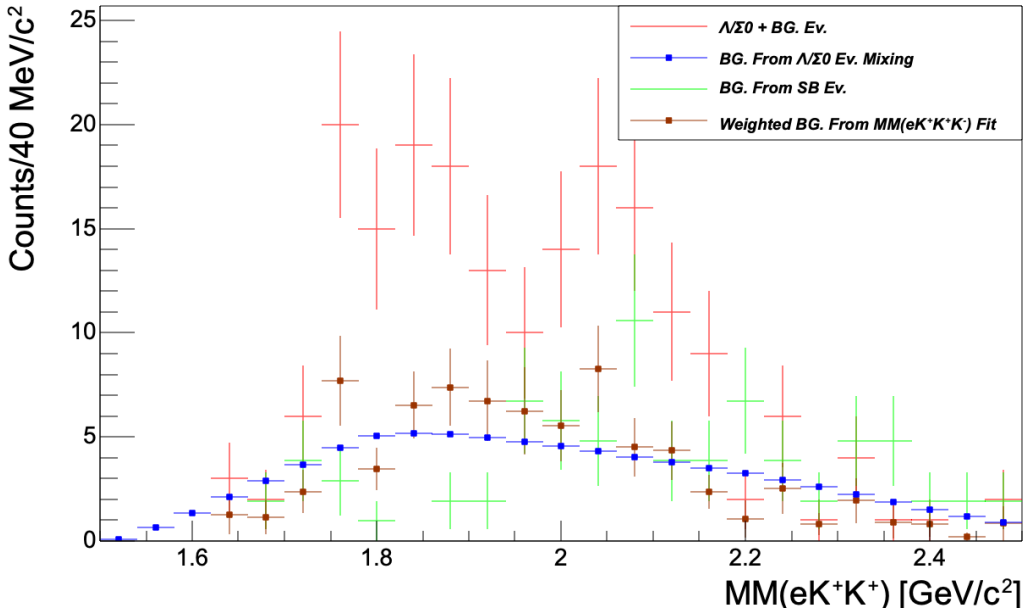

(a) Scattered electron detected in the FD.

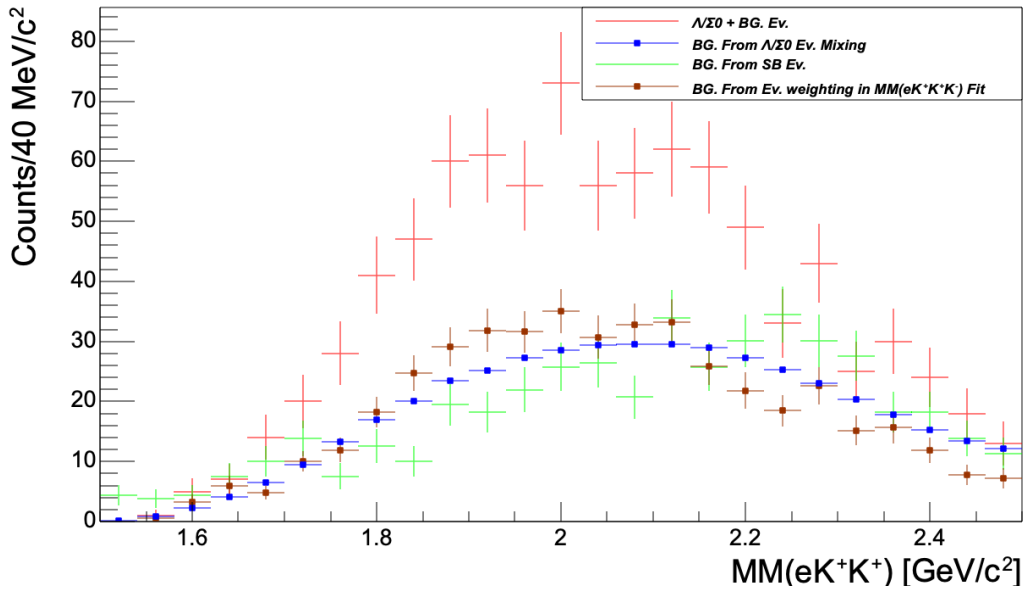

(b) Scattered electron detected in the FT.

Figure 5.6: Same as Fig. 5.5 but for the RG-A Fall 2018 inbending data set.

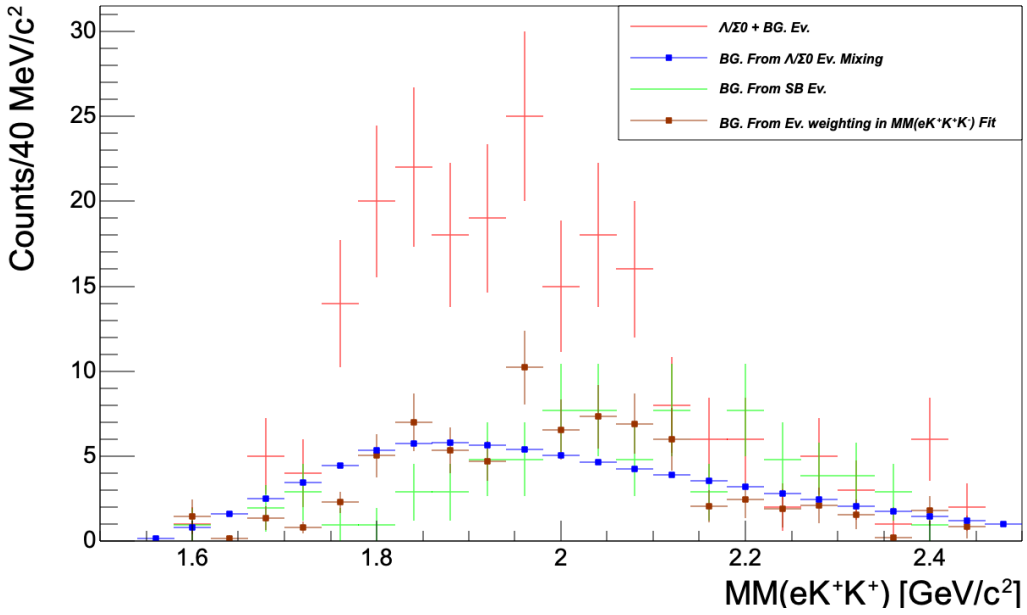

(a) Scattered electron detected in the FD.

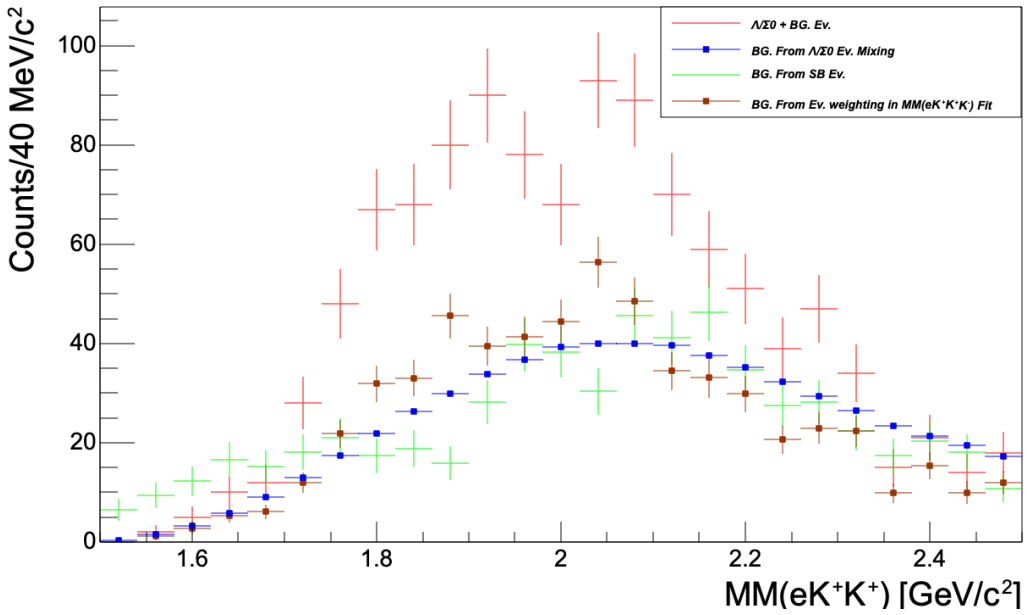

(b) Scattered electron detected in the FT.

Figure 5.7: Same as Fig. 5.5 but for the RG-A Spring 2019 inbending data set.

Comparison of Background Shape with Weighted Λ/Σ^0 Signal

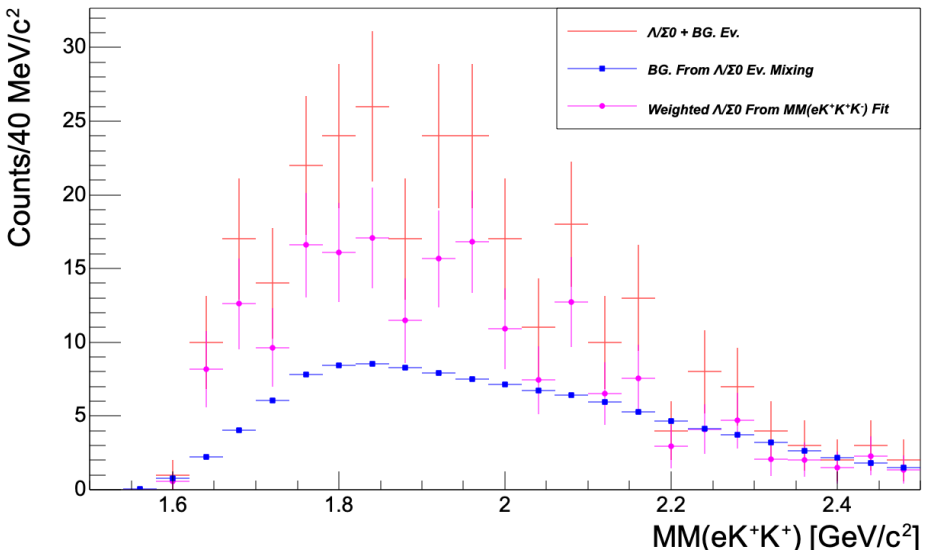

(a) Scattered electrons detected in the FD.

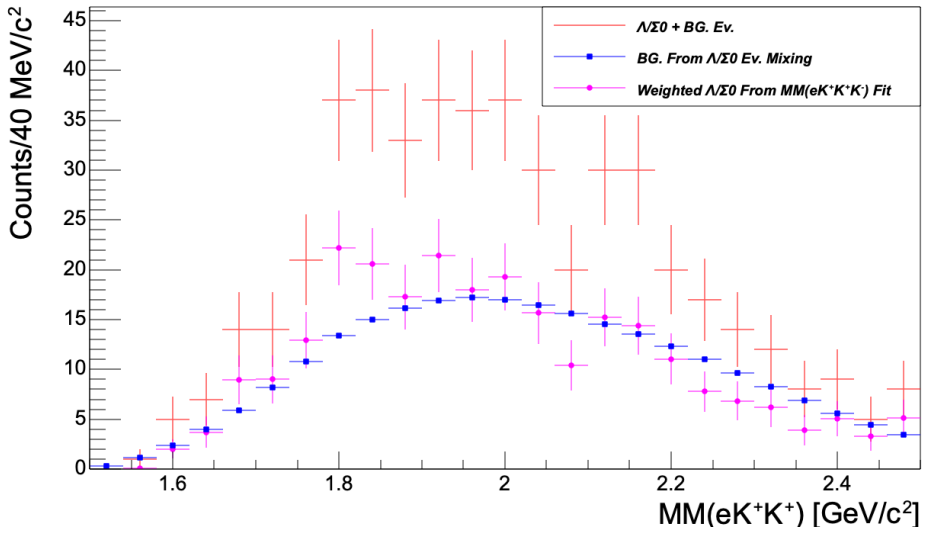

(b) Scattered electrons detected in the FT.

Figure 5.8: Comparison of the background distribution from the event mixing technique and the signal determined by weighting a double Gaussian fit function for the Λ/Σ^0 in the $MM(e'K^+K^+K^-)$ spectra for the Fall 2018 outbending data set. The blue histograms correspond to the normalized background distribution derived from the event mixing technique and the magenta histograms corresponds to the signal in $MM(e'K^+K^+)$ that decays to $K^-\Lambda/\Sigma^0$ obtained by weighting the missing mass off of $e'K^+K^+K^-$ on an event-by-event basis and assigning a probability according to the Λ/Σ^0 fit function with respect to the global fit function in the $MM(e'K^+K^+K^-)$ spectra.

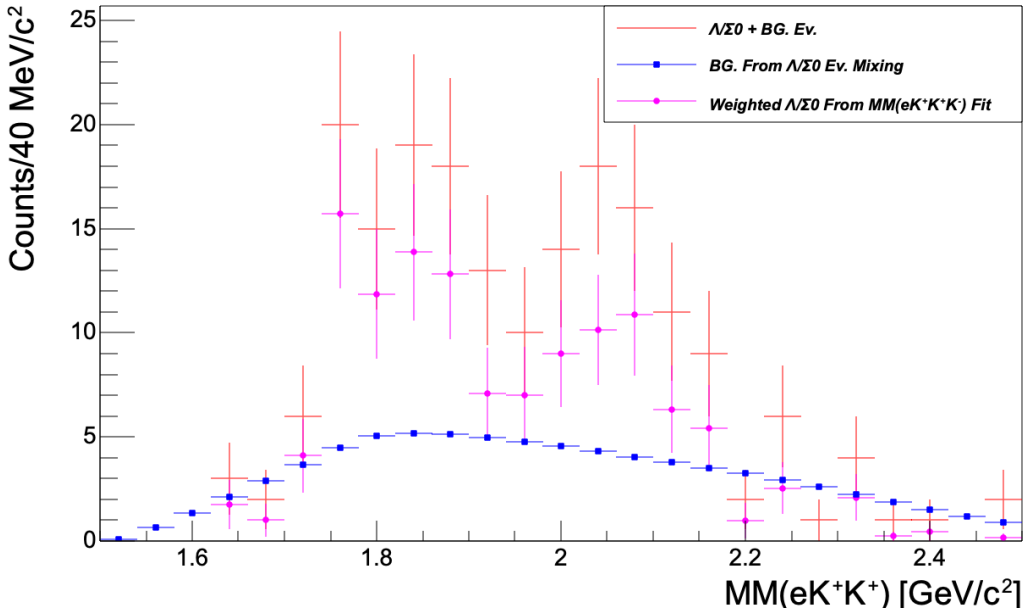

(a) Scattered electron detected in the FD.

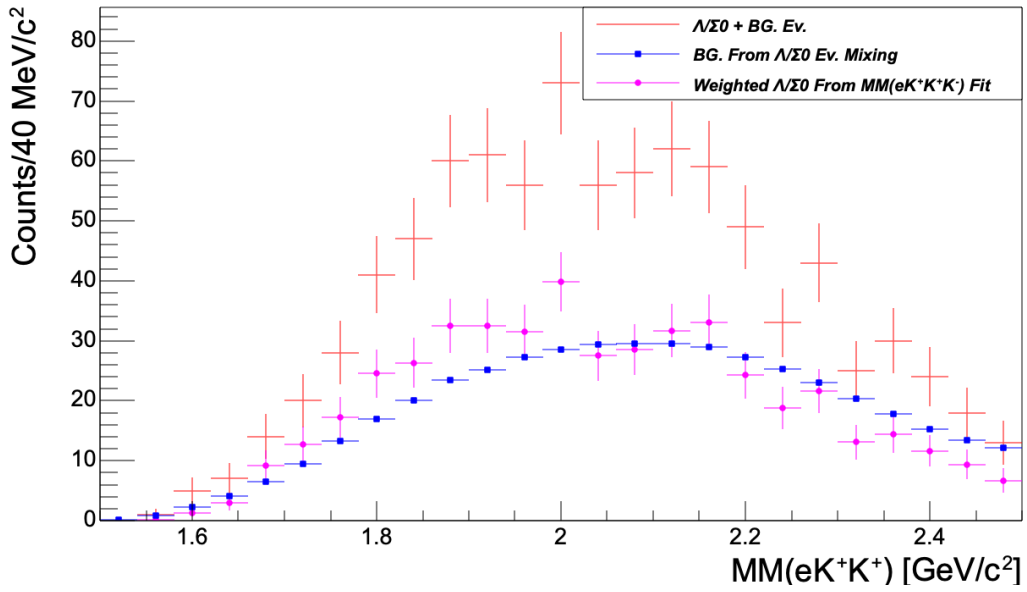

(b) Scattered electron detected in the FT.

Figure 5.9: Same as Fig. 5.8 but for the RG-A Fall 2018 inbending data set.

Comparison of Background Shape with Weighted Λ/Σ^0 Signal

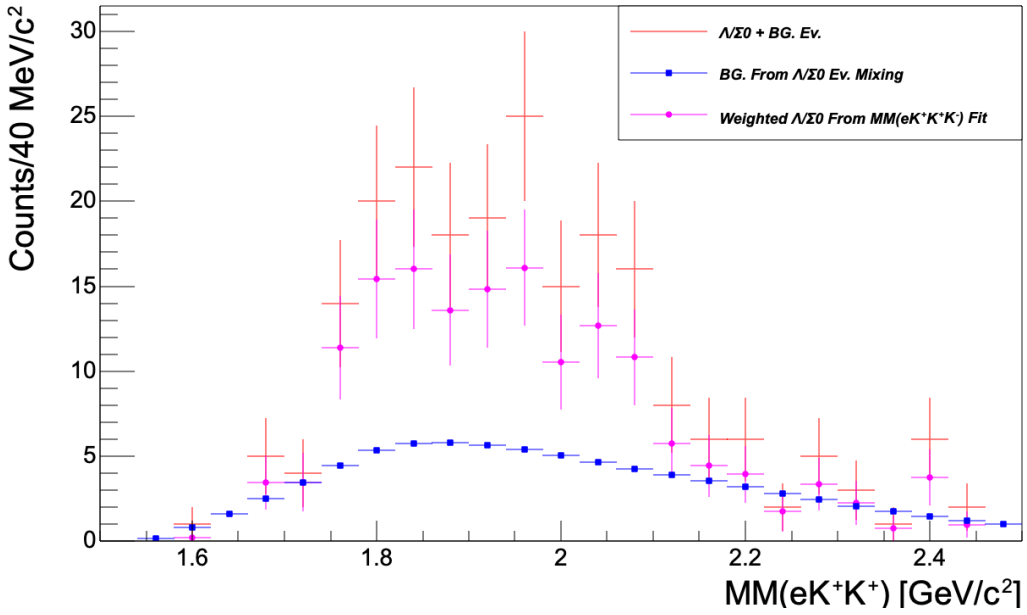

(a) Scattered electron detected in the FD.

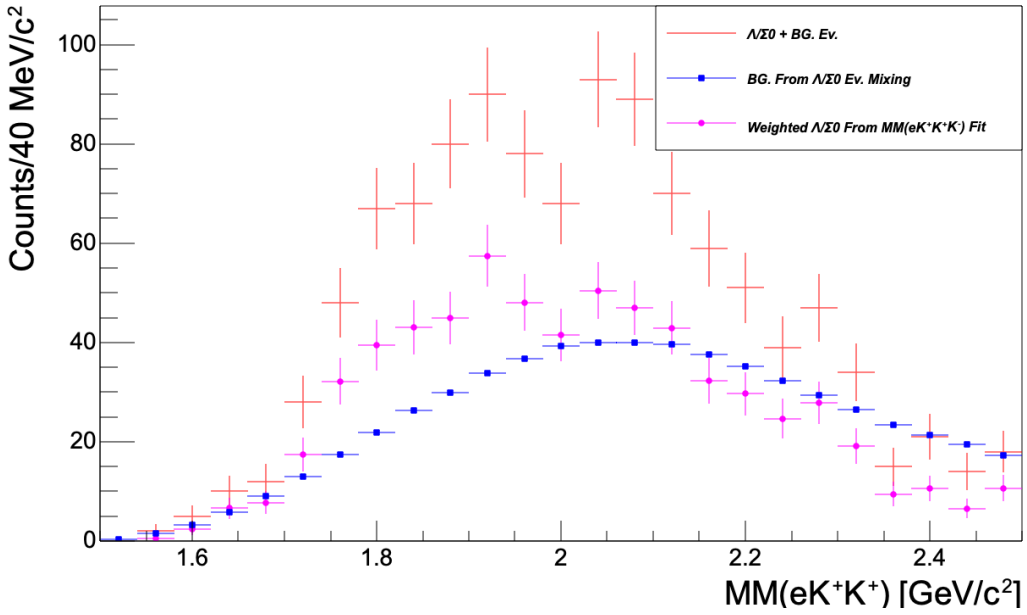

(b) Scattered electron detected in the FT.

Figure 5.10: Same as Fig. 5.8 but for the RG-A Spring 2019 inbending data set.

The Gaussian function used in the fit represents a possible $\Xi^{*-}(1820)$ resonance over the scaled background function that was determined using multiple approaches. The width and sigma of the Gaussian were fixed, respectively, to the $\Xi^{*-}(1820)$ nominal mass value from the PDG and mass resolution determined from the MC simulation summarized in Table 4.2. Two parameters that are allowed to vary in the fit are the amplitude of the Gaussian function, which represents the $\Xi^{*-}(1820)$ signal strength, and a factor that scales the entire background template by minimizing χ^2 in the fit. The integral of the fitted Gaussian was then calculated in a mass range corresponding to $\pm 1\sigma$ (total 2σ) from the Gaussian mean and estimated as an excess of $\Xi^{*-}(1820)$ events over the background events. The total number of background events ($N_{Bg.}$) was obtained by integrating the polynomial background function in the same $\pm 1\sigma$ mass range from the Gaussian mean. The integral of the global fit function within the range of $\pm 1\sigma$ from the Gaussian mean gives a total number of observed events ($N_{Obs.}$). The excess of $\Xi^{*-}(1820)$ events, which are also known as the raw yield, was calculated as,

$$N_{Sig.} = N_{Obs.} - N_{Bg.}. \tag{5.1}$$

Plots from Fig. 5.11 to 5.13 show the fit results for the $\Xi^{*-}(1820)$ in the missing mass distribution using the different data sets. The total number of observed events, background events, and excess events estimated from the integral of the fit with corresponding fit uncertainties on the integral calculated using the fit parameters from the converged fit, and corresponding parameter uncertainties are shown on each plot and summarized in Table 5.3. In general, the excess events estimated for the $\Xi^{*-}(1820)$ signal from all data sets analyzed is compatible with zero within $\approx 1-2\sigma$ of the uncertainties, demanding more statistics to claim a statistically significant $\Xi^{*-}(1820)$ signal in the data. The confidence on the estimated excess of signal depends on the uncertainty associated with it. If the excess is compatible with zero to within $\approx$

1σ, then the estimate is believed to be statistically significant within a 68% confidence level. If the excess is compatible with zero within $\approx 2\sigma$, then the estimate is believed to be statistically significant within a 95% confidence level.

$\Xi^{*-}(1820)$ **Excess Estimate for the Fall 2018 Outbending**

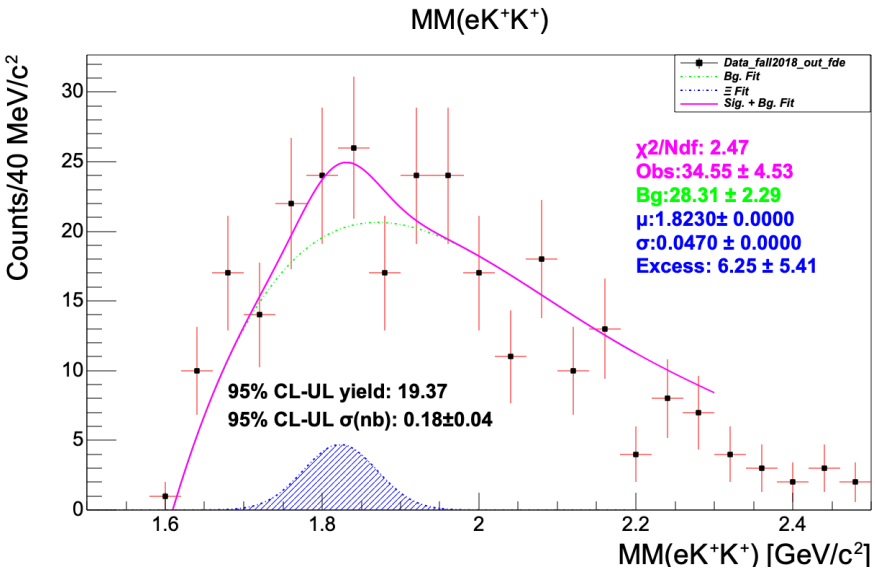

(a) Scattered electron detected in the FD.

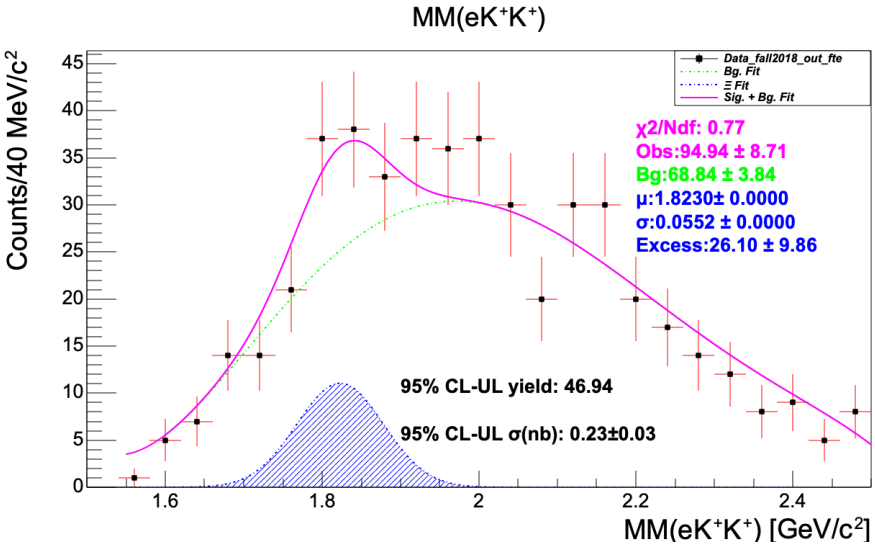

(b) Scattered electron detected in the FT.

Figure 5.11: Missing mass distribution for the RG-A Fall 2018 outbending data set fitted with a Gaussian function to represent the $\Xi^{*-}(1820)$ plus a sixth order polynomial background function obtained by scaling the background template. The mean and sigma of the Gaussian function and the background template from the event mixing technique were fixed in the fit, allowing only the Gaussian amplitude and the background scale factor to vary.

$\Xi^{*-}(1820)$ **Excess Estimate for the Fall 2018 Inbending**

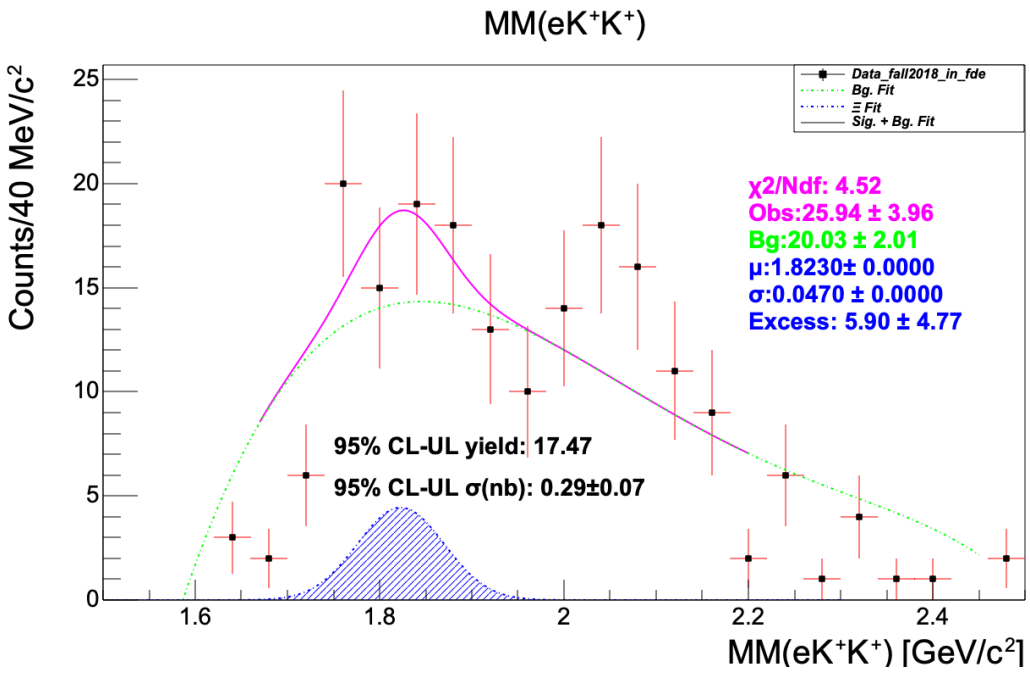

(a) Scattered electron detected in the FD.

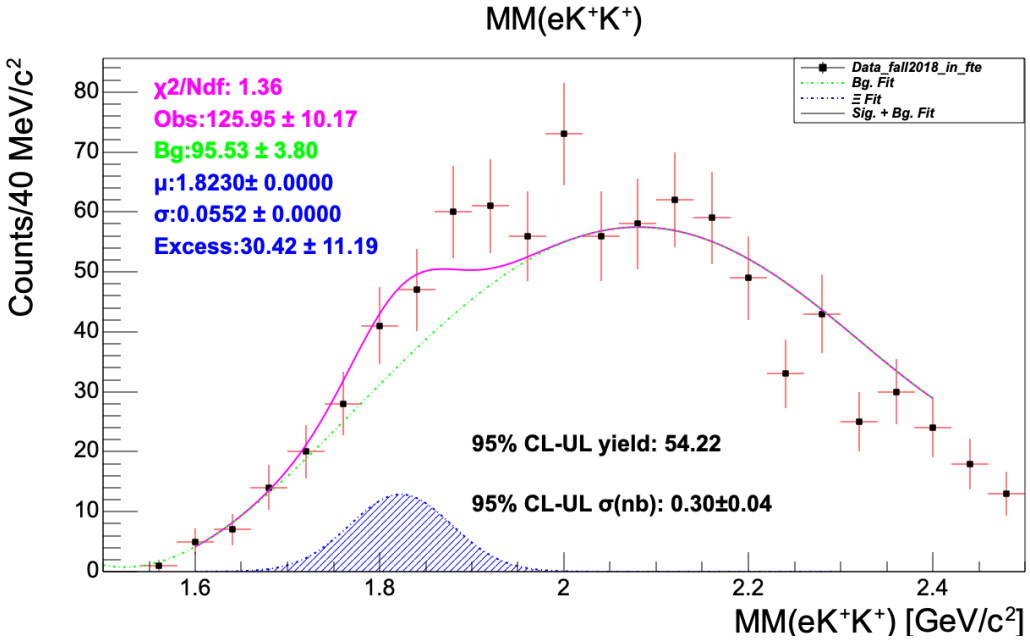

(b) Scattered electron detected in the FT.

Figure 5.12: Same as Fig. 5.11 but for the RG-A Fall 2018 inbending data set.

$\Xi^{*-}(1820)$ **Excess Estimate for the Spring 2019 Inbending**

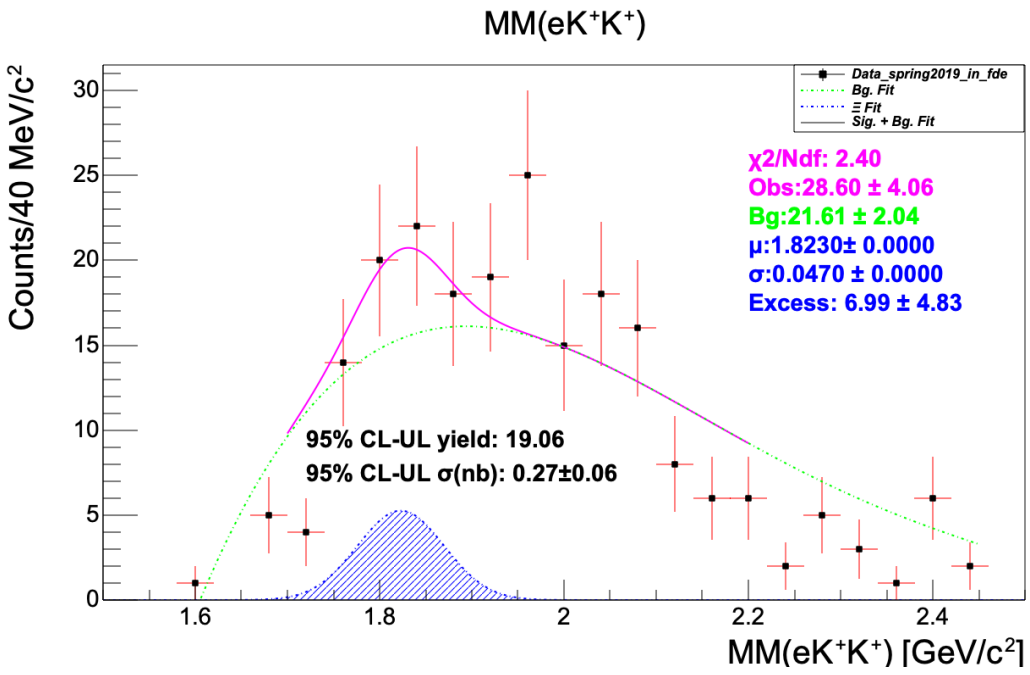

(a) Scattered electron detected in the FD.

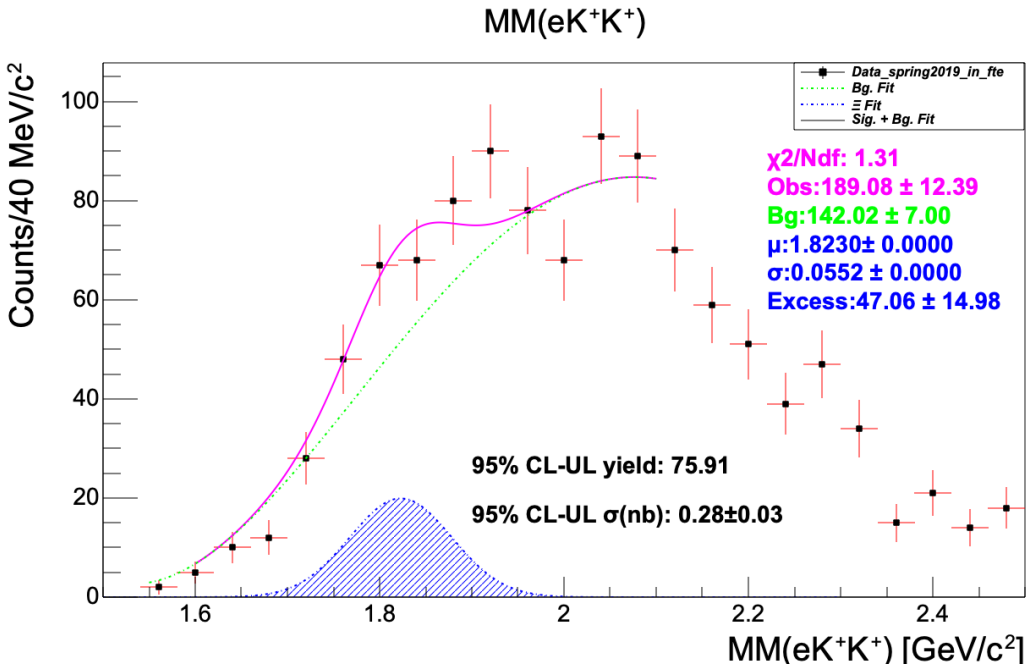

(b) Scattered electron detected in the FT.

Figure 5.13: Same as Fig. 5.11 but for the RG-A Spring 2019 inbending data set.

$\Xi^{*-}(1820)$ **Fit Summary**

Data	Obs. Events	Bg. Events	Excess (from fit)	μ (fixed)	σ (fixed)	PolBg. (fixed)
Fall 2018 outbending FT-e	95 ± 9	69 ± 4	26±10	55.22 MeV	1823 MeV	$Pol - 6$
Fall 2018 inbending FT-e	126 ± 10	96 ± 4	30±11	55.22 MeV	1823 MeV	$Pol - 6$
Spring 2019 inbending FT-e	189 ± 12	142±7	47±15	55.22 MeV	1823 MeV	$Pol - 6$
Fall 2018 outbending FD-e	35 ± 5	28 ± 2	6 ± 5	46.96 MeV	1823 MeV	$Pol - 6$
Fall 2018 inbending FD-e	26 ± 4	20 ± 2	6 ± 5	46.96 MeV	1823 MeV	$Pol - 6$
Spring 2019 inbending FD-e	29 ± 4	22 ± 2	7 ± 5	46.96 MeV	1823 MeV	$Pol - 6$

Table 5.3: The total number of observed, background, and estimated $\Xi^{*-}(1820)$ excess events calculated by integrating the global fit function, scaled sixth-order polynomial background function, and Gaussian signal function in the $\pm 1\sigma$ range from the Gaussian mean for the different data sets. The parameters of the sixth-order polynomial background template, mean, and width of the Gaussian function have been fixed in the fit allowing only the amplitude (signal strength) and background scale factor to vary. The yield uncertainties were calculated using the uncertainties in the fit parameters from the fit.

5.1.1 Upper Limit on the $\Xi^{*-}(1820)$ Raw Yields

The observed raw yield of $\Xi^{*-}(1820)$ events is converted into an upper limit on the $\Xi^{*-}(1820)$ yield using the two different methods described in this subsection.

5.1.1.1 Fit Method

A simple Gaussian fit method was implemented to estimate an upper limit on the $\Xi^{*-}(1820)$ yield. The uncertainty of the raw yield was determined using the resulting fit parameters from the fit discussed in Section 5.1 and the corresponding covariance matrix containing the fit parameter uncertainties and their correlations. The 95% confidence level upper limit was then calculated by adding two times the uncertainty of the $\Xi^{*-}(1820)$ raw yield.

5.1.1.2 Maximum Likelihood Ratio Test Method

The hypothesis test method was used to estimate the significance of the excess signal counts and uncertainties. Gammapy's[1] [82] CashCountsStatistic class [2] was used to compute the true $\Xi^{*-}(1820)$ signal counts and statistical significance, as well as to generate the confidence interval boundaries assuming the signal yield was positive definite and small. The CashCountsStatistic class implements the statistical analysis method of Webster Cash (W. Cash, 1978) [83] for parameter estimation through the application of the likelihood ratio test. The two input variables used by this routine class are the total number of observed events ($N_{Obs.}$) and the total number of expected background events ($N_{Bg.}$). The method then determines the true signal yield

[1] https://www.gammapy.org

[2] https://docs.gammapy.org/0.20/api/gammapy.stats.CashCountsStatistic.html

and statistical significance with proper confidence level boundaries by considering the background and signal statistical uncertainties.

One can naively estimate the statistical significance of the signal as $\frac{<N_{Sig.}>}{\sqrt{<N_{Obs.}>}}$ or $\frac{<N_{Sig.}>}{\sqrt{<N_{Bg.}>}}$ but these "naive" methods overestimate the significance on $< N_{Sig.} >$ ($\approx < N_{Obs.} > - < N_{Bg.>}$) either by underestimating the statistical uncertainty of the number of predicted background or signal events. Simply using $\frac{<N_{Sig.}>}{\sqrt{<N_{Sig.}>}}$ to calculate the statistical significance of the signal is wrong as $< N_{Sig.} >$ is calculated using two directly observed quantities $< N_{Obs.} >$ and $< N_{Bg.} >$. Hence, $N_{Sig.}$ does not follow a Poisson distribution. Therefore, the statistical significance of the estimated signal ($N_{Sig.}$) was calculated by taking the square root of the test statistics (TS) given by $-2\ln\lambda$. Where, $\lambda = \frac{maxL(X/H_{Bg.})}{maxL(X/H_{Sig.+Bg.})}$ is the ratio of the maximum likelihood function for a background-only (null) hypothesis ($H_{Bg.}$) claiming that all observed $\Xi^{*-}(1820)$ events are due to background and no signal exists ($< N_{Sig.} >= 0$) to that for a signal+background (alternative) hypothesis ($H_{Sig.+Bg.}$) positing that there is some positive signal yield ($< N_{Sig.} >\neq 0$). Here, $-2\ln\lambda$ simply represents the difference between the fit statistics values for the two hypotheses. In this analysis, only one unknown parameter, that is, signal strength ($< N_{Sig.} >$), is involved in the null hypothesis. Hence, according to Wilks's fundamental theorem of statistics [84], if the null hypothesis is true, $-2\ln\lambda$ will asymptotically follow a χ^2 distribution with one degree of freedom, which implies that the statistical significance can be estimated in terms of the number of σ as $\sqrt{-2\ln\lambda}$, which is equivalent to the Li&Ma significance for known backgrounds discussed in Ref. [85] by Ti−Pei Li and Yu-Qian Ma.

The CashCountsStatistic class of the gammapy Python library was created to fit models and estimate parameters for Poisson-distributed data with a known background. The total number of observed counts ($N_{Obs.}$) in this analysis was sampled from the Poisson process with a mean value of $< N_{Sig.} + N_{Bg.} >$, where $< N_{Sig.} >$

and $< N_{Bg.} >$ represent, respectively, the mean number of expected $\Xi^{*-}(1820)$ events, which is an unknown parameter of interest, and an average number of background events, which is known from the fit. A negative excess of events implies that the number of background events is overestimated from the fit. In such a case, the following convention was used to estimate the statistical significance ($\sqrt{TS}$) of the negative signal in terms of the number of σ as,

$$\text{Statistical Significance} = \begin{cases} -\sqrt{TS}, & \text{if excess} < 0 \\ \sqrt{TS}, & \text{otherwise.} \end{cases} \tag{5.2}$$

The maximum likelihood ratio test method provides a way to estimate the $p-$value of the data sample analyzed by following the background only hypothesis rather than the signal plus background hypothesis by combining both hypotheses together in a test. The $p-$value in a hypothesis test is a number calculated based on data to help make decisions about the statistical uncertainty by inferring how likely the data sample is consistent with the null hypothesis (background only hypothesis in our case). A higher $p-$value in a hypothesis test signifies that the data sample is highly consistent with the null hypothesis and the result tends more towards rejecting the corresponding alternative hypothesis (background plus signal hypothesis in our case).

Tables 5.4 and 5.5 summarize the 95% confidence level upper limit estimate on the $\Xi^{*-}(1820)$ yield from the different data sets calculated using the maximum likelihood ratio test method. The upper limit estimates are the output of the Gammapy's CashCountsStatistic software program after providing two variables $N_{Obs.}$ and $N_{Bg.}$ calculated from the fit for the different data sets as summarized in Table 5.3.

$\Xi^{*-}(1820)$ **Excess and Significance from the Likelihood Ratio Test Method**

Fit result	F18 FT-e out	F18 FT-e in	S19 FT-e in
Excess yield	26.10	30.42	47.06
Yield uncertainty	9.74	11.22	13.75
TS	8.84	8.80	14.11
$\sqrt{TS}$	2.97	2.97	3.76
$p-$value	0.0015	0.0015	0.0001
95%− CL range of excess yield	$(7.92, 46.94)$	$(9.29, 54.22)$	$(20.88, 75.91)$

Table 5.4: The 95% confidence level (CL) interval for the $\Xi^{*-}(1820)$ true yield based on the calculated statistics using the maximum log-likelihood ratio test method for the different data sets with the electron detected in the FT. The 95% confidence interval is constructed by searching the signal values for which the test statistics (TS) variation is $2^2 = 4$. These results are only as good as the quality of the missing mass spectra fits.

$\Xi^{*-}(1820)$ **Excess and Significance from the Likelihood Ratio Test Method**

Fit result	F18 FD-e out	F18 FD-e in	S19 FD-e in
Excess yield	6.25	5.90	6.99
Yield uncertainty	5.88	5.09	5.35
TS	1.29	1.59	2.05
$\sqrt{TS}$	1.13	1.26	1.43
$p-$value	0.1284	0.1036	0.0761
95%−CL range of excess yield	$(-4.22, 19.37)$	$(-2.99, 17.47)$	$(-2.42, 19.06)$

Table 5.5: Same information as in Table 5.4 but for the scattered electron detected in the FD.

5.1.2 Upper Limit on the $\Xi^{*-}(1820)$ Cross Section

The 95% confidence level upper limit on the $\Xi^{*-}(1820)$ yield calculated in Section 5.1.1 was used to estimate the upper limit on the total production cross section of the $\Xi^{*-}(1820)$ in the reaction $ep \rightarrow e'K^+K^+\Xi^{*-}(1820) \rightarrow e'K^+K^+K^-(\Lambda/\Sigma^0)$. The formula used to calculate the total cross section is,

$$\sigma_{tot} = \frac{Y_{\Xi^{*-}(1820)}(95\%CL)}{\epsilon * \mathcal{L}}, \tag{5.3}$$

where $Y_{\Xi^{*-}(1820)}(95\%CL)$ is the 95% confidence level upper limit on the $\Xi^{*-}(1820)$ yield, ϵ is the CLAS12 detection efficiency, and $\mathcal{L}$ is the integrated luminosity. The total cross section in this formula is the electroproduction cross section of the $\Xi^{*-}(1820)$ corresponding to the $\Xi^{*-}(1820) \rightarrow K^-(\Lambda/\Sigma^0)$ decay mode in the reaction $ep \rightarrow e'K^+K^+\Xi^{*-}(1820) \rightarrow e'K^+K^+K^-(\Lambda/\Sigma^0)$. The branching ratio for the $\Xi^{*-}(1820) \rightarrow K^-(\Lambda/\Sigma^0)$ decay mode is not available in the PDG. Hence, the total cross section calculated in Eq. (5.3) represents the scaled total cross section value (i.e. the appropriate branching ratio of the $\Xi^{*-}(1820) \rightarrow K^-(\Lambda/\Sigma^0)$ decay mode times the total cross section).

The integrated luminosity depends on the target factor (T), representing the total number of target particles (protons) per cross-sectional area and incoming beam flux on the target. The integrated luminosity is given by,

$$\mathcal{L} = T * Flux, \tag{5.4}$$

with the target factor defined as,

$$T = \frac{N_A * \rho_t * l_t}{A_W}, \tag{5.5}$$

LH_2-Target Characteristics

Parameters	Value
ρ_t (density)	0.07114 g/cm^3
l_t (length)	5 cm
A_w (atomic weight)	1.00794 g/mol
N_A (Avogadro's number)	$6.023 * 10^{23}$ mol^{-1}

Table 5.6: RG-A LH_2 target properties and constants used to calculate the cross sections.

where A_W, ρ_t, and l_t are, respectively, the atomic weight, mass density, and length of the target, and N_A is the Avogadro's number. Table 5.6 shows the characteristic properties of the target used.

The total beam flux on the target depends fully on the live-time-gated running time of the experiment and the beam current used. It was calculated experimentally using the total beam charge collected on the target, which is summarized in Table 3.1 for the different data sets. The total incident electron flux summed over the good runs included in this analysis corresponding to the different data sets was calculated using the total Faraday cup charge (FC_{charge}) in the formula $N_e = \frac{FC_{charge}}{Q_e}$, where Q_e is the magnitude of the electron charge. The total electron flux for the different data sets was used directly in Eq. 5.4 to calculate the total luminosity. The total number of incident electrons on the target is multiplied by a conversion factor Γ, known as the virtual photon flux factor, to calculate the equivalent virtual photon flux (i.e. $N_\gamma = \Gamma * N_e$) to describe the quasi-real photoproduction process (low-Q^2 electroproduction) and the pure electroproduction process (large-Q^2 electroproduction). The value of the virtual photon flux factor is different for different kinematics of the scattered electron and beam energies. The formula used to calculate the virtual photon flux factor for the

kinematic volume defined by the Q^2 and W range (i.e. ΔQ^2 and ΔW) covered by the different data sets in this analysis is given by,

$$\Gamma = \frac{\alpha}{4\pi} * \frac{< W >}{M E_b^2} * \frac{< W >^2 - M^2}{M < Q^2 >} * \frac{\Delta W \Delta Q^2}{1 - < \epsilon >}, \tag{5.6}$$

where $\alpha (= \frac{1}{137})$ is the fine structure constant, E_b is the electron beam energy (10.604 and 10.199 GeV, respectively, for the Fall 2018 and the Spring 2019 run periods), the $< W >$ and $< Q^2 >$ are the bin-averaged values of the W and Q^2 range, the ΔW and ΔQ^2 are the bin volumes of the W and Q^2 range covered by the Ξ^{*-} data sample, and $< \epsilon >= [1 + \ 2 \ (1 + \frac{<\nu^2>}{<Q^2>}) \tan^2 \frac{<\theta_e>}{2}]^{-1}$ is the virtual photon polarization parameter computed using the $< W >$ and $< Q^2 >$ values. The average energy transfer to the virtual photon $< \nu >= E_b - < E_e >$ used in the $< \epsilon >$ expression is also computed using $< \ W \ >$ and $< Q^2 >$ in the formula $< \nu >= \frac{<W>^2 + <Q^2> - M^2}{2M}$, where M is the mass of the proton. The average value of the scattered electron polar angle in the lab is computed using the formula $\theta_e = \cos^{-1}[(< W >^2 - M^2 - 2 < \ \nu \ > M - 2M_e^2 + 2E_b E_e)/2p_e p_p]$, where p_b, p_e, and M_e are, respectively, the average momentum of the beam, scattered electron, and the magnitude of the electron mass. The Gamma factor expression in Eq. (5.6) is identical to the one used in the CLAS e1f analysis note [86]. Table 5.7 shows values of the Γ factor computed using Eq. (5.6) for the Ξ^{*-} data samples from the different data sets with the different trigger conditions (i.e. FT-e or FD-e) and beam energies. These values were used in the cross section calculation for this analysis. An alternative approach to compute the equivalent quasi-real photon flux from the electron flux is discussed in the Ph.D. thesis (see page no. 110, Eq. (6.4) in Ref. [87]) by Andrea Celentano. In his approach, the Γ factor for the FT-e kinematics is derived by numerically integrating Eq.(5.7) in the low-Q^2

limit over the FT acceptance range summarized in Table 2.2.

$$d\Gamma(\Omega_e, E_e) = \frac{\alpha}{4\pi^2}\frac{E_e}{E_0}\frac{\nu}{Q^2}[\frac{(2E_0-\nu)^2}{\nu^2}+1]d\Omega_e dE_e. \quad (5.7)$$

Ξ^{*-} Data Sample Kinematic Coverage Summary

Ξ^{*-} data coverage	F18 FT-e out	F18 FT-e in	S19 FT-e in	F18 FD-e out	F18 FD-e in	S19 FD-e in
E_b	10.604 GeV	10.604 GeV	10.199 GeV	10.604 GeV	10.604 GeV	10.199 GeV
W range	[3.64:4.26] GeV	[3.64:4.26] GeV	[3.52:4.16] GeV	[3.3:4.3] GeV	[3.1:4.1] GeV	[3.0:4.0] GeV
ΔW	0.62 GeV	0.62 GeV	0.64 GeV	1.0 GeV	1.0 GeV	1.0 GeV
$< W >$	3.95 GeV	3.95 GeV	3.84 GeV	3.8 GeV	3.6 GeV	3.5 GeV
Q^2 range	[0.03:0.13] GeV^2	[0.03:0.13] GeV^2	[0.03:0.13] GeV^2	[0.16:1.28] GeV^2	[1.28:2.88] GeV^2	[1.28:2.88] GeV^2
ΔQ^2	0.10 GeV^2	0.10 GeV^2	0.10 GeV^2	1.12 GeV^2	1.60 GeV^2	1.60 GeV^2
$< Q^2 >$	0.08 GeV^2	0.08 GeV^2	0.08 GeV^2	0.72 GeV^2	2.08 GeV^2	2.08 GeV^2
Γ factor	$5.087E-04$	$5.087E-04$	$5.458E-04$	$9.769E-04$	$5.086E-04$	$4.150E-04$

Table 5.7: Summary of the kinematic coverage of the Ξ^{*-} data sample used to compute the Γ factor for the different data sets.

The upper limit estimates of the electroproduction cross section from the different data sets spanning different Q^2 range are summarized in Table 5.8. The extracted preliminary electroproduction upper limit cross section result for the $\Xi^{*-}(1820)$ state in the reaction $ep \to e'K^+K^+\Xi^{*-}(1820) \to e'K^+K^+K^-(\Lambda/\Sigma^0)$ is found to be approx-

imately around 0.3 nb. This estimate of the upper limit cross section does not include the statistical uncertainties due to the photon flux, the detector efficiency, and the systematic uncertainties from different sources. The cross section results obtained in this study are in agreement with the available published photoproduction cross section results from the CLAS $g12$ experiment discussed in Ref. [42]. The publication was based on the Ph.D. work by John Theodore Goetz (see Ref. [88]), which quoted a value of 1.01 nb for the upper limit on the photoproduction total cross section of the $\Xi^{*-}(1820)$ state by investigating the $MM(K^+K^+)$ missing mass spectra from the CLAS $g12$ data set. The quoted upper limit estimate in his thesis was obtained by applying an overall scaling factor of 35% in the result to account for the possible systematic uncertainties associated in the measurement.

5.1.3 Uncertainty

The estimates of the upper limit on the electroproduction cross section of the $\Xi^{*-}(1820)$ state obtained in the Section 5.1.2 have associated statistical and systematic uncertainties. These are detailed in this subsection.

5.1.3.1 Statistical Uncertainty

Statistical uncertainty is related to the overall data size analyzed for the measurement, and it comes from counting quantities such as electron/photon flux, signal/background events, etc. The data samples analyzed to search for the $\Xi^{*-}(1820)$ state have very poor statistics; hence, the results are dominated by statistical uncertainties. The statistical uncertainty associated with the measurement of the upper limit production cross section was calculated using,

$$\delta\sigma_{ul} = \sigma_{ul}\cdot\sqrt{\left(\frac{\delta N_{\gamma/e}}{N_{\gamma/e}}\right)^2 + \left(\frac{\delta Y_{ul}}{Y_{ul}}\right)^2 + \left(\frac{\delta\epsilon}{\epsilon}\right)^2}, \tag{5.8}$$

Electroproduction Cross Section (95% CL Upper Limit)

Data set	Q^2 range	Yield (95% UL)	Efficiency	σ (95% UL)
Fall 2018 outbending FT-e	$[0.03, 0.13]$ GeV^2	47	0.00884	0.23 nb
Fall 2018 inbending FT-e	$[0.03, 0.13]$ GeV^2	54	0.00715	0.30 nb
Spring 2019 inbending FT-e	$[0.03, 0.13]$ GeV^2	75	0.00739	0.28 nb
Fall 2018 outbending FD-e	$[0.16, 1.28]$ GeV^2	19	0.00244	0.18 nb
Fall 2018 inbending FD-e	$[1.28, 2.88]$ GeV^2	17	0.00237	0.29 nb
Spring 2019 inbending FD-e	$[1.28, 2.88]$ GeV^2	19	0.00252	0.27 nb

Table 5.8: Upper limit on the electroproduction cross section of the $\Xi^{*-}(1820)$ in the reaction $ep \to e'K^+K^+\Xi^{*-}(1820) \to e'K^+K^+K^-(\Lambda/\Sigma^0)$. The upper limit estimate does not include systematic uncertainties and corresponds to the $\Xi^{*-}(1820) \to K^-(\Lambda/\Sigma^0)$ decay mode only (i.e. scaled cross section by the appropriate branching ratio).

Counting Uncertainties Estimate

Data set	$\delta\sigma_{ul}$
Fall 2018 outbending FT-e	0.04 nb ($\approx$ 17%)
Fall 2018 inbending FT-e	0.06 nb ($\approx$ 20%)
Spring 2019 inbending FT-e	0.05 nb ($\approx$ 17%)
Fall 2018 outbending FD-e	0.04 nb ($\approx$ 20%)
Fall 2018 inbending FD-e	0.07 nb ($\approx$ 25%)
Spring 2019 inbending FD-e	0.06 nb ($\approx$ 23%)

Table 5.9: Counting uncertainties ($\delta\sigma_{ul}$) calculated using Eq. (5.8) for the different data sets.

where $N_{\gamma/e}$ represents the total number of the quasi-real photon flux used in the cross-section calculation and Y_{ul} is the upper limit estimate on the $\Xi^{*-}(1820)$ yield. σ_{ul} is the upper limit production cross section. The statistical uncertainties on these quantities are calculated using the Poisson counting uncertainty formula given by the square root of the total counts ($\sqrt{N}$). The last term in Eq. (5.8) is the relative statistical uncertainty associated with the detector efficiency. The statistical uncertainty in the detector efficiency, ($\delta\epsilon$), was calculated using the Binomial counting uncertainty formula given by Eq. (4.1). Table 5.9 shows the $\delta\sigma_{ul}$ value calculated using Eq. (5.8) for the different data sets. The results quoted in Table 5.8 do not include the counting uncertainties associated with $N_{\gamma/e}$ and ϵ. These results have to be rescaled in such a way to include the relative uncertainty contribution of the three terms in Eq. (5.8) when quoting the final upper limit estimates.

5.1.3.2 Systematic Uncertainty

Systematic uncertainty arises in the process of measuring the different parameters needed to calculate the cross section. Determining systematic uncertainties is almost always tied with the statistics of the measurement. Frequently, a systematic uncertainty emerges due to an unknown variation in a measurement that is correlated from run to run. In some cases, such unknown variations in a measurement contributing to a systematic uncertainty appear for the overall scale of the data (scale-type uncertainties). Contributions from each source of systematic uncertainty can be quantified by altering the parameter defining the source and calculating the difference in the measurement. The overall systematic uncertainty (excluding scale-type uncertainties) is then calculated by adding the individual contributions from different sources in quadrature assuming the individual systematic uncertainties are uncorrelated. The formula to calculate a relative systematic uncertainty associated with i^{th} source variation in the measurement is given by Eq. (5.9) and the quadrature sum is given by Eq. (5.10).

$$\delta_i = \frac{|\sigma_{ul} - \sigma_{ul}^{alt}|}{\sigma_{ul}}, \tag{5.9}$$

$$\delta^{syst} = \sqrt{\sum_{i=1} \delta_i^2}, \tag{5.10}$$

where σ_{ul} and σ_{ul}^{alt} are, respectively, the reference measurement and the measurement with the alternate cut or correction. δ^{syst} is the overall systematic uncertainty of the measurement. The sources of systematic uncertainties considered in this measurement of the upper limit production cross section for the $\Xi^{*-}(1820)$ state are defined below and summarized in Table 5.10.

5.1.3.2.1 Effect of momentum smearing factor and the $\Xi^{*-}(1820)$ mass resolution used in the fit. The width of the Gaussian function chosen to represent

the possible $\Xi^{*-}(1820)$ state in the missing mass distribution was inferred from the MC simulation with momentum smearing determined by comparing the observed resolution of the ground state Cascade resonance from data and MC. The momentum smearing factors were varied in the simulation while determining the experimental mass resolution for the $\Xi^{*-}(1820)$ state to see the effect because of the uncertainty associated with the determined momentum smearing factors, that is $(0.30 \pm 0.05)\%$ for FD-particle momenta and $(2.5 \pm 1.0)\%$ for FT-particle momenta. The resulting relative systematic uncertainty in the estimate of the upper limit of the $\Xi^{*-}(1820)$ production cross section because of the uncertainty in the $\Xi^{*-}(1820)$ experimental mass resolution due to the effect of the momentum smearing factor was found to be 2.9% and 4.4% for the FD-electron and FT-electron case, respectively, for the Fall 2018 outbending data set.

5.1.3.2.2 Spectrum fitting to extract background and signal yield. The background fitting functions were varied while fitting the background spectrum to determine the background shape. A systematic uncertainty has been assigned on the cross-section measurement based on changing the background fitting function. The relative systematic uncertainty on the cross section measurement while changing the fit function (third vs. sixth-order polynomial function) to define the background shape is in the range of $4 - 6\%$ for both data samples with electrons detected in the FD/FT for the Fall 2018 outbending data set.

5.1.3.2.3 Bin shift study. The effect of bin shift on the upper limit cross section estimate was studied by moving each bin by half the size of a bin width and re-fitting the missing mass spectra. The relative systematic uncertainty was estimated to be 0.9% and 1.3% for the FD-e and FT-e case, respectively, for the Fall 2018 outbending data set.

5.1.3.2.4 Background shape estimation process. Multiple approaches were implemented to determine the background shape in the missing mass spectra. The background function obtained using the signal region excluding technique was highly limited by the poor statistics compared to that obtained using the event mixing technique, which allowed for the inclusion of any desired statistics to get a better background function improving the cross section measurement. A systematic uncertainty assignment on the upper limit of the production cross section was estimated by comparing the results using background shapes derived from the two different fitting techniques. The resulting relative systematic uncertainty on the cross section associated with the choice of background function obtained from two techniques was found to be 26% and 16% for the FT-e and FD-e case, respectively, when calculated using the Fall 2018 outbending data set. The large relative systematic uncertainty found with this source in the cross section calculation was not unexpected since the true systematic uncertainty might be much overestimated when comparing a "superior" event mixing technique with an "inferior" signal exclusion technique. Hence, such an overestimated value of the systematic uncertainty observed with this source is not quoted in summary Table 5.10.

The upper limit results on the $\Xi^{*-}(1820)$ production cross section were all obtained using the background shape estimated from the event mixing technique as the analysis had better control over the background from this technique. Additionally, better control over the background shape from the event mixing technique also allowed for the determination of preliminary results on the production cross section of the reaction $ep \to e'K^+K^+\Xi^{*-}$ as a function of Ξ^{*-} mass for different Q^2 ranges with the assumption that the background model from the event mixing technique is complete.

List of Relative Systematic Uncertainties in Upper Limit Cross Section

Systematic	Fall 2018 out FT-e	Fall 2018 out FD-e
Smearing factor and the $\Xi^{*-}(1820)$ resolution	4.4%	2.9%
Background fit	4.5%	5.8%
Bin shift	0.9%	1.3%

Table 5.10: Size of relative systematic uncertainties estimated in the measurement of the upper limit production cross sections for the $\Xi^{*-}(1820)$ state quoted in Table 5.8 for the Fall 2018 outbending data set.

5.1.3.2.5 Choice of the event generator. All the necessary MC simulations for this work were carried out using a phase-space event generator (clas12-elSpectro) developed by Derek Glazier. An important source of the systematic uncertainty overlooked in this study is associated with the choice of the event generator and the model used to generate simulated events. In an ideal scenario, an appropriate production model should be used to generate simulated events for calculating efficiencies. An event generator that best reproduces the particle momenta and angular distributions in the data would be appropriate to minimize the systematic uncertainties associated with the MC simulations and efficiency calculations. Since the higher mass (> 1530 MeV) Ξ^{*-} production mechanism is unclear, it would be very informative to implement multiple production models to generate events and compare the results for a reasonable systematic uncertainty assignment. In this study, the systematic uncertainty associated with the choice of an event generator and the phase-space model used to generate events is not calculated as multiple event generators were not available to generate events and compare results against each other.

5.2 Upper Limit Cross Section of the Reaction $ep \rightarrow e'K^+K^+(\Xi^{*-}) \rightarrow e'K^+K^+K^-(\Lambda/\Sigma^0)$ as a Function of Ξ^{*-} Mass

The event mixing technique implemented in Section 5.1 allows for good control over the background in the missing mass spectra and provides a smooth background shape. For each missing mass bin from $1.7-2.3$ GeV, an estimate of the average background events can be determined. The remaining events after subtracting the average background events in each bin must come from physics processes explained by the exclusive process $ep \rightarrow e'K^+K^+(\Xi^{*-}) \rightarrow e'K^+K^+K^-(\Lambda/\Sigma^0)$ under the assumption that the background model from the event mixing technique is complete.

In this section, the 95% upper limit cross section of the reaction $ep \rightarrow e'K^+K^+(\Xi^{*-}) \rightarrow e'K^+K^+K^-(\Lambda/\Sigma^0)$ for different missing Ξ^{*-} bins are presented. The same log likelihood ratio test method that was discussed in Section 5.1.1.2 was employed to determine an estimate of the 95% confidence level upper limit yield for each missing mass bin. The total number of observed events ($N_{Obs.}(i)$) for the signal plus background and the total number of expected background events ($N_{Bg.}(i)$) estimated from the event mixing technique were used as input variables in the CashCountsStatistics routine class to estimate the true signal yield and the statistical significance with proper confidence level boundaries for each i^{th} missing mass bin. The estimated 95% confidence level upper limit yield of the true signal for each bin was then combined with the CLAS12 reaction reconstruction efficiency for that bin and the global luminosity information to calculate the upper limit cross section of the exclusive reaction for the different missing mass and Q^2 bins. Figures 5.14 to 5.19 show the 95% confidence level upper limit yield and corresponding upper limit production cross section estimate for the different missing mass and Q^2 bins using the different data sets.

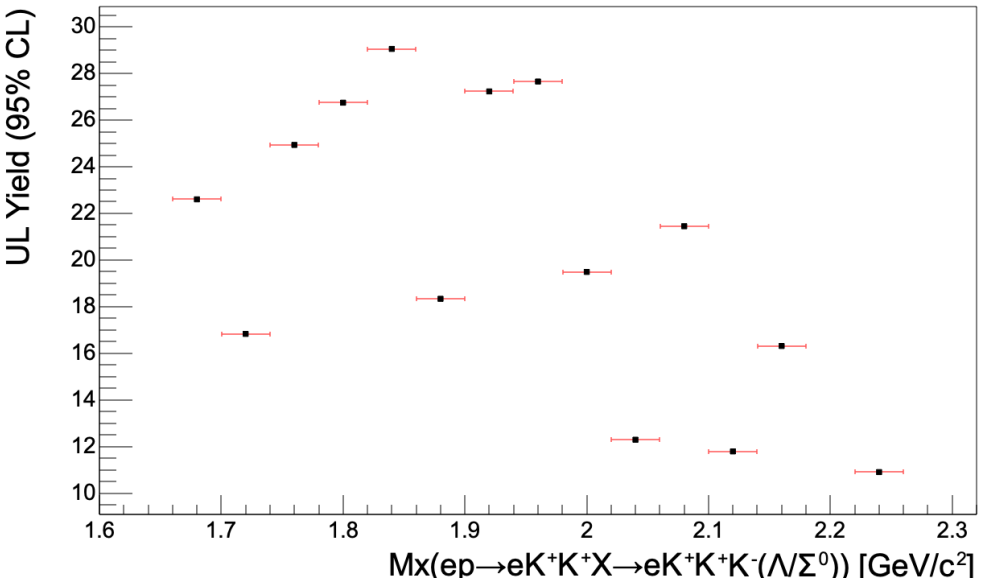

(a) Fall 2018 out FD-e Q^2 : $[0.16, 1.28]$ GeV^2.

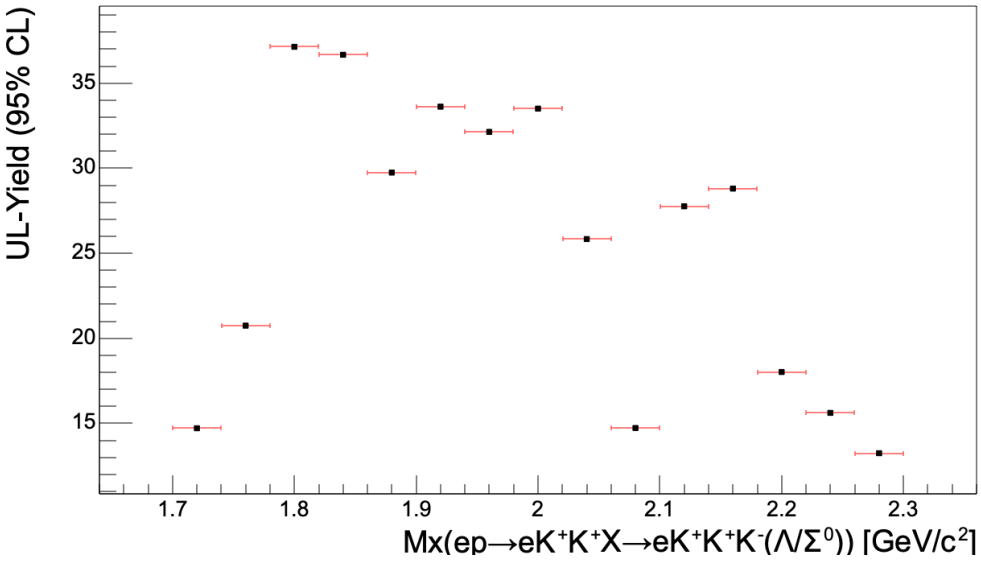

(b) Fall 2018 out FT-e Q^2 : $[0.03, 0.13]$ GeV^2.

Figure 5.14: The 95% confidence level upper limit yield estimate for the reaction $ep \rightarrow e'K^+K^+(\Xi^{*-}) \rightarrow e'K^+K^+K^-(\Lambda/\Sigma^0)$ using the RG-A Fall 2018 outbending data set with electrons in the FD (see Fig. 5.14a) and FT (see Fig. 5.14b). The maximum log likelihood ratio test was used to estimate the upper limit yield for the different missing mass bins. The Q^2 coverage for each mass bin of the different plots is indicated in the captions of each plot.

95% **Confidence Level Upper Limit Yield**

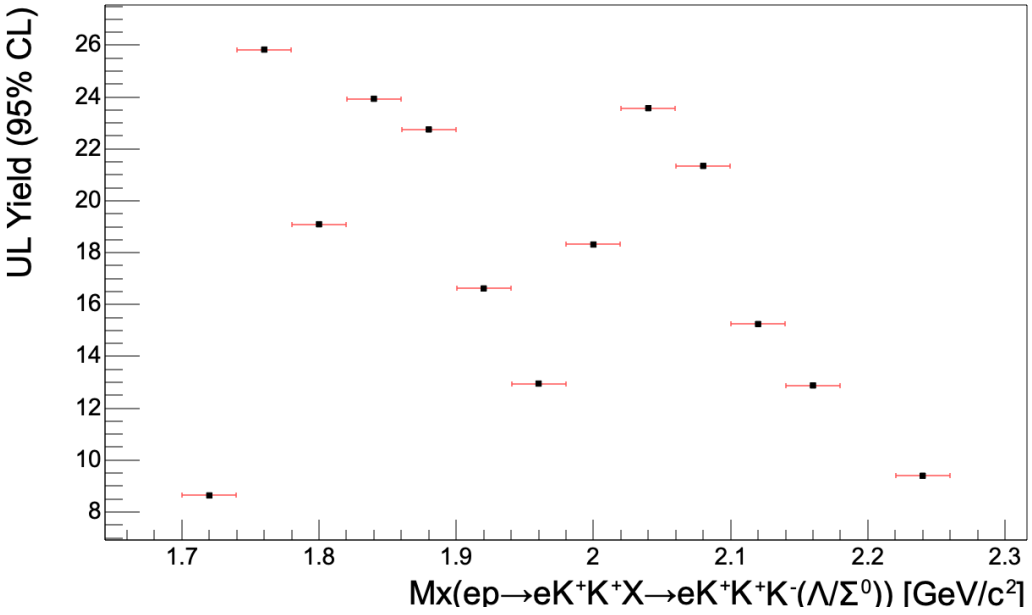

(a) Fall 2018 in FD-e Q^2 : $[1.28, 1.88]$ GeV^2.

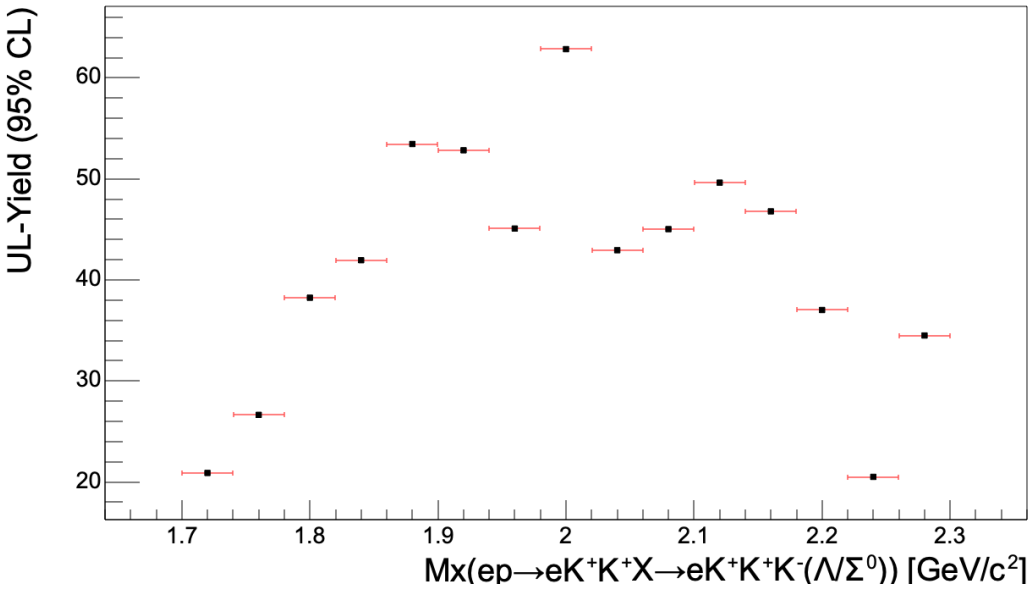

(b) Fall 2018 in FT-e Q^2 : $[0.03, 0.13]$ GeV^2.

Figure 5.15: Same as Fig. 5.14 but for the RG-A Fall 2018 inbending data set.

95% **Confidence Level Upper Limit Yield**

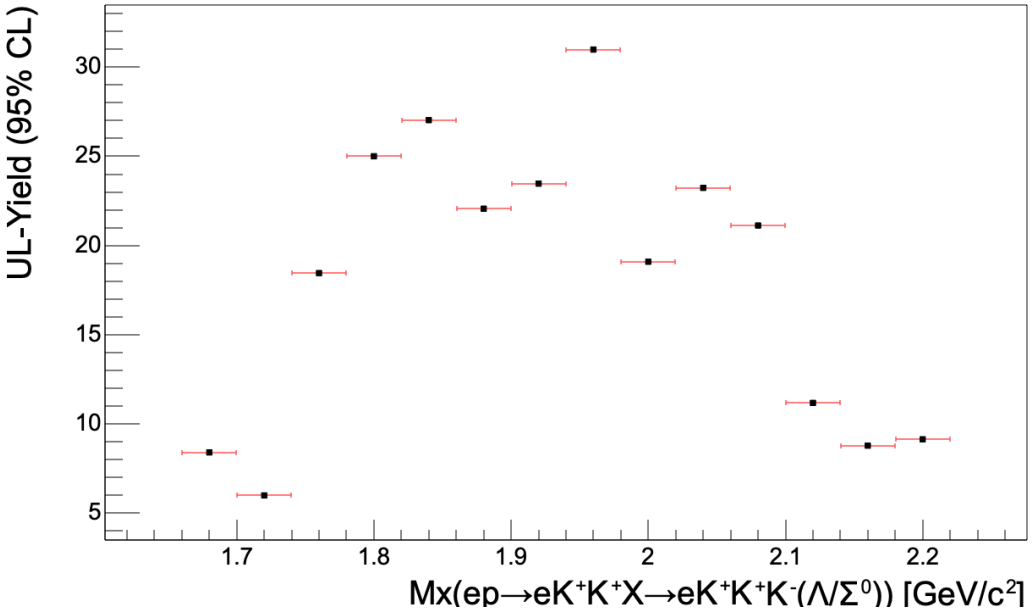

(a) Spring 2019 in FD-e Q^2 : $[1.28, 1.88]$ GeV^2.

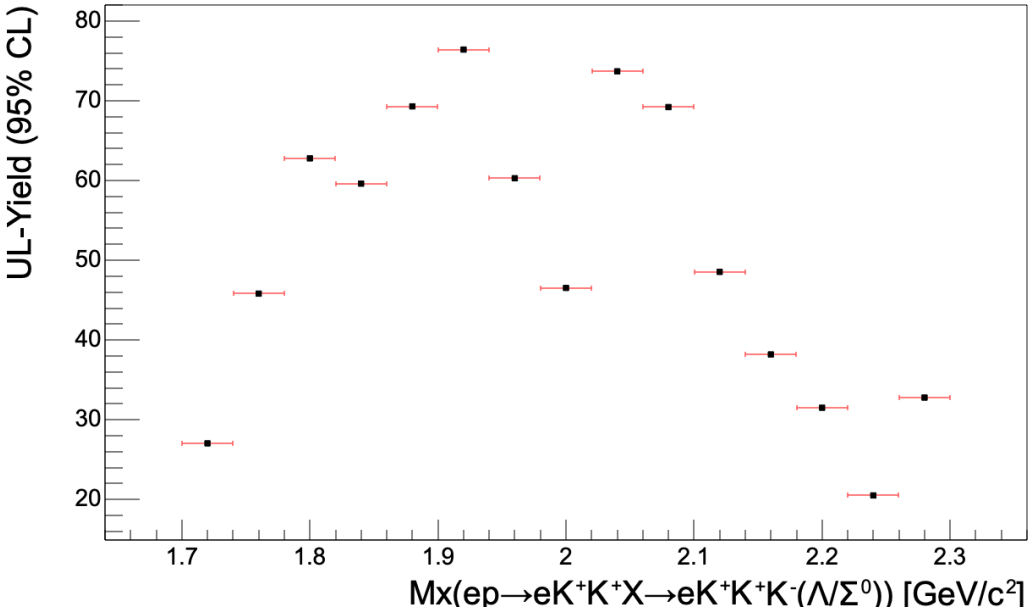

(b) Spring 2019 in FT-e Q^2 : $[0.03, 0.13]$ GeV^2.

Figure 5.16: Same as Fig. 5.14 but for the RG-A Spring 2019 inbending data set.

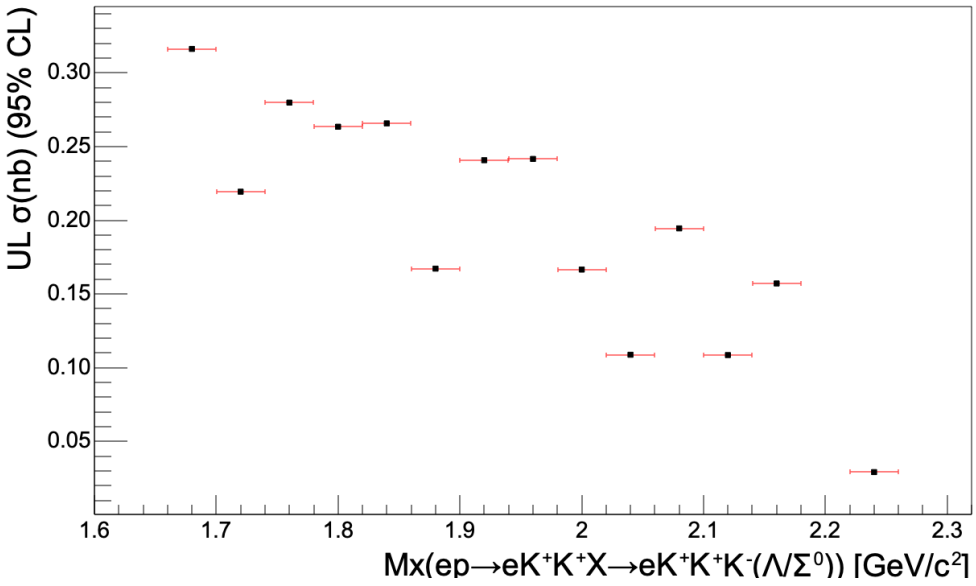

(a) Fall 2018 out FD-e Q^2 : $[0.16, 1.28]$ GeV^2.

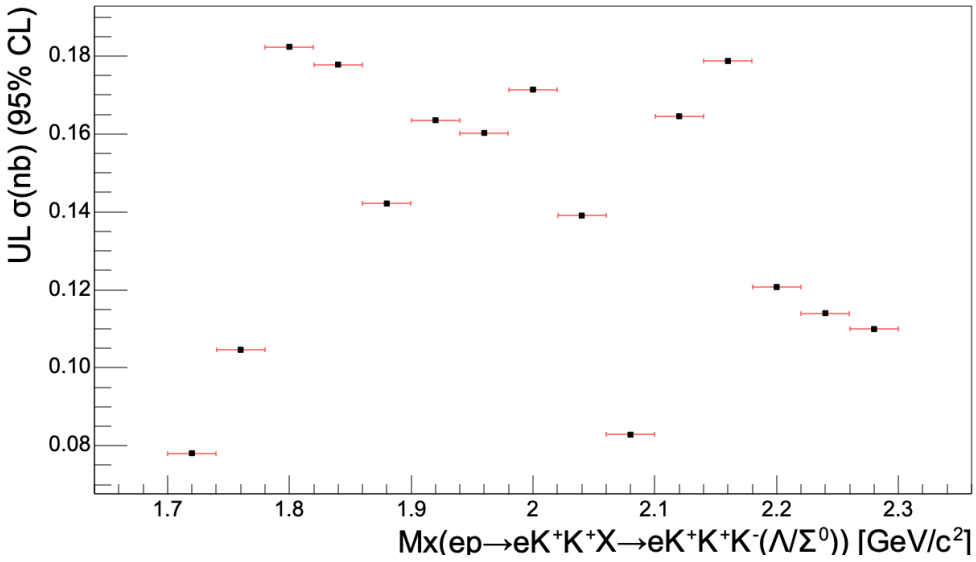

(b) Fall 2018 out FT-e Q^2 : $[0.03, 0.13]$ GeV^2.

Figure 5.17: The 95% confidence level upper limit cross section estimate for the reaction $ep \to e'K^+K^+(\Xi^{*-}) \to e'K^+K^+K^-(\Lambda/\Sigma^0)$ using the RG-A Fall 2018 outbending data set with electrons in the FD (see Fig. 5.17a) and FT (see Fig. 5.17b) for the different intermediate Ξ^{*-} missing mass bins spanning from $1.65 - 2.3$ GeV. The Q^2 coverage for each mass bin of the different plots is indicated in the captions.

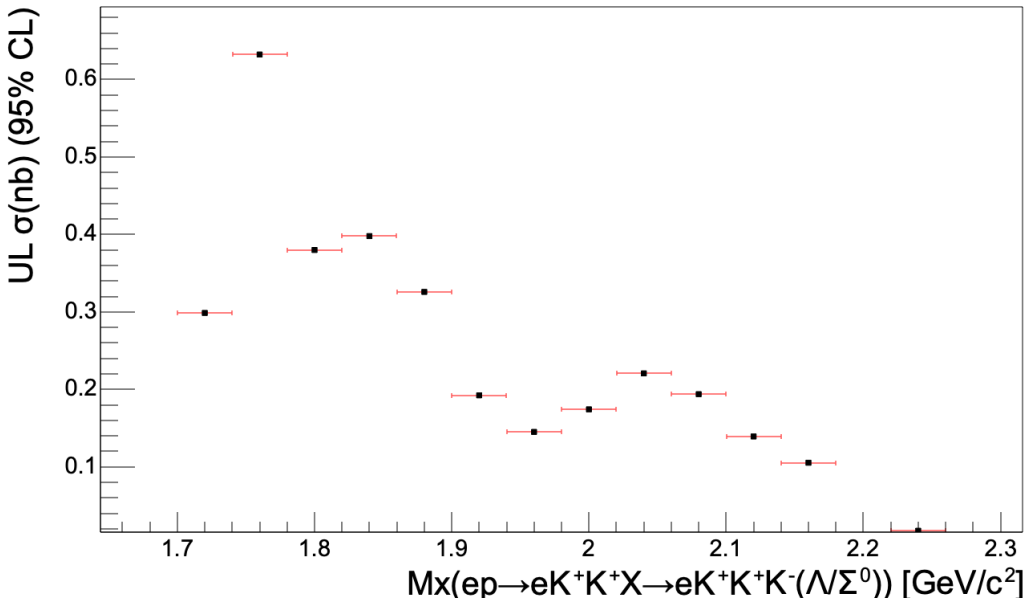

(a) Fall 2018 in FD-e Q^2 : $[1.28, 1.88]$ GeV^2.

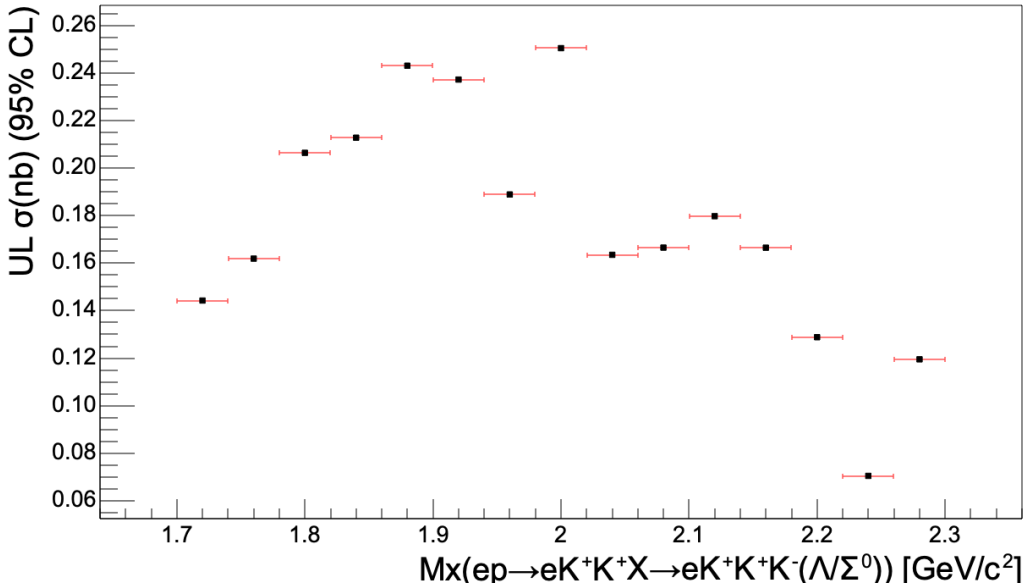

(b) Fall 2018 in FT-e Q^2 : $[0.03, 0.13]$ GeV^2.

Figure 5.18: Same as Fig. 5.17 but for the RG-A Fall 2018 inbending data set.

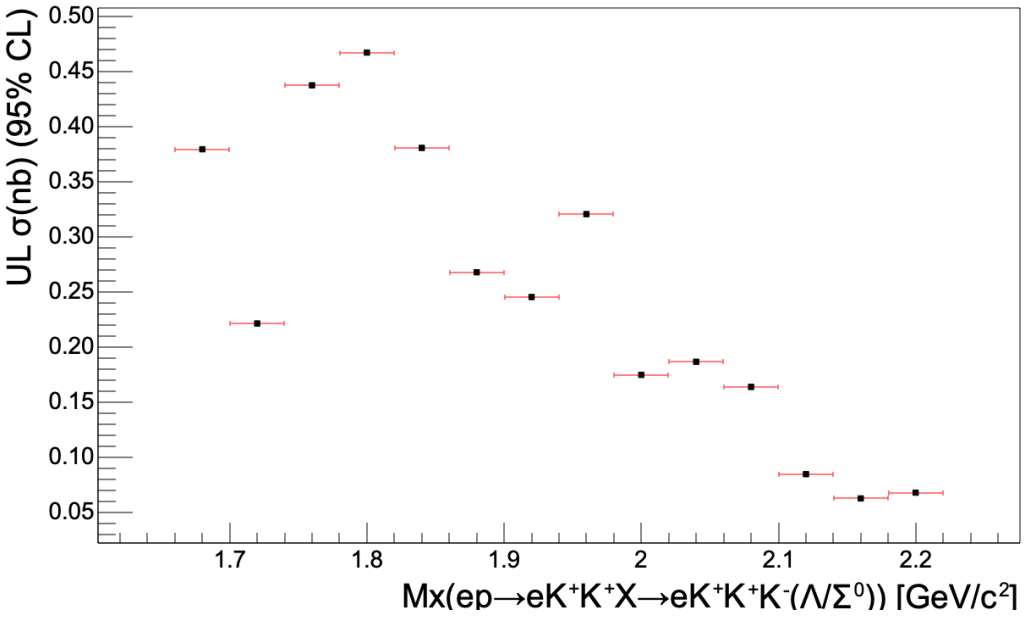

(a) Spring 2019 in FD-e Q^2 : $[1.28, 1.88]$ GeV^2.

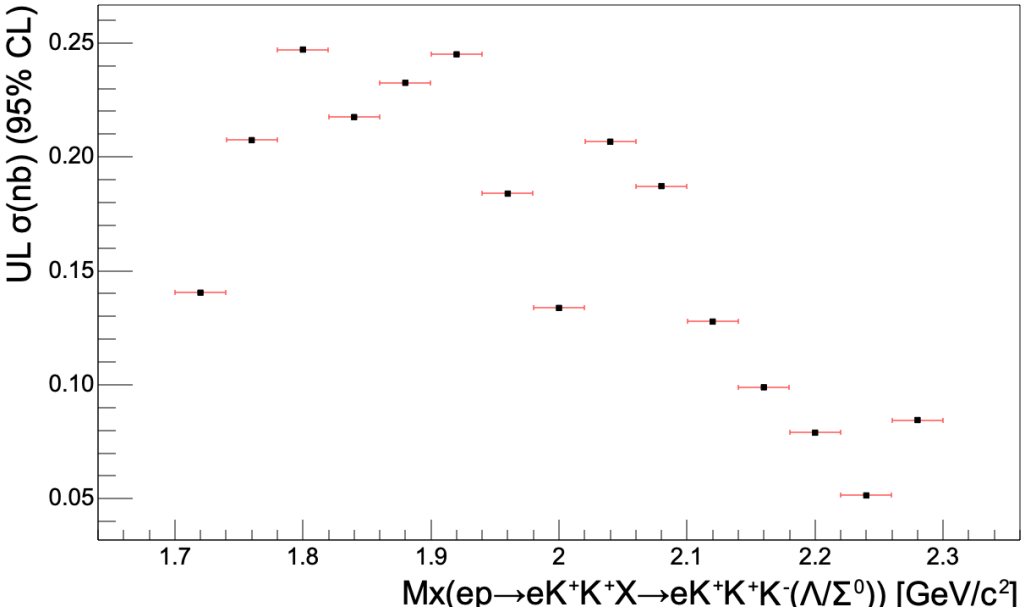

(b) Spring 2019 in FT-e Q^2 : $[0.03, 0.13]$ GeV^2.

Figure 5.19: Same as Fig. 5.17 but for the RG-A Spring 2019 inbending data set.

5.3 Differential Cross Section of the Reaction $ep \rightarrow e'K^+K^+(\Xi^{*-}) \rightarrow e'K^+K^+K^-(\Lambda/\Sigma^0)$ as a Function of Missing Mass

In the previous sections it was seen that the background estimate from the event mixing technique is very promising and provides a smooth background for the missing mass spectra off of $e'K^+K^+$. Therefore, the background estimate from the event mixing technique can be used for the different missing mass bins in the missing spectra as a good estimate of the total background events for that bin coming from all possible sources in an assumption that the background model from the event mixing technique is complete. In so doing, the remaining events in each missing mass bin must be the total signal yield of the electroproduced intermediate Ξ^{*-} states and the difference as a total signal yield can be estimated. The signal yield (Y_i) estimated for the different missing mass bins can then be used in Eq. (5.11) along with the Q^2 dependent reaction reconstruction efficiency (ϵ_i) calculated in Section 4.4 and bin width ($\Delta_i(MM)$) information for that missing mass bin to calculate the differential cross section $\frac{d\sigma}{dMM(e'K^+K^+)}$ as a function of the missing mass $MM(e'K^+K^+)$. The formula used to calculate the differential cross section for the different missing mass bins is given by,

$$\frac{d\sigma}{dMM(e'K^+K^+)} = \frac{Y_i}{\mathcal{L}.\epsilon_i.\Delta_i(MM)}, \tag{5.11}$$

where $\mathcal{L}$ is the integrated luminosity discussed in Section 5.1.2. Since the efficiency used in Eq. (5.11) is calculated for the exclusive process corresponding to the $\Xi^{*-} \rightarrow K^-(\Lambda/\Sigma^0)$ decay mode only, the corresponding differential cross section represents the scaled differential cross section scaled by a factor which is equivalent to the branching fraction for the $\Xi^{*-} \rightarrow K^-(\Lambda/\Sigma^0)$ decay mode.

Figures 5.20 to 5.22 show the differential cross section as a function of the missing mass off of $e'K^+K^+$. The different data sets used have different Q^2 coverages.

In this analysis, the same Q^2 range was used for the different missing mass bins in a given run configuration. The Q^2 bin chosen for the different run configurations was decided by checking the Q^2 vs. $MM(e'K^+K^+K^-)$ plots summarized in Fig. 3.36.

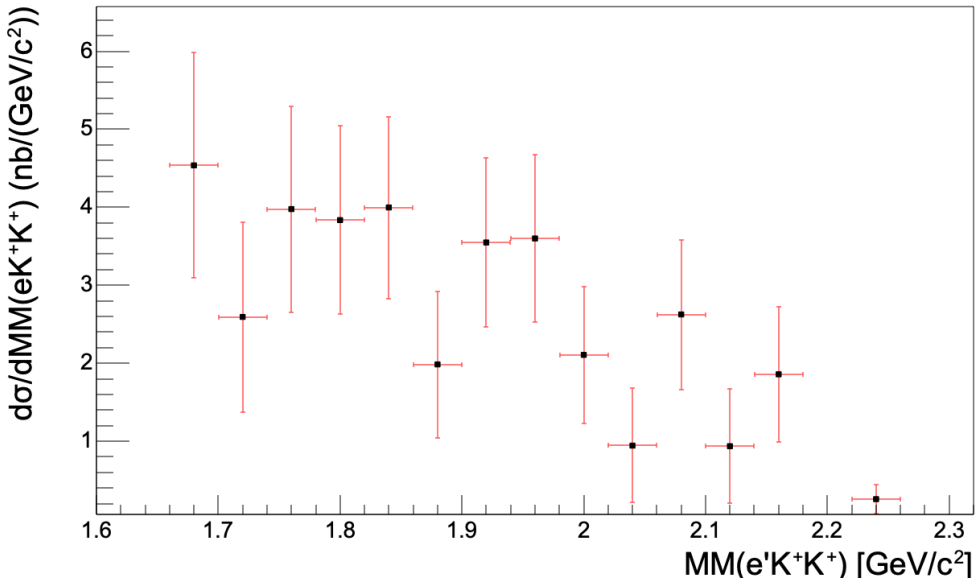

(a) Fall 2018 out FD-e Q^2 : $[0.16, 1.28]$ GeV^2.

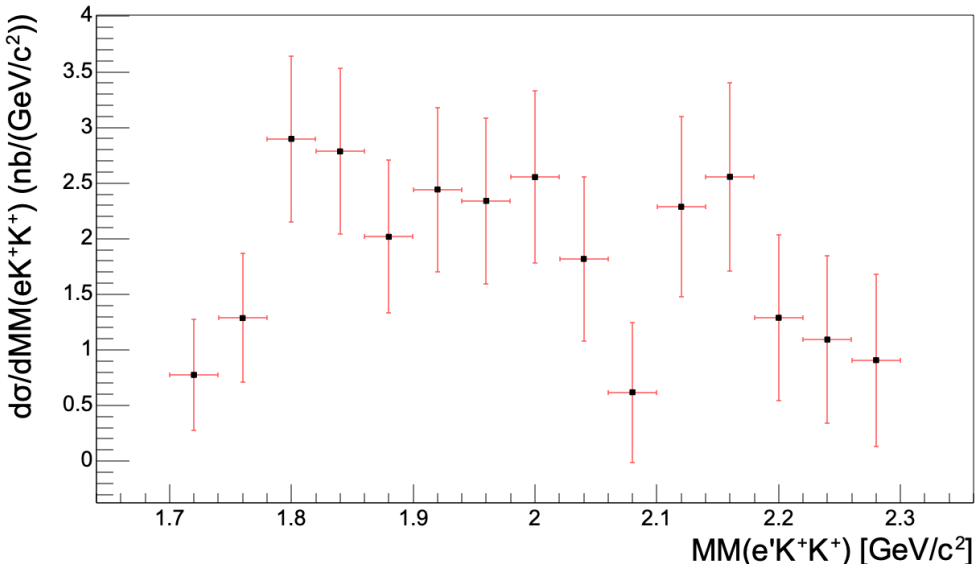

(b) Fall 2018 out FT-e Q^2 : $[0.03, 0.13]$ GeV^2.

Figure 5.20: The differential cross section $\frac{d\sigma}{dMM}$ as a function of $MM(e'K^+K^+)$ missing mass in the reaction $ep \to e'K^+K^+(\Xi^{*-}) \to e'K^+K^+K^-(\Lambda/\Sigma^0)$ using the RG-A Fall 2018 outbending data set with electrons in the FD (see Fig. 5.20a) and FT (see Fig. 5.20b). The Ξ^{*-} mass bins in the exclusive reaction span from $1.65 - 2.3$ GeV. The Q^2 coverage for each mass bin of different plots is indicated in caption of each plot. The error bars on these plots corresponds to statistical uncertainties only.

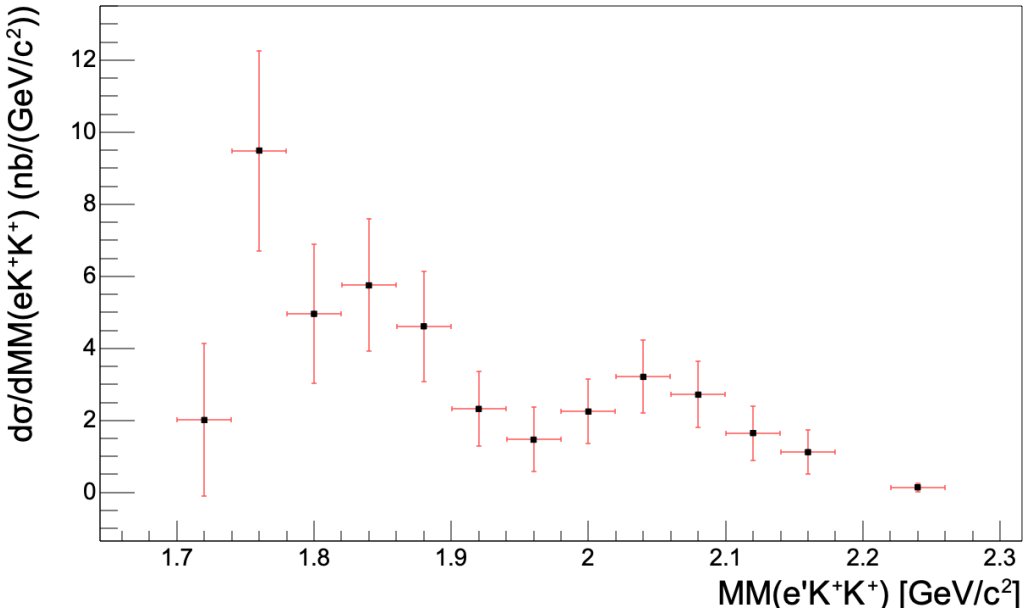

(a) Fall 2018 in FD-e Q^2 : $[1.28, 1.88]$ GeV^2.

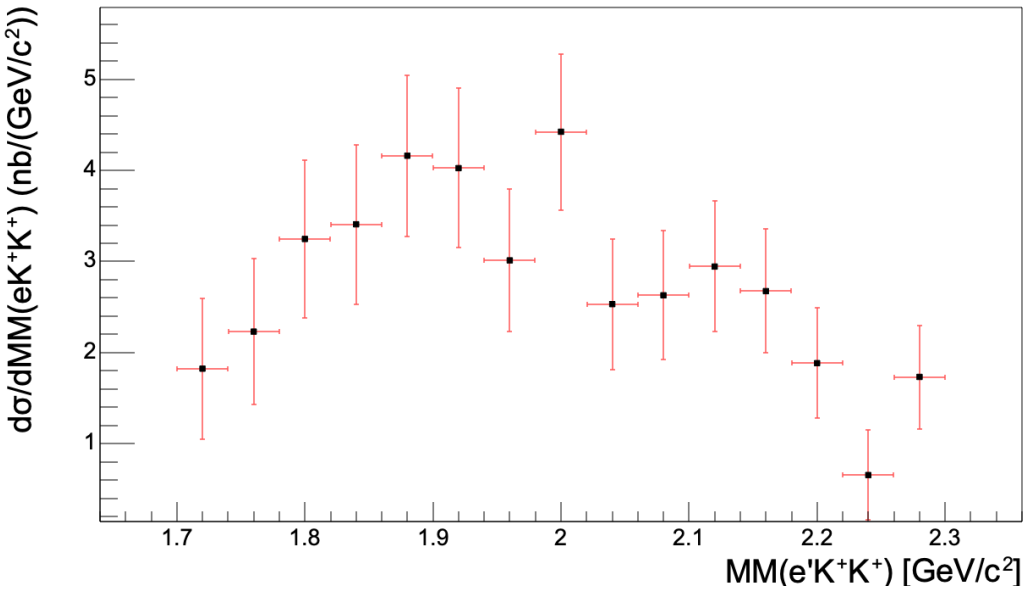

(b) Fall 2018 in FT-e Q^2 : $[0.03, 0.13]$ GeV^2.

Figure 5.21: Same as Fig. 5.20 but for the RG-A Fall 2018 inbending data set.

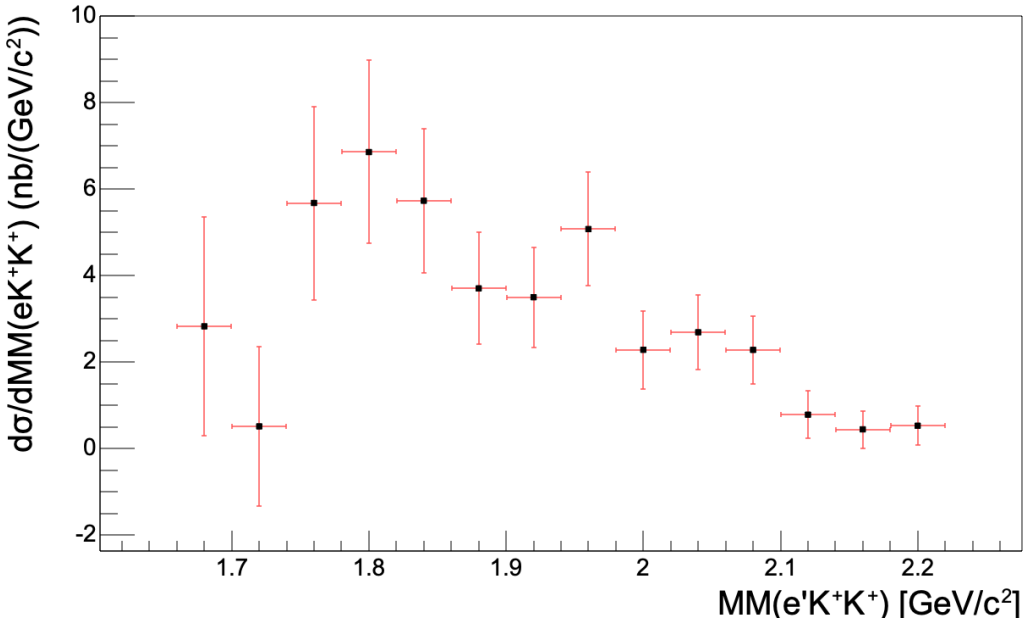

(a) Spring 2019 in FD-e Q^2 : $[1.28, 1.88]$ GeV^2.

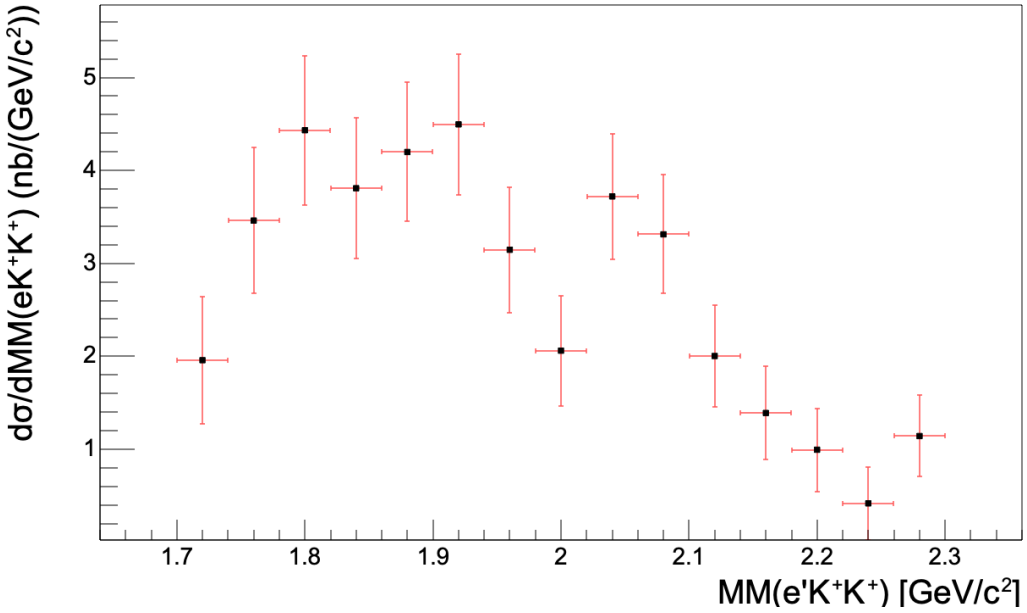

(b) Spring 2019 in FT-e Q^2 : $[0.03, 0.13]$ GeV^2.

Figure 5.22: Same as Fig. 5.20 but for the RG-A Spring 2019 inbending data set.

CHAPTER 6

Results and Discussion

It has been demonstrated that cascade electroproduction can be studied utilizing the CEBAF ~ 11 GeV electron beam incident on a proton target via exclusive reactions such as $ep \rightarrow e'K^+K^+(X)$ using the CLAS12 spectrometer in Hall B JLab. The preliminary study of the reaction $ep \rightarrow e'K^+K^+(X)$, where double strangeness is tagged by detecting two positive kaons in the final state using the CLAS12 Forward Detector system, shows a clear peak of the octet ground state $\Xi^-(1320)$ and an evident peak of the decuplet ground state $\Xi^-(1530)$ (a clear peak with FD-e resolution and a shoulder with FT-e resolution) in the $MM(e'K^+K^+)$ distributions. The observed $\Xi^-(1320)$ and $\Xi^-(1530)$ resonances in this work mark the first time that Cascade states have been seen in the electroproduction process to date. The centroid of the Gaussian fit to the observed $\Xi^-(1320)$ and $\Xi^-(1530)$ resonances in the missing mass distributions was found to be shifted towards higher mass value by $10-18$ MeV than their nominal mass values from the PDG. The known CLAS12 momentum distortions that are present in the pass-1 data sets can contribute to such mass shift. These known momentum distortions observed and understood by analyzing available pass-1 data are being studied and are expected to be minimized in the next pass of the data processing. The major contribution to the observed mass shift can come from the energy loss effects and momentum distortions for the detected electrons and kaons that are not properly accounted for in the reconstruction. There were no statistically significant peaks visible in the missing mass spectrum above the $\Xi^-(1530)$ mass that correspond to any other experimentally known or theoretically predicted Ξ^* states.

The exclusive reaction $ep \rightarrow e'K^+K^+\Xi^{*-} \rightarrow e'K^+K^+K^-(\Lambda/\Sigma^0)$ was investigated by analyzing events with an additional K^- detected in the CLAS12 Forward

Detector system to extensively search for the higher mass Ξ^{*-} states that are accessible with the upgraded 11 GeV CEBAF electron beam energy. Clear evidence of non-separable smeared Λ and Σ^0 hyperons was observed in the missing mass off of the $e'K^+K^+K^-$ system while analyzing the pass-1 RG-A data sets by detecting two K^+, and one K^- tracks in the Forward Detector with the scattered electron in the FT and FD. The momentum resolution in the pass-1 data for the particle tracks reconstructed in the Central Detector is such that the $MM(e'K^+K^+K^-)$ missing mass spectrum did not show a Λ/Σ^0 hyperon peak if any one of the charged kaon tracks was detected in the Central Detector. No statistically significant higher mass Ξ^{*-} states above the $\Xi^-(1530)$ mass that decay to K^- and Λ/Σ^0 hyperons were observed by analyzing the currently available data.

Further study to establish the upper limit on the production cross section of the $\Xi^{*-}(1820)$ state for low-Q^2 $(0.03 - 0.13$ GeV$^2)$ quasi-real photoproduction and high-Q^2 $(0.16 - 1.28$ and $1.28 - 2.88$ GeV$^2)$ electroproduction processes was performed. The 95% confidence level upper limit on the $\Xi^{*-}(1820)$ yield was estimated from the different data sets using the maximum log-likelihood test for counts and fit statistics. The maximum log-likelihood test implemented the technique of a hypothesis test to estimate the statistical significance of the true $\Xi^{*-}(1820)$ signal by considering the statistical fluctuation of the background counts as well as that of the signal counts to determine the proper confidence level boundaries for statistically insignificant signals hidden under an extensive background with a constraint that the true $\Xi^{*-}(1820)$ signal is either positive or zero. The 95% confidence level upper-limit yields, along with the CLAS12 detection efficiency derived from the GEMC simulation, were then used to set the upper limits on the electroproduction cross section of the reaction $ep \rightarrow e'K^+K^+\Xi^{*-}(1820) \rightarrow e'K^+K^+K^-(\Lambda/\Sigma^0)$. Table 5.8 summarizes the upper-limit results on the production cross section of the reaction.

The extracted preliminary electroproduction upper limit cross section result is estimated to be around 0.3 nb by investigating the $\Xi^{*-}(1820) \rightarrow K^{-}(\Lambda/\Sigma^{0})$ decay mode. This estimate does not include any systematic uncertainties associated with the measurement process. As expected, the upper limit cross section result is found to be small. The electroproduction process on the proton target requires the formation of two $s\bar{s}$ quark pairs from the vacuum to create the $\Xi^{*-}(1820)$ ($S = 2$) in the final state when there are no strange quarks in the initial state. The overall change in baryon strangeness number ($\Delta S = 2$) from the initial to the final state is one of the causes for a small cross section result. Such physics processes are rare and demand high-energy probes to occur in experiments. The electroproduction result obtained in this study is consistent with the reported photoproduction result from the CLAS $g12$ experiment. In both cases, the signal for the higher mass Ξ^{*-} states above the 1530 MeV mass are not visible in the missing mass spectrum, and the cross section of the $\Xi^{*-}(1820)$ production is estimated to be < 1 nb. The CLAS $g12$ experiment reports a value of 0.73 nb (1 nb with an overall scale factor of 34% applied to account for the possible systematic uncertainties associated in the measurement) for the 90% confidence level upper limit photoproduction total cross section of the $\Xi^{*-}(1820)$ state in the process $\gamma p \rightarrow K^{+}K^{+}\Xi^{*-}(1820)$ (see Ref. [88]). Such evidence for the small production cross section of the $\Xi^{*-}(1820)$ state is poorly understood in the electroproduction and photoproduction processes. This clearly indicates the lack of current theoretical knowledge to explain the production mechanism of the higher mass Ξ^{*-} states and demands more precise theoretical calculations and explanations in the future.

Finally, the electroproduction upper limit cross section as a function of the electroproduced Ξ^{*-} mass and the differential electroproduction cross section $\frac{d\sigma}{dMM(e'K^{+}K^{+})}$ as a function of $MM(e'K^{+}K^{+})$ were investigated by implementing the event mixing

technique to estimate the average background in different missing mass bins and with the assumption that the background model from the event mixing technique is complete. Figures 5.14 to 5.22 summarize the 95% upper limit yield, upper limit cross section, and differential cross section results for the different Q^2 coverage.

As more data become available for analysis in the future (an order of magnitude more statistics expected in total), the preliminary cross section results obtained in this study will continue to evolve. The major boost in the statistics for the study from the currently available data sets is expected to come in the next pass of the data processing. Significant advancements in the Central Detector tracking, improved particle identification, momentum corrections, and good knowledge of the alignment of the Forward Detector, Central Detector, and Forward Tagger in the next pass of the data processing will allow improvement in this analysis by combining tracks from the Central Detector as well. Improved efficiency studies have to be performed in the future by implementing realistic model dependency in the simulation, which will allow for a better understanding of the theoretically proposed Ξ^{*-} production mechanism. The momentum smearing method implemented in this analysis to reproduce the data missing mass resolution in the MC simulation is very preliminary. A single momentum smearing factor was used for particles irrespective of their momentum and scattering angle range. Additional work to compare particle momenta as well as angular distributions is necessary in the future once more statistics are available to fine tune the MC simulations so that they better reproduce the data distributions with reduced systematic uncertainties.

Bibliography

[1] R. W. McAllister and R. Hofstadter. Elastic scattering of 188-MeV electrons from the proton and the alpha particle. *Phys. Rev.*, 102:851–856, May 1956.

[2] M. R. Yearian and R. Hofstadter. Magnetic form factor of the neutron. *Phys. Rev.*, 110:552–564, Apr 1958.

[3] Y. Ne'eman. Derivation of strong interactions from a gauge invariance. *Nuclear Physics*, 26(2):222–229, 1961.

[4] M. Gell-Mann. A schematic model of baryons and mesons. *Phys. Lett.*, 8(3):214–215, 1964.

[5] M. Gell-Mann and Y. Ne'eman. *The eightfold way: a review, with a collection of reprints*. Frontiers in physics. W.A. Benjamin, 1964.

[6] V. E. Barnes *et al.* Observation of a hyperon with strangeness minus three. *Phys. Rev. Lett.*, 12:204–206, Feb 1964.

[7] Wikimedia Commons: MissMJ. Standard Model of Elementary Particles, 2021. Available online at https://upload.wikimedia.org/wikipedia/commons/0/00/Standard_Model_of_Elementary_Particles.svg. Accessed: 26-November-2021.

[8] M. Gell-Mann. Symmetries of baryons and mesons. *Phys. Rev.*, 125:1067–1084, Feb 1962.

[9] B. R. Stella and H.-J. Meyer. γ(9.46 GeV) and the gluon discovery (a critical recollection of PLUTO results). *Eur. Phys. J.*, H36:203–243, 2011.

[10] C. N. Yang and R. L. Mills. Conservation of isotopic spin and isotopic gauge invariance. *Phys. Rev.*, 96:191–195, Oct 1954.

[11] H. David Politzer. Reliable perturbative results for strong interactions? *Phys. Rev. Lett.*, 30:1346–1349, Jun 1973.

[12] David J. Gross and Frank Wilczek. Ultraviolet behavior of non-abelian gauge theories. *Phys. Rev. Lett.*, 30:1343–1346, Jun 1973.

[13] F. Halzen and A.D. Martin. *QUARK & LEPTONS: AN INTRODUCTORY COURSE IN MODERN PARTICLE PHYSICS*. Wiley India Pvt. Limited, 2008.

[14] Kenneth G. Wilson. Confinement of quarks. *Phys. Rev. D*, 10:2445–2459, Oct 1974.

[15] M. Tanabashi *et al.* (Particle Data Group). Review of Particle Physics. *Phys. Rev. D*, 98:030001, 2018.

[16] S. Capstick and W. Roberts. Quark models of baryon masses and decays. *Progress in Particle and Nuclear Physics*, 45:S241–S331, 2000.

[17] N. P. Samios, M. Goldberg, and B. T. Meadows. Hadrons and SU(3): A critical review. *Rev. Mod. Phys.*, 46:49–81, Jan 1974.

[18] L.Ya. Glozman and D.O. Riska. The spectrum of the nucleons and the strange hyperons and chiral dynamics. *Physics Reports*, 268(4):263–303, 1996.

[19] R. Bijker, F. Iachello, and A. Leviatan. Algebraic Models of Hadron Structure: II. Strange Baryons. *Annals of Physics*, 284(1):89–133, 2000.

[20] J. W. Price. *Cascade Physics: a New Window on Baryon Spectroscopy*. NSTAR 2005: Preceedings of the Workshop on the Physics of Excited Nucleons, 2005.

[21] Robert G. Edwards, Nilmani Mathur, David G. Richards, and Stephen J. Wallace. Flavor structure of the excited baryon spectra from lattice QCD. *Phys. Rev. D*, 87:054506, Mar 2013.

[22] K. A. Olive *et al.* The Review of Particle Physics. *Chin. Phys. C*, 38:090001, 2014.

[23] J. Richard Hubbard, J. Peter Berge, George R. Kalbfleisch, Janice B. Shafer, Frank T. Solmitz, M. Lynn Stevenson, Stanley G. Wocjicki, and Peter G. Wohlmut. Lifetimes of the Ξ^- and Ξ^0 hyperons. *Phys. Rev.*, 135:B183–B187, Jul 1964.

[24] J. Peter Berge, Philippe Eberhard, J. Richard Hubbard, Deane W. Merrill, J. Button-Shafer, Frank T. Solmitz, and M. Lynn Stevenson. Some properties of Ξ^- and Ξ^0 hyperons produced in K^-p interactions between 1.05 and 1.7 BeV/c. *Phys. Rev.*, 147:945–961, Jul 1966.

[25] Deane W. Merrill and Janice Button-Shafer. Properties of the Ξ^- and the $\Xi^*(1817)$ from K^-p interactions above 1.7 BeV/c. *Phys. Rev.*, 167:1202–1224, Mar 1968.

[26] Philip M. Dauber, J. Peter Berge, J. Richard Hubbard, Deane W. Merrill, and Richard A. Muller. Production and decay of cascade hyperons. *Phys. Rev.*, 179:1262–1285, Mar 1969.

[27] E. L. Goldwasser and P. F. Schultz. Ξ^- production in 5.5-GeV/c K^-p interactions. *Phys. Rev. D*, 1:1960–1966, Apr 1970.

[28] J. Alitti, E. Flaminio, W. Metzger, D. Radojicic, R. R. Rau, N. P. Samios, I. Skillicorn, C. R. Richardson, D. Bassano, M. Goldberg, and J. Leitner. Evidence for Ξ^* resonance with mass 1930 MeV. *Phys. Rev. Lett.*, 21:1119–1123, Oct 1968.

[29] J. Alitti, V. E. Barnes, E. Flaminio, W. Metzger, D. Radojičić, R. R. Rau, C. R. Richardson, N. P. Samios, D. Bassano, M. Goldberg, and J. Leitner. Strangeness $S = -2$ baryon resonance. *Phys. Rev. Lett.*, 22:79–82, Jan 1969.

[30] S. Apsell, N. Barash-Schmidt, L. Kirsch, P. Schmidt, C. Y. Chang, R. J. Hemingway, B. V. Khoury, A. R. Stottlemyer, H. Whiteside, G. B. Yodh, M. Goldberg, K. Jaeger, C. McCarthy, B. Meadows, G. C. Moneti, J. Bartley, R. M. Dowd, J. Schneps, and G. Wolsky. Ξ resonances in $K^-p \to \Xi\pi K$ at 2.87 gev/c. *Phys. Rev. Lett.*, 23:884–886, Oct 1969.

[31] S. Apsell, N. Barash-Schmidt, L. Kirsch, P. Schmidt, C. Y. Chang, R. J. Hemingway, B. V. Khoury, A. R. Stottlemyer, H. Whiteside, G. B. Yodh, S. Glickman, M. Goldberg, S. Jacobs, K. Jaeger, C. McCarthy, B. Meadows, G. C. Moneti, J. Bartley, R. M. Dowd, J. Schneps, and G. Wolsky. Evidence for Ξ resonances in the $\Xi(1530)\pi$ system. *Phys. Rev. Lett.*, 24:777–781, Apr 1970.

[32] C. Dionisi, J. Diaz, R. Armenteros, Ph. Gavillet, A. Gurtu, R.J. Hemingway, M. Mazzucato, R. Blokzijl, J.C. Kluyver, G.G.G. Massaro, W.J. Metzger, J. Schotanus, H.G. Tiecke, B. Foster, P.R. Lamb, and W.L. McDowell. An enhancement at the ΣK threshold (1680) MeV observed in K^-p reactions at 4.2 GeV/c. *Physics Letters B*, 80(1):145–149, 1978.

[33] D. Teodoro, J. Diaz, C. Dionisi, J.B. Gay, R.J. Hemingway, M.J. Losty, M. Mazzucato, R. Blokzijl, G.G.G. Massaro, H. Voorthuis, W.J. Metzger, J.J.M. Timmermans, R.T. van de Walle, B. Foster, P. Grossmann, and W.L. McDowell. A spin determination of the $\Xi^*(1820)$ resonance. *Physics Letters B*, 77(4):451–453, 1978.

[34] M. Bourquin and J.-P. Repellin. Experiments with the CERN SPS hyperon beam. *Physics Reports*, 114(2):99–180, 1984.

[35] S. F. Biagi *et al.* Production of Hyperons and Hyperon Resonances in Ξ^-N Interactions at 102 and 135 GeV/c. *Z. Phys. C − Particles and Fields*, 9:305–314, 1981.

[36] S. F. Biagi *et al.* Ξ^* Resonances in Ξ^-Be Interactions I. Diffractive Production in the ΛK^- and $\Xi^-\pi^+\pi^-$ Channels. *Z. Phys. C − Particles and Fields*, 34:15–22, 1987.

[37] S. F. Biagi *et al.* Ξ^* Resonances in Ξ^-Be Interactions II. Properties of $\Xi(1820)$ and $\Xi(1960)$ in the $\Lambda\bar{K}^0$ and $\Sigma^0\bar{K}^0$ Channels. *Z. Phys. C − Particles and Fields*, 34:175–185, 1987.

[38] C. M. Jenkins, J. R. Albright, R. N. Diamond, H. Fenker, J. H. Goldman, S. Hagopian, V. Hagopian, W. Morris, L. Kirsch, R. Poster, P. Schmidt, S. U.

Chung, R. C. Fernow, H. Kirk, S. D. Protopopescu, D. P. Weygand, B. T. Meadows, Z. Bar-Yam, J. Dowd, W. Kern, and M. Winik. Existence of Ξ Resonances above 2 GeV. *Phys. Rev. Lett.*, 51:951–954, Sep 1983.

[39] L. Guo *et al.* (CLAS Collaboration). Cascade production in the reactions $\gamma p \to K^+K^+(x)$ and $\gamma p \to K^+K^+\pi^-(x)$. *Phys. Rev. C*, 76:025208, Aug 2007.

[40] K. Nakayama, Yongseok Oh, and H. Haberzettl. Photoproduction of Ξ off nucleons. *Phys. Rev. C*, 74:035205, Sep 2006.

[41] J. W. Price *et al.* (CLAS Collaboration). Exclusive photoproduction of the Cascade (Ξ) hyperons. *Phys. Rev. C*, 71:058201, May 2005.

[42] J. T. Goetz *et al.* (CLAS Collaboration). Ξ^* photoproduction from threshold to $W = 3.3$ GeV. *Phys. Rev. C*, 98:062201, Dec 2018.

[43] Jefferson Lab. CEBAF at Jefferson Lab, 2022. Available online at https://www.jlab.org/brochures. Accessed: 26-March-2022.

[44] V.D. Burkert *et al.* (CLAS Collaboration). The CLAS12 Spectrometer at Jefferson Laboratory. *Nuclear Instruments and Methods in Physics Research Section A: Accelerators, Spectrometers, Detectors and Associated Equipment*, 959:163419, 2020.

[45] C. W. Leemann *et al.* THE CONTINUOUS ELECTRON BEAM ACCELERATOR FACILITY: CEBAF at the Jefferson Laboratory. *Annual Review of Nuclear and Particle Science*, 51(1):413–450, 2001.

[46] R. Kazimi. Simultaneous Four-hall Operation for 12 GeV CEBAF. In *4th International Particle Accelerator Conference*, page THPFI091, 2013.

[47] N. Baltzell *et al.* The CLAS12 beamline and its performance. *Nuclear Instruments and Methods in Physics Research Section A: Accelerators, Spectrometers, Detectors and Associated Equipment*, 959:163421, 2020.

[48] R. Fair *et al.* The CLAS12 superconducting magnets. *Nuclear Instruments and Methods in Physics Research Section A: Accelerators, Spectrometers, Detectors and Associated Equipment*, 962:163578, 2020.

[49] M.D. Mestayer *et al.* The CLAS12 drift chamber system. *Nuclear Instruments and Methods in Physics Research Section A: Accelerators, Spectrometers, Detectors and Associated Equipment*, 959:163518, 2020.

[50] Y.G. Sharabian *et al.* The CLAS12 high threshold Cherenkov counter. *Nuclear Instruments and Methods in Physics Research Section A: Accelerators, Spectrometers, Detectors and Associated Equipment*, 968:163824, 2020.

[51] M. Ungaro *et al.* The CLAS12 Low Threshold Cherenkov detector. *Nuclear Instruments and Methods in Physics Research Section A: Accelerators, Spectrometers, Detectors and Associated Equipment*, 957:163420, 2020.

[52] M. Contalbrigo *et al.* The CLAS12 Ring Imaging Cherenkov detector. *Nuclear Instruments and Methods in Physics Research Section A: Accelerators, Spectrometers, Detectors and Associated Equipment*, 964:163791, 2020.

[53] D.S. Carman *et al.* The CLAS12 Forward Time-of-Flight system. *Nuclear Instruments and Methods in Physics Research Section A: Accelerators, Spectrometers, Detectors and Associated Equipment*, 960:163629, 2020.

[54] B.A. Mecking *et al.* The CEBAF large acceptance spectrometer (CLAS). *Nuclear Instruments and Methods in Physics Research Section A: Accelerators, Spectrometers, Detectors and Associated Equipment*, 503(3):513–553, 2003.

[55] G. Asryan *et al.* The CLAS12 forward electromagnetic calorimeter. *Nuclear Instruments and Methods in Physics Research Section A: Accelerators, Spectrometers, Detectors and Associated Equipment*, 959:163425, 2020.

[56] A. Acker *et al.* The CLAS12 Forward Tagger. *Nuclear Instruments and Methods in Physics Research Section A: Accelerators, Spectrometers, Detectors and Associated Equipment*, 959:163475, 2020.

[57] The CLAS12 Collaboration at Jefferson Laboratory. CLAS12 Forward Tagger (FT) Technical Design Report, 2012. Available online at https://www.ge.infn.it/~batta/jlab/ft-tdr.2.2.pdf. Accessed:22-May-2022.

[58] M.A. Antonioli *et al.* The CLAS12 Silicon Vertex Tracker. *Nuclear Instruments and Methods in Physics Research Section A: Accelerators, Spectrometers, Detectors and Associated Equipment*, 962:163701, 2020.

[59] A. Acker *et al.* The CLAS12 Micromegas Vertex Tracker. *Nuclear Instruments and Methods in Physics Research Section A: Accelerators, Spectrometers, Detectors and Associated Equipment*, 957:163423, 2020.

[60] D.S. Carman *et al.* The CLAS12 Central Time-of-Flight system. *Nuclear Instruments and Methods in Physics Research Section A: Accelerators, Spectrometers, Detectors and Associated Equipment*, 960:163626, 2020.

[61] S. Niccolai *et al.* The central neutron detector for CLAS12. *Nuclear Instruments and Methods in Physics Research Section A: Accelerators, Spectrometers, Detectors and Associated Equipment*, 904:81–92, 2018.

[62] P. Chatagnon *et al.* The CLAS12 Central Neutron Detector. *Nuclear Instruments and Methods in Physics Research Section A: Accelerators, Spectrometers, Detectors and Associated Equipment*, 959:163441, 2020.

[63] S. Boyarinov *et al.* The CLAS12 Data Acquisition System. *Nuclear Instruments and Methods in Physics Research Section A: Accelerators, Spectrometers, Detectors and Associated Equipment*, 966:163698, 2020.

[64] B. Raydo *et al.* The CLAS12 Trigger System. *Nuclear Instruments and Methods in Physics Research Section A: Accelerators, Spectrometers, Detectors and Associated Equipment*, 960:163529, 2020.

[65] Valery Kubarovsky. CLAS12 trigger, 2022. Available online at https://misportal.jlab.org/mis/physics/clas12/viewFile.cfm/2022-001.pdf?documentId=78.

[66] V. Ziegler *et al.* The CLAS12 software framework and event reconstruction. *Nuclear Instruments and Methods in Physics Research Section A: Accelerators, Spectrometers, Detectors and Associated Equipment*, 959:163472, 2020.

[67] CLAS Collaboration at Jefferson Laboratory. CLAS12 DSTs, 2022. Available online at https://clasweb.jlab.org/wiki/index.php/CLAS12_DSTs. Accessed: 27-January-2022.

[68] CLAS Collaboration at Jefferson Laboratory. CLAS12 Offline Software, 2022. Available online at https://github.com/JeffersonLab/clas12-offline-software. Accessed: 29-April-2022.

[69] CLAS Collaboration at Jefferson Laboratory. CLAS12 Event Builder, 2022. Available online at https://clasweb.jlab.org/wiki/index.php/CLAS12_EventBuilder. Accessed: 27-January-2022.

[70] CLAS Collaboration at Jefferson Laboratory. CLAS12 RG-A - Analysis Note Overview and Procedures Phase I Towards SIDIS CLAS12 First Publications, 2022. Available online at https://clas12-docdb.jlab.org/DocDB/0008/000897/001/RGA_Analysis_Overview_and_Procedures-23.pdf.

[71] CLAS Collaboration at Jefferson Laboratory. CLAS12 monitoring tool, 2022. Available online at https://clas12mon.jlab.org/runs/summaries/. Accessed: 15-September-2022.

[72] Jefferson Lab. Hall B RCDB, 2022. Available online at https://clasweb.jlab.org/rcdb#.

[73] Maurik Holtrop. Rundata/rundata, 2022. Available online at https://github.com/mholtrop/RunData/tree/master/RunData. Accessed: 15-September-2022.

[74] Jefferson Lab. Jeffersonlab/grapes, 2022. Available online at https://github.com/JeffersonLab/grapes/tree/master/src/main/java/org/jlab/jnp/grapes/services.

[75] S. Diehl and CLAS Collaboration at Jefferson Laboratory. ECAL sub-sampling fraction studies for pass 2, 2022. Available online at https://clasweb.jlab.org/wiki/images/1/1c/Sampling_fraction_monitoring.pdf. Accessed: 22-May-2022.

[76] CLAS Collaboration at Jefferson Laboratory. CLAS12 Drift Chamber Fiducial Cut Study, 2022. Available online at https://clas12-docdb.jlab.org/DocDB/0006/000609/006/CLAS12_PID_fiducial.pdf and https://clas12-docdb.jlab.org/DocDB/0006/000609/006/DC_fiducial.pdf. Accessed: 22-May-2022.

[77] M. Ungaro *et al.* The CLAS12 Geant4 simulation. *Nuclear Instruments and Methods in Physics Research Section A: Accelerators, Spectrometers, Detectors and Associated Equipment*, 959:163422, 2020.

[78] CLAS Collaboration at Jefferson Laboratory. gemc/clas12tags/4.4.2, 2022. Available online at https://github.com/gemc/clas12Tags/tree/master/4.4.2. Accessed: 23-March-2022.

[79] Derek Glazier. clas12-elspectro, 2022. Available online at https://github.com/dglazier/clas12-elSpectro.git. Accessed: 29-April-2022.

[80] CLAS Collaboration at Jefferson Laboratory. CLAS12 FD charge particle reconstruction efficiency and the beam background merging, 2022. Available online at https://misportal.jlab.org/mis/physics/clas12/viewFile.cfm/2020-005.pdf?documentId=70.

[81] R. L. Workman and V. D. Burkert *et al.* (Particle Data Group). Review of Particle Physics. *Progress of Theoretical and Experimental Physics*, 2022(8), 08 2022. 083C01.

[82] C. Deil *et al.* Gammapy - A prototype for the CTA science tools. In *35th International Cosmic Ray Conference (ICRC2017)*, volume 301 of *International Cosmic Ray Conference*, page 766, January 2017.

[83] W. Cash. Parameter estimation in astronomy through application of the likelihood ratio. *Astrophysical Journal*, 228:939–947, March 1979. Provided by the SAO/NASA Astrophysics Data System.

[84] S. S. Wilks. The Large-Sample Distribution of the Likelihood Ratio for Testing Composite Hypotheses. *The Annals of Mathematical Statistics*, 9(1):60 – 62, 1938.

[85] T. P. Li and Y. Q. Ma. Analysis methods for results in gamma-ray astronomy. *Astrophysical Journal*, 272:317–324, September 1983. Provided by the SAO/NASA Astrophysics Data System.

[86] D. S. Carman, K. Park, and B. A. Raue. Differential Cross Sections and Separated Structure Function Extractions from e1f for the Reactions $p(\vec{e}, e'K^+)\Lambda$ and $p(\vec{e}, e'K^+)\Sigma^0$, 2012. Available online at https://clasweb.jlab.org/rungroups/e1f/carman/e1f-note-v3.pdf.

[87] A. Celentano. *The Forward Tagger detector for CLAS12 at Jefferson Laboratory and the MesonEx experiment*. PhD Thesis: Universita degli Studi di Genova Facolta di Scienze M.F.N., 2014. Available online at https://www.jlab.org/Hall-B/general/thesis/Celentano_thesis.pdf.

[88] J.T. Goetz. *Ξ Hyperon Photoproduction from Threshold to 5.4 GeV with the CEBAF Large Acceptance Spectrometer*. PhD Thesis: University of California, Los Angeles, 2010. Available online at https://www.jlab.org/Hall-B/general/thesis/Goetz_thesis.pdf.

APPENDIX

A.1 List of Good Runs

1) Good run lists for the RG-A Fall 2018 outbending data set (34.08 mC): 5666 5665 5664 5663 5662 5656 5655 5654 5652 5651 5650 5649 5648 5647 5646 5645 5644 5643 5641 5639 5638 5637 5635 5633 5632 5631 5630 5629 5628 5626 5625 5624 5623 5621 5619 5618 5616 5615 5614 5613 5612 5611 5607 5606 5603 5602 5601 5598 5597 5594 5592 5591 5578 5577 5574 5573 5572 5571 5570 5569 5567 5562 5561 5559 5558 5557 5556 5555 5554 5552 5551 5550 5549 5548 5547 5546 5545 5544 5543 5541 5540 5538 5537 5536 5535 5534 5533 5532 5530 5528 5527 5526 5525 5524 5523 5522 5521 5520 5519 5518 5517 5516 5507 5505 5500 5499 5498 5497 5487 5486 5485 5483 5482 5481 5480 5479 5478 5476 5475 5474 5473 5472 5471 5470 5469 5468 5467 5466 5465 5464 5460 5456 5455 5454 5453 5452 5451 5450 5449 5448 5447 5445 5441 5440 5438 5437 5436 5435 5434 5432 5430 5429 5426 5425 5424 5423

2) Good run lists for the RG-A Fall 2018 inbending data set (37.06 mC): 5036 5038 5039 5040 5041 5043 5045 5046 5047 5051 5052 5053 5116 5117 5119 5120 5124 5125 5126 5127 5128 5129 5130 5137 5139 5153 5158 5159 5162 5163 5165 5166 5167 5168 5169 5180 5181 5182 5183 5190 5191 5193 5194 5195 5196 5197 5198 5199 5200 5201 5202 5203 5204 5205 5206 5208 5211 5212 5215 5216 5219 5220 5221 5222 5223 5230 5231 5232 5233 5234 5235 5237 5238 5247 5248 5249 5250 5252 5253 5257 5258 5259 5261 5262 5303 5304 5305 5306 5307 5310 5311 5315 5317 5318 5319 5320 5324 5325 5333 5334 5339 5341 5342 5343 5344 5345 5346 5347 5349 5351 5354 5355 5356 5357 5358 5359 5360 5361 5362 5366 5367 5368 5369 5372 5373 5374 5375 5376 5377 5378 5379 5380 5381 5383 5386 5390 5391 5392 5393 5394 5398 5400 5401 5403 5404 5406 5407

3) Good run lists for the RG-A Spring 2019 inbending data set (50.53 mC): 6619 6620 6631 6632 6636 6637 6638 6639 6640 6642 6645 6647 6648 6650 6651 6652 6654 6655 6656 6657 6658 6660 6661 6662 6663 6664 6665 6666 6667 6668 6669 6670 6672 6673 6675 6676 6677 6678 6680 6682 6683 6684 6685 6687 6688 6689 6691 6692 6693 6694 6695 6696 6697 6698 6699 6704 6705 6706 6707 6708 6709 6710 6711 6712 6713 6714 6715 6716 6717 6718 6719 6728 6729 6730 6731 6732 6733 6734 6736 6737 6738 6739 6740 6741 6742 6743 6744 6746 6747 6748 6749 6750 6753 6754 6755 6756 6757 6759 6760 6762 6763 6764 6765 6767 6768 6769 6775 6776 6777 6778 6779 6780 6781 6783

A.2 Preliminary Missing Mass Distributions: Kaons Detected in the CLAS12 (FD/CD)

Preliminary $MM(e'K^+K^+K^-)$ Distributions

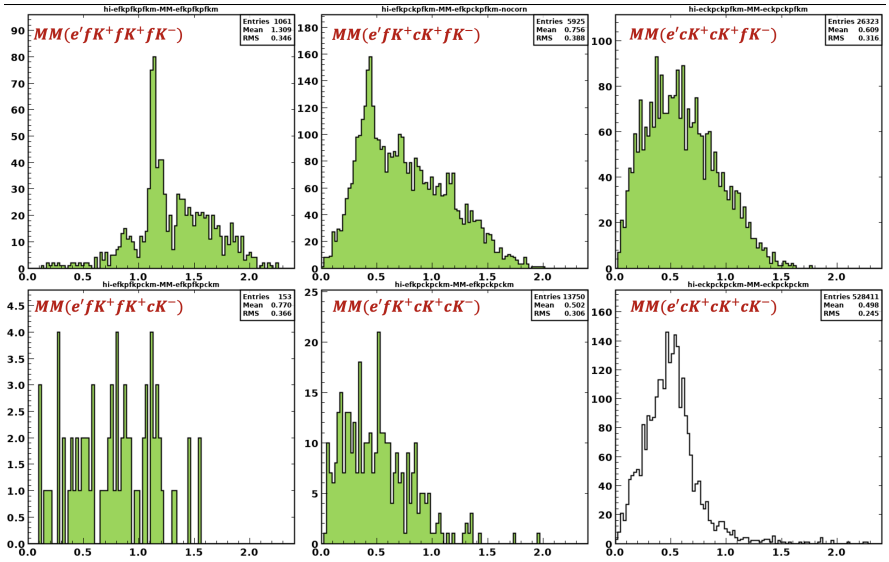

(a) Fall 2018 outbending FD-e.

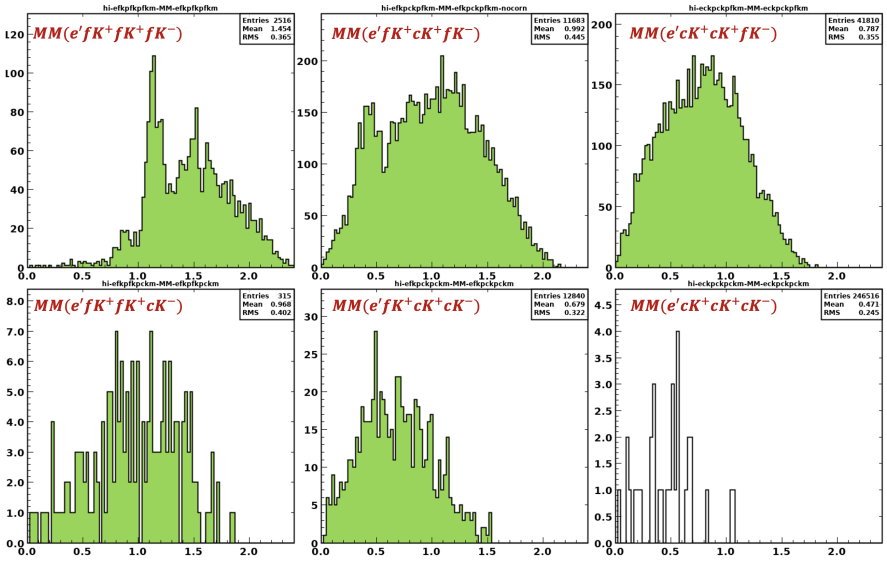

(b) Fall 2018 outbending FT-e.

Figure 1: $MM(e'K^+K^+K^-)$ distributions with kaons detected in the different parts (CD/FD) of CLAS12. $cK^\pm$ and $fK^\pm$ refers to charged kaons detected in the CD and FD, respectively. $MM(e'fK^+fK^+fK^-)$, $MM(e'fK^+cK^+fK^-)$, and $MM(e'cK^+cK^+fK^-)$ are shown in the top row and $MM(e'fK^+fK^+cK^-)$, $MM(e'fK^+cK^+cK^-)$, and $MM(\ e'cK^+cK^+cK^-)$ are shown in the bottom row, respectively, from left to right. Figs. 1a and 1b are for the Fall 2018 outbending data set with the electron detected in the FD and FT, respectively. The set of missing mass plots with at least one kaon in the CD does not show clear Λ/Σ^0 peaks because of issues in the CD leading to the particle misidentification, poor CD momentum resolution, and misalignment of the CLAS12 subsystems (CD, FD, and FT) with respect to the target position in the pass-1 data.

Preliminary $MM(e'K^+K^+K^-)$ Distributions

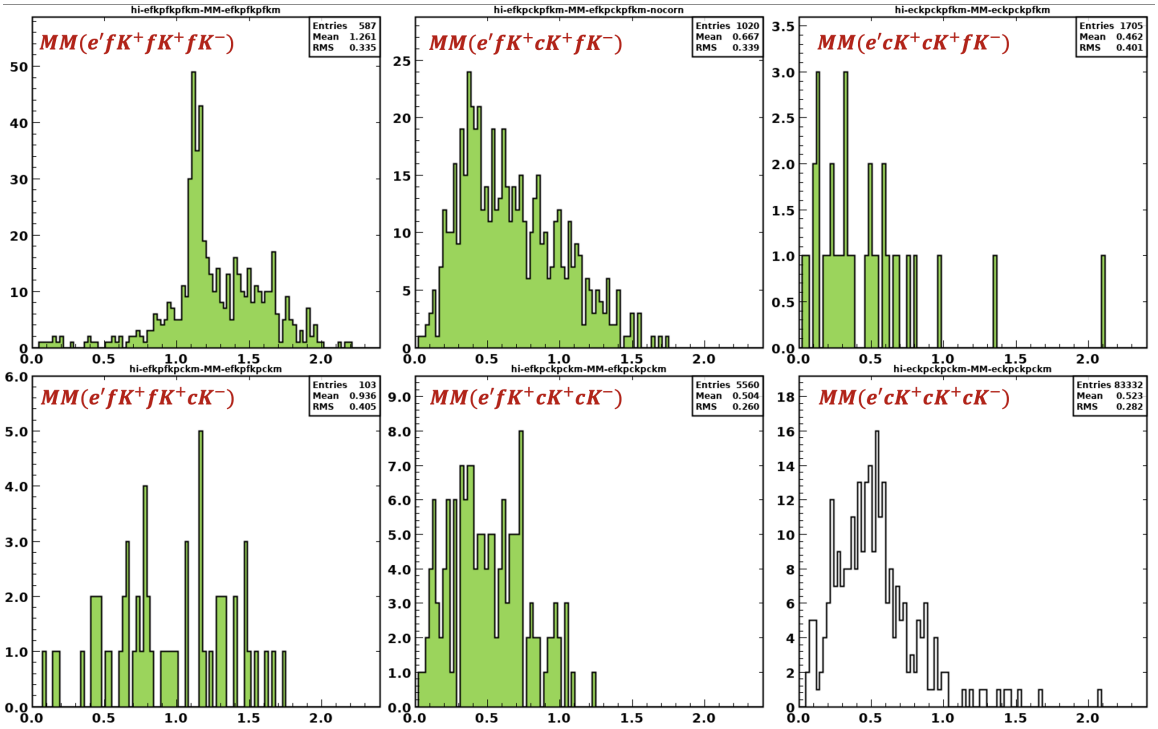

(a) Fall 2018 inbending FD-e.

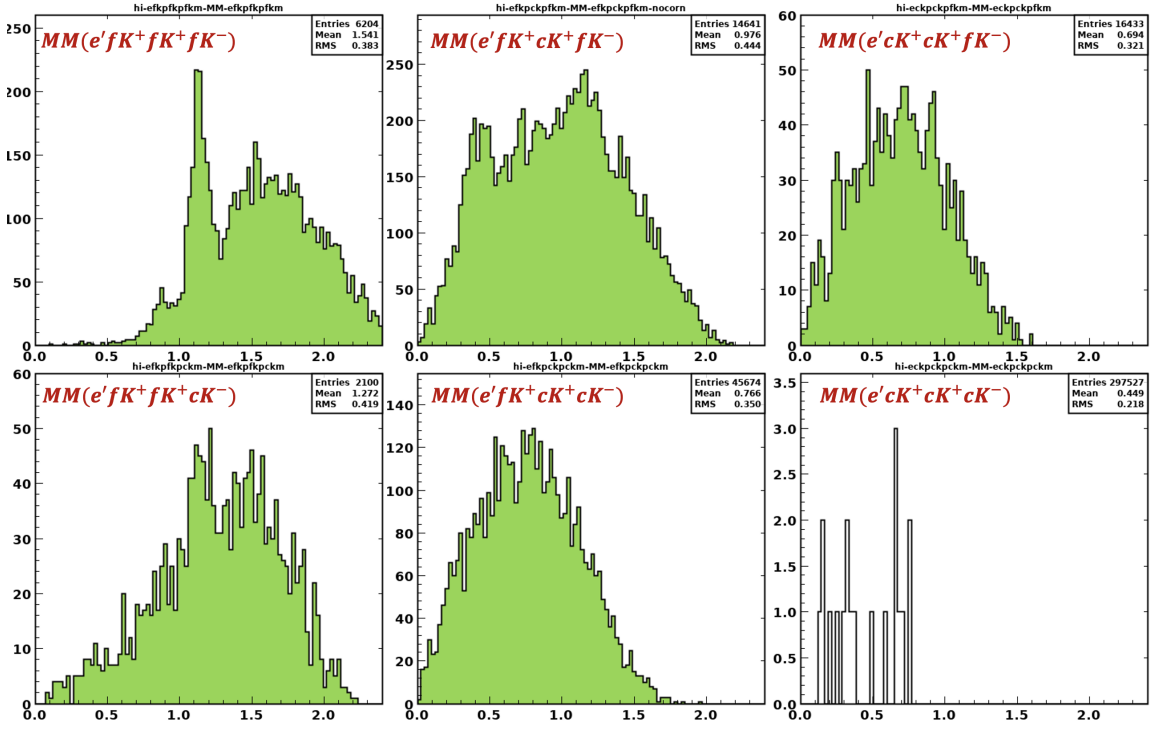

(b) Fall 2018 inbending FT-e.

Figure 2: Same as Fig. 1 but for the Fall 2018 inbending data set.

Preliminary $MM(e'K^+K^+K^-)$ Distributions

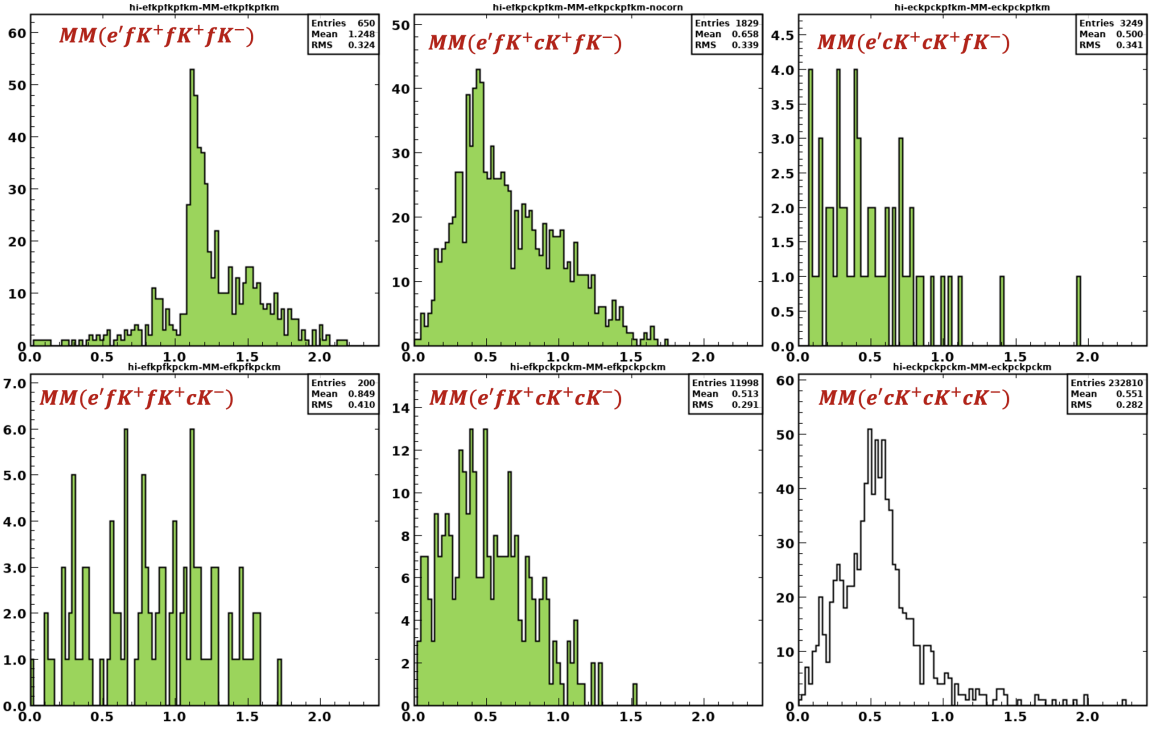

(a) Spring 2019 inbending FD-e.

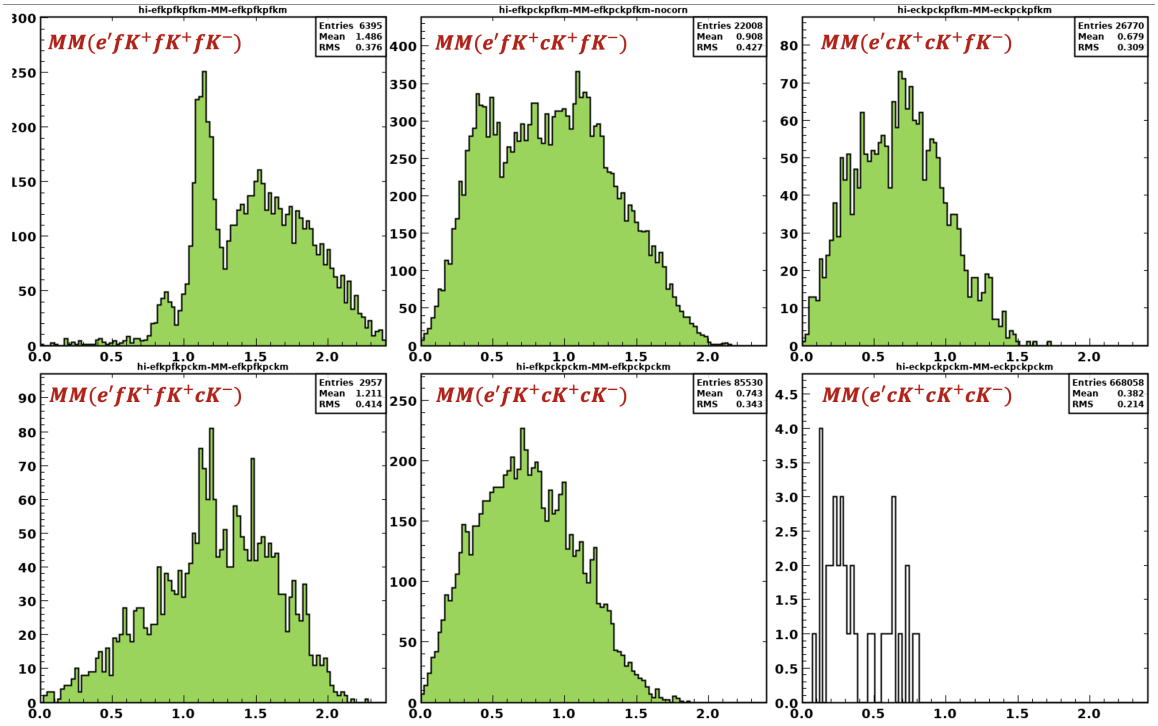

(b) Spring 2019 inbending FT-e.

Figure 3: Same as Fig. 1 but for the Spring 2019 inbending data set.

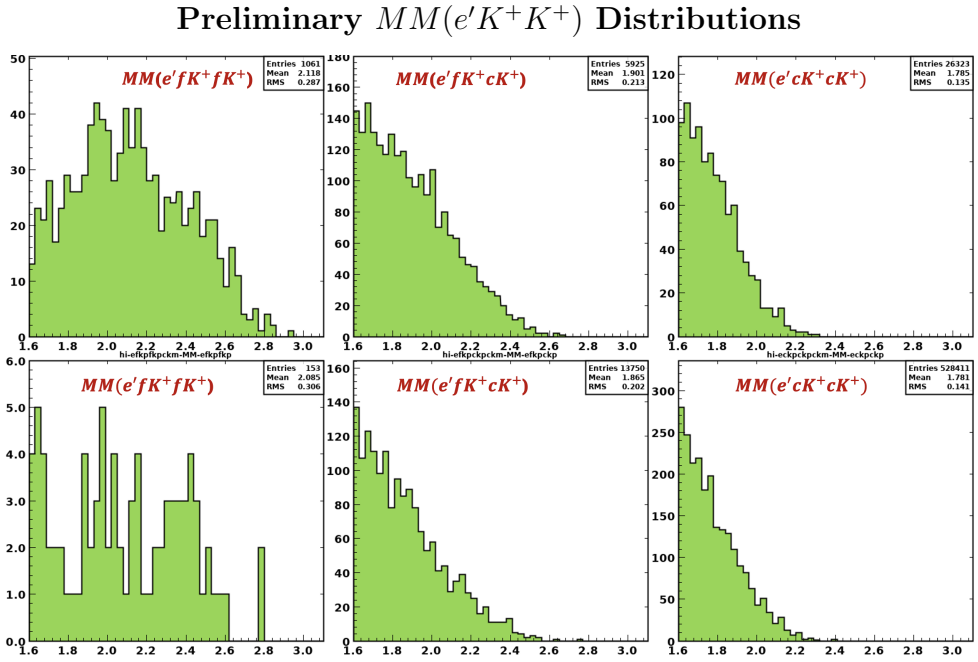

(a) Fall 2018 outbending FD-e.

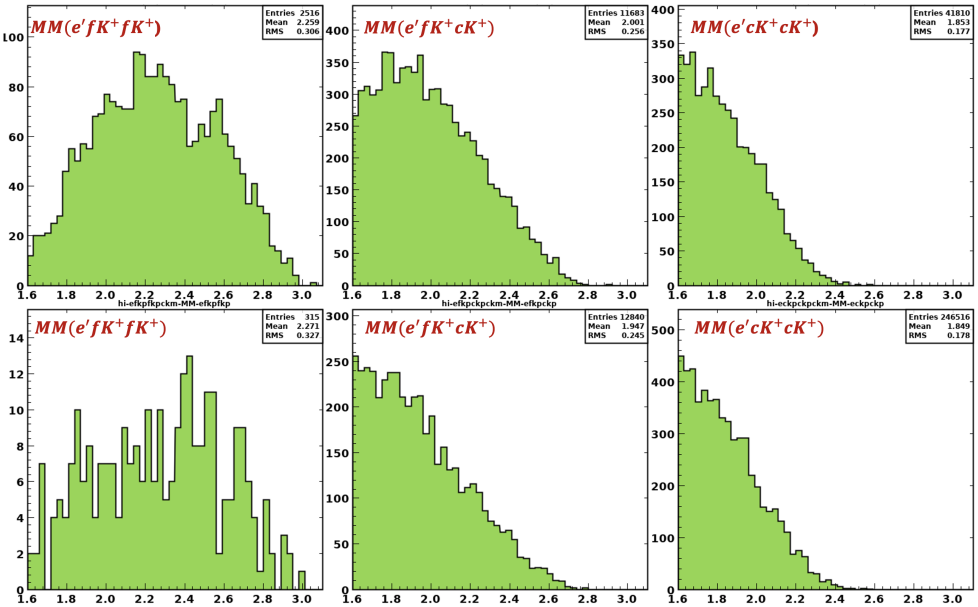

(b) Fall 2018 outbending FT-e.

Figure 4: $MM(e'K^+K^+)$ distributions with two K^+ and one K^- detected in the different parts (CD/FD) of CLAS12. $cK^\pm$ and $fK^\pm$ refers to charged kaons detected in the CD and FD, respectively. $MM(e'fK^+fK^+)$, $MM(e'fK^+cK^+)$, and $MM(e'cK^+cK^+)$ are shown in the top row from left to right for an additional K^- detected in the FD and $MM(e'fK^+fK^+)$, $MM(e'fK^+cK^+)$, and $MM(e'cK^+cK^+)$ are shown in the bottom row from left to right for an additional K^- detected in the CD. Figs. 4a and 4b are for the Fall 2018 outbending data set with the electron detected in the FD and FT, respectively.

Preliminary $MM(e'K^+K^+)$ Distributions

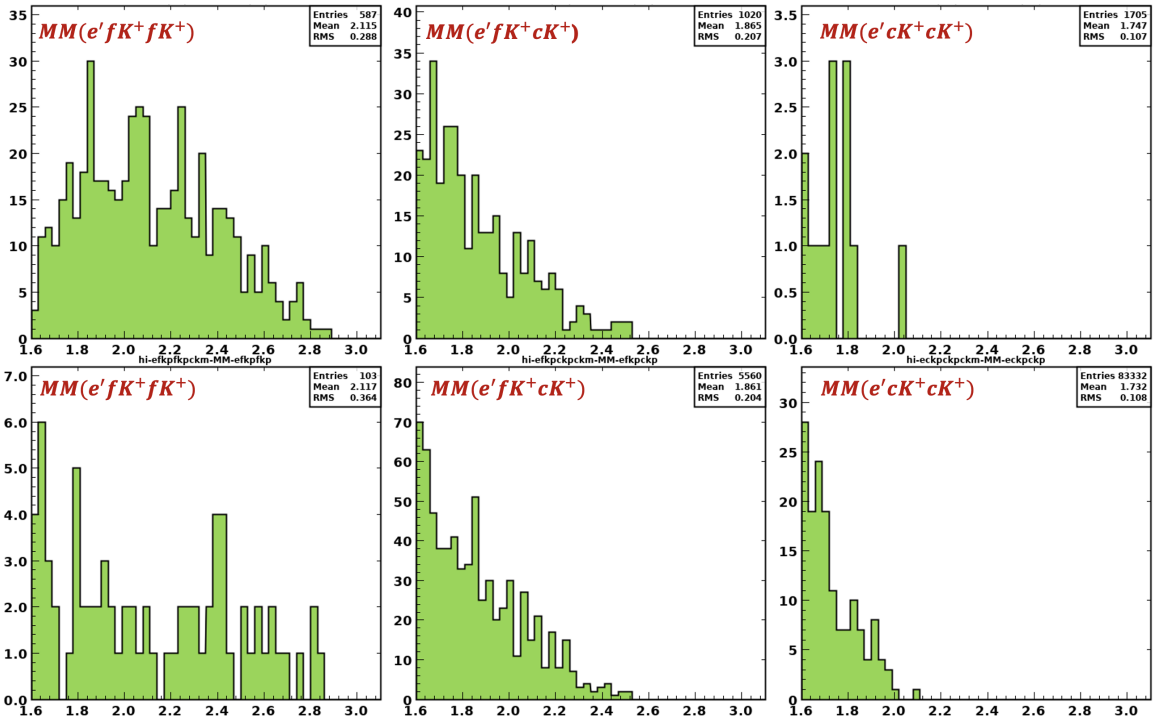

(a) Fall 2018 inbending FD-e.

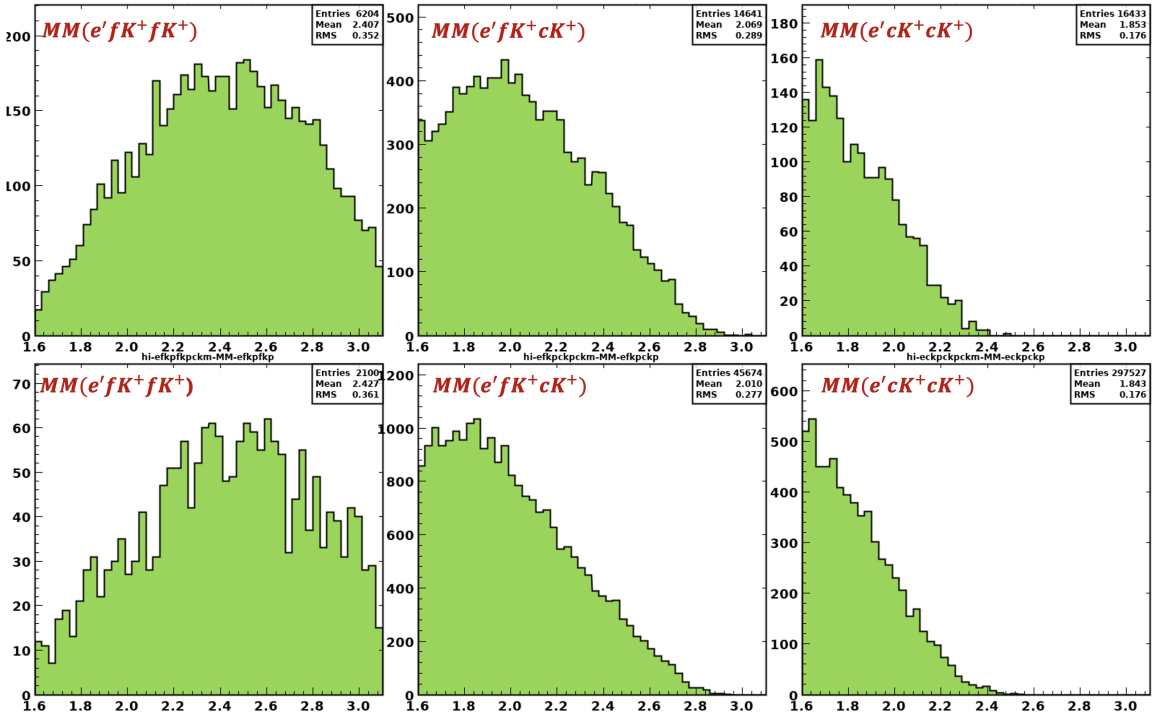

(b) Fall 2018 inbending FT-e.

Figure 5: Same as Fig. 4 but for the Fall 2018 inbending data set.

Preliminary $MM(e'K^+K^+)$ Distributions

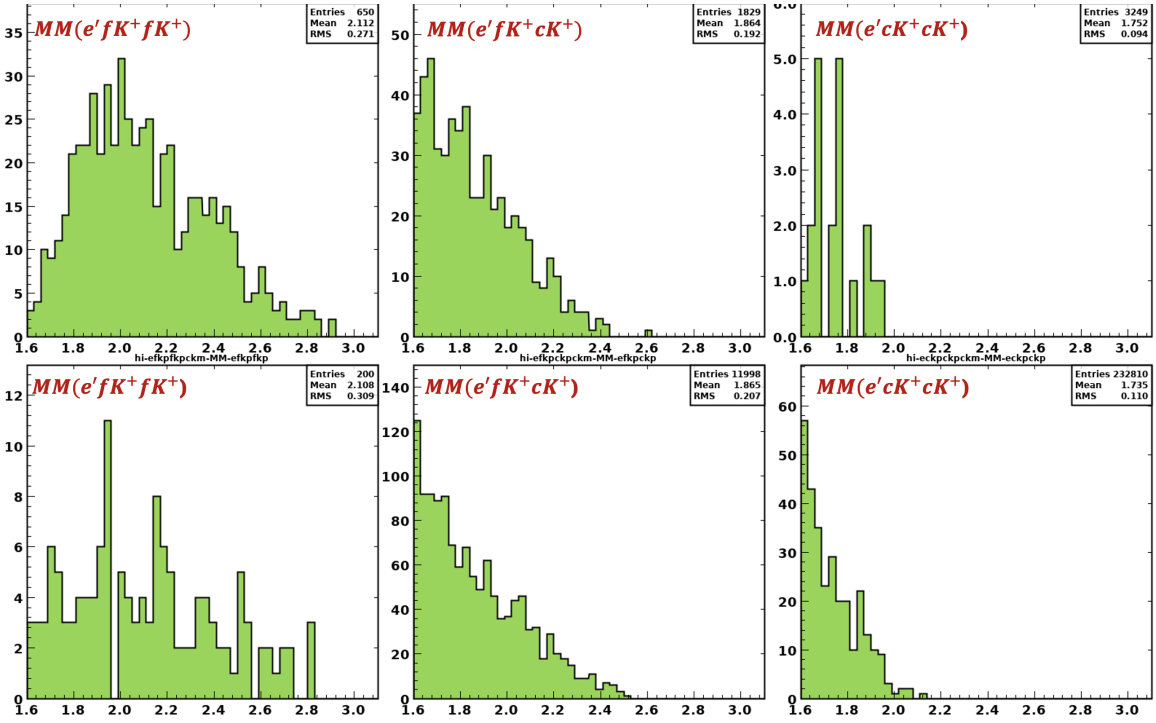

(a) Spring 2019 inbending FD-e.

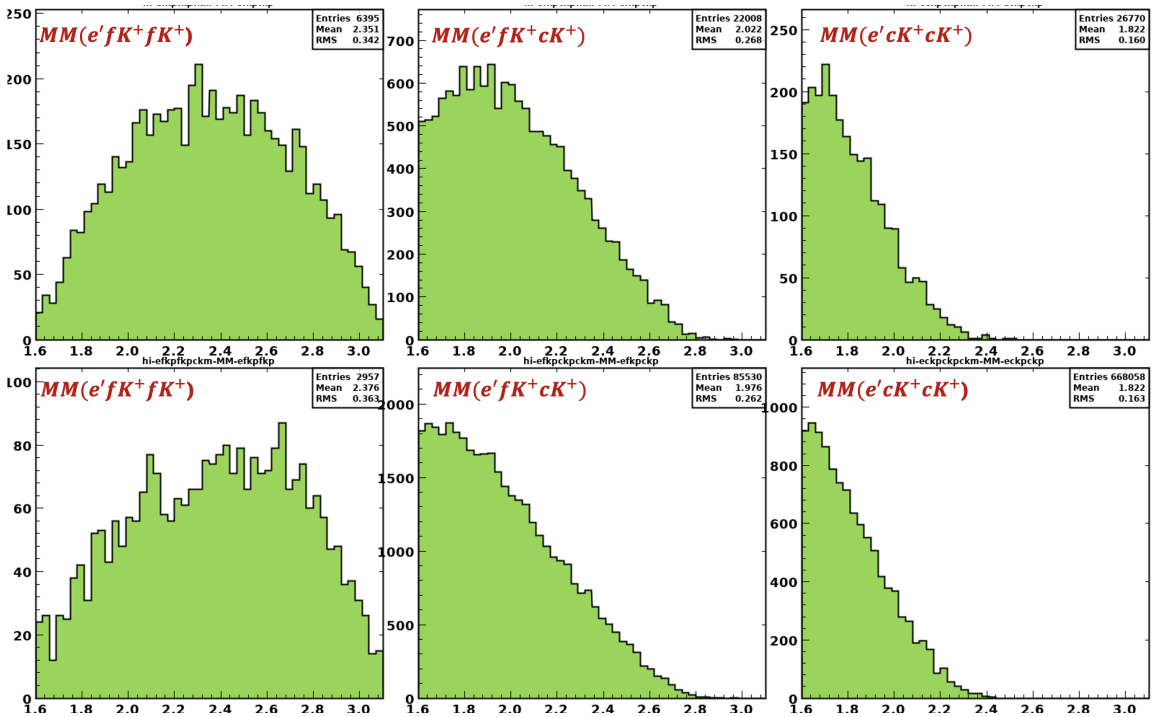

(b) Spring 2019 inbending FT-e.

Figure 6: Same as Fig. 4 but for the Spring 2019 inbending data set.

Preliminary $MM(e'K^+K^+)$ vs. $MM(e'K^+K^+K^-)$ Distributions

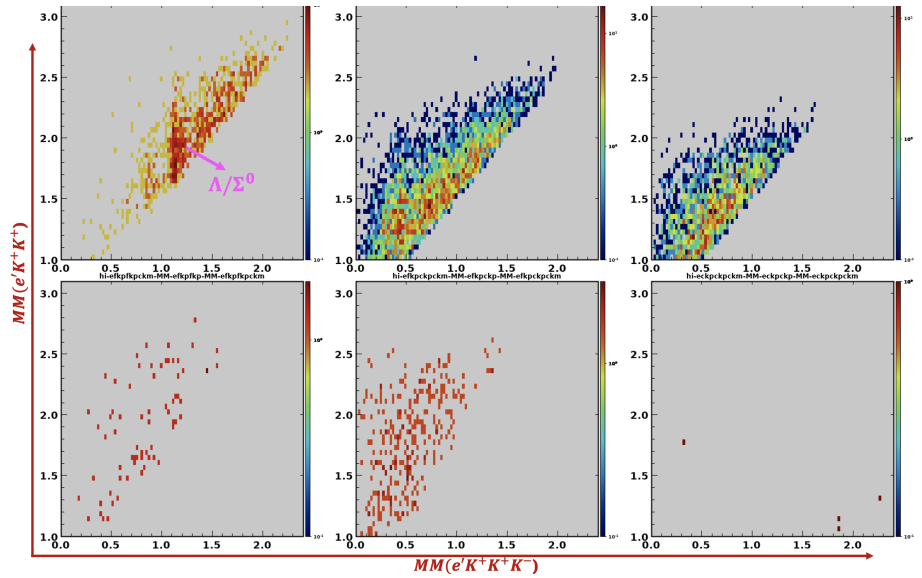

(a) Fall 2018 outbending FD-e.

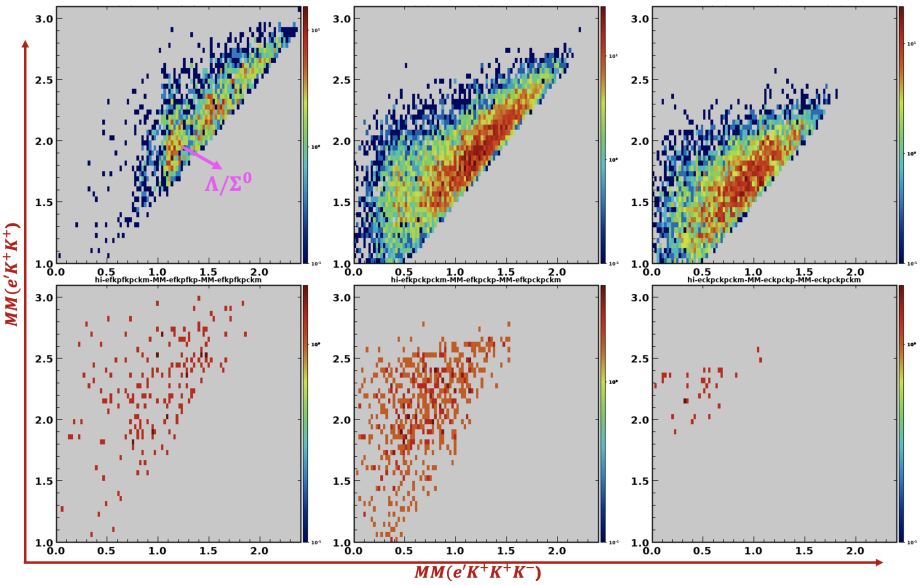

(b) Fall 2018 outbending FT-e.

Figure 7: $MM(e'K^+K^+)$ vs. $MM(e'K^+K^+K^-)$ scatterplots with kaons detected in the different parts (CD/FD) of CLAS12. $cK^\pm$ and $fK^\pm$ refers to charged kaons detected in the CD and FD, respectively. $MM(e'fK^+fK^+)$ vs. $MM(e'fK^+fK^+fK^-)$, $MM(e'fK^+cK^+)$ vs. $MM(e'fK^+cK^+fK^-)$, and $MM(e'cK^+cK^+)$ vs. $MM(e'cK^+cK^+fK^-)$ are shown in the top row and $MM(e'fK^+fK^+)$ vs. $MM(e'fK^+fK^+cK^-)$, $MM(e'fK^+cK^+)$ vs. $MM(e'fK^+cK^+c\ K^-)$, and $MM(e'cK^+cK^+)$ vs. $MM(e'cK^+cK^+cK^-)$ are shown in the bottom row, respectively, from left to right. Figs. 7a and 7b are for the Fall 2018 outbending data set with the electron detected in the FD and FT, respectively.

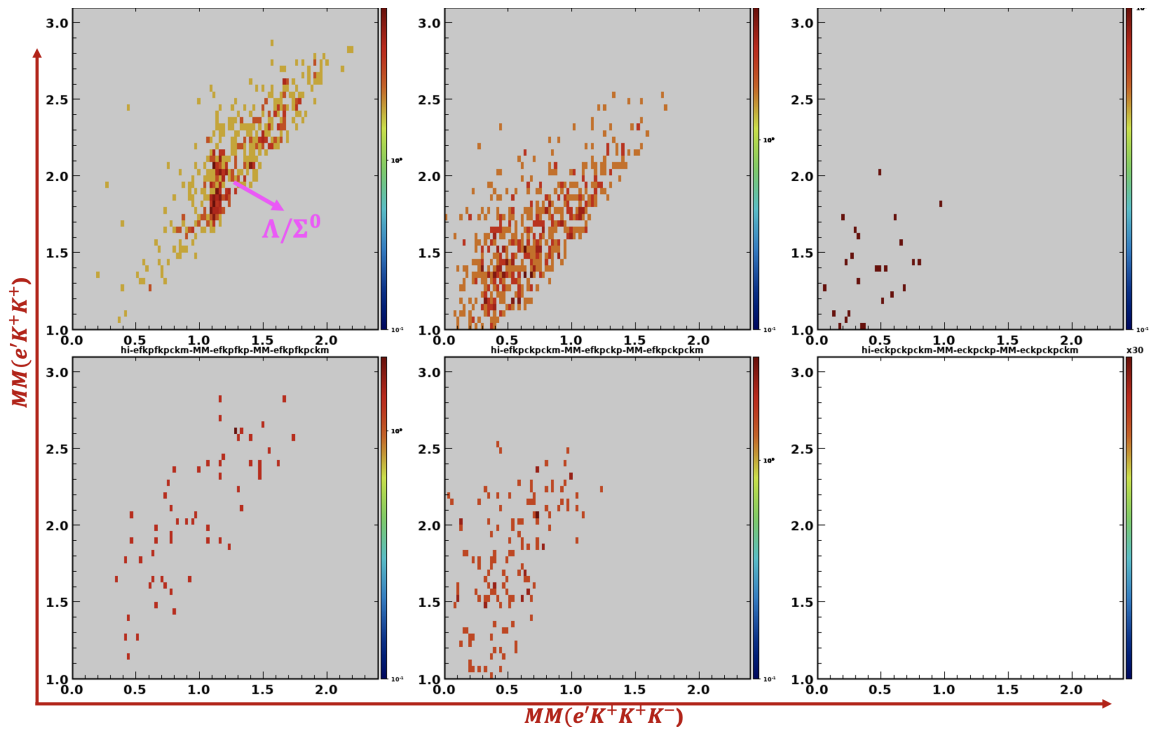

(a) Fall 2018 inbending FD-e.

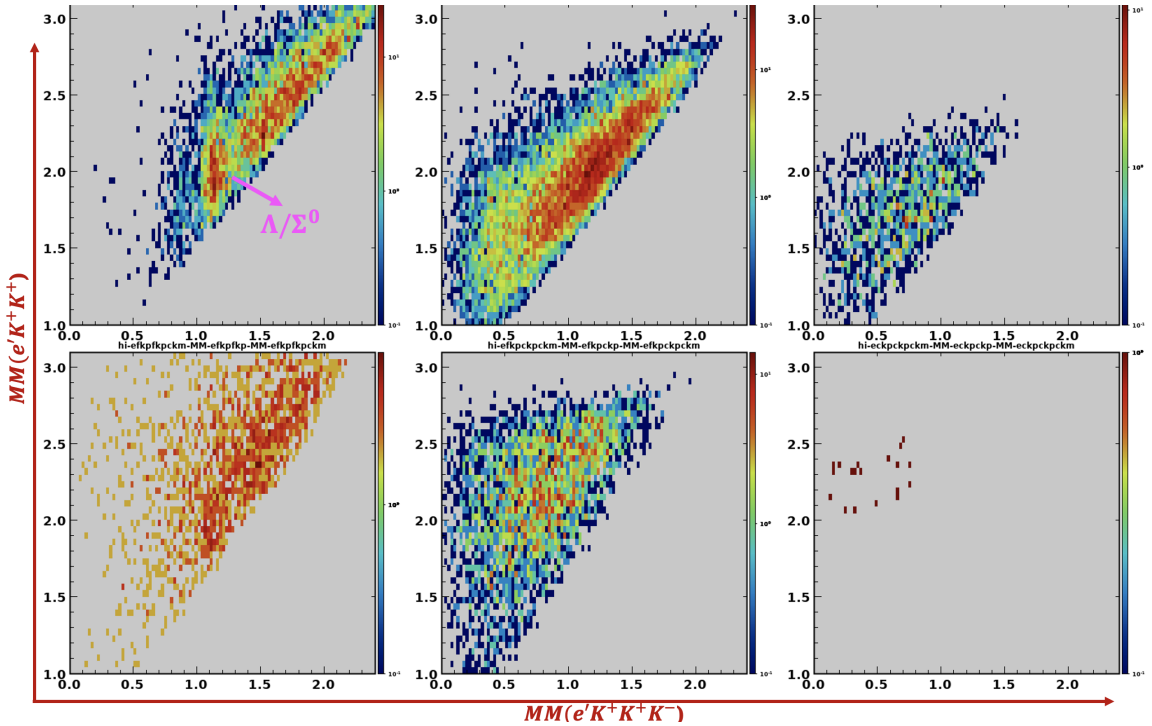

(b) Fall 2018 inbending FT-e.

Figure 8: Same as Fig. 7 but for the Fall 2018 inbending data set.

Preliminary $MM(e'K^+K^+)$ vs. $MM(e'K^+K^+K^-)$ Distributions

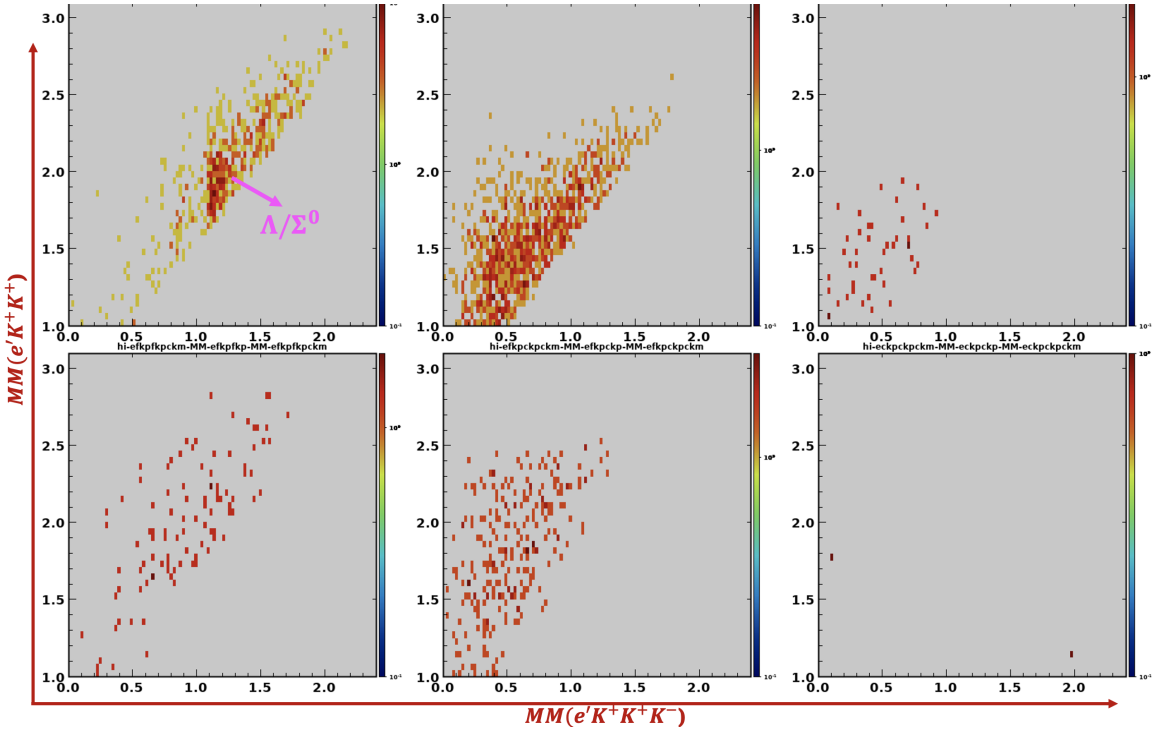

(a) Spring 2019 inbending FD-e.

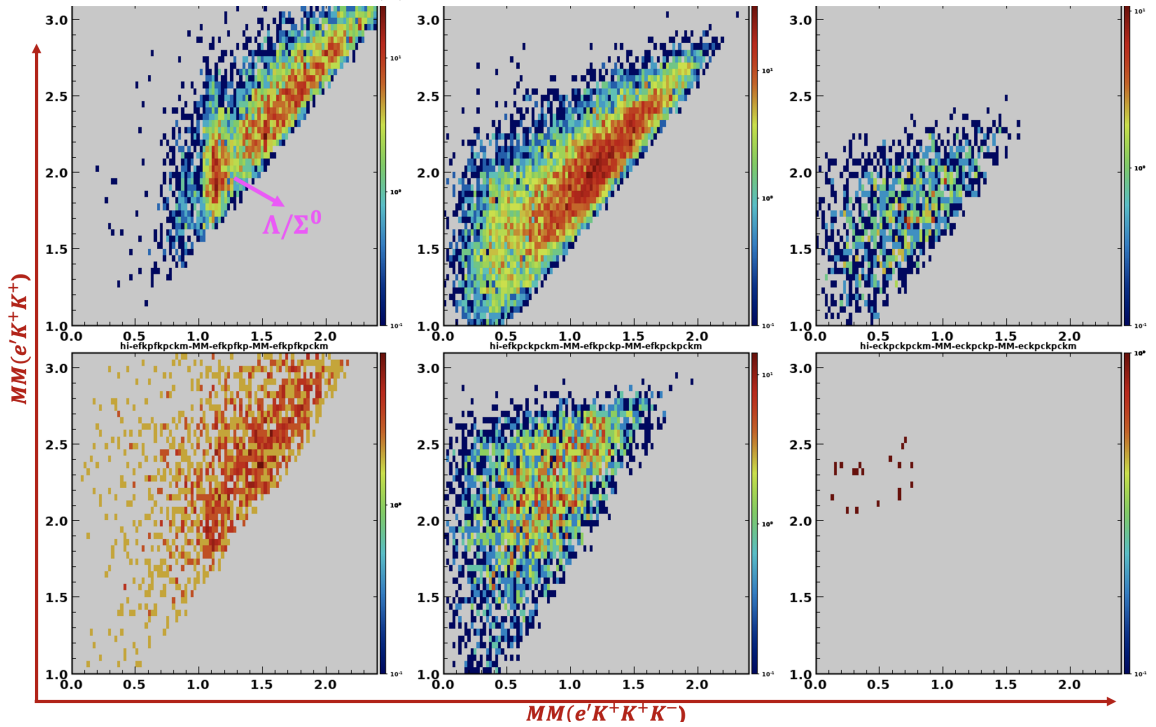

(b) Spring 2019 inbending FT-e.

Figure 9: Same as Fig. 7 but for the Spring 2019 inbending data set.

VITA

ACHYUT KHANAL

2006 - 2010	B.S., Physics Tribhuvan University Kirtipur, Nepal
2010 - 2013	M.S., Physics Tribhuvan University Kirtipur, Nepal
2015 - 2019	M.S., Physics Florida International University Miami, Florida
2015 - 2022	Ph.D. Candidate, Physics Florida International University Miami, Florida

PRINCIPAL PUBLICATIONS AND PRESENTATIONS

1. A. Khanal, L. Guo, B. Raue *et al.* (CLAS Collaboration),"*Search for intermediate cascade Ξ state in the reaction $ep \to e^{'}K^{+}K^{+}K^{-}(\Lambda/\Sigma^{0})$ using CLAS12*," DNP meeting, Bulletin of the American Physical Society 66(2021).

2. A. Khanal, L. Guo, B. Raue *et al.* (CLAS Collaboration),"*Excited Cascade (Ξ) Hyperons search in the reaction $ep \to e^{'}K^{+}K^{+}K^{-}(\Lambda/\Sigma^{0})$ using CLAS12*," Poster, The Gordon Research Conference on Photonuclear Reactions, Holderness, NH, August 2022.

3. V. D. Burkert *et al.* (CLAS Collaboration), "*The CLAS12 Spectrometer at Jefferson Laboratory*," Nucl. Inst. and Meth. A 959, 163419(2020).

4. D. S. Carman *et al.* (CLAS Collaboration), "*Beam-Recoil Transferred Polarization in $K^{+}Y$ Electroproduction in the Nucleon Resonance Region with CLAS12*," Phys. Rev. C 105, 065201(2022).

5. P. Chatagnon *et al.* (CLAS Collaboration), "*First measurement of Timelike Compton Scattering*," Phys. Rev. Lett. 127, 262501(2021).

6. T. B. Hayward *et al.* (CLAS Collaboration), "*Observation of Beam Spin Asymmetries in the Process* $ep \to e^{'}\pi^{+}\pi^{-}X$ *with CLAS12*," Phys. Rev. Lett. 126, 152501(2021).

7. S. J. Paul *et al.* (CLAS Collaboration), "*Alignment of the CLAS12 central hybrid tracker with a Kalman Filter*," arXiv preprint arXiv:2208.05054 (2022).

8. H. Avakian *et al.* (CLAS Collaboration), "*First observation of correlations between spin and transverse momenta in back-to-back dihadron production at CLAS12*," arXiv preprint arXiv:2208.05086 (2022).

9. S. Diehl *et al.* (CLAS Collaboration), "*A multidimensional study of the structure function ratio* $\sigma_{LT'}/\sigma_0$ *from hard exclusive* π^+ *electro-production off protons in the GPD regime*," arXiv preprint arXiv:2210.14557 (2022).

10. D. Bhetuwal *et al.* (Jefferson Lab Hall C Collaboration), "*Ruling out Color Transparency in Quasielastic* $^{12}C(e,e^{'}p)$ *up to* Q^2 *of* 14.2 *(GeV/c)*^{2}," Phys. Rev. Lett. 126, 082301(2021).

11. R. Cruz-Torres *et al.* (Jefferson Lab Hall A Tritium Collaboration), "*Probing Few-Body Nuclear Dynamics via* $3H$ *and* $3He(e,e^{'}p)pn$ *Cross-Section Measurements*," Phys. Rev. Lett. 124, 212501(2020).

12. C. Yero *et al.* (Jefferson Lab Hall C Collaboration), "*Probing the Deuteron at Very Large Internal Momenta*," Phys. Rev. Lett. 125, 262501(2020).